

Hydrometeorological Applications: Severe Weather Precipitation Detection, Estimation, and Forecast

Guest Editors: Youcun Qi, Qing Cao, Bin Yong, Ke Zhang, and Zhe Li





Hydrometeorological Applications: Severe Weather Precipitation Detection, Estimation, and Forecast

Advances in Meteorology

Hydrometeorological Applications: Severe Weather Precipitation Detection, Estimation, and Forecast

Guest Editors: Youcun Qi, Qing Cao, Bin Yong, Ke Zhang,
and Zhe Li



Copyright © 2017 Hindawi. All rights reserved.

This is a special issue published in "Advances in Meteorology." All articles are open access articles distributed under the Creative Commons Attribution License, which permits unrestricted use, distribution, and reproduction in any medium, provided the original work is properly cited.

Editorial Board

J. Antonio Adame, Spain	Roberto Fraile, Spain	Samantha Melani, Italy
Cesar Azorin-Molina, Sweden	Charmaine Franklin, Australia	Nicholas Meskhidze, USA
Guillermo Baigorria, USA	Jan Friesen, Germany	Christophe Messager, France
Marina Baldi, Italy	M. Ángeles García, Spain	Mario M. Miglietta, Italy
A. Bentamy, France	H. García Mozo, Spain	Takashi Mochizuki, Japan
Massimo A. Bollasina, UK	E. García-Ortega, Spain	Goro Mouri, Japan
Stefania Bonafoni, Italy	Luis Gimeno, Spain	Brian R. Nelson, USA
Isabella Bordi, Italy	Jorge E. Gonzalez, USA	E. I. Nikolopoulos, USA
Claudio Carbone, Italy	Ismail Gultepe, Canada	Sandip Pal, USA
Dominique Carrer, France	Rafiq Hamdi, Belgium	Giulia Panegrossi, Italy
Charles Chemel, UK	Adel Hanna, USA	Giulia Pavese, Italy
Annalisa Cherchi, Italy	Hiroyuki Hashiguchi, Japan	Kyaw T. Paw, USA
James Cleverly, Australia	Tareq Hussein, Jordan	Olivier P. Prat, USA
Jill S. M. Coleman, USA	Bradley G. Illston, USA	Sara C. Pryor, USA
Gabriele Curci, Italy	Ivar S A Isaksen, Norway	Philippe Ricaud, France
Mladjen Ćurić, Serbia	P. Jiménez-Guerrero, Spain	Tomeu Rigo, Spain
Maher A. Dayeh, USA	Kuruvilla John, USA	Filomena Romano, Italy
Klaus Dethloff, Germany	George Kallos, Greece	Haydee Salmun, USA
P. CS Devara, India	Harry D. Kambezidis, Greece	Pedro Salvador, Spain
Paolo Di Girolamo, Italy	Nir Y. Krakauer, USA	Andres Schmidt, Germany
Julio Diaz, Spain	Hisayuki Kubota, Japan	Shraddhanand Shukla, USA
Arona Diedhiou, France	Haim Kutiel, Israel	Fiona Smith, UK
Stefano Dietrich, Italy	Richard Leaitch, Canada	Francisco J. Tapiador, Spain
E. D. Vilches, Spain	Monique Leclerc, USA	Yoshihiro Tomikawa, Japan
Antonio Donateo, Italy	Ilan Levy, Israel	Tomoo Ushio, Japan
Igor Esau, Norway	Gwo-Fong Lin, Taiwan	Rogier Van Der Velde, Netherlands
Stefano Federico, Italy	Anthony R. Lupo, USA	Francesco Viola, Italy
Enrico Ferrero, Italy	Paolo Madonia, Italy	Alastair Williams, Australia
Rossella Ferretti, Italy	A. Matzarakis, Germany	Olga Zolina, France

Contents

Hydrometeorological Applications: Severe Weather Precipitation Detection, Estimation, and Forecast

Youcun Qi, Qing Cao, Bin Yong, Ke Zhang, and Zhe Li
Volume 2017, Article ID 8365319, 2 pages

Two Different Integration Methods for Weather Radar-Based Quantitative Precipitation Estimation

Jing Ren, Yong Huang, Li Guan, and Jie Zhou
Volume 2017, Article ID 1269748, 12 pages

An Integrated Method of Multiradar Quantitative Precipitation Estimation Based on Cloud Classification and Dynamic Error Analysis

Yong Huang, Huijuan Liu, Yun Yao, Ting Ni, and Yan Feng
Volume 2017, Article ID 1475029, 6 pages

Statistical Comparison of Cloud and Aerosol Vertical Properties between Two Eastern China Regions Based on CloudSat/CALIPSO Data

Yujun Qiu, Jing Wang, and Keran Yang
Volume 2017, Article ID 5204537, 12 pages

Early Detection of Baby-Rain-Cell Aloft in a Severe Storm and Risk Projection for Urban Flash Flood

Eiichi Nakakita, Hiroto Sato, Ryuta Nishiwaki, Hiroyuki Yamabe, and Kosei Yamaguchi
Volume 2017, Article ID 5962356, 15 pages

Evaluation of TRMM Multisatellite Precipitation Analysis in the Yangtze River Basin with a Typical Monsoon Climate

Zengxin Zhang, Qiu Jin, Xi Chen, Chong-Yu Xu, Sheng Chen, Elica M. Moss, and Yuhan Huang
Volume 2016, Article ID 7329765, 13 pages

Flood Forecasting Based on TIGGE Precipitation Ensemble Forecast

Jinyin Ye, Yuehong Shao, and Zhijia Li
Volume 2016, Article ID 9129734, 9 pages

Radar-Derived Quantitative Precipitation Estimation Based on Precipitation Classification

Lili Yang, Yi Yang, Peng Liu, and Lina Wang
Volume 2016, Article ID 2457489, 16 pages

Mesoscale and Local Scale Evaluations of Quantitative Precipitation Estimates by Weather Radar Products during a Heavy Rainfall Event

Basile Pauthier, Benjamin Bois, Thierry Castel, D. Thévenin, Carmela Chateau Smith, and Yves Richard
Volume 2016, Article ID 6089319, 9 pages

Evaluation and Correction of Quantitative Precipitation Forecast by Storm-Scale NWP Model in Jiangsu, China

Gaili Wang, Dan Wang, Ji Yang, and Liping Liu
Volume 2016, Article ID 8476720, 13 pages

Editorial

Hydrometeorological Applications: Severe Weather Precipitation Detection, Estimation, and Forecast

Youcun Qi,¹ Qing Cao,² Bin Yong,³ Ke Zhang,⁴ and Zhe Li¹

¹Key Laboratory of Water Cycle and Related Land Surface Processes, Institute of Geographic Sciences and Natural Resources Research, Chinese Academy of Sciences, Beijing, China

²Enterprise Electronics Corporation, Norman, OK, USA

³Earth System Science Interdisciplinary Center (ESSIC), College Park, MD, USA

⁴State Key Laboratory of Hydrology-Water Resources and Hydraulic Engineering and College of Hydrology and Water Resources, Hohai University, 1 Xikang Road, Nanjing, Jiangsu Province 210098, China

Correspondence should be addressed to Youcun Qi; youcun.qi@gmail.com

Received 2 April 2017; Accepted 2 April 2017; Published 15 May 2017

Copyright © 2017 Youcun Qi et al. This is an open access article distributed under the Creative Commons Attribution License, which permits unrestricted use, distribution, and reproduction in any medium, provided the original work is properly cited.

Severe weather with heavy precipitation could bring unexpected hydrometeorological hazards, such as flash floods and landslides, which might become disasters and cause significant injuries, deaths, infrastructure damage, transportation paralysis, and/or many other problems. These natural hazards occur all over the world, although their frequency and intensity are quite different from region to region. Therefore, it is critically important to accurately monitor and estimate the heavy precipitation so that the occurrence and intensity of associated hydrometeorological hazards can be well identified, detected, and forecasted. Currently, the most powerful technique to monitor and study the severe weather is remote sensing (e.g., radar). Associated observations on the ground are necessary for calibrating remote sensing products, providing accurate and high-resolution precipitation estimates, improving the accuracy flash flood forecasting, and enhancing the understanding of causation and geophysical processes of these natural hazards.

Many regions in the world experience severe thunderstorms and violent tornadoes every year. In the United States (US), there are 58 tornadoes that occurred in Oklahoma only on May 03, 1999, and 45 people died and more than 600 got injured [1]. Throughout the severe weather events, the US emergency managers (EMs) use a variety of information sources, particularly radar products [2, 3], and the radar algorithms, attempting to detect, classify, and track the presence of severe thunderstorm cells, mesocyclone circulations, tornadic vortex signatures, downbursts/microbursts, and

hail, among others. The severe weather detection algorithms are based on radar observations and developed suites of severe weather and aviation products [3]. The severe weather detection algorithms have evolved over years, even though the designs between the algorithms and the configurations are different. Severe weather usually comes with heavy precipitation and causes flash floods or landslides. Zhang et al. (2016) [4] developed the Multiradar Multisensor (MRMS) system to generate a suite of quantitative precipitation estimation (QPE) product with very high spatial (1 km) and temporal (2 min) resolutions. The generated QPE products are used to improve the tools for flash flood monitoring and prediction across the US [5–7]. This special issue includes selected articles that report recent investigations/advances in *Severe Weather Precipitation Detection, Estimation, and Forecast* through observational and numerical approaches.

Tropical rainfall generally has high-efficiency precipitation and may cause heavy precipitation in a short time. However, it cannot be directly reflected in the reflectivity field because the raindrop size is relatively small. L. Yang et al. proposed one algorithm for improving the radar-derived QPE based on the vertical profile of reflectivity (VPR). Upon identifying a tropical VPR, the rainfall is classified as either tropical-stratiform or tropical-convective rainfall by a fuzzy logic (FL) algorithm. The results show that the rainfall rates match closely the gauge observations. Y. Huang et al. developed one classification system and flagged the precipitation types into five categories with radar and

satellite data, which finally improved the accuracy of radar QPE.

Satellite-based precipitation products are expected to offer an alternate to ground-based rainfall estimates in the present and the foreseeable future. Z. Zhang et al. evaluated the performance of TRMM 3B42 precipitation products in the Yangtze River basin for the period of 2003~2010 and suggested that more attention should be paid to the influence of complex climate and topography. In northeastern France on Nov 03-04 2014, a 24-hour heavy rainfall event occurred. B. Pauthier et al. evaluated the accuracy of radar QPE at both mesoscale and local scales with two sets of rain gauge observations and suggested that the merged products could be invaluable for applications at very high resolution. With the development of high-performance computer systems and data assimilation techniques, storm-scale numerical weather prediction (NWP) models are gradually used for short-term deterministic forecasts. G. Wang et al. evaluated and corrected the precipitation forecasts of a storm-scale NWP model called the advanced regional prediction system (ARPS).

In July 2008, five people were killed by a tragic flash flood caused by a local torrential heavy rainfall in a short time in Toga River. E. Nakakita et al. analyzed this event and verified that the first radar echo aloft could be a practical and important sign for early warning of flash flood. Development of meteorological-hydrologic coupled flood forecasting model and early warning model based on the TIGGE precipitation ensemble forecast can provide the flood probability forecast, extend the lead time of flood forecast, and gain more time for decision-makers to make the right decision. In this study, precipitation ensemble forecast products from ECMWF, NCEP, and CMA were used to derive distributed hydrologic model TOPX. J. Ye et al. developed one flood forecast and early warning system for Yi River catchment.

Aerosol properties are closely related to cloud generation and severe weather precipitation. Y. Qiu et al. extracted the cloud and aerosol profiles properties with The Cloud-Sat/CALIPSO data. They found that the mean value of cloud occurrence probability (COP) was the highest in the mixed cloud layer ($-40^{\circ}\text{C} \sim 0^{\circ}\text{C}$) and the lowest in the warm cloud layer ($>0^{\circ}\text{C}$). The atmospheric humidity was more statistically relevant to COP in the warm cloud layer than aerosol condition. The differences in COP between the two regions in the mixed cloud layer and ice cloud layer ($<-40^{\circ}\text{C}$) had good correlations with those in the aerosol extinction coefficient. A radar reflectivity factor greater than -10 dBZ occurred mainly in warm cloud layers and mixed cloud layers.

There is no doubt that there are much more studies representing recent advances and research directions in Severe Weather Precipitation Detection, Estimation, and Forecast. However, the papers collected in this special issue cover a wide range of research topics and shed light on some of recent progress and ideas in the field. It will serve as valuable asset for the scientists and engineers in hydrometeorology and related fields.

Acknowledgments

We thank all the authors who contributed to this issue and all the reviewers who provide valuable, constructive comments to the manuscripts and help to improve the quality of these papers published in this issue.

Youcun Qi
Qing Cao
Bin Yong
Ke Zhang
Zhe Li

References

- [1] S. Brown, P. Archer, E. Kruger, and S. Mallonee, "Tornado-related deaths and injuries on Oklahoma due to the 3 May 1999 tornadoes," *Weather and Forecasting*, vol. 17, no. 3, pp. 343–353, 2002.
- [2] P. Joe, D. Burgess, R. Potts, T. Keenan, G. Stumpf, and A. Treloar, "The S2K severe weather detection algorithms and their performance," *Weather and Forecasting*, vol. 19, no. 1, pp. 43–63, 2004.
- [3] T. M. Smith, V. Lakshmanan, G. J. Stumpf et al., "Multi-Radar Multi-Sensor (MRMS) severe weather and aviation products: initial operating capabilities," *Bulletin of the American Meteorological Society*, vol. 97, no. 9, pp. 1617–1630, 2016.
- [4] J. Zhang, K. Howard, C. Langston et al., "Multi-Radar Multi-Sensor (MRMS) quantitative precipitation estimation: initial operating capabilities," *Bulletin of the American Meteorological Society*, vol. 97, no. 4, pp. 621–638, 2016.
- [5] J. J. Gourley, Z. L. Flamig, H. Vergara et al., "The FLASH Project: improving the tools for flash flood monitoring and prediction across the united states," *Bulletin of the American Meteorological Society*, vol. 98, no. 2, pp. 361–372, 2017.
- [6] S. Zhang and H. Gao, "A novel algorithm for monitoring reservoirs under all-weather conditions at a high temporal resolution through passive microwave remote sensing," *Geophysical Research Letters*, vol. 43, no. 15, pp. 8052–8059, 2016.
- [7] S. Zhang, H. Gao, and B. S. Naz, "Monitoring reservoir storage in South Asia from multisatellite remote sensing," *Water Resources Research*, vol. 50, no. 11, pp. 8927–8943, 2014.

Research Article

Two Different Integration Methods for Weather Radar-Based Quantitative Precipitation Estimation

Jing Ren,^{1,2,3} Yong Huang,^{1,3} Li Guan,² and Jie Zhou^{1,2,3}

¹Key Laboratory of Atmospheric Sciences and Satellite Remote Sensing of Anhui Province, Anhui Meteorology Institute, Hefei 230031, China

²Nanjing University of Information Science & Technology, Nanjing 210044, China

³Shouxian Climatology Observatory, Shouxian 232200, China

Correspondence should be addressed to Yong Huang; hy121_2000@126.com

Received 17 November 2016; Revised 19 January 2017; Accepted 20 March 2017; Published 11 April 2017

Academic Editor: Roberto Fraile

Copyright © 2017 Jing Ren et al. This is an open access article distributed under the Creative Commons Attribution License, which permits unrestricted use, distribution, and reproduction in any medium, provided the original work is properly cited.

We discuss two different integration methods for radar-based quantitative precipitation estimation (QPE): the echo intensity integral and the rain intensity integral. Theoretical analyses and simulations were used to test differences between these two methods. Cumulative rainfall calculated by the echo intensity integral is usually greater than that from rain intensity integral. The difference of calculated precipitation using these two methods is generally smaller for stable precipitation systems and larger for unstable precipitation systems. If the echo intensity signal is sinusoidal, the discrepancy between the two methods is most significant. For stratiform and convective precipitation, the normalized error ranges from -0.138 to -0.15 and from -0.11 to -0.122, respectively. If the echo intensity signal is linear, the normalized error ranges from 0 to -0.13 and from 0 to -0.11, respectively. If the echo intensity signal is exponential, the normalized error ranges from 0 to -0.35 and from 0 to -0.30, respectively. When both the integration scheme and real radar data were used to estimate cumulative precipitation for one day, their spatial distributions were similar.

1. Introduction

Weather radar is an effective tool for precipitation estimation and it can provide useful regional flood forecasts. In many studies, weather radar has been used for quantitative precipitation estimates [1–3] and also to develop monitoring techniques [4–7] and integrated applications of multiple estimation methods that are combined with rain gauge data [8, 9].

Radar was first used for quantitative precipitation estimation in the late 1940s. Marshall et al. [10] introduced a formula for calculating rainfall intensity (I) from the radar reflectivity factor (Z) termed the $Z-I$ model. Byers and Braham [11] found a strong correlation between the volume of a convective storm and the amount of precipitation. For the radar echo beyond a threshold, the average rainfall intensity is closely related to the radar echo. Several methods for estimating precipitation were introduced later, including the

Brandes objective analysis method [12], regional calibration method [13], the Vertical Profiles of Reflectivity (VPR) method [14], and the Mean Vertical Profiles of Reflectivity (MVPR) method [15].

Precipitation estimation has been improved using new methods such as a combination of satellite-based precipitation products [16–19], merging radar and satellite precipitation [20], machine learning [18, 21], the fusion of multiple radar-based precipitation products method [22], probabilistic quantitative precipitation estimation (PQPE) [23, 24], and the Climatological Vertical Profiles of Reflectivity Identification and Enhancement (CVPR-IE) method [25]. On the basis of Meteosat Second Generation (MSG) and Tropical Rainfall Measuring Mission (TRMM) data, Ouallouche and Ameur [18] used an artificial neural network (ANN) for modelling and presented a new method to delineate rain areas in Algeria. Their approach worked well and overcame the shortcomings of the scattering index (SI) method. Lee et al. [20]

proposed a method based on the optimal weights needed to fill the radar gap using surrounding radar estimated precipitation and observations from the COMS satellite. This method was tested for major precipitation events during the summer of 2011 with assumed radar gap areas. The results suggested that successful merging appears to be closely related to the quality of the satellite precipitation estimates. Rafieeinab et al. [22] evaluated four procedures for fusing QPEs of different resolutions based on Fisher estimation and its conditional bias-penalized variant. They searched for a fusion algorithm that can be implemented as a postprocessor to the QPE operation in which multiple gridded QPE products are processed. Their approach was successful in improving the accuracy of high-resolution QPE. Kirstetter et al. [24] used WSR-88D radar data and rain gauge observations to develop a model that quantitatively describes the relationship between radar reflectivity and observed precipitation. They calculated the probability distributions of precipitation rates instead of the deterministic values. This approach reduced the uncertainty structure of radar quantitative precipitation estimation (QPE) at very fine spatiotemporal scales. Based on VPR-IE (vertical profile of reflectivity identification and enhancement) method, Wen et al. [25] obtained climatological VPRs for different seasons, rain types, and rain intensities from 11 years of Tropical Rainfall Measuring Mission (TRMM) Precipitation Radar (PR) data. When these climatological VPRs are used, the TRMM PR products are integrated into the ground-based rainfall estimation system in real time and the precipitation estimate can be significantly improved.

The Z - I relation [26–28] remains one of the most widely used methods for quantitative precipitation estimation. According to the Z - I relation formula, two different integration orders can be adopted to calculate cumulative precipitation. However, due to the nonlinear relationship between the variables, the results from two different integration orders are different. One approach is to first carry out the rainfall intensity conversion through the Z - I relationship, then the rainfall intensity is integrated to obtain the total rainfall (termed the rainfall intensity integral). This is the most widely used method for quantitative precipitation estimation using the Z to I conversion [26–28]. Another approach is to first obtain the distribution of the radar reflectivity factor, integrate the radar reflectivity factor, and finally convert the integral radar reflectivity factor to the precipitation intensity (termed the echo intensity integral). Based on theoretical analysis and simulation studies, we discuss the differences as well as the advantages and disadvantages of each method. The results will help improve the accuracy of precipitation estimation.

2. Fundamental Principles

The scattering of radar electromagnetic waves by precipitation particles is the basis for radar detection of precipitation. After radar sends out a signal, the information returned is closely related to the backscattering coefficient of precipitation particles. The weather radar measurement is the sum of the backscatter power of precipitation particles within the

effective radiation volume. The echo intensity, denoted as dBZ , represents the magnitude of the echo power, and it is defined as

$$\text{dBZ} = 10 \lg Z, \quad (1)$$

where Z (dB) is the radar reflectivity factor, and it is defined as

$$Z = \int_0^{\infty} n(D) D^6 dD. \quad (2)$$

When the vertical airflow near the ground is ignored, the precipitation intensity, denoted as I (mm/h), can be calculated from the following formula:

$$I = \int_0^{\infty} n(D) M(D) v(D) dD. \quad (3)$$

In this formula, D is the diameter of raindrops, $n(D)$ is the number of raindrops per unit volume, $n(D)dD$ represents the number of particles per unit volume of the raindrops whose diameter ranges between D and $D + dD$, and $M(D)$ and $v(D)$ indicate the mass and the terminal falling velocity of raindrops with a diameter of D , respectively.

The definitions of the radar reflectivity factor (Z) and precipitation intensity (I) show that they have close relationships with the raindrop size distribution spectrum. The raindrop spectrum characteristics reflect the particle size and the corresponding particle number concentration. Z is proportional to the sixth power of the drop diameter (D) and its number, so the reflectivity factor can be calculated by the raindrop spectrum data. Wu et al. studied raindrop influence of spectrum change on precipitation estimation and found that the echo intensity of radar observation is usually less than the echo intensity calculated from the Ground Raindrop spectrometer. The farther away from the ground, the greater the underestimation of radar echo [28].

Because the raindrop size distribution varies with time and space, especially with different types of precipitation [29, 30], the Z - I relation can only be derived theoretically using several assumptions. The current widely used Z - I relation is $Z = aI^b$. Radar detection of convective cloud precipitation is characterized by strong reflectivity and a large horizontal reflectivity gradient. When radar is used to detect stratiform cloud precipitation, it is mainly characterized by a relatively weak reflectivity factor and a fairly small horizontal reflectivity gradient. For different precipitation types, the corresponding relation can be obtained from a statistical model with a large amount of raindrop distribution data as input [31]. For example, according to statistical analysis of United States summer convective precipitation, Mueller and Sims [32] found a quantitative relationship between the radar reflectivity factor Z and precipitation intensity I . The Z to I conversion derived by Gerrish and Hiser [33] used the average value of the coefficient and index to obtain a Z - I model of convective precipitation: $Z = 300I^{1.4}$. Marshall and Palmer [34] deduced the stratiform precipitation Z - I relationship using a classical exponential raindrop size distribution (M-P distribution): $Z = 200I^{1.6}$.

Using the change of radar echo intensity over time, we divided precipitation into stable and unstable precipitation components. If, during a set time period, the echo intensity does not change abruptly, there is no significant change in its maximum, and the waveform remains the same, then it is a stable precipitation. If, during a set time period, the echo intensity abruptly changes, there is a clear change in its maximum, and the waveform undulates; it is an unstable precipitation.

For the total amount of precipitation during a period of time (T), two independent methods can be used to obtain the estimate. One method initially estimates the precipitation intensity $I(t)$ based on the radar reflectivity factor $Z(t)$ obtained from the radar detection and then integrates the estimated precipitation intensity over the period for the total rainfall amount. It is the most widely used method for quantitative precipitation estimation using Z to I conversion. Because it first estimates the instantaneous precipitation intensity and then integrates the total rainfall intensity according to the rainfall intensity, this method is called rain intensity integral, (RI), and the formula is shown as follows:

$$\text{RI}_T = \int_T I(t) dt = \int_T \sqrt[b]{\frac{Z(t)}{a}} dt. \quad (4)$$

In this formula, a and b are the coefficient and index of Z to I conversion ($Z = aI^b$), respectively.

From formula (2), we see that the radar reflectivity factor (Z) is proportional to the sixth power of the drop diameter (D), and the greatest contribution comes from large particles. The radar reflectivity factor contains information on the size and quantity of precipitation particles. The other method first obtains the distribution of radar reflectivity factor (Z) and then integrates the radar reflectivity factor $Z(t)$ over a period of time (T). It then converts the integral radar reflectivity factor to the precipitation intensity. This method is termed the echo intensity integral (EI), and the formula is as follows:

$$\text{EI}_T = \sqrt[b]{\frac{\int_T Z(t) dt}{a}} = \sqrt[b]{\frac{\int_T Z(t) dt}{a}}. \quad (5)$$

There are two ways to calculate the total precipitation over a region (with S radar detection units in the area) and these are similar to calculating the total rainfall amount over a period of time. $Z(x)$ represents the echo intensity of detection unit x

$$\text{RI}_S = \int_S \sqrt[b]{\frac{Z(x)}{a}} dx, \quad (6)$$

$$\text{EI}_S = \sqrt[b]{\frac{\int_S Z(x) dx}{a}}. \quad (7)$$

Formulas (4)–(7) all indicate the relationships between cumulative rainfall and the radar reflectivity factor Z . In formulas (5) and (7), the echo intensity is first integrated to obtain raindrop spectrum distribution, and then the cumulative rainfall is calculated through the Z - I relation. In

formulas (4) and (6), the instantaneous rainfall intensity is first calculated according to the Z - I relation, and then the rainfall intensity is integrated to obtain cumulative rainfall. Because the relationship between Z and I is nonlinear, the results of the two methods are different when Z changes with time. The differences between the two methods for calculating the cumulative rainfall are discussed in the following.

3. Discussion of Different Integration Methods

After discretizing the integrals in formulas (4)–(7), we obtain two formulas to calculate the cumulative precipitation over a period of time (T) and/or within a certain region (region S). These are shown in formulas (8) (discretizing calculation for the cumulative precipitation over a period of time (T interval) and/or within a certain region (region S)).

Formulas (8) show that the cumulative precipitation calculated from the echo intensity integral method is larger than that calculated by the rainfall intensity integral method.

To analyze the characteristics of the difference $f(Z_1, Z_2, Z_3, \dots, Z_n)$ between the two integration methods, we used three different functions to represent the variations of echo intensity. Specifically, the sinusoidal, linear, and the exponential functions are used to simulate echo intensity, and then the accumulative rainfalls for both stratiform and convective precipitation are calculated with these two methods

$$\begin{aligned} \text{EI}_T &= \sqrt[b]{\frac{\int_T Z(t) dt}{a}} \approx \sqrt[b]{\frac{\sum_T Z(t) \cdot \Delta t}{a}} \\ &= \sqrt[b]{\frac{(Z_1 + Z_2 + Z_3 + \dots + Z_n)}{a}} \\ &= \sqrt[b]{\frac{Z_1}{a}} + \sqrt[b]{\frac{Z_2}{a}} + \sqrt[b]{\frac{Z_3}{a}} + \dots + \sqrt[b]{\frac{Z_n}{a}} \\ &\quad + f(Z_1, Z_2, Z_3, \dots, Z_n), \\ \text{RI}_T &= \int_T \sqrt[b]{\frac{Z(t)}{a}} dt \approx \sum_T \sqrt[b]{\frac{Z(t) \cdot \Delta t}{a}} \\ &= \sqrt[b]{\frac{Z_1}{a}} + \sqrt[b]{\frac{Z_2}{a}} + \sqrt[b]{\frac{Z_3}{a}} + \dots + \sqrt[b]{\frac{Z_n}{a}}, \\ \text{EI}_S &= \sqrt[b]{\frac{\int_S Z(x) dx}{a}} \\ &\approx \sqrt[b]{\frac{Z_1}{a}} + \sqrt[b]{\frac{Z_2}{a}} + \sqrt[b]{\frac{Z_3}{a}} + \dots + \sqrt[b]{\frac{Z_n}{a}} \\ &\quad + f(Z_1, Z_2, Z_3, \dots, Z_n), \end{aligned}$$

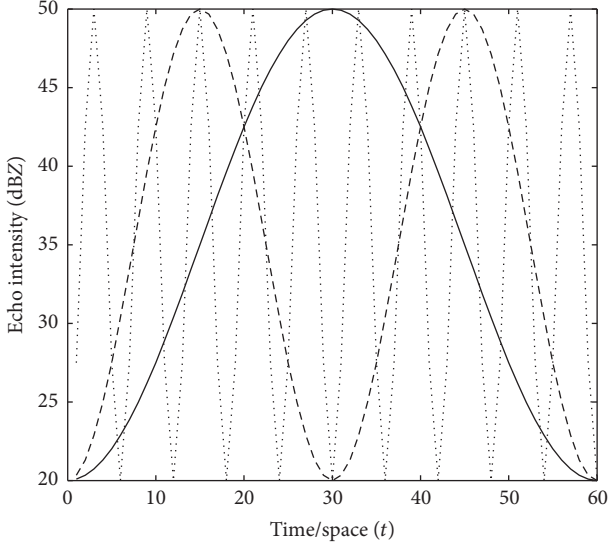


FIGURE 1: Variation of echo intensity with time/space (lines: $n = 1$; dash line: $n = 0.5$; dotted line: $n = 0.1$).

$$\begin{aligned} \text{RI}_S &= \int_S \sqrt[b]{\frac{Z(x)}{a}} dx \\ &\approx \sqrt[b]{\frac{Z_1}{a}} + \sqrt[b]{\frac{Z_2}{a}} + \sqrt[b]{\frac{Z_3}{a}} + \dots + \sqrt[b]{\frac{Z_n}{a}}, \end{aligned} \quad (8)$$

in which $f(Z_1, Z_2, Z_3, \dots, Z_n)$ is a function of Z .

3.1. Sinusoidal Variation. To make accurate quantitative precipitation forecasts, the probability distribution of the precipitation must be considered. Previous studies have demonstrated that the summer rainfall in China generally exhibits a normal distribution [35–38]. In this section, the temporal/spatial variation of the precipitation echo is represented by a sinusoidal function, and the echo intensity formula is as follows:

$$\text{dBZ}(t) = 15 \sin\left(\frac{2\pi}{60n} \cdot t - \frac{\pi}{2}\right) + 35, \quad (9)$$

where t represents the detection unit within a period/region (60 units in total); n is a parameter used to control the speed of the sine wave; and its range is 0.02~2. When n is 0.1, 0.5, and 1, the variations of the echo intensity with t are shown in Figure 1. The figure shows that the curve is similar to the curve of normal distribution, and the variability of the echo intensity increased with a decreased n . The total amounts of reflectivity collected by each experiment with different frequency are almost 50% of the rectangle area (outlined by maximum echo functions).

According to formula (9), if $n = 2$, the echo intensity curve is exactly a half sine wave; if $n > 2$, the curve is only a portion of a half sine wave; if n is very large, the curve is similar to a linear signal. The variations of cumulative rainfall from the two integration methods are shown in Figure 2. The cumulative rainfall calculated using the echo intensity

integral is always greater than that from the rainfall intensity integral. The changes of cumulative rainfall calculated from the two methods are consistent with the change of n . As illustrated in Figure 2, the cumulative stratiform rainfall (a) calculated by the echo intensity integral ranges from 17.5 to 20 mm, and the cumulative rainfall calculated via rain intensity integral ranges from 13 to 15 mm. For convective precipitation (b), the estimated cumulative rainfall from the echo intensity integral ranges from 19.8 to 22.5 mm, and the cumulative rainfall calculated via rain intensity integral ranges from 15.5 to 18 mm.

To compare the difference between the two integration methods, we used the normalized error, defined as RE ($\text{RE} = (\text{RI} - \text{EI}) / (\text{RI} + \text{EI})$), to quantitatively represent the difference between the two integration methods. Figure 3 shows the variation of normalized error with n for stratiform precipitation (a) and convective precipitation (b). The normalized error ranged from -0.138 to -0.5 and from -0.11 to -0.122 , respectively.

The above analysis shows that if echo intensity varies as a sinusoidal wave, the difference between the two methods is not obviously related to frequency. The normalized error exhibited a small fluctuation that was smaller for convective precipitation than for stratiform precipitation.

3.2. Linear Variation. If the temporal/spatial variation of the radar echo is simulated by a linear function, then the formula of the echo intensity is as follows:

$$\text{dBZ}(t) = \frac{m \cdot t}{60} + 20. \quad (10)$$

In this formula, t represents the detection unit (60 units total) within a period/region. The parameter m controls the speed of the linear wave and it ranges from 0 to 30. Given $m = 30$, $m = 20$, and $m = 10$, the variation of the echo intensity with the time and space is shown in Figure 4. The echo intensity increases with time, and the variation rate of the echo intensity increases with m .

The parameter m indicates the variation rate of the input signal which reflects the stability of the precipitation process. A greater m indicates a greater change of the echo intensity and a more unstable system. The variation of cumulative rainfall of these two integral methods with m is shown in Figure 5. Similar to sinusoidal wave simulation, the accumulative rainfall from echo intensity integral is always greater than that from the rainfall intensity integral. With an increase of m , the linear amplification speed of echo intensity increases. As a result, the maximum value of the simulated echo also increases, which ultimately increases the total accumulated rainfall. According to Figure 5, (1) if $m = 0$, the simulated echo intensity is a constant (20 dBZ), and the accumulated rainfall from two integration methods are the same; (2) if $m = 30$, the echo intensity changes from 20 dBZ to 50 dBZ, and the difference of the accumulated rainfall is greatest, which is 4.5 mm (stratiform) and 3.3 mm (convective), respectively.

Analysis of the variation of normalized error with m for different precipitation types (Figure 6) shows that the normalized error always increases with m . For stratiform

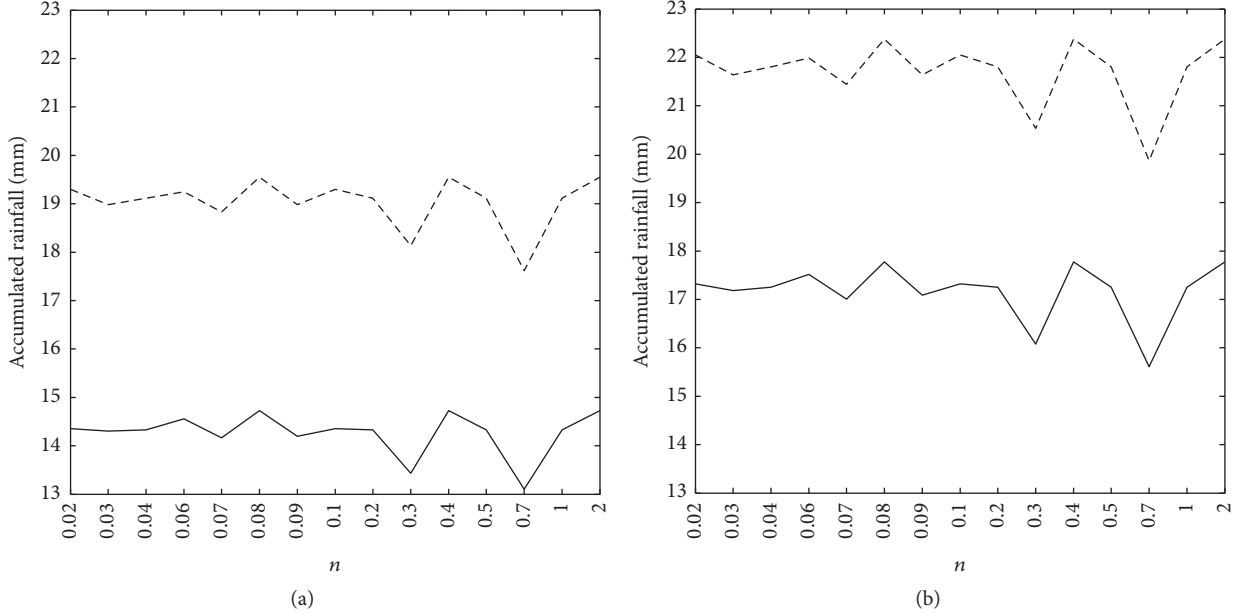


FIGURE 2: Variation of cumulative rainfall in two methods with the change of n (lines: rain intensity integral; dash line: echo intensity integral; (a) $Z = 200I^{1.6}$; (b) $Z = 300I^{1.4}$, the same in the following figures).

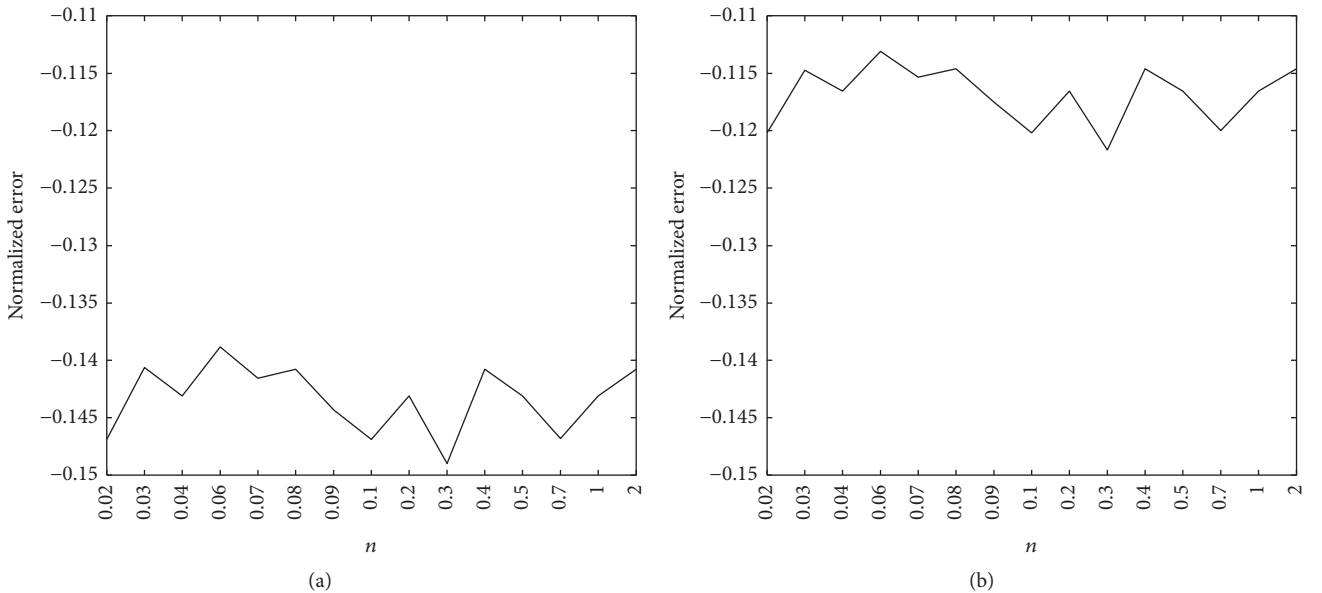


FIGURE 3: Variation of normalized error between the two cumulative methods with the change of n ((a) $Z = 200I^{1.6}$; (b) $Z = 300I^{1.4}$, the same in the following figures).

precipitation, the normalized error ranges from 0 to -0.13 , and for convective precipitation, the normalized error ranges from 0 to -0.11 .

Therefore, if the echo intensity has linear variation, the normalized error between the two methods depends on the value of m . If m increases, the normalized error of the two methods also increases. The normalized error of the cumulative rainfall between these two integration methods is relatively smaller for convective precipitation than the error for stratiform precipitation.

3.3. Exponential Variation. The temporal/spatial variation of the echo intensity is also simulated by the exponential function, and the formula is as follows:

$$\text{dBZ}(t) = 30 \cdot \left(\frac{t}{60} \right)^m + 20, \quad (11)$$

where t represents the detection unit within a period and a region and there are 60 units in total. The parameter m controls the speed of the exponential variation and it ranges

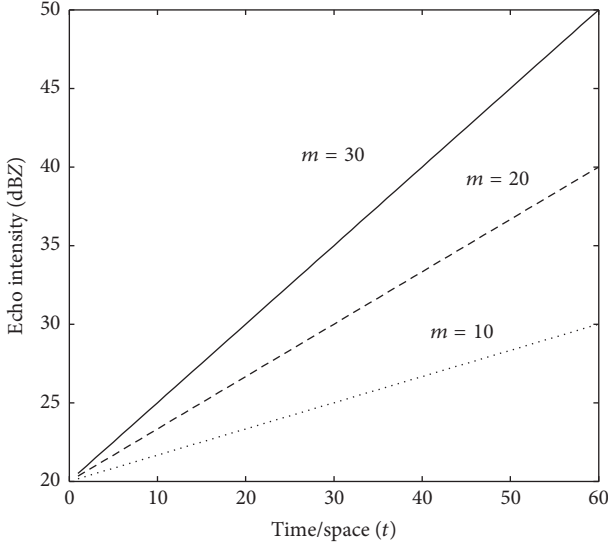


FIGURE 4: Variation of echo intensity with time/space.

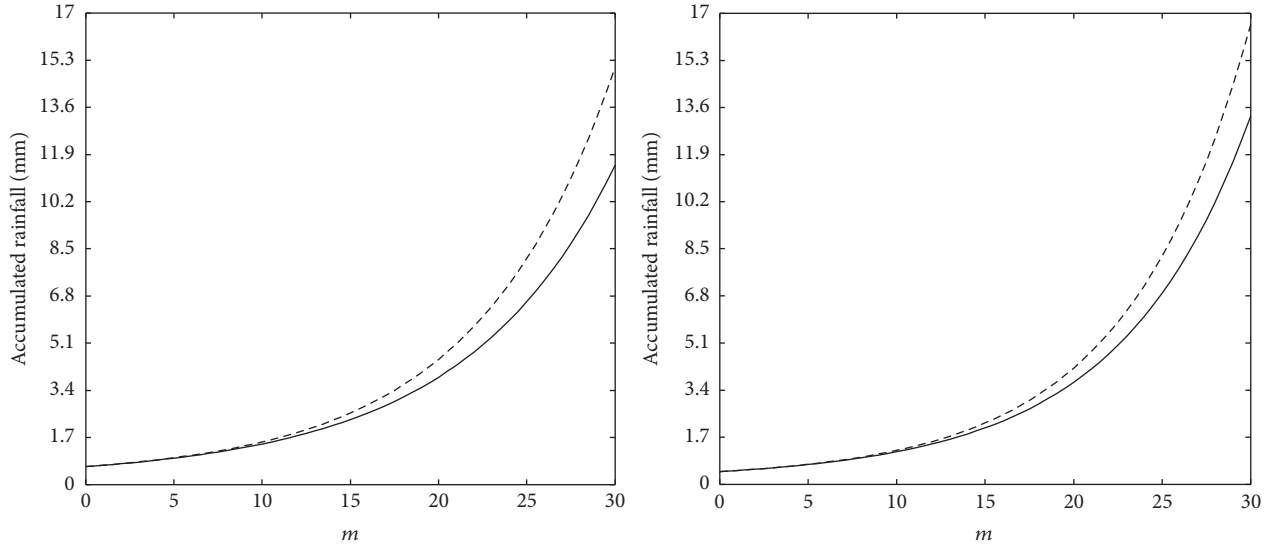


FIGURE 5: Variation of cumulative rainfall of two methods with the change of m .

from 0 to 10. Given $m = 0.1$, $m = 1$, $m = 2$, and $m = 10$, the variation of the echo intensity with the time and space is shown in Figure 7. According to Figure 7, (1) if $m = 0.1$, the change of echo intensity is initially rapid from 0 to 40 dBZ and then decreases from 40 to 50 dBZ; (2) if $m = 1$, the echo intensity curve is similar to linear simulation; (3) if $m = 10$, the change of echo intensity is generally opposite to the case when $m = 0.1$. It changes slowly in the beginning and then rapidly increases from 0 to 50 dBZ after $t = 40$.

Based on the characteristics of the exponential function, the variation of the echo intensity is not determined solely by m . According to formula (11) and Figure 7, it is clear that the echo intensity has abrupt changes. If there are fewer radar detection units, the abrupt changes occur when m is small;

if there are more radar detection units, the abrupt changes occur when m is large.

The variations of cumulative rainfall with m for these two methods are shown in Figure 8. The results from both methods show a similar trend which is an abrupt decrease for $0 < m < 1$ followed by a smooth gradual decrease after $m > 1$. The accumulative rainfall from the echo intensity integral is greater than that from the rainfall intensity integral. For $m < 1$, the change of the echo intensity is abrupt with the decrease of m . It increases from about 16 to more than 40 dBZ in a short time at the beginning and sustains for a long time, resulting in stronger echo intensity and more estimated accumulative precipitation. For $m > 1$, the abrupt increase of the echo intensity does not occur until after

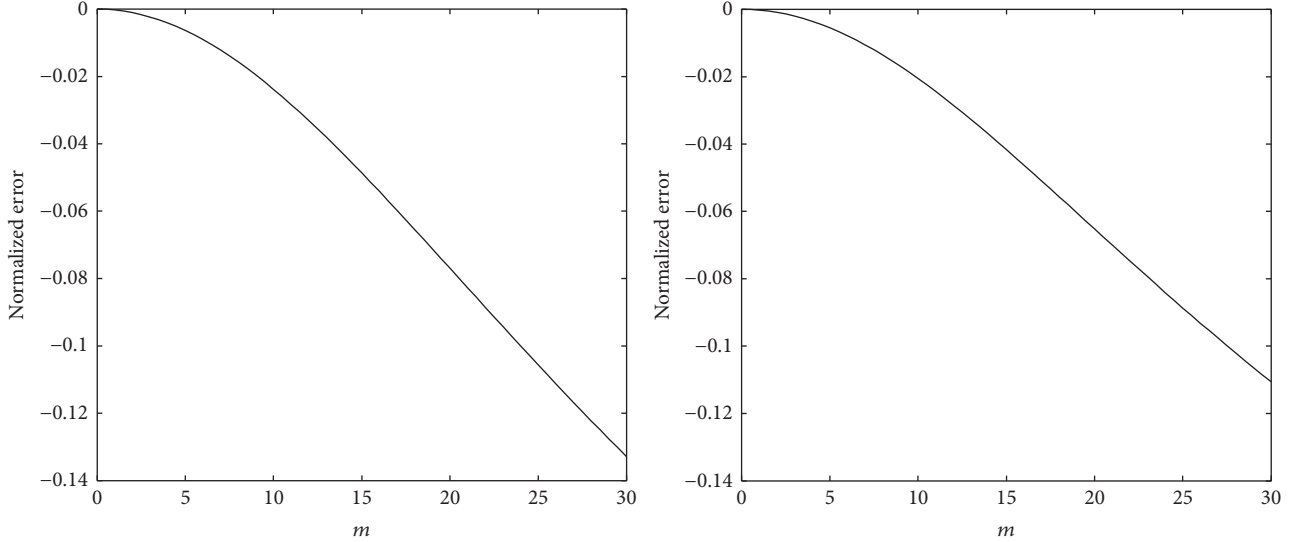


FIGURE 6: Variation of normalized error between two cumulative methods with the change of m .

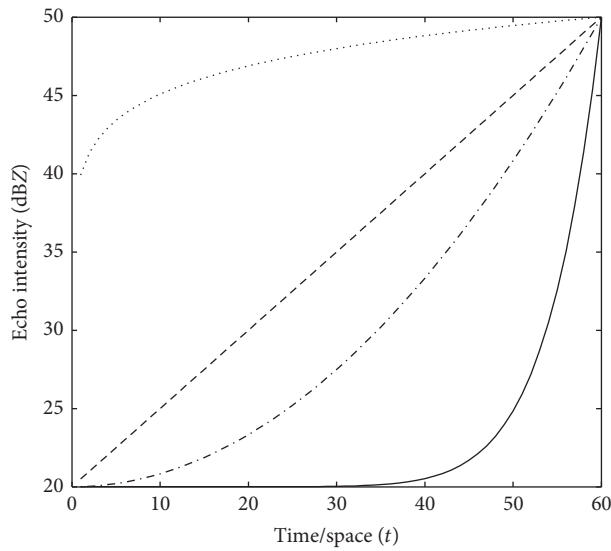


FIGURE 7: Variation of echo intensity with time/space (dotted line: $m = 0.1$; dash line: $m = 1$; dash dotted line: $m = 2$; lines: $m = 10$).

a long interval with weak echo intensity, resulting in less estimated accumulative precipitation. As m approaches 0, the echo intensity rapidly increases to 50 dBZ, and the cumulative stratiform precipitation and convective precipitation values are 48.6 mm and 63.4 mm, respectively (Figure 8). If m is very large, the calculated cumulative rainfall is reduced and gradually decreases as m decreases. As m reaches infinity, the cumulative rainfall calculated by the echo intensity integral is 3.90 mm (stratiform) and 3.55 mm (convective), and the calculated accumulative rainfall from rainfall intensity integral is 1.45 (stratiform) and 1.50 mm (convective).

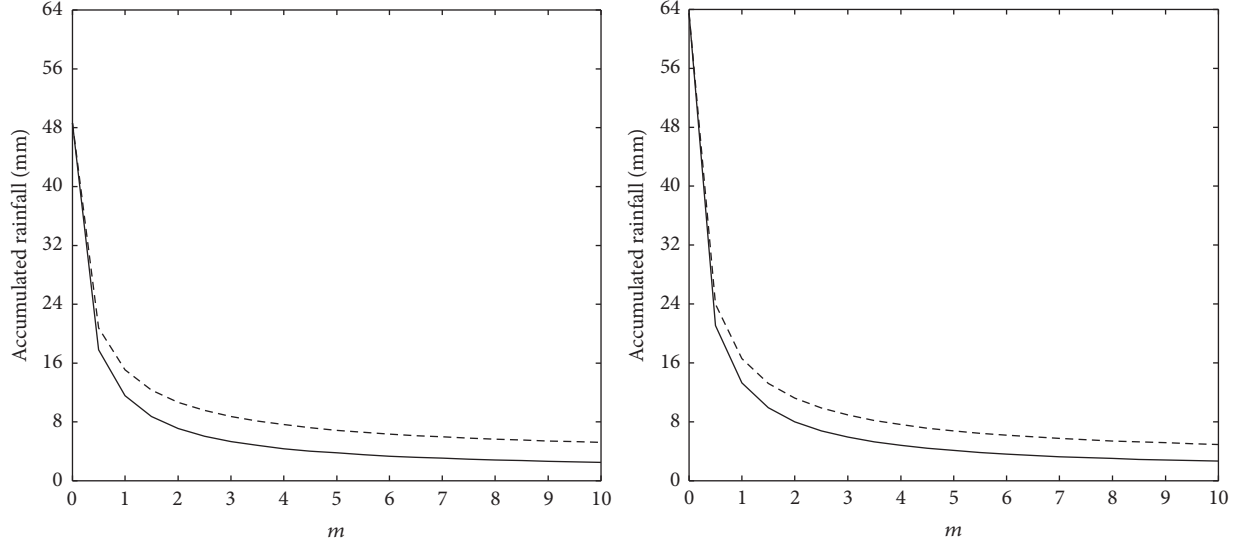
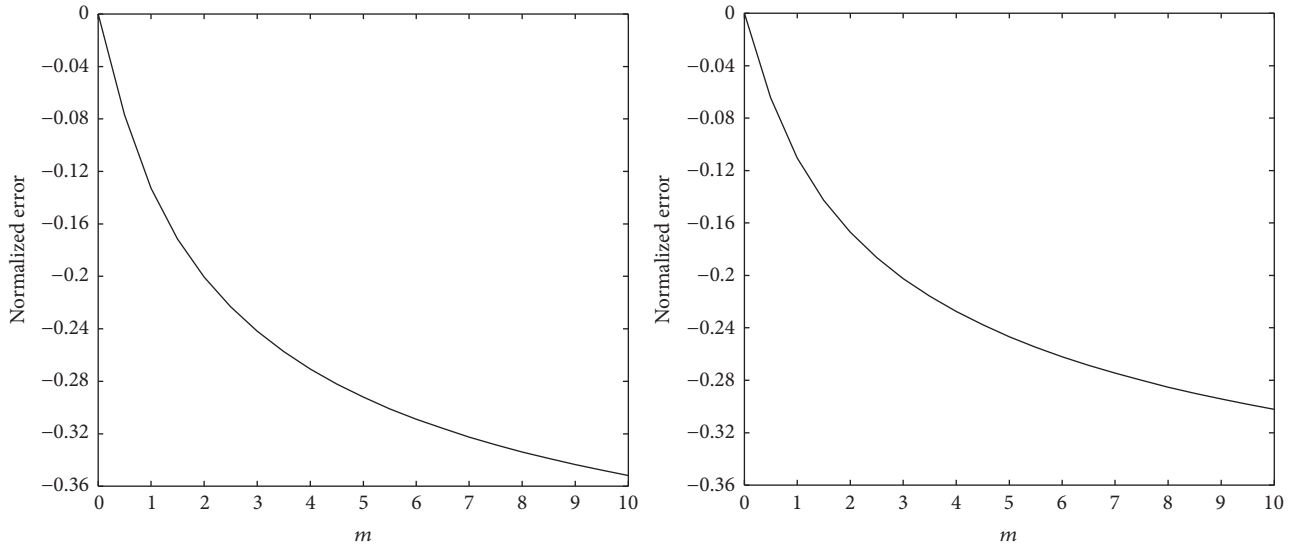
The variation of normalized error with m (Figure 9) indicates that the differences range from 0 to -0.35 for stratiform precipitation and 0 to -0.30 for convective precipitation. As m approaches infinity, the differences approach

-2.71 for stratiform precipitation and -2.29 for convective precipitation.

This analysis indicates that when the change of echo intensity is exponential, the normalized error between the two methods increases with m and that the difference is smaller for convective precipitation than it is for stratiform precipitation.

4. Analysis with Actual Radar Observation

Based on the $Z-I$ relation for stratiform precipitation, the cumulative precipitation for a 24 hr period was calculated by both the echo intensity integral and the rainfall intensity integral. The radar observable data were taken from over the Huaihe River Basin on June 10, 2011. The ground station

FIGURE 8: Variation of cumulative rainfall of two methods with the change of m .FIGURE 9: Variation of normalized error between the two cumulative methods with the change of m .

pluviometer data were from one hr of precipitation in the Huaihe River Basin on the same day. These data were used to verify the two integration schemes. The spatial distributions of the two integration schemes and the observation data are shown in Figures 10 and 11, respectively. Figure 10 shows that there are two high intensity zones (bottom and mid portions of Figure 10). In comparison with a topographic map, the large value areas lie between the mountains and the river. The larger value is between Dabie Mountain and the Yangtze River, and the other value is between Funiu Mountain and the Yellow River (which is within the range of radar detection in Zhumadian). Figure 11 shows that there is only one high intensity zone (bottom of Figure 11). A possible reason for this discrepancy is that there was a problem with the Zhumadian

radar (a previous study found problems with the Zhumadian radar data).

The following is a statistical analysis of this case. The average accumulated rainfall calculated with the rainfall intensity integral and echo intensity integral was regarded as radar estimated rainfall. From the scatter density diagram of radar estimate precipitation (Figure 12(a)) and the difference between the two integration methods, it is clear that as the estimated rainfall increased, the difference between the two estimates increases. From the scatter density diagram of site observation (Figure 12(b)) and the difference between the two integration methods, we found that as observed rainfall increased, the difference between the two estimate approaches increases. The average difference between the

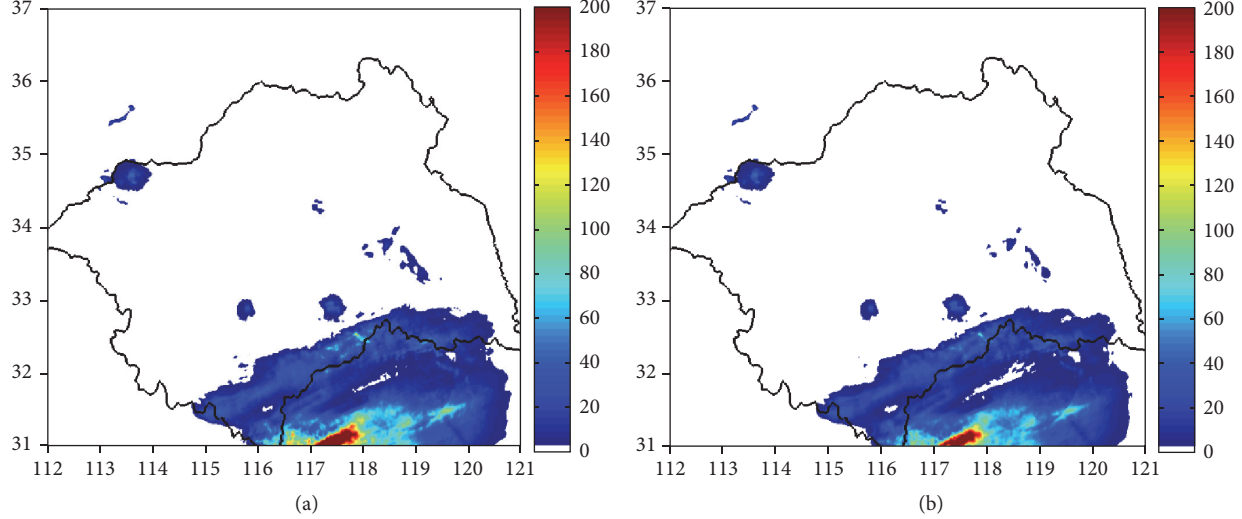


FIGURE 10: Spatial distribution of daily precipitation using echo intensity integral (a) and rainfall intensity integral (b).

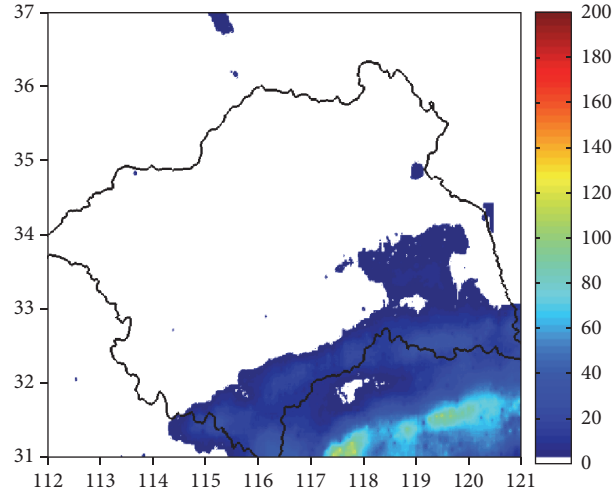


FIGURE 11: Spatial distribution of daily precipitation from site observation.

two methods was 3.367 mm, and the standard deviation was 5.663 mm.

5. Conclusions

The $Z-I$ relation method is widely used for quantitative precipitation estimation based on weather radar data. It establishes a statistical relationship between the radar reflectivity and the precipitation intensity. We introduced two methods associated with the $Z-I$ relation approach to calculate cumulative precipitation. The results demonstrated that cumulative precipitation calculated from the echo intensity integration method was greater than that calculated by the rainfall intensity integration method. The normalized error of the calculated cumulative precipitation from these two methods depends on the variation of the echo intensity. The difference is small if the echo intensity changes slightly and gradually, but large if the echo intensity changes frequently (multiple peaks) and abruptly. When the echo intensity is

simulated with a sinusoidal wave, the difference is larger than that simulated with a linear function. This is because the frequency of echo intensity can reach the maximum multiple times for a sinusoidal wave simulation, while it can only reach the maximum once for a linear signal simulation. If the echo intensity is an exponential signal, despite its single peak aspect, the difference can still be large due to abrupt change of the echo intensity.

When the echo intensity is simulated with a sinusoidal wave, the difference between the two methods is large, and the normalized error ranges from -0.15 to -0.138 and from -0.122 to -0.11 for two precipitation types. The variation of cumulative rainfall and normalized error with n is always consistent.

When the echo intensity is simulated with a linear function, the normalized error increases with the parameter m . The normalized error ranges from 0 to -0.13 for stratiform precipitation and from 0 to -0.11 for convective precipitation.

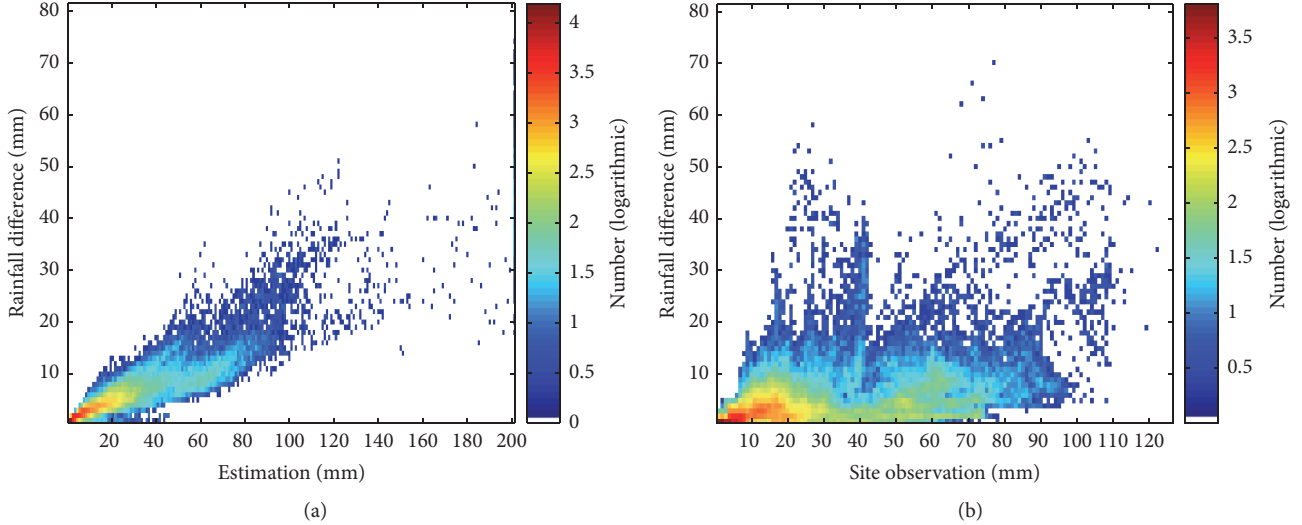


FIGURE 12: Scatter density diagrams of precipitation ((a) radar estimation; (b) site observation) and the difference between the two integration methods.

When the echo intensity was simulated with an exponential function, the normalized error first increased rapidly and then slowed down and stabilized. The normalized error ranged from 0 to -0.35 for stratiform precipitation and from 0 to -0.30 for convective precipitation.

When the two integration schemes with real radar were used to estimate cumulative precipitation for a day, their spatial distributions were similar.

He et al. (2004) showed that the $Z-I$ relation method can underestimate the precipitation of heavy rainfall events [37]. Wang et al. (2008) found the $Z-I$ relation method could overestimate the precipitation for weak rainfall events [38]. According to the simulation and observation data results, the cumulative precipitation from the echo intensity integral is greater than that from the rain intensity integral. The rain intensity integral usually underestimates the precipitation for heavy rainfall events, so application of the integral method of echo intensity can increase the estimated rainfall in the case of heavy precipitation and improve the estimate accuracy.

Time limit is a key issue discussed in this review. Based on the simulation results of the sinusoidal echo sequence, if the variation period of the radar echo intensity is more than one cycle, then the difference between the two kinds of cumulative rainfall appears to be irregular. The findings of this review are only relevant for rainfall accumulation within one change cycle of the precipitation system. The accumulated time should not exceed the life history of the precipitation system. For frequent summer precipitation events, the life histories of the systems are short and rainfall accumulates over several hours. For longer time scale systems, the precipitation is more stable and the life cycle may span several days.

Conflicts of Interest

The authors declare no conflicts of interest.

Authors' Contributions

The work presented here was carried out with collaboration among all the authors. Jing Ren, Yong Huang, Li Guan, and Jie Zhou defined the research theme. All authors carried out the simulations. This manuscript was finished by Jing Ren. Yong Huang and Li Guan checked the experimental results. All authors agreed to the manuscript being submitted.

Acknowledgments

This study was supported by the National Natural Science Foundation of China Grant no. 41275030, the R & D Special Foundation for Public Welfare Industry (meteorology) of China under Grant no. GYHY201306040, the National Natural Science Foundation of Anhui Province under Grant no. 1508085MD64, the Public welfare Technology Application Research Plan of Anhui Province under Grant no. 1604f0804002, and Shanxi Meteorological Research Foundation under Grant no. SXKKFRY20100101. The authors acknowledge LetPub ([www.letpub.com](http://www letpub.com)) for its linguistic assistance during the preparation of this manuscript.

References

- [1] G. Wang, L. Liu, and Z. Ruan, "Application of doppler radar data to nowcasting of heavy rainfall," *Journal of Applied Meteorological Science*, vol. 18, no. 3, pp. 388–395, 2007.
- [2] J. Pan and P. Zhang, "Estimating precipitation by radar measured vertical integration of liquid water," *Journal of Nanjing Institute of Meteorology*, vol. 23, no. 1, pp. 87–92, 2000.
- [3] M. Smalley, T. L'Ecuyer, M. Lebsack, and J. Haynes, "A comparison of precipitation occurrence from the NCEP stage IV QPE product and the CloudSat cloud profiling radar," *Journal of Hydrometeorology*, vol. 15, no. 1, pp. 444–458, 2014.
- [4] X.-Y. Liu, J.-T. Mao, J.-R. Li, and Y.-J. Zhu, "Application of radar-raingauge estimated mean area precipitation to runoff

- simulation," *Journal of Hydraulic Engineering*, vol. 22, no. 4, pp. 51–55, 2002.
- [5] X. Liu, J. Mao, J. Li, and Y. Zhu, "Radar rainfall estimation and its application on runoff simulation over SHIGUANHE catchments," *Acta Scientiarum Naturalium Universitatis Pekinensis*, vol. 38, no. 3, pp. 342–349, 2002.
- [6] K. Zhao, G. Liu, and W. Ge, "Precipitation calibration by using Kalman filter to determine the coefficients of the variational equation," *Climatic and Environmental Research*, vol. 6, no. 2, pp. 180–185, 2001.
- [7] T. Zhou, B. Nijssen, G. J. Huffman, and D. P. Lettenmaier, "Evaluation of real-time satellite precipitation data for global drought monitoring," *Journal of Hydrometeorology*, vol. 15, no. 4, pp. 1651–1660, 2014.
- [8] Z. Wang, X. Pei, J. Li, and L. Guan, "Application of principal characteristics extraction to consensus analysis of weather radar rainfall estimate," *Inverse Problems*, vol. 19, no. 3, pp. 525–531, 2003.
- [9] L. Guan, Z. Wang, and X. Pei, "The consensus methods and effects of estimating rainfall using radar," *Scientia Meteorologica Sinica*, vol. 24, no. 1, pp. 104–111, 2004.
- [10] J. S. Marshall, R. C. Langille, and W. M. Palmer, "Measurement of rainfall by radar," *Journal of the Atmospheric Sciences*, vol. 4, no. 4, pp. 186–192, 1947.
- [11] H. R. Byers and P. R. Braham, "Thunderstorm structure and circulation," *Journal of the Atmospheric Sciences*, vol. 5, no. 3, pp. 71–86, 1948.
- [12] E. A. Brandes, "Optimizing rainfall estimates with the aid of radar," *Journal of Applied Meteorology*, vol. 14, no. 7, pp. 1339–1345, 1975.
- [13] C. G. Collier, P. R. Larke, and B. R. May, "A weather radar correction procedure for real-time estimation of surface rainfall," *Quarterly Journal of the Royal Meteorological Society*, vol. 109, no. 461, pp. 589–608, 1983.
- [14] M. Kitchen, R. Brown, and A. G. Davies, "Real-time correction of weather radar data for the effects of bright band, range and orographic growth in widespread precipitation," *Quarterly Journal of the Royal Meteorological Society*, vol. 120, no. 519, pp. 1231–1254, 1994.
- [15] C. Wu, Y. Wan, T. Wu, and H. Jin, "Vertical profile of radar echo and its determination methods," *Journal of Applied Meteorological Science*, vol. 17, no. 2, pp. 232–239, 2006.
- [16] A. K. Mishra, R. M. Gairola, and V. K. Agarwal, "Rainfall estimation from combined observations using KALPANA-IR and TRMM- precipitation radar measurements over Indian region," *Journal of the Indian Society of Remote Sensing*, vol. 40, no. 1, pp. 65–74, 2012.
- [17] X. Li, Q. Zhang, and C.-Y. Xu, "Assessing the performance of satellite-based precipitation products and its dependence on topography over Poyang Lake basin," *Theoretical and Applied Climatology*, vol. 115, no. 3–4, pp. 713–729, 2014.
- [18] F. Ouallouche and S. Ameur, "Rainfall detection over northern Algeria by combining MSG and TRMM data," *Applied Water Science*, vol. 6, no. 1, pp. 1–10, 2016.
- [19] S. Jiang, L. Ren, Y. Hong et al., "Improvement of multi-satellite real-time precipitation products for ensemble streamflow simulation in a middle latitude basin in South China," *Water Resources Management*, vol. 28, no. 8, pp. 2259–2278, 2014.
- [20] Y.-R. Lee, D.-B. Shin, J.-H. Kim, and H.-S. Park, "Precipitation estimation over radar gap areas based on satellite and adjacent radar observations," *Atmospheric Measurement Techniques*, vol. 8, no. 2, pp. 719–728, 2015.
- [21] P. Nguyen, A. Thorstensen, S. Sorooshian, K. Hsu, and A. Aghakouchak, "Flood forecasting and inundation mapping using HiResFlood-UCI and near-real-time satellite precipitation data: the 2008 Iowa flood," *Journal of Hydrometeorology*, vol. 16, no. 3, pp. 1171–1183, 2015.
- [22] A. Rafieeinab, A. Norouzi, D.-J. Seo, and B. Nelson, "Improving high-resolution quantitative precipitation estimation via fusion of multiple radar-based precipitation products," *Journal of Hydrology*, vol. 531, no. 2, pp. 320–336, 2015.
- [23] H. M. Grams, J. Zhang, and K. L. Elmore, "Automated identification of enhanced rainfall rates using the near-storm environment for radar precipitation estimates," *Journal of Hydrometeorology*, vol. 15, no. 3, pp. 1238–1254, 2014.
- [24] P.-E. Kirstetter, J. J. Gourley, Y. Hong et al., "Probabilistic precipitation rate estimates with ground-based radar networks," *Water Resources Research*, vol. 51, no. 3, pp. 1422–1442, 2015.
- [25] Y. Wen, P. Kirstetter, Y. Hong et al., "Evaluation of a method to enhance real-time, ground radar-based rainfall estimates using climatological profiles of reflectivity from space," *Journal of Hydrometeorology*, vol. 17, no. 3, pp. 761–775, 2016.
- [26] X. Yang and L. Wei, "Radar rainfall estimation and its application in Haihe river basin," *Haihe Water Resources*, vol. 5, pp. 46–50, 2013.
- [27] Q. Wei, Z. Hu, L. Liu, and L. Wu, "C-band polarization radar data preprocessing and its application to rainfall estimation," *Plateau Meteorology*, vol. 35, no. 1, pp. 231–243, 2016.
- [28] Y. Wu, L. Liu, Y. Zhou, J. Yang, and J. Zheng, "Study of raindrop influence of spectrum change on precipitation estimation," *Plateau Meteorology*, vol. 35, no. 1, pp. 220–230, 2016.
- [29] B. Chen, W. Hu, and J. Pu, "Characteristics of the raindrop size distribution for freezing precipitation observed in southern China," *Journal of Geophysical Research Atmospheres*, vol. 116, no. 6, Article ID D06201, 2011.
- [30] L. Zhou, J. Wang, D. Gong, H. Zhang, and R. Sheng, "A study on the distribution of raindrop size in three types of precipitation in Shandong province," *Transactions of Atmospheric Sciences*, vol. 35, no. 3, pp. 355–371, 2014.
- [31] L. Jin, Q. Feng, J. Li, H. Sun, D. Shen, and X. Ren, "Application of automatic laser raindrops spectrometer in radar rainfall estimation," *Climatic and Environmental Research*, vol. 17, no. 6, pp. 740–746, 2012.
- [32] E. A. Mueller and A. L. Sims, "Investigation of the quantitative determination of point and areal precipitation by radar echo measurements: final report," *Ophthalmic Surgery Lasers and Imaging Retina*, vol. 82, no. 9, pp. 567–573, 1963.
- [33] H. P. Gerrish and H. W. Hiser, "Mesoscale studies of instability patterns and winds in the tropics," Miami Univ Fl Marine Lab. no. 82262, 1963.
- [34] J. S. Marshall and K. Palmer, "The distribution of raindrops with size," *Journal of the Atmospheric Sciences*, vol. 5, no. 4, pp. 165–166, 1948.
- [35] J. Cao and Y. Tao, "Does the rainfall in China fit the normal distribution?" *Journal of Natural Disasters*, vol. 11, no. 3, pp. 115–120, 2002.
- [36] Y. Tao and X. Duan, "The research of normal distribution characteristics of the precipitation in Yunnan province," *Scientia Meteorologica Sinica*, vol. 23, no. 2, pp. 161–167, 2003.

- [37] Y. He, Y. Zhang, S. Liu, and S. Gu, "Evaluation of the precision of weather radar rainfall estimation algorithms," *Journal of Nanjing Institute of Meteorology*, vol. 27, no. 6, pp. 743–752, 2004.
- [38] L. Wang, Y. Pei, and K. Meng, "Application of probability-fitting technique in radar quantitative estimation precipitation," *Meteorological and Environmental Sciences*, vol. 31, supplement 1, pp. 195–199, 2008.

Research Article

An Integrated Method of Multiradar Quantitative Precipitation Estimation Based on Cloud Classification and Dynamic Error Analysis

Yong Huang,^{1,2} Huijuan Liu,¹ Yun Yao,¹ Ting Ni,² and Yan Feng¹

¹*Anhui Meteorology Institute, Anhui Key Lab of Atmospheric Science and Satellite Remote Sensing, Hefei, Anhui 230031, China*

²*Shouxian National Climate Observation Station, Huainan, Anhui 232200, China*

Correspondence should be addressed to Yong Huang; hy121_2000@126.com

Received 17 November 2016; Accepted 15 February 2017; Published 5 March 2017

Academic Editor: Zhe Li

Copyright © 2017 Yong Huang et al. This is an open access article distributed under the Creative Commons Attribution License, which permits unrestricted use, distribution, and reproduction in any medium, provided the original work is properly cited.

Relationships between radar reflectivity factor and rainfall are different in various precipitation cloud systems. In this study, the cloud systems are firstly classified into five categories with radar and satellite data to improve radar quantitative precipitation estimation (QPE) algorithm. Secondly, the errors of multiradar QPE algorithms are assumed to be different in convective and stratiform clouds. The QPE data are then derived with methods of Z - R , Kalman filter (KF), optimum interpolation (OI), Kalman filter plus optimum interpolation (KFOI), and average calibration (AC) based on error analysis on the Huaihe River Basin. In the case of flood on the early of July 2007, the KFOI is applied to obtain the QPE product. Applications show that the KFOI can improve precision of estimating precipitation for multiple precipitation types.

1. Introduction

With operational running of the China New Generation Weather Radar in mainland China, a lot of studies have been reported with focus on radar quantitative precipitation estimation (QPE) in China [1–6]. QPE algorithms in these studies include the relationship between the radar echo and the observed precipitation, precipitation estimation using merged radar and rain gauge data, integrated approach of multiradar precipitation estimation methods, and QPE for specific region.

In the end of the 1940s, Marshall et al. [7] proposed the Z - R model to estimate rainfall intensity with radar reflectivity factor. The Z - R relation is a precipitation estimation method based on the relationship between the radar reflectivity factor (Z) and rainfall intensity (R). The merging methods actually start from Z - R relation estimation procedure but have additional correction procedures, such as Hu et al. [8] using Kalman filter to determine the coefficients of the variation equation and calibrating precipitation; more details can be seen in [3, 8–12]. For the operational monitoring of

rainfall, the widely used radar precipitation estimation methods include Z (radar reflectivity factor)- R (rainfall intensity) relationship method [7] and radar-gauge merging methods, such as average calibration (AC) method [10], Kalman filter (KF) method [8, 13], optimal interpolation (OI) method [14, 15], and integrated Kalman filter and optimal interpolation (KFOI) [9].

In recent years, several kinds of algorithms have been developed to improve the accuracy of radar QPE. There algorithms include the merging approaches based on radar observations and the approaches based on vertical profiles of reflectivity identification and enhancement (VPR-IE) [16, 17].

Besides, a feasible approach is to merge different kinds of observations to improve the precision of radar precipitation estimation. Previous studies showed that more accurate precipitation estimate can be obtained with application of the integrated methods [6, 18, 19]. The results of Guan's study show that the accuracy of rainfall estimation can be improved based on the combination of different approach with Principal Component Analysis (PCA) method. PCA is a multidimensional orthogonal linear transformation based

on Karhunen-Loèv transform, which is also named K-L transform integrated method (KL) [19]. As shown in the results of Huang et al. [18], the accuracy of QPE can be improved by using the integrate technique, which is to calculate the variation of QPE errors in different areas and select the optimal one with minimum error variation.

The objective of this study is to improve the accuracy of previous integrated method based on error analysis in fixed boundary of regions in Huaihe River Basin (HRB) [18]. The previous error analysis method is thus also named as Fixed Errors Analysis (FEA). According to FEA, the whole HRB has been classified into 15 areas with fixed boundary for errors statistic. The areas of errors analysis are fixed and do not vary with the change of precipitation system in these 15 areas. Since the rainfall is related to the precipitating cloud system and not related to the boundary of river basin or boundaries of administrative areas, the errors of QPEs are only calculated in fixed 15 areas in previous error analysis. In addition, the QPE errors of whole rainfall system could not be evaluated. To overcome the shortcoming of error analysis in fixed areas FEA, satellite and radar data are applied to classify cloud system. Then the optimal QPE method is selected from five methods by assessing the variation of the random errors from latest precipitation estimates for different precipitation cloud systems. Because the regions of error analysis are dynamically changing with the cloud system, the method in this study is named as Dynamic Errors Analysis (DEA).

2. Dynamic Errors Analysis Integrated Method

For a specific precipitation type, application of the Z - R relation method and four joint radar-gauge correction methods can generate different estimation errors. By comparing the precipitation estimates with the observations from rain gauges, the best method can be selected for further bias correction. The selected method with bias correction is expected to generate more accurate precipitation estimates for future rainfall.

2.1. Assumptions. There are two assumptions in this method. One is about estimation error; the other is related to precipitation systems. First, we assume that the errors of radar QPE are composed of systematic bias and random errors. Second, we assume that the errors of radar QPE vary with the transformation of precipitation system. There is an optimal QPE method with the minimum random error for a precipitation system among these methods.

The systemic bias is a constant, while the random error varies with the different algorithms and the evolution rainfall cloud system. The better algorithm is the small random error, and vice versa. The error of rainfall can be evaluated by analyzing the selected time series of the random errors.

The rainfall estimation error is defined as $W(t) = W_s + \widetilde{W}(t)$, where W_s is systematic bias, and it is a constant. $\widetilde{W}(t)$ represents random error and it varies with time. The estimation error of a specific period can be calculated by

$$W(t) = R_g(t) - R_r(t). \quad (1)$$

The systematic bias W_s is assumed as the average of errors in a specific period.

$$W_s = \frac{1}{T} \times \sum_{t=1}^T (R_g(t) - R_r(t)) \quad (2)$$

$$\widetilde{W}(t) = (R_g(t) - R_r(t)) - W_s,$$

where $R_g(t)$ is observed precipitation at t time by ground gauge and $R_r(t)$ is estimated precipitation at t time by radar.

The variance of estimation error (S_W) is applied to evaluate the stability of errors as the following formula:

$$\begin{aligned} S_W &= \frac{1}{T} \times \sum_{t=1}^T (W(t) - \overline{W})^2 = \frac{1}{T} \times \sum_{t=1}^T (W(t) - W_s)^2 \\ &= \frac{1}{T} \times \sum_{t=1}^T \widetilde{W}(t)^2. \end{aligned} \quad (3)$$

According to (3), the variance of observation errors is actually also the value of random errors. Therefore, the value of the random errors during a specific period can be obtained by evaluating the variance of the estimation errors during that period, so the ability of estimation can be acquired.

For the precipitation systems, it is assumed that there are different rainfall patterns (warm convective precipitation, cold convective precipitation, warm stratiform precipitation, cold stratiform precipitation, and mixed precipitation), and the abilities of the estimation method for different patterns are various, because the rain drop size distribution (DSD) is different for several patterns. The ability of estimation for a method can be evaluated by analyzing the variance of the estimation errors. Small variance indicates small random errors and a stable time series of estimation errors, suggesting that the estimation method is good, and vice versa.

Based on the assumptions and analysis of the estimation error time series, the optimal method is screened out from several QPE methods.

2.2. Integrated Method. The Z - R relation varies with precipitation types. Each estimation method has its preferred precipitation pattern. To improve the efficiency of the integrated method, we first determine the cloud pattern according to satellite brightness temperature and radar echo info and then apply different Z - R relationship on different precipitation pattern. The detailed procedures include the following.

Step 1. Determine cloud type by analyzing satellite brightness temperature and radar reflectivity factor database using threshold technique based on satellite cloud classification method [20]. To improve the rainfall estimation, this threshold-based techniques is revised using new experiential radar reflectivity (R) thresholds; that is, $R > 15 \text{ Dbz}$ for stratiform rainfall, $R > 30 \text{ Dbz}$ for convective rainfall, and $R > 50 \text{ dBZ}$ for deep convective rainfall. In addition, the satellite infrared temperature, coupled with radar reflectivity, is used to classify the cloud into 5 categories. The specific thresholds can be seen in Table 1.

TABLE 1: Thresholds of cloud type Determined.

	Thresholds	Z-I relationship
Warm stratiform precipitation	$15 \text{ dBZ} < R < 35 \text{ dBZ}$ and $T > 267 \text{ K}$	$Z = 131I^{1.44}$
Cold stratiform precipitation	$15 \text{ dBZ} < R < 35 \text{ dBZ}$ and $241 \text{ K} < T \leq 267 \text{ K}$	$Z = 200I^{1.6}$
Mixed precipitation	$15 \text{ dBZ} < R < 35 \text{ dBZ}$ and $221 \text{ K} < T \leq 241 \text{ K}$	$Z = 200I^{1.35}$
Warm convective precipitation	$35 \text{ dBZ} \leq R < 50 \text{ dBZ}$ and $T > 267 \text{ K}$	$Z = 300I^{1.4}$
Cold convective precipitation	(1) $35 \text{ dBZ} \leq R < 50 \text{ dBZ}$ and $T \leq 267 \text{ K}$ (2) $R \geq 50 \text{ dBZ}$ or $T \leq 221 \text{ K}$	$Z = 403I^{1.29}$

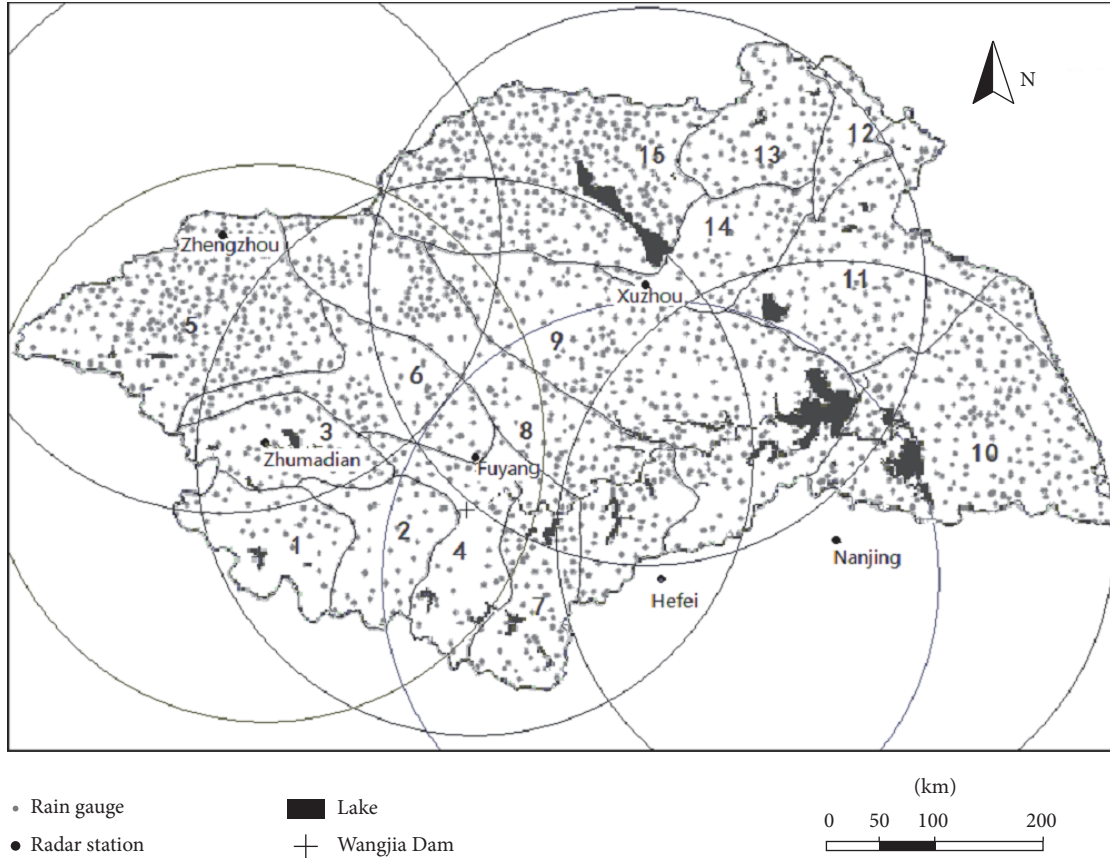


FIGURE 1: Distribution of the radars and rain gauges in Huaihe River Basin.

Step 2. Compute rainfall with 6-minute interval radar data from six radars (Hefei, Nanjing, Zhengzhou, Fuyang, Zhumadian, and Xuzhou radar) in HRB (Figure 1). The popular $Z-R$ relationships of stratiform and convective rainfall [21, 22] are applied to compute the cold stratiform and warm convective precipitation. For the other 3 cloud types, the drop size distribution (DSD) data in Huainan weather station from 2009 to 2012 are collected to compute the mode of $Z-R$ relationship with regression method.

Step 3. Correct the radar quality precipitation using ground gauge observations (Figure 1) with four correction methods (AC, KF, OI, and KFOI).

Step 4. With the results of cloud type, determine precipitation pattern, and errors of five QPE methods ($Z-R$ relationship and four correction methods) for five rainfall patterns are calculated in the latest one hour (10 times QPE data with 6-minute interval). The most best QPE method is the one with the smallest variance of the estimation errors in the past.

Step 5. Correct system bias for QPE data of the best method. The system bias is calculated by averaging the error of radar QPE and rain gauge data in the latest one hour (10 times QPE data with 6-minute interval). Then subtract the system bias from the selected radar QPE data.

TABLE 2: Relative errors and correlation coefficients of QPE and rain gauge from June 30 to July 9, 2007.

	Relative error		Correlation coefficients	
	All cases	>10 mm/h	All cases	>10 mm/h
DEA	0.33	0.26	0.86	0.68
FEA	0.34	0.32	0.87	0.65
KL	0.41	0.30	0.82	0.68
AC	0.42	0.3	0.81	0.66
KF	0.42	0.3	0.81	0.66
OI	0.41	0.28	0.82	0.68
KFOI	0.41	0.28	0.82	0.68
Z-R	0.45	0.61	0.70	0.47

3. Verification

During June 30 to July 9, 2007, due to the stable west Pacific subtropical high pressure, strong monsoon surge, dry cold air from middle-high latitudes, and propagating eastward convection disturbance over the Tibetan Plateau, a Meiyu front cloud system with heavy rainfall takes shape over HRB [23]. It is noted that a belt of heavy rainfall is over HRB. The HRB experienced several heavy rainfall storm cases successively, which lead to the greatest flood over HRB since 1954.

The successive heavy rainfall storms lead to two peak discharges passing the main hydrologic station (Wangjia Dam) in the main channel of Huaihe River. A major flood event was recorded in the downstream Huaihe River lower the Runheji hydrologic station. And flood events were recorded for most of the tributaries. The heavy rainfall event includes three stages: June 30–July 2, July 4–July 5, and July 8–July 9. The most intense precipitation occurred in the last stage, during which new records of maximum daily precipitation were recorded for several stations. The strong rainfall eventually leads to flood diversion in Wangjia Dam.

To estimate the precipitation, observations from six radars and surface rain gauges (Figure 1) are used to demonstrate the integrated method of precipitation estimation. And the Z-R relationship method and four rain gauge correction methods (AC, KF, OI, and KFOI) of QPE are applied in heavy rain period from June 30 to July 9, 2007.

Figure 2 shows the precipitation estimation of middle stage of heavy rainfall case at 17:00–18:00 July 5 2007 (UCT) with Z-R method, four correction methods, three integrated methods mentioned in Section 2, and the observations from rain gauge (using the Kriging interpolation technique of the Golden Software Surfer 8).

The results from estimates and observations are shown in graded color shading in Figure 2. According to the rain gauge observations, there is one major rainfall belt from west to east. The maximum rainfall area (MRA1) is located in the middle of the HRB. The second strong rainfall area (MRA 2) is located in the southeast corner. The rainfall intensity of west section (WS) of the rainfall belt is weaker than the east section (ES).

As shown in Figure 2, all methods can produce similar pattern and magnitude of the precipitation with observations.

It is noted that DEA is more close to the observation in the WS. In the ES, the maximum rainfall in MRA1 was recorded by rain gauge more than 20 mm within one hour. KL, KFOI, and OI significantly overestimated the heavy precipitation in the MRA1. Other methods yielded similar precipitation estimation closed to the observation.

Compared with FEA, DEA could overcome the discontinuity of rainfall pattern in the east-south section. For the west section rain belt with weak precipitation, the maximum rainfall for one hour is recorded by gauge less than 20 mm. The FEA produced heavy precipitation with intensity more than 20 mm/h. However, the DEA yielded much weaker precipitation less than 20 mm/h, which is close to the observation, indicating the promising performance of DEA in improving QPE.

In general, these 8 QPE methods (including 3 integrate methods) show the good performance for the event occurring at 17:00 to 18:00 (UCT) July 5, 2007, and all have some skills in estimating the precipitation. To quantitatively evaluate the estimation errors for all these QPEs, the relative errors ($RE = (R_r(t) - R_s(t))/R_s(t)$) and correlation coefficients are analyzed for all rainfall patterns and strong intensity patterns (>10 mm/h) cases from June 30 to July 9, 2007. According to Table 2, the following can be seen:

- (1) For all precipitation patterns, three integrated methods (KL, DEA, and FEA) show better performance with reduced relative errors and higher correlation coefficients than other methods.
- (2) For the heavy precipitation region (>10 mm/hour), the KL and FEA are worse than AC. The DEA is more appropriate for QPE with reduced relative errors, and the correlation coefficient is equal to the maximum of Z-R and four gauge correction methods. Generally speaking, DEA is the best and most effective method for precipitation estimation.

4. Conclusion

An integrated system for precipitation estimation was introduced in this paper. This system can effectively select the optimal QPE method from five different QPE methods for specific precipitation event by evaluating the variation of the random errors for different cloud types from latest

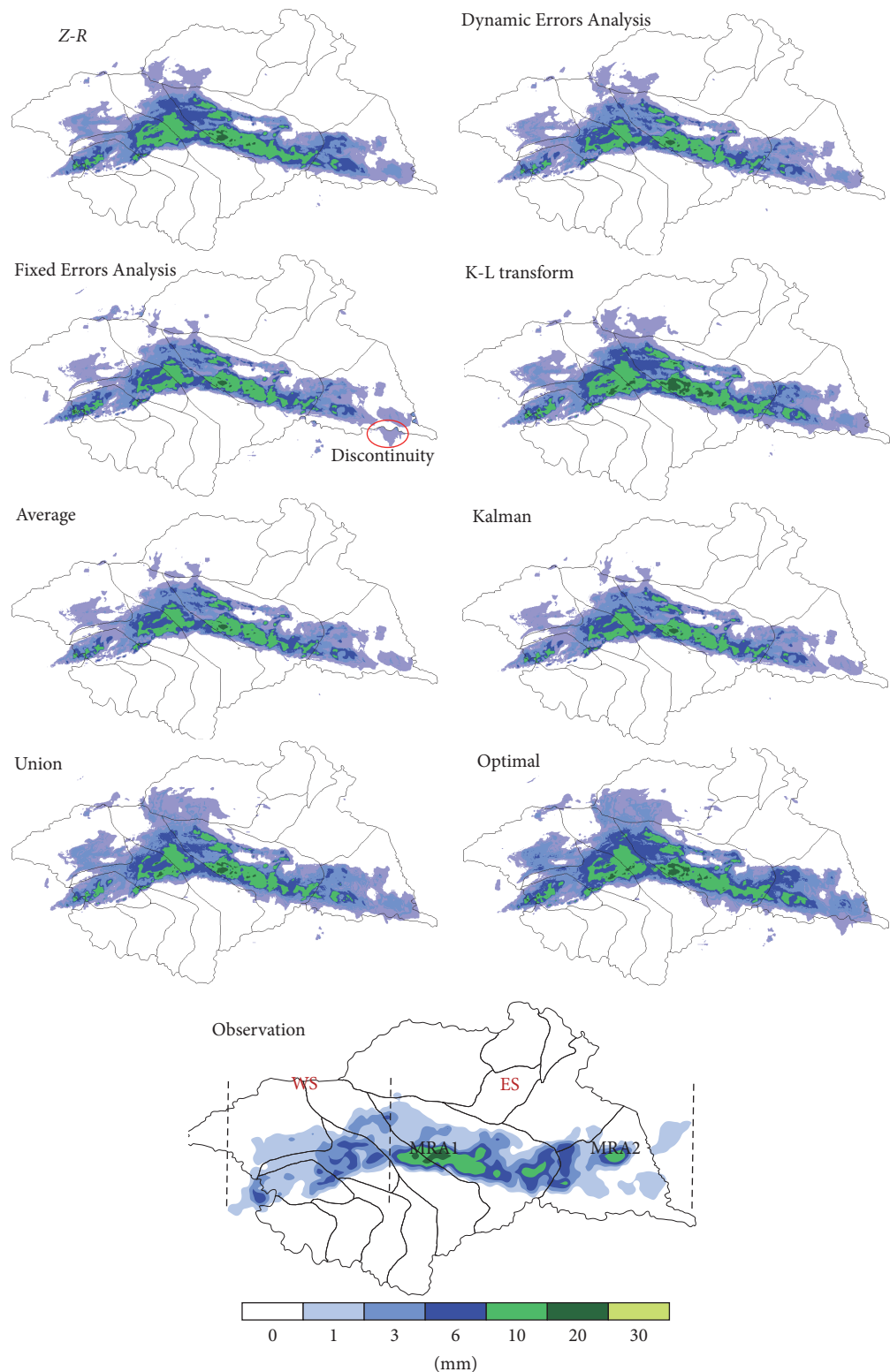


FIGURE 2: Rainfall distributions from 17:00 to 18:00 (UCT) July 5, 2007.

precipitation estimates. The application of this integrated system on the event occurring in early July of 2007 shows that it can effectively determine the best estimation results from different QPE methods based on the capability of the stability of the precipitation estimation. This integrated method DEA with rainfall cloud classification could improve the application ability and precision of estimating precipitation for multiple precipitation types.

Competing Interests

The authors declare that they have no competing interests.

Acknowledgments

This study was supported by the National Natural Science Foundation of China under Grant no. 41275030, the R & D Special Foundation for Public Welfare Industry (meteorology) of China under Grant no. GYHY201306040, the National Natural Science Foundation of Anhui Province under Grant no. 1508085MD64, and Shanxi Meteorological Research Foundation under Grant no. SXKKFRY20100101.

References

- [1] J. Liu, Z. Song, D. F. Liu et al., "Classified Z-I relationship and its application to the measurement of rainfall by radar over the Huaihe River Basin," *Scientia Meteorologica Sinica*, vol. 19, no. 6, pp. 213–219, 1999 (Chinese).
- [2] J. Pan and P. C. Zhang, "Estimating precipitation by radar measured vertical integration of liquid water," *Journal of Nanjing Institute of Meteorology*, vol. 23, no. 1, pp. 87–92, 2000 (Chinese).
- [3] X.-Y. Liu, J.-T. Mao, J.-R. Li, and Y.-J. Zhu, "Application of radar-raingauge estimated mean area precipitation to runoff simulation," *Journal of Hydraulic Engineering*, vol. 22, no. 4, pp. 51–55, 2002.
- [4] Y. Huang, W. Hu, A. Zhang et al., "Flood-causing torrential rain forecasting and warning system for Haihe River," *Meteorological Monthly*, vol. 32, no. 5, pp. 105–109, 2006 (Chinese).
- [5] W. Zhenhui, P. Xiaofang, L. Jiantong, and G. Li, "Application of the principal characteristics extraction technique to consensus analysis of weather radar rainfall estimates," *Inverse Problems*, vol. 19, no. 3, pp. 525–531, 2003.
- [6] L. Guan, Z. H. Wang, and X. F. Pei, "The consensus methods and effects of estimatiing rainfall using radar," *Scientia Meteorologica Sinica*, vol. 24, no. 1, pp. 104–111, 2004.
- [7] J. S. Marshall, R. C. Langille, and W. M. Palmer, "Measurement of rainfall by radar," *Journal of the Atmospheric Sciences*, vol. 4, no. 4, pp. 186–192, 1947.
- [8] L. Hu, Y. Zhao, Y. Liu, C. Scheepens, and A. Bouchard, "Updating multipoint simulations using the ensemble Kalman filter," *Journal of Hydraulic Engineering*, vol. 22, pp. 7–55, 2013.
- [9] X. Liu, J. Mao, Y. Zhu, and J. Li, "Radar rainfall estimation and its application on runoff simulation over SHIGUANHE catchments," *Acta Scientiarum Naturalium Universitatis Pekinensis*, vol. 38, no. 3, pp. 342–349, 2002.
- [10] E. A. Brandes, "Optimizing rainfall estimates with the aid of radar," *Journal of Applied Meteorology*, vol. 14, no. 7, pp. 1339–1345, 1975.
- [11] J. Koistinen and T. Puhakka, "An improved spatial gage-radar adjustment technique," *Bulletin of the American Meteorological Society*, vol. 62, no. 6, p. 926, 1981.
- [12] A. Rafieeinab, A. Norouzi, D.-J. Seo, and B. Nelson, "Improving high-resolution quantitative precipitation estimation via fusion of multiple radar-based precipitation products," *Journal of Hydrology*, vol. 531, pp. 320–336, 2015.
- [13] R. A. Fulton, J. P. Breidenbach, D.-J. Seo, D. A. Miller, and T. O'Bannon, "The WSR-88D rainfall algorithm," *Weather and Forecasting*, vol. 13, no. 2, pp. 377–395, 1998.
- [14] WILSON JW, "Integration of radar and raingage data for improved rainfall measurement," *Journal of Applied Meteorology*, vol. 9, no. 3, pp. 489–498, 1970.
- [15] R. Daley, *Atmospheric Data Analysis*, Cambridge University Press, New York, NY, USA, 1991.
- [16] Y. Wen, P. Kirstetter, Y. Hong et al., "Evaluation of a method to enhance real-time, ground radar-based rainfall estimates using climatological profiles of reflectivity from space," *Journal of Hydrometeorology*, vol. 17, no. 3, pp. 761–775, 2016.
- [17] Q. Wei, Z. Q. Hu, L. P. Liu et al., "C-band polarization radar data preprocessing and its application to rainfall estimation," *Plateau Meteorology*, vol. 35, no. 1, pp. 231–243, 2016 (Chinese).
- [18] Y. Huang, J. Ye, and G. Chen, "Consensus methods of estimating rainfall using radar base on error analysis," *Journal of Atmospheric and Environmental Optics*, vol. 5, no. 5, pp. 342–349, 2010.
- [19] J.-Y. Ye, Y. Huang, Z.-J. Li, and Z.-B. Yu, "Rainfall estimation method based on multiple-doppler radar over the Huaihe river basin," *Journal of Hydrologic Engineering*, vol. 18, no. 11, pp. 1471–1476, 2013.
- [20] Y. Huang, W. Hu, and H. Liu, "A method of cloud classification base on image entropy," in *Proceedings of the 2nd International Congress on Image and Signal Processing (CISP '09)*, IEEE, Tianjin, China, October 2009.
- [21] M. L. Baeck and J. A. Smith, "Rainfall estimation by the WSR-88D for heavy rainfall events," *Weather and Forecasting*, vol. 13, no. 2, pp. 416–436, 1998.
- [22] C. W. Ulbrich and L. G. Lee, "Rainfall measurement error by WSR-88D radars due to variations in Z-R law parameters and the radar constant," *Journal of Atmospheric and Oceanic Technology*, vol. 16, no. 8, pp. 1017–1024, 1999.
- [23] Z. Xiaohong, J. Tianshan, and H. Wen, "Multiscale circulation features of heavy rain over Huaihe River Basin in rainy season in 2007," *Journal of Nanjing Institute of Meteorology*, vol. 32, no. 2, pp. 321–326, 2009 (Chinese).

Research Article

Statistical Comparison of Cloud and Aerosol Vertical Properties between Two Eastern China Regions Based on CloudSat/CALIPSO Data

Yujun Qiu,¹ Jing Wang,¹ and Keran Yang²

¹Key Laboratory of Meteorological Disaster, Ministry of Education (KLME) and Joint International Research Laboratory of Climate and Environment Change (ILCEC) and Collaborative Innovation Center on Forecast and Evaluation of Meteorological Disasters (CIC-FEMD) and Key Laboratory for Aerosol-Cloud-Precipitation of China Meteorological Administration, Nanjing University of Information Science & Technology, Nanjing 210044, China

²Xinping Meteorological Bureau, Yuxi, Yunnan 653499, China

Correspondence should be addressed to Yujun Qiu; qyj@nuist.edu.cn

Received 19 September 2016; Revised 19 December 2016; Accepted 26 January 2017; Published 2 March 2017

Academic Editor: Ke Zhang

Copyright © 2017 Yujun Qiu et al. This is an open access article distributed under the Creative Commons Attribution License, which permits unrestricted use, distribution, and reproduction in any medium, provided the original work is properly cited.

The relationship between cloud and aerosol properties was investigated over two $4^\circ \times 4^\circ$ adjacent regions in the south (R1) and in the north (R2) in eastern China. The CloudSat/CALIPSO data were used to extract the cloud and aerosol profiles properties. The mean value of cloud occurrence probability (COP) was the highest in the mixed cloud layer ($-40^\circ\text{C} \sim 0^\circ\text{C}$) and the lowest in the warm cloud layer ($>0^\circ\text{C}$). The atmospheric humidity was more statistically relevant to COP in the warm cloud layer than aerosol condition. The differences in COP between the two regions in the mixed cloud layer and ice cloud layer ($<-40^\circ\text{C}$) had good correlations with those in the aerosol extinction coefficient. A radar reflectivity factor greater than -10 dBZ occurred mainly in warm cloud layers and mixed cloud layers. A high-COP zone appeared in the above- 0°C layer with cloud thicknesses of 2–3 km in both regions and in all the four seasons, but the distribution of the zonal layer in R2 was more continuous than that in R1, which was consistent with the higher aerosol optical thickness in R2 than in R1 in the above- 0°C layer, indicating a positive correlation between aerosol and cloud probability.

1. Introduction

Aerosol and cloud vertical structures directly affect the atmospheric heating rate [1] and exert great influence on atmospheric radiation and circulation [2–6]. Aerosols are known to have great impacts on cloud properties [7–9]. Earlier studies using aircraft and satellite sounding data have shown that, under the condition of sufficient cloud liquid water, increased aerosol concentrations will increase cloud droplet concentrations, decrease cloud droplet sizes, and increase the lifespans of clouds [10–13].

China has experienced rapid economic growth and dramatic urbanization and thus has experienced increased aerosol loading [14–16]. For example, frequent heavy aerosol loadings have occurred in the Jing-jin-ji metropolis circle

(the northern part of East China, including Beijing, Tianjin, and Northern Hebei province) due to its dense population and industry in this region and surrounding areas [14, 17]. Aerosol loadings in the atmospheric boundary layer in this region reached levels of $10^3\text{--}10^4/\text{cm}^3$, with submicron particles dominating the loading [18–22]. Local sources and long-range transport both contributed to the high levels of aerosol concentrations [23–25].

To investigate the impacts of aerosols on cloud distributions and other properties in different atmospheric environments such as aerosol pollution levels and humidity conditions, two adjacent regions in the south and north of East China were selected and compared in terms of the distribution characteristics of clouds of different phases. The northern high-latitude region is adjacent to the Jing-jin-ji metropolis

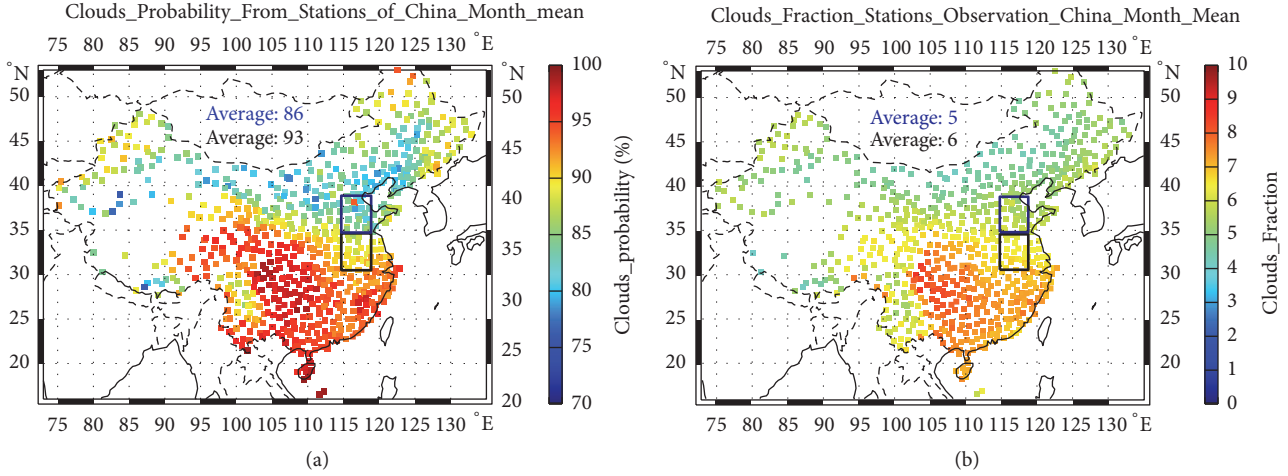


FIGURE 1: Distributions of monthly mean values of cloud occurrence frequencies and cloud covers observed by the ground observation station. The top rectangular zone represents Region 2 and the bottom one represents Region 1.

circle, and the southern region is located in the Huaihe River drainage area. Aerosol pollution (such as dust and urban pollution aerosols) in the northern region is severer than that in the southern region. Humidity and aerosol conditions in the two regions were first compared. COPs in different cloud layers defined by temperature condition were then compared in four seasons. Finally, the characteristics of COP in different cloud layers were analyzed and discussed under combined humidity and temperature conditions. Research results from the present study are expected to provide the knowledge that is needed for parameterizing cloud formation in climate models.

2. Data and Methods

2.1. Data Source. Two regions were selected for comparative research (see Figure 1). Region 1 (R1) is centered at Shouxian County in Anhui Province, and Region 2 (R2) is centered at Tai'an in Shandong province. Both regions are of size 4° longitude by 4° latitude. R2 is located just to the south of the Jin-Jing city circle. The observed cloud cover data at the ground weather stations (from the beginning of station observation to 2005; data were obtained from the China Meteorological Administration Resource Center) showed obvious regional characteristics in cloud occurrence frequency and cloud cover fraction in the two regions. From the long-term data, the monthly mean values of cloud occurrence frequency and cloud cover fraction in R1 were, on average, 1.1 and 1.2 times those in R2, respectively, which showed the climate differences of the two regions.

The CloudSat/CALIPSO data (including 2B-GERPROF, 2B-temp, and 2B-lidar) used in the present study covered the period from June 14, 2006, to December 31, 2010. The 2B-GERPROF data contained the radar reflectivity factors of millimeter-wave radar at different altitudes. The temperature data in 2B-temp were obtained from the European Center for Medium-range Weather Forecasts. The 2B-Lidar data were

obtained by combining CloudSat and CALIPSO data, including cloud cover and single-layer and multilayer cloud-base and cloud-top heights. Cloud cover data at different heights were used in this study. Data from CloudSat/CALIPSO were obtained by scanning from top to bottom. Data at the lowest levels were believed to have large uncertainties due to the strong reflectivity of the surface leading to anomalously high detection signal. Thus, only data above the 0.5 km level were used here. Each level (at 0.24 km increments) scanned by CloudSat was treated as a pixel to obtain statistically the sample size of the pixels within each radar reflectivity factor range, as shown in Figure 2.

Data from the CALIPSO level 2 (CAL_LID_L2_05kmAPro-Prov-V3-01) product for the period from June 13, 2006, to Sep. 17, 2008, were also used in the present study. This dataset provides aerosol extinction coefficients (532 nm and 1064 nm bands) and cylinder optical thickness.

2.2. Methodology. The 2B-GEOPROF and 2B-GEOPROF-Lidar data of the CloudSat/CALIPSO product were used to judge the occurrence and positions of clouds. Three criteria needed to be met simultaneously for cloud occurrence: (1) The cloud reflectivity factor is larger than -40 dBZ and smaller than 50 dBZ, which is the dBZ range of CloudSat cloud radar reflectivity; (2) the CPR cloud mask is larger than 20 and smaller than 40, which is the standard under which CloudSat determines if there is a cloud; and (3) cloud cover is larger than 5% and smaller than 100%, which reduces the uncertainty of cloud identification and misidentifications such as when aerosols are mistaken as clouds.

The COP at any height was calculated as the ratio of the number of sites with cloud occurrence to the total number of sites scanned in an orbit. The monthly average COP was first obtained for each level before averaging into seasonal values. March, April, and May were treated as spring; June, July, and August as summer; September, October, and November as autumn; and December, January, and February as winter. The COPs and vertical distribution characteristics in the

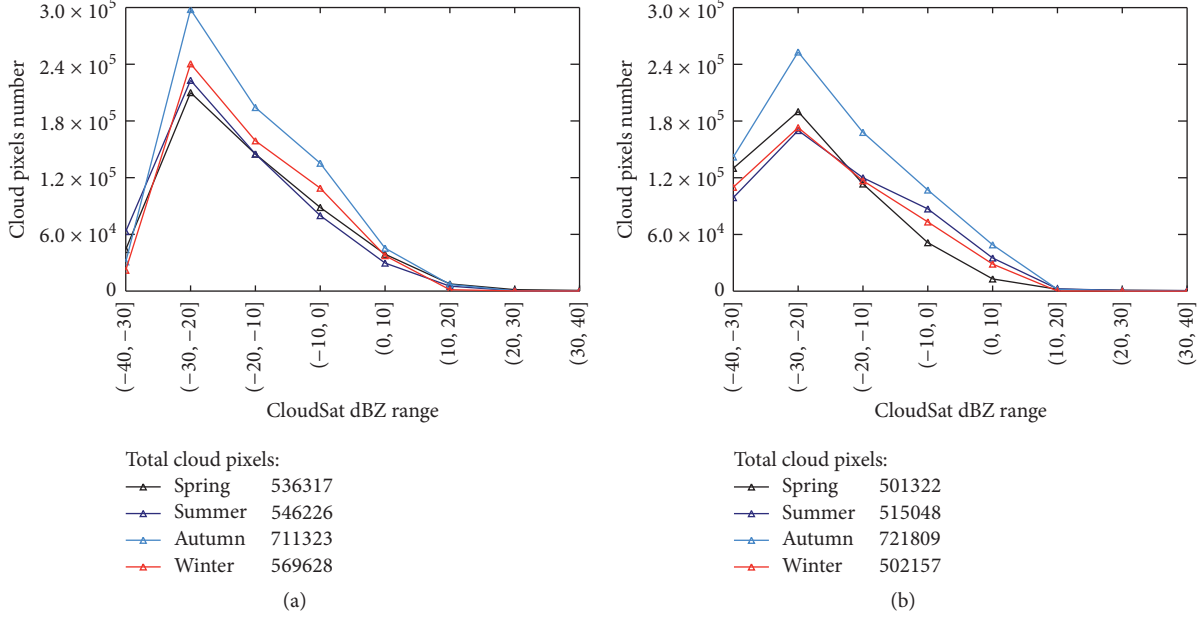


FIGURE 2: Number of pixels within each radar reflectivity factor range during the four seasons when CloudSat passed through Regions 1 (a) and 2 (b).

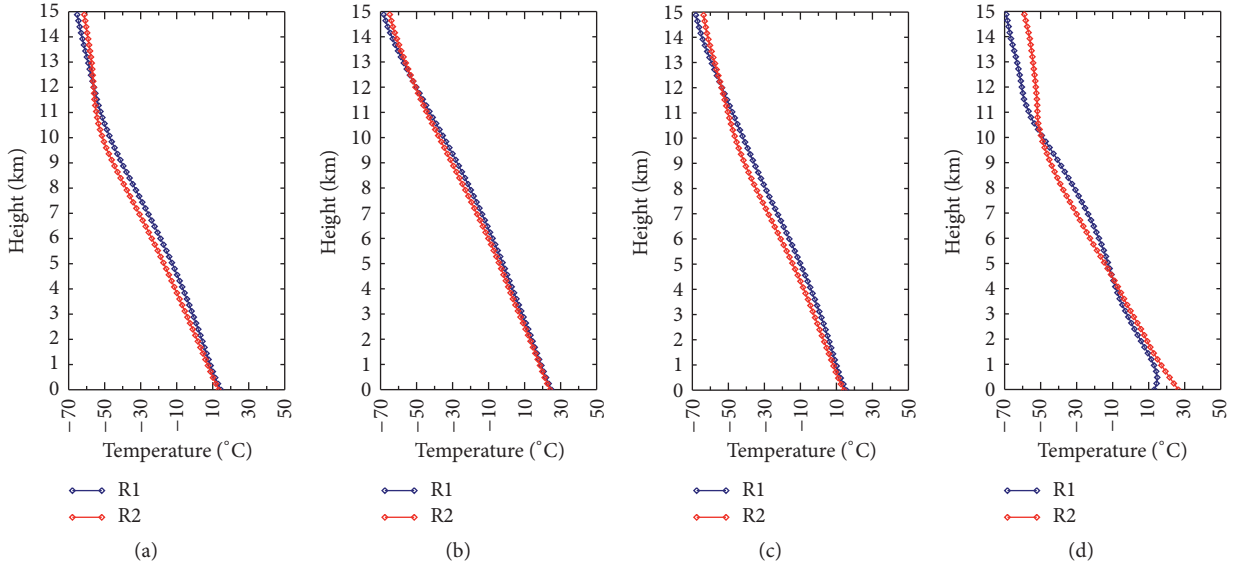


FIGURE 3: The seasonal temperature profiles in R1 and R2 in (a) spring, (b) summer, (c) autumn, and (d) winter.

two regions and during different seasons were statistically calculated using the nearly five years of data. The COP at any height was obtained by dividing the total number of pixels with cloud occurrence at this height by the total number scanned.

The aerosol extinction coefficient includes both the 532 nm and 1064 nm bands. To avoid the influence of certain special weather conditions, only those data with daily mean extinction coefficients larger than 0 for more than two consecutive scanning days were used in the analysis. Seasonal average vertical profiles of extinction coefficients were obtained for the two regions.

3. Results

3.1. Atmospheric Environment Differences between R1 and R2. The cloud vertical structure varies greatly with geographical location and time due to many factors, such as the underlying surface conditions and aerosol loading [26–28]. R1 and R2 belong to the monsoon climate zone in East Asia, with higher temperatures in summer and lower ones in winter throughout all vertical levels. The vertical structures of the temperature were similar between the two regions (Figure 3). The difference in temperature was the smallest in summer and biggest in winter. The average temperatures in R1 in

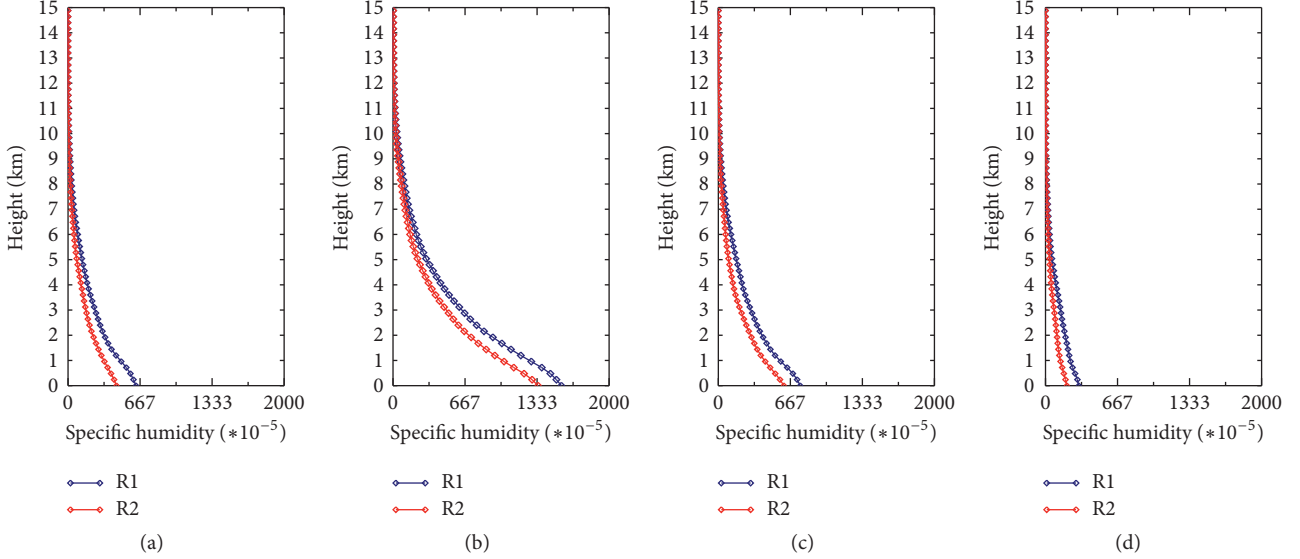


FIGURE 4: The seasonal profiles of specific humidity in R1 and R2 in (a) spring, (b) summer, (c) autumn, and (d) winter.

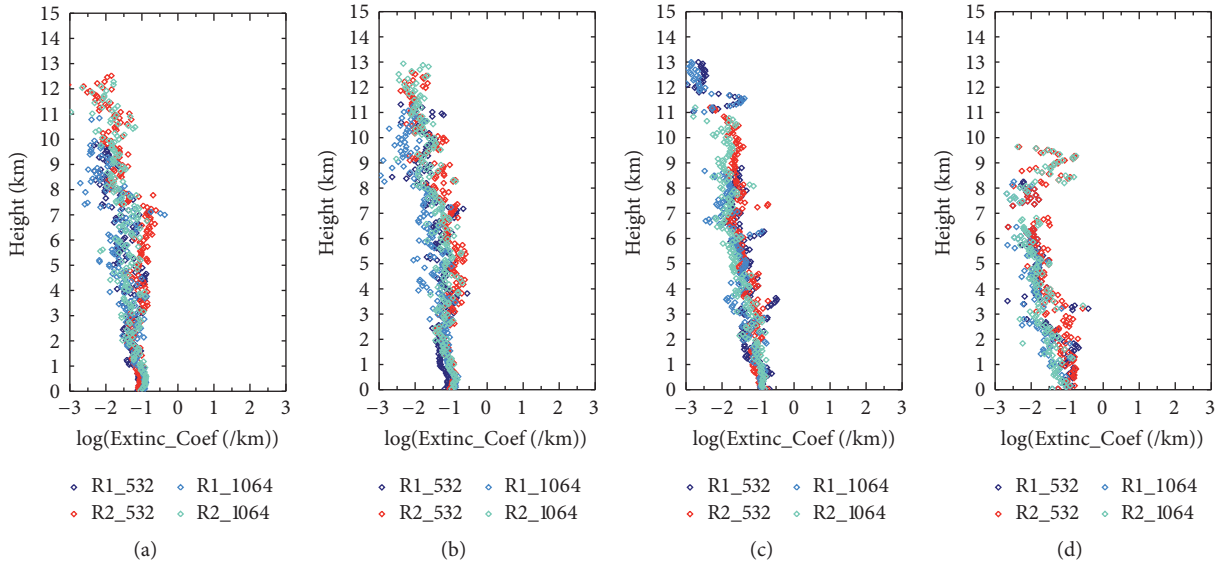


FIGURE 5: CALIPSO aerosol extinction coefficient vertical profile in (a) spring, (b) summer, (c) autumn, and (d) winter. Shx_532 represents the extinction coefficient of Region 1 at 532 nm band; Shd_532 represents the extinction coefficient of Region 2 at 532 nm band; Shx_1064 represents the extinction coefficient of Region 1 at 1064 nm band; and Shd_1064 represents the extinction coefficient of Region 2 at 1064 nm band.

spring, summer, and autumn were 2.5, 1.2, and 2.5°C higher than those in R2, respectively. The temperatures below 4.3 km height in R2 in winter were higher by 0.48°C than those in R1, and the greater temperature differences were close to the ground, which might be due to the impact of winter heating and the Greenhouse Effect of aerosols in R2 [29].

From Figure 4, the average specific humidities in R1 in spring, summer, autumn, and winter were 1.5, 1.3, 1.4, and 1.7 times those in R2, respectively, implying that the water contents in R1 were higher than those in R2.

The aerosol optical depths (AODs) in R2 calculated from the aerosol extinction coefficient profile at the 532 nm

band were approximately 1.9, 2.2, 0.9, and 1.1 times those in R1 in spring, summer, autumn, and winter, respectively (Figure 5) and 1.2, 1.5, 1.1, and 1.7 times the 1064 nm band. To avoid the influence of the high extinction coefficient of an extreme aerosol pollution event on the mean value of the extinction coefficient, the extinction coefficient was also calculated based on the frequency spectrum of the aerosol extinction coefficient (see Figure 6). The whole extinction coefficient range ($0.0\text{--}1.5\text{ km}^{-1}$) was divided into 10 equally sized subranges; for example, the first range is from 0 to 0.125 km^{-1} , and the tenth range is from $1.25\text{ to }1.5\text{ km}^{-1}$. The average value of the aerosol coefficient in R2 was larger than

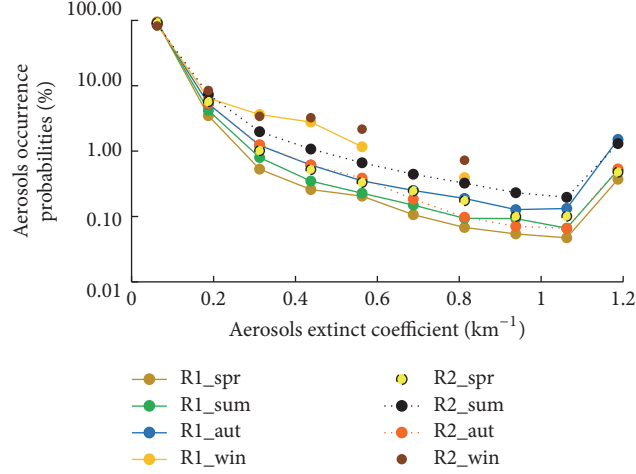


FIGURE 6: The probability of aerosol extinction coefficient at 532 nm band in the four seasons and two regions.

TABLE 1: The ratio of the COPs, specific humidities, and aerosol extinction coefficients at the 532 nm band in Regions 1 and 2 in different cloud layers.

R1/R2	COP				Specific humidity				Extint_532 nm			
	Spr	Sum	Aut	Win	Spr	Sum	Aut	Win	Spr	Sum	Aut	Win
WCL	1.5	1.1	1.3	3.8	1.3	1.2	1.2	1.8	1.2	0.8	1.2	0.9
MCLLT	1.6	0.8	1.4	1.5	1.2	1.2	1.3	1.8	0.6	0.5	1.4	1.2
MCLHT	1.1	0.8	0.8	0.7	1.1	1.1	1.1	1.0	0.4	0.5	0.4	0.2
ICL	0.9	1.4	0.8	0.8	1.1	1.3	1.0	1.0	0.1	0.6	0.5	0.1

that in R1. It is noted that R2 covers Shijiazhuang City and is also adjacent to the south of the Jing-Jin area where aerosol loadings were high. For example, aerosol concentrations in Jing-Jin region in the layers below 4.5 km were up to 10^3 cm^{-3} , with average particle sizes from 0.16 to $0.19 \mu\text{m}$ [21]. Aerosol concentrations at the 5 km layer above Shijiazhuang City were up to 10^3 cm^{-3} , with average particle sizes from 0.15 to $0.22 \mu\text{m}$ [22]. Aerosol concentrations in Hebei province were up to 10^3 – 10^4 cm^{-3} in the layers below 3 km, with average particle sizes of $0.15 \mu\text{m}$ [30].

3.2. COP Vertical Structure. Clouds of different phases have different heating and thermodynamic and radiation processes [31]. Here, the cloud layer with temperatures higher than 0°C is referred to as the warm cloud layer (WCL); with temperatures between -40°C and -20°C as the mixed cloud layer (MCL) with lower temperature (MCLLT); with temperatures between -20°C and 0°C as the mixed cloud layer with higher temperature (MCLHT); and with temperatures lower than -40°C as the ice cloud layer (ICL). Figure 7 presents the vertical profiles of COP in the two regions during the four seasons. The differences in COPs between R1 and R2 in spring and winter were greater than those in summer and autumn. The COP in R1 in spring was approximately 1.1 times that in R2. The COPs in R2 in the other seasons were higher than those in R1.

From Figure 7, the COPs within different cloud-phase layers differed significantly. For the COP in the WCL, the

average values in R1 were 0.7%, 1.4%, 1.0%, and 0.4% in spring, summer, autumn, and winter, respectively and were 1.5, 1.1, 1.3, and 3.8 times, respectively, those in R2. Cloud formation can be influenced by humid conditions and cloud nucleation, which changes the concentration or properties of aerosols. The comparison of the COP results between R1 and R2 was similar to the comparison of the specific humidity between R1 and R2; in the four seasons; the specific humidities in R1 were approximately 1.3, 1.2, 1.2, and 1.8 times those in R2 in the corresponding seasons (see Table 1). Observations show that the high aerosol concentrations in R2 provided rich condensation nuclei for cloud formation [17, 32]. The seasonal mean occurrence probabilities of the aerosol extinction coefficients at the 532 nm band in the range of 1.125 – 1.25 km^{-1} in R1 and R2 were compared (see Figure 8). The difference between the aerosol extinction coefficients in R1 and R2 was not similar to that for COP. From Figure 9, the average values of the aerosol extinction coefficient in R2 in the WCL were approximately 1.2 times those in R1 in both spring and autumn, and the mean extinction coefficients in R2 were approximately 1.3 and 1.1 times those in R1 in summer and winter, respectively. These results implied that water vapor condition may affect COP on the WCL stronger than aerosols.

The COPs in R1 and R2 in the MCL were 70% and 70.6%, respectively, which were higher than those in the WCL and ICL. The two regions both reached the highest values of COP in autumn. Compared to the COPs in the WCL, the difference in COPs between the two regions in the MCLLT was larger. The ratio of the COP in R1 to that in R2 showed slight

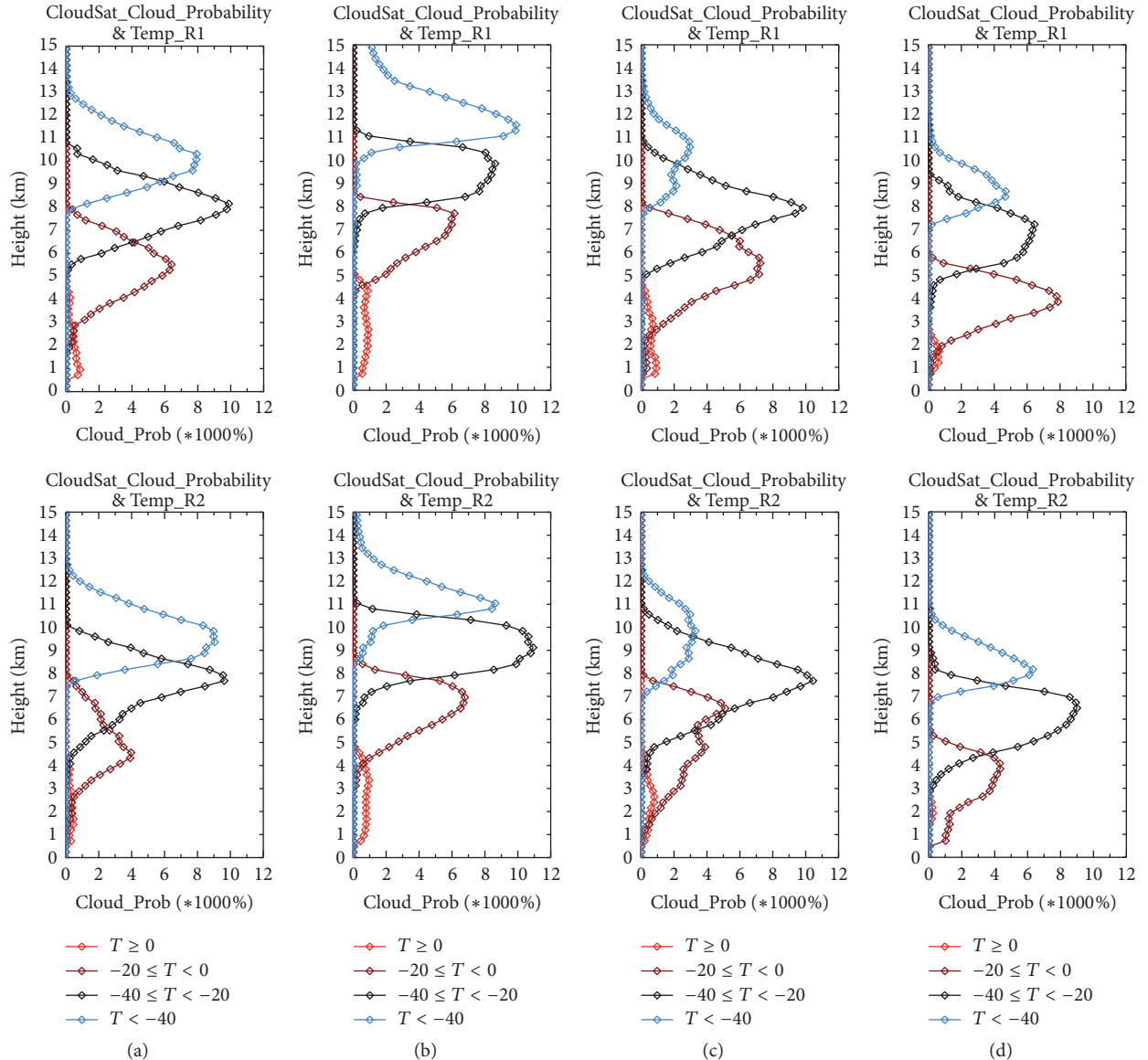


FIGURE 7: Vertical profiles of COP in R1 and R2 in (a) spring, (b) summer, (c) autumn, and (d) winter, respectively. Red, brown, black, and blue dotted lines refer to the COPs in the warm cloud layer with temperatures higher than 0°C , mixed cloud layer with temperatures between -20°C and 0°C , mixed cloud layer with temperatures between -40°C and -20°C , and ice cloud layer with temperatures lower than -40°C , respectively.

increases in spring and autumn and decreases in summer and winter. The ratio of the COP in R1 to that in R2 in winter decreased from 3.8 in the WCL to 1.5 in the MCLLT. The ratio of the specific humidity between R1 and R2 was compared to check the condition of the atmospheric environment. The ratio of the specific humidity in R1 to that in R2 in the MCLLT was similar to that in the WCL in the four seasons. However, the ratio of the extinction coefficient in R1 to that in R2 revealed larger differences in summer and winter. The COP in the MCLLT in summer increased to 3.7 times that in the WCL in R1 and to 5.1 times in R2, which was due to the COP in R2 being higher than that in R1 in the MCLLT. At the same time, the aerosol extinction coefficient in R2 was approximately 2.0 times that in R1. In addition, the COP in R1 in winter

was approximately 1.5 times that in R2 in the MCLLT, and the aerosol extinction coefficient was 1.2 times higher, which implied that the content of aerosols has a positive correlation with cloud occurrence in the MCLLT.

The COPs in R1 and R2 in the MCLHT were higher than those in the MCLLT in all the four seasons. The COPs increased by 3.1%, 2.9%, 0.8%, and 0.2% in spring, summer, autumn, and winter, respectively, in R1 and 5.4%, 4.2%, 5.8%, and 5.8% in R2; the differences were greater in R2 than in R1. The ratio of specific humidity in R1 to that in R2 changed smoothly in the whole troposphere. However, the extinction coefficients in R2 were approximately 2.2, 2.1, 2.5, and 4.2 times those in R1 in the MCLLT, which implied that the aerosols were closely correlated with the COP in the MCLLT.

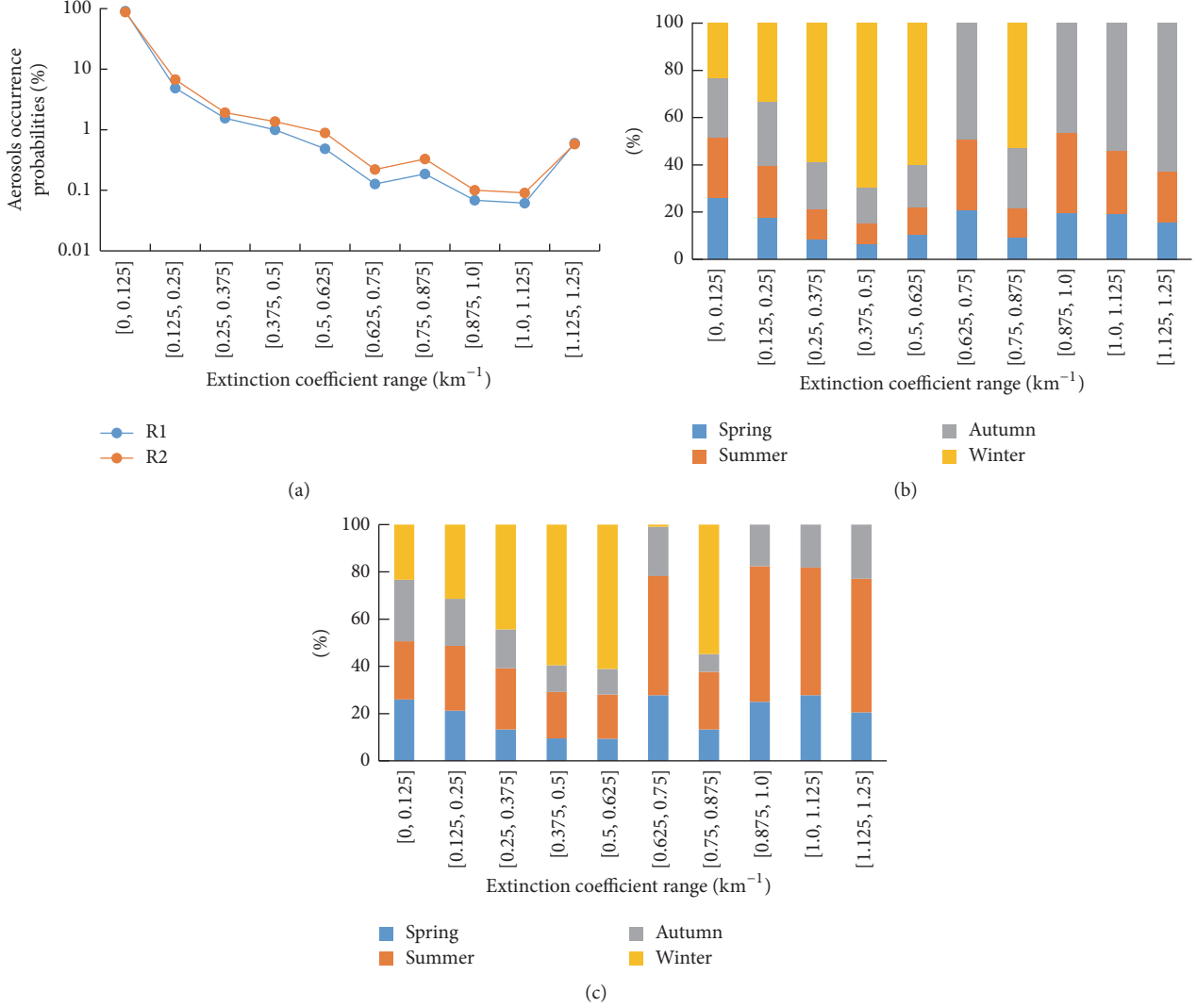


FIGURE 8: The mean occurrence probability of aerosol extinction coefficient at 532 nm band in the range of $1.125\text{--}1.25 \text{ km}^{-1}$. (a) Total occurrence probability of aerosol extinction coefficient of four seasons in Region 1 and Region 2. (b) and (c) present that the percent of the occurrence probability in all of the ranges in each season is equal to 100% in Region 1 and Region 2, respectively. The blue, yellow, gray, and green color represent summer, autumn, winter, and spring, respectively.

The COPs in the ICL were lower than those in the MCL in both of the regions and in all the four seasons. The mean COPs were 26.7% and 26.8% in R1 and R2, respectively. Except in summer, the COPs in R2 in each season were higher than those in R1. The mean values of the aerosol extinction coefficients at the 532 nm band in the ICL in R2 were 10.0, 1.7, 2.0, and 10.0 times greater than those in R1 in the four seasons. The COP in R2 in spring reached the highest value for all the four seasons, which may be due to the influence of the long-distance transport of dust as ice nuclei from the Taklamakan desert in western China and Inner Mongolia in downwind areas [24, 25]. Dust in the upwind directions of the two regions and mixed aerosols in the transmission processes may have been incorporated into the troposphere [25, 33], which is effected by the East Asian subtropical westerly jet zone [34–36]. This process enhanced cloud condensation nuclei in this

layer and thus affected cloud distribution characteristics. R2 is closer than R1 to the westerly jet central zone [37].

3.3. Vertical Structure of the Cloud Reflectivity Factor. COP with different radar reflectivities was also investigated here. From the discussion above, the COPs in R1 and R2 mainly appeared in the mixed cloud layers and had good correlations with the aerosol extinction coefficient. Figure 10 shows the vertical profiles of COP within the mixed clouds with cloud-base temperatures higher than 0°C and cloud-top temperatures lower than 0°C as a function of radar reflectivity in each season.

According to Figure 10, high values of COP were mainly concentrated below 6 km and in the range of radar reflectivity factors above -10 dBZ in both of the two regions and during all of the four seasons. The range of the reflectivity

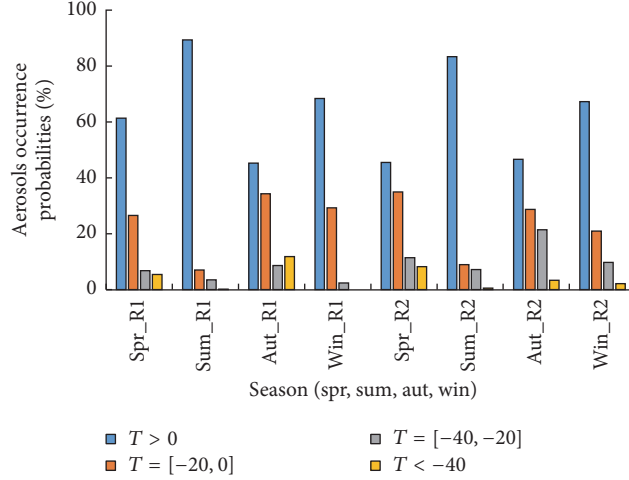


FIGURE 9: CALIPSO aerosol extinction coefficient at 532 nm band in R1 and R2 in the four seasons. Spr_R1, Sum_R1, Aut_R1, and Win_R1 represent the extinction coefficient of R1 at 532 nm band in spring, summer, autumn, and winter, respectively; $T > 0$, $T = [-20, 0]$, $T = [-40, -20]$, and $T < -40^\circ\text{C}$ represent the cloud layers of WCL, MCLLT, MCLHT, and ICL, respectively.

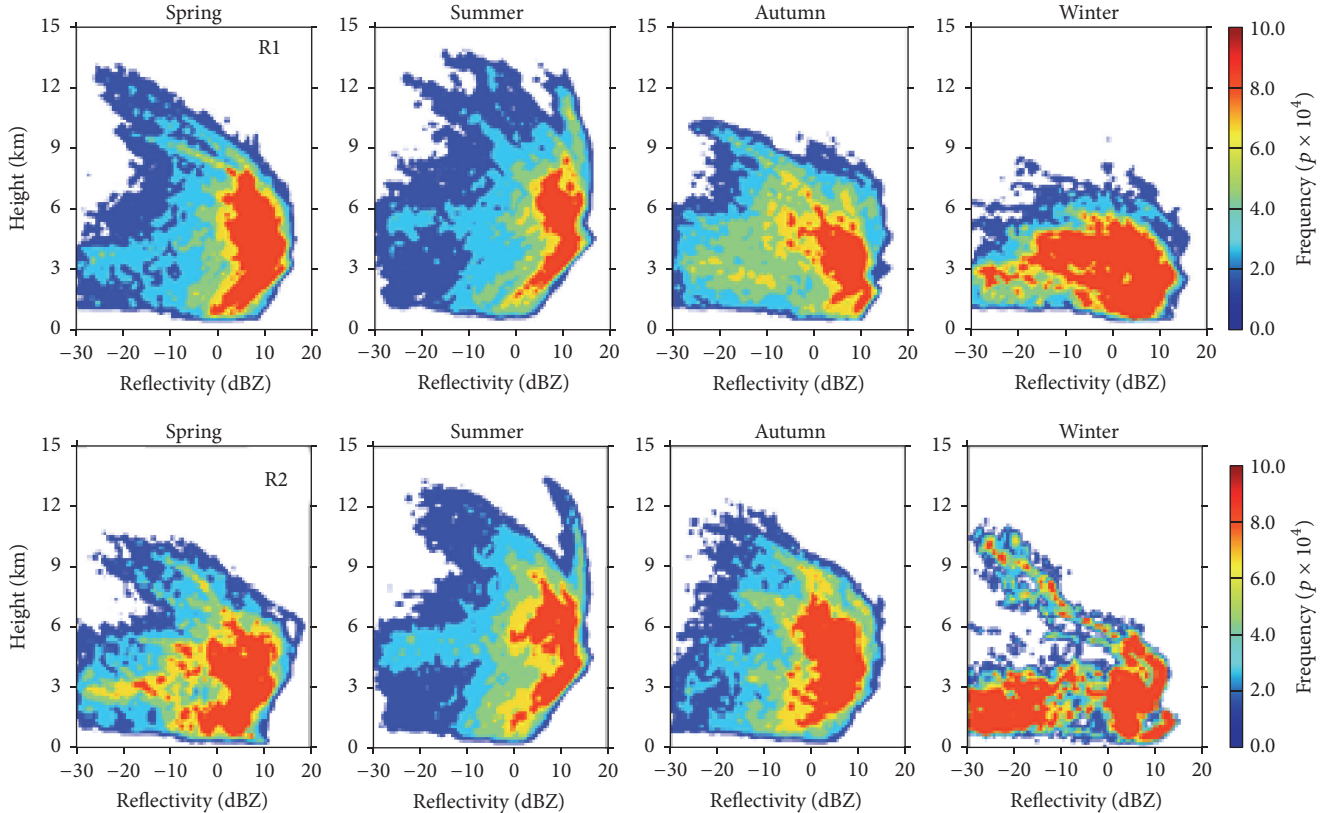


FIGURE 10: COPs of mixed phase clouds in Regions 1 and 2 under different reflectivity factors.

factors with high-COP values (greater than 0.0008%) was the narrowest in summer and the widest in winter. Affected by many factors, including temperature and water vapor content, the maximum value of the corresponding radar reflectivity factor decreased with increasing height, and its range became narrower with increasing height. Such trends were more obvious in R2 than R1 during all of the seasons

except autumn. In addition, the COP in the layer above 9 km in summer showed extended high values at approximately 10 dBZ over both regions, which may be due to the influence of strong convective clouds in summer (heap cloud). Tropical convective clouds can be as high as 15 km [38].

A high-COP layer with a thickness of 2 to 3 km appeared in the layer above 0°C , which was determined according

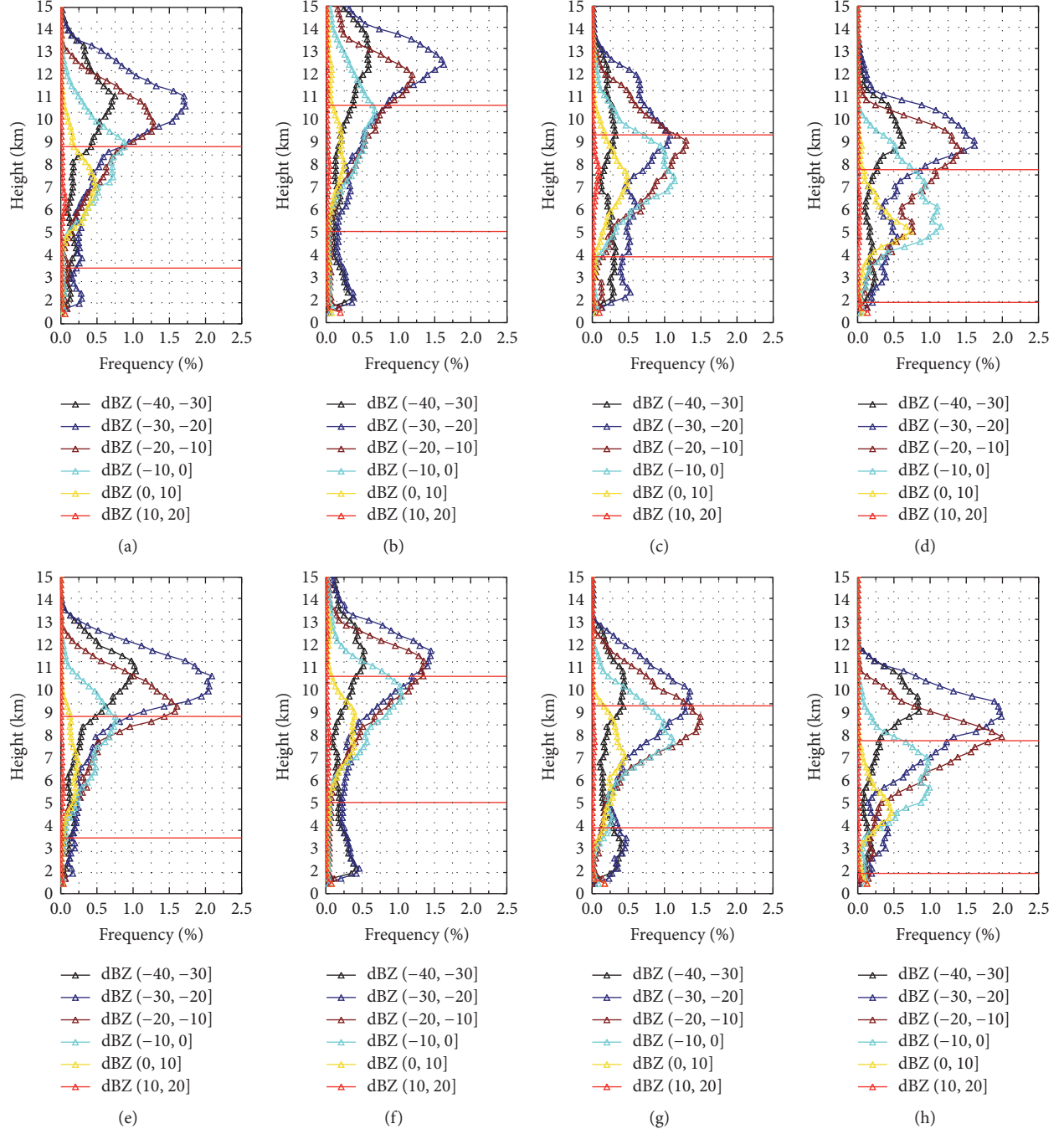


FIGURE 11: COP in Regions 1 (upper row) and 2 (lower row) within the different ranges of radar reflectivity factor during the four seasons (from left: spring, summer, fall, and winter). The upper and lower horizontal straight red lines represent the -40°C and 0°C layer, respectively.

to the temperature in Figure 3, in the -30 dBZ to 15 dBZ reflectivity factor range over both of the regions and during all the four seasons (See Figure 10). The high-COP values of R2 were more continuous than those of R1 in spring, summer, and winter. Different from that of R1, the COP of R2 in winter showed a narrow high-value vertical zone with COP value increasing with height, and the corresponding radar reflectivity factor was linearly reduced to -30 dBZ at approximately 11 km. The range of the corresponding aerosol

extinction coefficients in the high-continuous-value zones of COP in the two regions in all the four seasons was also wide according to the data in Figure 5. The aerosol optical thicknesses in R2 over the 0°C layer in the four seasons were 2.5, 2.0, 1.0, and 1.0, respectively, for the 532 nm band and 1.5, 2.5, 1.3, and 3.5 for the 1064 nm band, which were greater than those in R1. The aerosol levels differed greatly between the two regions in spring, summer, and winter. Huang et al. [25] studied the vertical distribution characteristics of

dust in the Taklamakan desert in the western China Inner Mongolia Gobi sand source area and its downwind direction and determined that R2 was located in the central area of the downwind zone of the dust. The dust transport from the sand source areas to East China showed a two-layer structure, with the highest dust frequencies appearing at 9 to 11 km and at 3 km. Even in summer, dust can be transported for long distances [24]. Li et al. [39] showed that large aerosol particles were mainly distributed over the 2.5 km height in this region, indicating that the dust aerosols from the upwind directions and other types of aerosols mixed in the transportation processes had great influences on the cloud distribution characteristics in R1 and R2. R2 was affected more than R1 by upwind dust sources.

To further investigate the COPs of clouds of different intensities, Figure 11 shows the vertical profiles of COP within different ranges of the radar reflectivity factor, at an interval factor of 10 dBZ, during the four seasons over the two regions. R1 and R2 had similar monsoon climates and thus showed similar seasonal COP distribution characteristics. Clouds in the two regions mainly occurred where the reflectivity factors were less than -10 dBZ, such as in the ICL. The COP in R1 with the reflectivity factor ranging from -30 dBZ to -20 dBZ showed a larger value than those in other reflectivity ranges. The percentages of COP were approximately 35.1%, 35.9%, 30.8%, and 30.8% in spring, summer, autumn, and winter, respectively, in R1 and 37.1%, 32.6%, 31.1%, and 31.1% in R2. The COPs in R1 in the range of the reflectivity factor larger than -10 dBZ were 24.1%, 22.0%, 30.0%, and 30.0% in spring, summer, autumn, and winter, respectively, in R1 and 18.7%, 26.6%, 28.2%, and 28.2% in R2. These results showed that the clouds with high reflectivity factors mainly appeared in the MCL and WCL where the water vapor and aerosols were mainly concentrated.

The largest COP in all reflectivity ranges was located at a similar height to where the largest COP in the ICL appeared for all four seasons (Figure 7). The local maxima of the COP appeared in the -10°C to -15°C layer in the two regions in spring and winter, at approximately the -12°C layer in R1 and the -15°C layer in R2. Zhang et al. [40] also showed that the maximum COP appeared in the mixed cloud layer in the cold season in the Qinghai-Tibet plateau area. Similar results were also found over the East Asia continent [41], which were attributed to favorable ice particle growth process conditions due to sublimation-accretion mechanisms. Through a chamber experiment, Hallett and Mossop [42] observed the occurrence of a large number of secondary ice particles under mixed-layer temperature conditions, and the occurrence probability peaked in the range of -3°C to -7°C . These results indicated that the key temperature conditions within the mixed layer increased the occurrence probabilities of the mixed clouds at the corresponding heights.

4. Conclusions

The interaction between aerosols and clouds has a complex feedback effect on the changes in aerosol and liquid water content. By investigating the statistical characteristics of cloud and aerosol vertical distributions over two south and

north regions in East China, with each region having a size of 4° latitude by 4° longitude, stronger correlation was found between water vapor condition and COP than that between aerosol condition and COP in the WCL. The COPs in the mixed cloud layers were approximately 70.0% and 70.6% in Regions 1 and 2, respectively, and in the ice cloud layers, 26.7% and 26.8%. The differences in COP between the two regions in the mixed cloud layer and ice cloud layer were highly correlated with those in the aerosol extinction coefficient.

In addition, the highest cloud proportions in R1 and R2 appeared in the mixed cloud layer in all of the four seasons. High values of COP occurred in a cloud layer of 2 to 3 km thickness above the 0°C layer in all the four seasons. The corresponding reflectivity factors were continuously distributed from -30 dBZ to 15 dBZ. The high values of COP in R2 in this layer were more continuous than those in R1. The clouds with high reflectivity factors mainly appeared in the mixed cloud layers and WCL. The mean values of the aerosol extinction coefficient were higher in R2 than in R1 in the layers above the 0°C layer in all four seasons, indicating great influences of aerosols on mixed cloud formation.

Competing Interests

The authors declare that they have no competing interests.

Acknowledgments

The authors greatly appreciate NASA CloudSat Data Processing Center and China Meteorological Administration for providing data used in the present study. This study was funded by the grant of China Scholarship Council (no. 201608320050), the National Natural Science Foundation of China (Grant no. 41475035), and the Open Funding from the Key Laboratory for Aerosol-Cloud-Precipitation of China Meteorological Administration (Grant no. KDW1102).

References

- [1] G. G. Mace and S. Benson, "The vertical structure of cloud occurrence and radiative forcing at the SGP ARM site as revealed by 8 years of continuous data," *Journal of Climate*, vol. 21, no. 11, pp. 2591–2610, 2008.
- [2] J. Wang and W. B. Rossow, "Effects of cloud vertical structure on atmospheric circulation in the GISS GCM," *Journal of Climate*, vol. 11, no. 11, pp. 3010–3029, 1998.
- [3] B. C. Weare, "Insights into the importance of cloud vertical structure in climate," *Geophysical Research Letters*, vol. 27, no. 6, pp. 907–910, 2000.
- [4] G. L. Stephens, "Cloud feedbacks in the climate system: a critical review," *Journal of Climate*, vol. 18, no. 2, pp. 237–273, 2005.
- [5] P. Knippertz, M. J. Evans, P. R. Field, A. H. Fink, C. Lioussse, and J. H. Marsham, "The possible role of local air pollution in climate change in West Africa," *Nature Climate Change*, vol. 5, no. 9, pp. 815–822, 2015.
- [6] J. H. Seinfeld, C. Bretherton, K. S. Carslaw et al., "Improving our fundamental understanding of the role of aerosol-cloud interactions in the climate system," *Proceedings of the National*

- Academy of Sciences of the United States of America*, vol. 113, no. 21, pp. 5781–5790, 2016.
- [7] I. Koren, Y. J. Kaufman, D. Rosenfeld, L. A. Remer, and Y. Rudich, “Aerosol invigoration and restructuring of Atlantic convective clouds,” *Geophysical Research Letters*, vol. 32, no. 14, Article ID L14828, 2005.
 - [8] Z. Li, F. Niu, J. Fan, Y. Liu, D. Rosenfeld, and Y. Ding, “Long-term impacts of aerosols on the vertical development of clouds and precipitation,” *Nature Geoscience*, vol. 4, no. 12, pp. 888–894, 2011.
 - [9] P. C. S. Devara and M. G. Manoj, “Aerosol-cloud-precipitation interactions: a challenging problem in regional environment and climate research,” *Particuology*, vol. 11, no. 1, pp. 25–33, 2013.
 - [10] D. Rosenfeld and W. L. Woodley, “Deep convective clouds with sustained supercooled liquid water down to -37.5°C ,” *Nature*, vol. 405, no. 6785, pp. 440–442, 2000.
 - [11] J. Huang, P. Minnis, B. Lin et al., “Possible influences of Asian dust aerosols on cloud properties and radiative forcing observed from MODIS and CERES,” *Geophysical Research Letters*, vol. 33, no. 6, Article ID L06824, 2006.
 - [12] D. Rosenfeld, U. Lohmann, G. B. Raga et al., “Flood or drought: how do aerosols affect precipitation?” *Science*, vol. 321, no. 5894, pp. 1309–1313, 2008.
 - [13] Y. Ma and H. Xue, “A study of aerosol effects on stratocumulus clouds using CloudSat and MODIS data,” *Beijing Daxue Xuebao (Ziran Kexue Ban)/Acta Scientiarum Naturalium Universitatis Pekinensis*, vol. 48, no. 2, pp. 239–245, 2012.
 - [14] X. Tie and J. Cao, “Aerosol pollution in China: present and future impact on environment,” *Particuology*, vol. 7, no. 6, pp. 426–431, 2009.
 - [15] Y. Lei, Q. Zhang, K. B. He, and D. G. Streets, “Primary anthropogenic aerosol emission trends for China, 1990–2005,” *Atmospheric Chemistry and Physics*, vol. 11, no. 3, pp. 931–954, 2011.
 - [16] X. Deng, C. Shi, B. Wu et al., “Analysis of aerosol characteristics and their relationships with meteorological parameters over Anhui province in China,” *Atmospheric Research*, vol. 109–110, pp. 52–63, 2012.
 - [17] X. Xu, X. Shi, S. Zhang, G. Ding, Q. Miao, and L. Zhou, “Aerosol influence domain of Beijing and peripheral city agglomeration and its climatic effect,” *Chinese Science Bulletin*, vol. 51, no. 16, pp. 2016–2026, 2006.
 - [18] Y. Fan, X. Guo, D. Fu, and H. Li, “Observational studies on aerosol distribution during August to September in 2004 over Beijing and its surrounding areas,” *Climatic and Environmental Research*, vol. 12, no. 1, pp. 49–62, 2007.
 - [19] D. G. Zhang, X. L. Guo, and W. Xiao, “Distributive characters of aerosols and cloud droplets in the summer and autumn of 2003 over Beijing and its peripheral areas,” *Journal of Nanjing Institute of Meteorology*, vol. 30, no. 3, pp. 402–410, 2007.
 - [20] Y. Zhang, Y. Yin, L. X. Shi et al., “An observational study of aerosol property under typical polluted weather condition,” *Plateau Meteorology*, vol. 31, no. 5, pp. 1432–1438, 2012.
 - [21] G. Lu and X. Guo, “Distribution and origin of aerosol and its transform relationship with CCN derived from the spring multi-aircraft measurements of Beijing Cloud Experiment (BCE),” *Chinese Science Bulletin*, vol. 57, no. 19, pp. 2460–2469, 2012.
 - [22] L. C. Ma, Y. Yin, and C. M. Bureau, “Research on airplane observations of atmospheric aerosols over Shijiazhuang area in 2009,” *Journal of the Meteorological Sciences*, vol. 34, no. 1, pp. 47–53, 2014.
 - [23] Q. Zhang, C. Zhao, X. Tie et al., “Characterizations of aerosols over the Beijing region: a case study of aircraft measurements,” *Atmospheric Environment*, vol. 40, no. 24, pp. 4513–4527, 2006.
 - [24] J. Huang, P. Minnis, Y. Yi et al., “Summer dust aerosols detected from CALIPSO over the Tibetan Plateau,” *Geophysical Research Letters*, vol. 34, no. 18, Article ID L18805, 2007.
 - [25] J. Huang, P. Minnis, B. Chen et al., “Long-range transport and vertical structure of Asian dust from CALIPSO and surface measurements during PACDEX,” *Journal of Geophysical Research Atmospheres*, vol. 113, no. 23, Article ID D23212, 2008.
 - [26] K. Sassen, Z. Wang, and D. Liu, “Global distribution of cirrus clouds from CloudSat/cloud-aerosol lidar and infrared pathfinder satellite observations (CALIPSO) measurements,” *Journal of Geophysical Research Atmospheres*, vol. 114, no. D8, 2009.
 - [27] J. Huo and D. Lu, “Physical properties of high-level cloud over land and ocean from CloudSat—CALIPSO data,” *Journal of Climate*, vol. 27, pp. 8966–8978, 2014.
 - [28] J. Peng, H. Zhang, and Z. Li, “Temporal and spatial variations of global deep cloud systems based on CloudSat and CALIPSO satellite observations,” *Advances in Atmospheric Sciences*, vol. 31, no. 3, pp. 593–603, 2014.
 - [29] N. Sheng and U. W. Tang, “The first official city ranking by air quality in China—a review and analysis,” *Cities*, vol. 51, pp. 139–149, 2016.
 - [30] D. G. Zhang, X. L. Guo, D. L. Gong, and Z. Y. Yao, “The observational results of the clouds microphysical structure based on the data obtained by 23 sorties between 1989 and 2008 in Shandong Province,” *Acta Meteorologica Sinica*, vol. 69, no. 1, pp. 195–207, 2011.
 - [31] Z. T. Gu, *Cloud Precipitation Physics*, Science Press, Beijing, China, 1980.
 - [32] X. H. Shi, “Progress in the study of regional impact of aerosol and related features of heavy fog in Beijing City,” *Chinese Journal of Geophysics*, vol. 55, pp. 3230–3239, 2012.
 - [33] A. Shimizu, N. Sugimoto, I. Matsui et al., “Continuous observations of Asian dust and other aerosols by polarization lidars in China and Japan during ACE-Asia,” *Journal of Geophysical Research D: Atmospheres*, vol. 109, no. 19, pp. D19–S17, 2004.
 - [34] X. Y. Zhang, R. Arimoto, and Z. S. An, “Dust emission from Chinese desert sources linked to variations in atmospheric circulation,” *Journal of Geophysical Research Atmospheres*, vol. 102, no. 23, pp. 28041–28047, 1997.
 - [35] Y. Du, Y. Zhang, and Z. Xie, “Location variation of the East Asia subtropical westerly jet and its effect on the summer precipitation anomaly over eastern China,” *Chinese Journal of Atmospheric Sciences*, vol. 33, no. 3, pp. 581–592, 2009 (Chinese).
 - [36] R. Jin, W. Li, B. Zhang et al., “A study of the relationship between East Asia subtropical westerly jet and abnormal Meiyu in the middle-lower reaches of the Yangtze River,” *Chinese Journal of Atmospheric Sciences*, vol. 36, no. 4, pp. 722–732, 2012.
 - [37] X. Kuang, Y. C. Zhang, and J. Liu, “Relationship between Subtropical Upper-Tropospheric Westerly Jet and East Asian Winter Monsoon,” *Plateau Meteorology*, vol. 27, no. 4, pp. 701–712, 2008.
 - [38] Y. Luo, R. Zhang, and H. Wang, “Comparing occurrences and vertical structures of hydrometeors between eastern China and the Indian monsoon region using cloudsat/CALIPSO data,” *Journal of Climate*, vol. 22, no. 4, pp. 1052–1064, 2009.
 - [39] J. X. Li, Y. Yin, P. Li, R. Li, L. J. Jin, and J. Li, “Aircraft measurements of aerosol spacial distribution properties in

- Shanxi Province in summer," *China Environmental Science*, vol. 34, no. 8, pp. 1950–1959, 2014.
- [40] Y. Zhang, H. Chen, and R. Yu, "Vertical structures and physical properties of the cold-season stratus clouds Downstream of the Tibetan Plateau: differences between daytime and nighttime," *Journal of Climate*, vol. 27, no. 18, pp. 6857–6876, 2014.
- [41] J. F. Yin, D. H. Wang, G. Q. Zhai, and W. Zhien, "A study of cloud vertical profiles from the CloudSat data over the East Asian Continent," *Acta Meteorologica Sinica*, vol. 71, no. 1, pp. 121–133, 2013.
- [42] J. Hallett and S. C. Mossop, "Production of secondary ice particles during the riming process," *Nature*, vol. 249, no. 5452, pp. 26–28, 1974.

Research Article

Early Detection of Baby-Rain-Cell Aloft in a Severe Storm and Risk Projection for Urban Flash Flood

Eiichi Nakakita,¹ Hiroto Sato,² Ryuta Nishiwaki,³
Hiroyuki Yamabe,⁴ and Kosei Yamaguchi¹

¹Disaster Prevention Research Institute, Kyoto University, Uji, Kyoto 611-0011, Japan

²Graduate School of Engineering, Kyoto University, Uji, Kyoto 611-0011, Japan

³Sumitomo Heavy Industries, Ltd., Shinagawa, Tokyo 141-6025, Japan

⁴Tokyo Electric Power Company Holdings, Inc., Chiyoda, Tokyo 100-8560, Japan

Correspondence should be addressed to Eiichi Nakakita; nakakita@hmd.dpri.kyoto-u.ac.jp

Received 22 July 2016; Revised 10 November 2016; Accepted 15 December 2016; Published 22 January 2017

Academic Editor: Ke Zhang

Copyright © 2017 Eiichi Nakakita et al. This is an open access article distributed under the Creative Commons Attribution License, which permits unrestricted use, distribution, and reproduction in any medium, provided the original work is properly cited.

In July 2008, five people were killed by a tragic flash flood caused by a local torrential heavy rainfall in a short time in Toga River. From this tragic accident, we realized that a system which can detect hazardous rain-cells in the earlier stage is strongly needed and would provide an additional 5 to 10 min for evacuation. By analyzing this event, we verified that a first radar echo aloft, by volume scan observation, is a practical and important sign for early warning of flash flood, and we named a first echo as a “baby-rain-cell” of Guerrilla-heavy rainfall. Also, we found a vertical vorticity criterion for identifying hazardous rain-cells and developed a heavy rainfall prediction system that has the important feature of not missing any hazardous rain-cell. Being able to detect heavy rainfall by 23.6 min on average before it reaches the ground, this system is implemented in XRAIN in the Kinki area. Additionally, to resolve the relationship between baby-rain-cell growth and vorticity behavior, we carried out an analysis of vorticity inside baby-rain-cells and verified that a pair of positive and negative vertical vortex tubes as well as an updraft between them existed in a rain-cell in the early stage.

1. Introduction

On July 28, 2008, a tragic flash flood occurred in Toga River, Kobe City, Japan, washing away fifty people who were enjoying sunny weather and playing in river parks; this disaster resulted in five fatalities. This disaster drew much attention from government authorities and the engineering community for investigation of disaster factors. A survey report [1] showed that the runoff response of this incident was about 10 min, and most of the flood water came from the sewer system of urban areas during a severely localized heavy rainfall. Therefore, this tragic disaster was the result of a combination of paved urban area and severely localized heavy rainfall.

Recently, weather analyses have shown that localized heavy rainfalls have become increasingly frequent during the summer season. In Japan, there are many short rivers similar to Toga River with small basins about only 10 km^2 and sewage

systems, and most of the rivers are used as public parks. Thus, these public parks in rivers are likely to be dangerous during severely localized heavy rainfall events, for example, 30 min rainfall at an intensity of 50 mm/h.

In addition, based on photos recorded by a public monitoring camera near the location of the flood incident, there was no obvious in situ sign before the sudden approach of the flood. This indicates that the time for response after the flood arrived was not sufficient. Therefore, it is imperative to develop a methodology for early warning of flash floods before localized heavy rainfalls reach the ground. Such localized torrential rainfalls are known as “Guerrilla-heavy rainfalls,” which is a popular term in Japanese news media denoting a short localized heavy rainfall. A Guerrilla-heavy rainfall is generally formed by even an isolated cumulonimbus cloud which is suddenly generated aloft and develops rapidly in a very short time. Therefore, it is very difficult to predict a flash flood caused by Guerrilla-heavy rainfall. For

example, in the Toga River case, there was only about ten minutes for the operating radar, which observed using Plan Position Indicator (PPI) scans at a low elevation angle, to receive signals of the rainfall event before the flood reached the incident location. Thus, in order to prevent such flash flood disasters, it is very necessary to develop a system that can detect hazardous rain-cells in the earlier stage to save more than 5 to 10 min and issue an alert for people to evacuate from river parks to a higher position before flood arrival. This is the main objective of the present research.

In this paper, we shall propose a novel Guerrilla-heavy rainfall prediction system. The structure of this paper is as follows. Section 2 introduces an analysis of the Toga River event using a C-band radar. The result shows that monitoring by volume scan operation is very effective for observing a first radar echo of a rain-cell in an upper atmospheric layer and facilitates detection of a severe storm that might cause Guerrilla-heavy rainfall. Further, Section 3 describes a method for identifying hazardous rain-cells that may cause Guerrilla-heavy rainfalls using vertical vorticity values inside rain-cells obtained by Doppler radar observation. Then, the novel Guerrilla-heavy rainfall prediction system is introduced. To resolve the relationship between growth of a rain-cell and vorticity inside the rain-cell, Section 4 presents an analysis of the structure of vertical vortex tubes inside rain-cells. Finally, Section 5 summarizes and discusses the advantages of the system as well as our ongoing research.

2. Early Detection of Rain-Cells Using Volume Scan Radar Observation

In this study, early detection is defined as detecting the existence of a first radar echo from a rain-cell in an upper atmospheric layer. This is because it is very essential to broadcast the risk information of a flash flood to the public people before a raindrop reaches the ground or before a tragic flash flood approaches even if the information is distributed at the timing of first radar echo appearance aloft.

Nakakita et al. [2] analyzed the Toga River flash flood event and verified that the first radar echo in an upper atmospheric layer was detected through a volume scan observation with an operational C-band radar. Nakakita et al. [3] named a first radar echo aloft in a cumulonimbus cloud as a “baby-rain-cell” and emphasized that a baby-rain-cell was a very effective sign for issuing early flash flood evacuation warnings. Based on this research, the Ministry of Land, Infrastructure, Transport and Tourism (MLIT) of Japan has finished installing a new weather radar network, called “X-band polarimetric RAdar Information Network” (XRAIN), in major urban areas around Japan since 2010 in order to prevent flash flood disasters through faster detection of localized heavy rainfall events.

In the following section, we present an analysis of the Toga River event using a C-band radar as well as the introduction of XRAIN.

2.1. Analysis of Toga River Event Using a C-Band Radar. Toga River, which is located in Kobe City in Japan, is a popular

place for people to enjoy the waterfront during sunny days in the summer season (see Figure 1(a) for field photo). On July 28, 2008, as usual, many people were enjoying the sunny weather in the river parks in Toga River. A slight shower occurred, and then, without any significant sign or time of react, a flash flood surge suddenly struck the river parks at 14:42 and washed away the people. Figure 1(b) shows field snapshots at different times of the day in Toga River during this flood event. As is shown in Figure 2, according to figures of rainfall intensity from low angle observation by C-band radars operated by the MLIT, heavy rainfall occurred over the basin of Toga River at 14:35. This means that seven minutes was available to issue a flash flood warning. Seven minutes may appear to be sufficient for issuing an evacuation warning; however, in fact, it took about ten minutes to finalize procedures of making figures and distributing it to the public officials. Thus, conventional methods for rainfall observation may not provide early enough detection to protect people from disasters caused by flash floods. Therefore, it is emphasized that an additional five to ten minutes for early detection of heavy rainfall is absolutely and imperatively required.

In the last few decades, for scientific purposes, many researchers have focused on a first radar echo of a thunderstorm to analyze cloud structure, for example, [4, 5], and to understand the mechanism of precipitation onsets, for example, [6, 7]. We focused on a first radar echo and attempted to use it as a sign of early detection [2]. It should be noted that while there have been many studies focused on a first radar echoes, this was the first trial utilizing a first radar echo in a practical rainstorm prediction algorithm based on an operational radar network.

We analyzed the three-dimensional structure of reflectivity in the upper atmospheric layer over the target basin using volume scan radar observation data, as is shown in Figure 3 [2]. Data were obtained from the Miyama C-band radar, operated by the MLIT and the time interval of observation was seven minutes and thirty seconds. The first echo of the hazardous cloud in the upper atmospheric layer was captured at around 14:13. At that time, any raindrops have not reached the ground yet. Most importantly, data from volume scan observations indicate that a hazardous cloud was detected about 30 min before the flood occurrence. According to this result, it is obvious that detecting a first radar echo is quite effective to predict a flash flood. Hence, we termed a first radar echo aloft in a cumulonimbus cloud as a “baby-rain-cell” and argued that a baby-rain-cell is a very effective sign for issuing an early flood evacuation warning [3].

To sum up, the three-dimensional information provided by volume scan mode has been proven to be practical and useful for the detection of hazardous rain-cells in the early stage.

2.2. New Japanese Radar Network Using X-Band Radars. Owing to the advantage of volume scan observations [2], the MLIT has started installing many X-band radars, which provide volume scan observation data with high spatial and temporal resolutions, throughout Japan. Table 1 lists the specifications of the installed X-band radar and the Miyama C-band radar in 2008. We can see the X-band radar has much

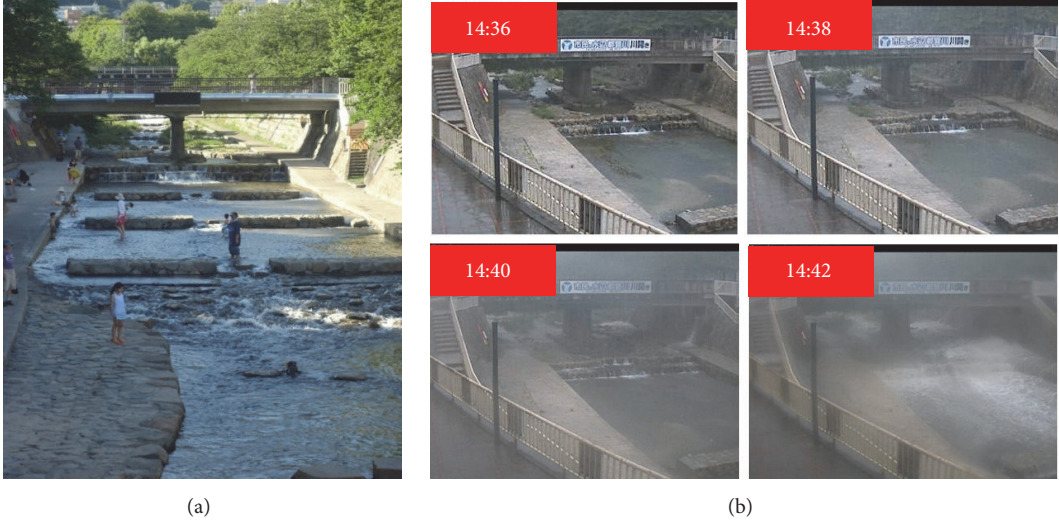


FIGURE 1: (a) Photograph of Toga River (July 17, 2012). (b) Field snapshots at different times in Toga River during the flood event.

TABLE 1: List of specifications of the installed X-band radars and the Miyama C-band radar.

Radar name	X-band multiparameter radar	Miyama C-band radar in 2008
Time resolution	5 min/volume scan	7.5 min/volume scan
Range resolution (maximum range)	150 m (80 km)	300 m (120 km)
Azimuth resolution	1.2°	1.4°
Parameters	Reflectivity, Doppler velocity, polarimetric parameters	Reflectivity, Doppler velocity

higher spatial and temporal resolutions than the Miyama C-band radar. Additionally, the X-band radar observes not only reflectivity and Doppler velocity but also various polarimetric parameters. These new parameters are used operationally for calculating the rainfall intensity as well as experimentally for many fundamental researches. However, compared with the C-band radar, the X-band radar has two disadvantages: (1) high rain attenuation and (2) short observation range. To overcome the two drawbacks, many similar concepts of densely overlapped radar observation networks have been proposed, for example, [8–10]. Following this concept, the MLIT has constructed a new weather radar network, XRAIN in major urban areas in Japan since 2010. As of now, the MLIT has finished installing 39 X-band radars. Figure 4 illustrates the radar distribution as well as the observation ranges. For more precise observation in some specific areas, more radars were installed for greater overlapping of the observation ranges. Each X-band radar finishes one volume scan observation in 5 min. Additionally, to overcome the attenuation problem, the MLIT corrects the observed reflectivity and differential reflectivity (Z_{DR}) using specific differential phase (K_{DP}) [11, 12]. After correction, only the surface data from all individual radar is operationally processed and condensed together into one composite surface rain data with high

spatial (250 m by 250 m) and temporal resolutions (one minute interval) [12]. The data is operationally distributed to the public as a standard real-time product [13]. However, different from the surface rain data, three-dimensional volume scan data is not distributed to the public. For different objectives, we processed the volume scan data in different manners. For earlier detection, volume scan data of four radars in the Kinki area was merged into three-dimensional Cartesian coordinate system, as is mentioned in Section 3; for basic analysis, volume scan data of each four radars was utilized directly without any interpolation or composition, as is shown in Section 4.

Then, with the data from XRAIN, Nakakita et al. [14] proposed a prediction methodology for Guerrilla-heavy rainfall using vertical vorticity values inside a rain-cell. This methodology is elaborated in Section 3.

3. Early Detection and Risk Prediction System for Guerrilla-Heavy Rainfall

As mentioned in Section 2, XRAIN is applicable for detection of baby-rain-cells aloft in the very early stage. However, as not all rain-cells aloft develop into severe storms, identification of the danger level of the detected rain-cell is a critical issue for precise flood warning. Nakakita et al. [14] found that rain-cells that caused Guerrilla-heavy rainfalls had vertical vorticity values greater than or equal to 0.03 s^{-1} inside the rain-cells and proposed a methodology for the prediction of Guerrilla-heavy rainfalls by utilizing vertical vorticity, as introduced in the following section.

3.1. Vorticity in the Early Stage of a Supercell. Referring to cloud dynamics [15–17], the characteristic behavior of supercell evolution in the early stage is vortex tube tilting. Figure 5 schematically illustrates the early stage of the development of a cumulonimbus cloud that will develop into a supercell. The vertical shear of horizontal wind generates a horizontally

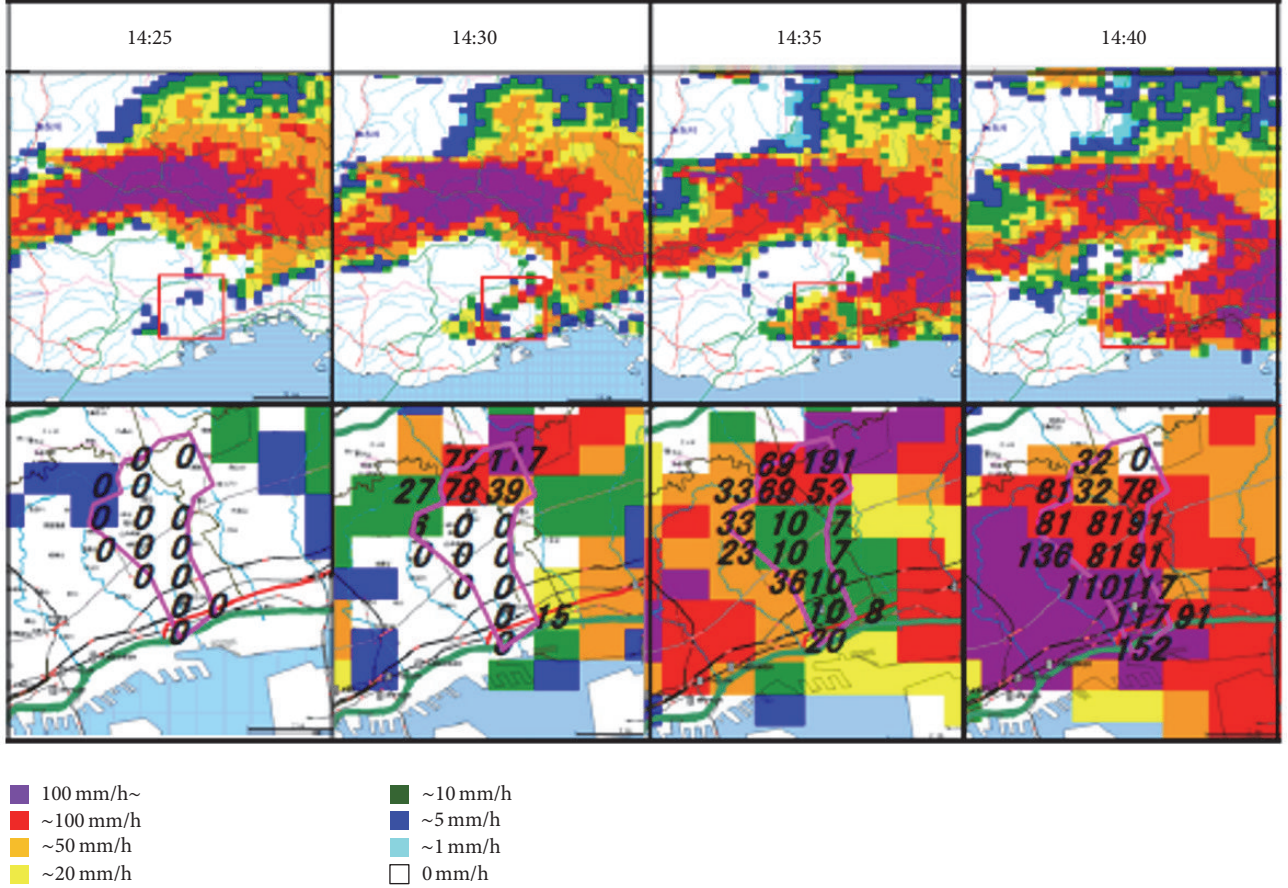


FIGURE 2: Rainfall intensity from low angle observation by C-band radars operated by the MLIT. Lower figures show zoom-in distributions in the range of the red rectangular in upper figures. The numbers in lower figures mean the radar estimated value of rainfall intensity.

oriented vortex tube, which is indicated by circular arrows in Figure 5(a). If this horizontal vortex tube meets an updraft, the tube is tilted and transferred into the vertical vortex tube along the updraft. Hence, a pair of positive and negative vertical vortex tubes appears in the rain-cell, as shown in Figure 5(b). However, even though the behavior of vortex tube tilting is well understood for the formation of a supercell in the early stage, the early stage of development of baby-raincells, which form Guerrilla-heavy rainfalls, is still unknown. Nevertheless, by physical intuition, a rain-cell for a Guerrilla-heavy rainfall can be reasonably assumed to have the motion of vertical vorticities, analogous to a supercell. Therefore, in order to appropriately identify the potential danger level of a baby-rain-cell aloft, Nakakita et al. [18] proposed a methodology for identifying danger level using vertical vorticity values inside a baby-rain-cell. Data processing and efficacy verification of this method are described in the next section.

3.2. Identification of Hazardous Rain-Cells Using Vertical Vorticity

3.2.1. Methodology of Data Processing. Three-dimensional volume scan data from four radars in the Kinki area, as is shown in Figure 6, was used for the research. As one

cycle for volume scan observation takes five minutes, the time interval for analysis was set to be five minutes. In this study, reflectivity and Doppler velocity in the polar coordinate system were used. For calculation of vorticity, all data were transformed into three-dimensional Cartesian coordinate system by interpolation. For the transformation, the initial dimension of a unit rectangular element for the two types of data is $200\text{ m} \times 200\text{ m} \times 200\text{ m}$. However, to exclude interruption from noisy echoes in the background, reflectivity data was further averaged into a larger unit element with a dimension of $500\text{ m} \times 500\text{ m} \times 250\text{ m}$, and its threshold was set to be 20 dBZ .

For calculation of vertical vorticity inside a baby-rain-cell, the transformed Doppler velocity data was used [18]. As Doppler velocity can only measure the radial component of a target's velocity relative to the radar, it cannot provide complete information of a target with a large tangential velocity component. This means that some estimations are required to obtain reasonable values of vorticity using Doppler velocity data. To solve this, we used Doppler velocity along the beam line with multiple radar observation. To calculate approximate vorticity, we introduced an eight-direction classification and eight different equations for more precise estimation [18], as shown in Figure 7. Then, at a given location, from all vorticities calculated using volume scan

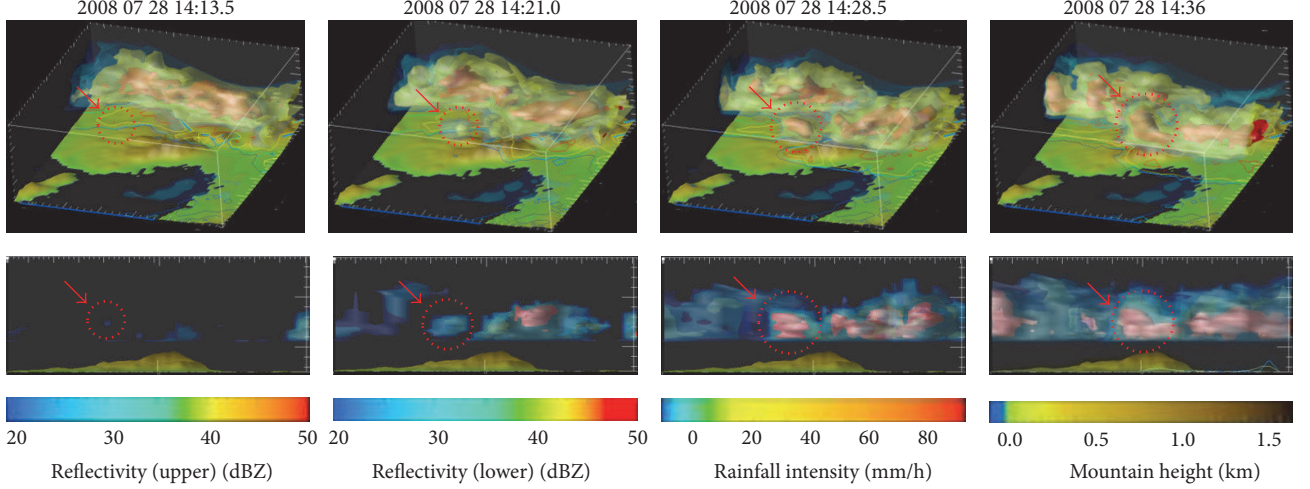


FIGURE 3: Three-dimensional reflectivity detected by the Miyama C-band radar operated by the MLIT. Contour lines of rainfall intensity are described on the ground. Toga River is located at the center of each figure.

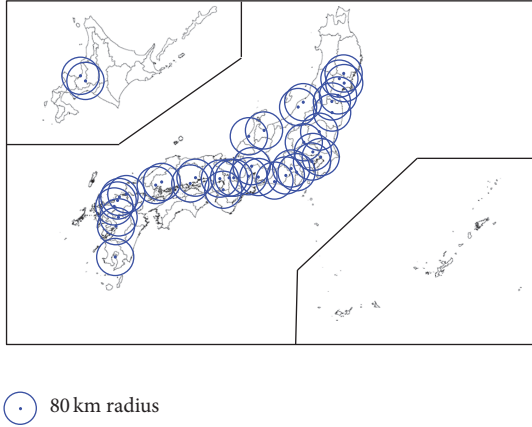


FIGURE 4: Distribution of all radars in XRAIN and their detection areas. The maximum detecting radius of each radar is 80 km.

observation data from the four radars in the Kinki area, the largest one is selected as the representative vorticity. With this methodology, approximate vorticity can be obtained. The vorticity criterion is set to be 0.03 s^{-1} , which denotes that vorticity with a value greater than 0.03 s^{-1} is considered as our target in a rain-cell in the early stage. Special attention is given such that even if the real vorticity is unavailable, the approximate one is applicable to the purpose of qualitative identification of the danger level of a baby-rain-cell.

In the next section, we introduce the evaluation of the largest vertical vorticity for detection of a hazardous rain-cell.

3.2.2. Evaluation of the Efficiency of Vorticity. A Guerrilla-heavy rainfall is defined as a rainstorm generated by an isolated cumulonimbus cloud with an intensity of more than 50 mm/h within 30 min after rainfall reaches the ground. To evaluate the efficiency of vorticity for identification of the danger level, we investigated 35 Guerrilla-heavy rainfall

events, including the ones in Nakakita et al. [14], from 2010 to 2013. Details of the collected events are tabulated in Table 2, including occurrence date, time of first echo detection, first time of detection of vorticity greater than or equal to 0.03 s^{-1} , and time and maximum rainfall intensity on the ground. All the events had vertical vorticity in the early stages before severe rainfall reached the ground.

Figure 8(a) shows statistics of the elapsed time since the first echo of a rain-cell was detected. Green bars denote the time interval between the vorticity detection and the first echo detection; the average time was 1.7 min. Orange bars represent the time interval between the maximum rainfall intensity observation and the first radar echo detection; the average time was 25.3 min. By average values, vorticity was detected 23.6 min earlier than the time at which maximum rainfall intensity occurred. As is shown in Figure 8(a), special attention was given such that, in our collected events, there was no event where vorticity and maximum rainfall intensity were detected simultaneously. In addition, Figure 8(b) illustrates the interval between the time of maximum rainfall intensity and vorticity detection. We found that the time at which the vorticity was detected was at least 10 min earlier than time at which the Guerrilla-heavy rainfall reached the ground. From this, vertical vorticity is proven to be an effective index for detection of a hazardous rain-cell and, further, for a Guerrilla-heavy rainfall prediction system, as is introduced in the next subsection.

3.3. Development of Guerrilla-Heavy Rainfall Prediction System. Vorticity is an effective index to identify hazardous rain-cells that may develop into a severe storm leading to a Guerrilla-heavy rainfall. Based on this result, we developed a Guerrilla-heavy rainfall prediction system that include three major steps in the algorithm [14]: (1) detection of a baby-rain-cell in the early stage of a rainstorm, (2) identification of the initial danger level of baby-rain-cells using estimated vorticity, and (3) three-dimensional tracking of the rain-cell until it develops into a rainstorm. The methodologies of early

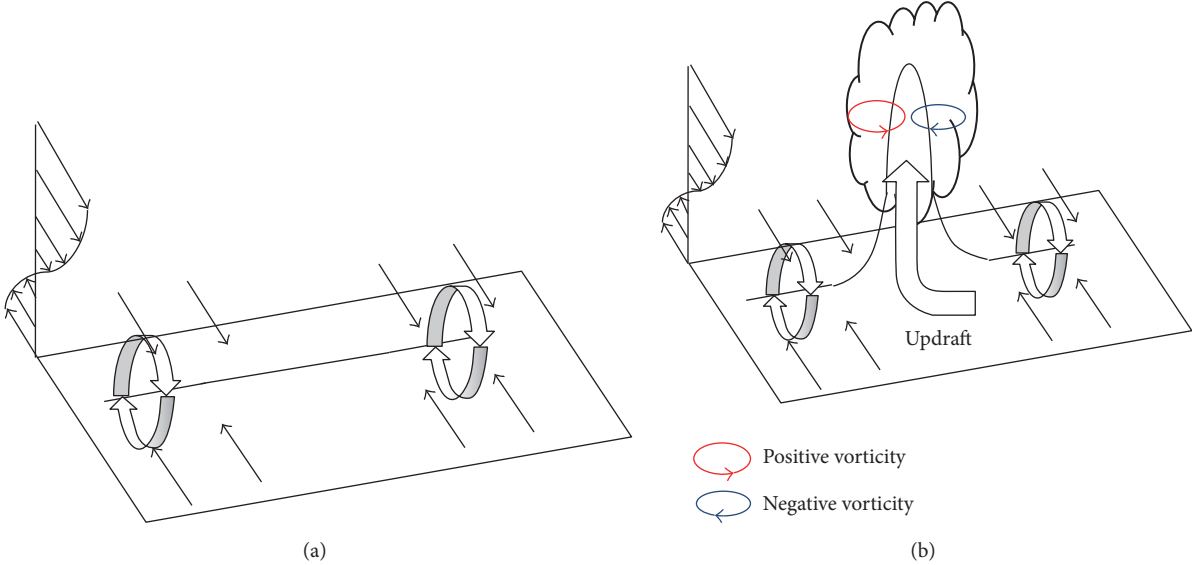


FIGURE 5: Schematic figures of formation of a vertical vortex tube. Circular arrows show circulations of horizontal vortex tube. (a) The vertical shear of horizontal wind generates a horizontally oriented vortex tube. (b) Updraft tilts a horizontal vortex tube into a vertical one (reproduced based on [15–17]).

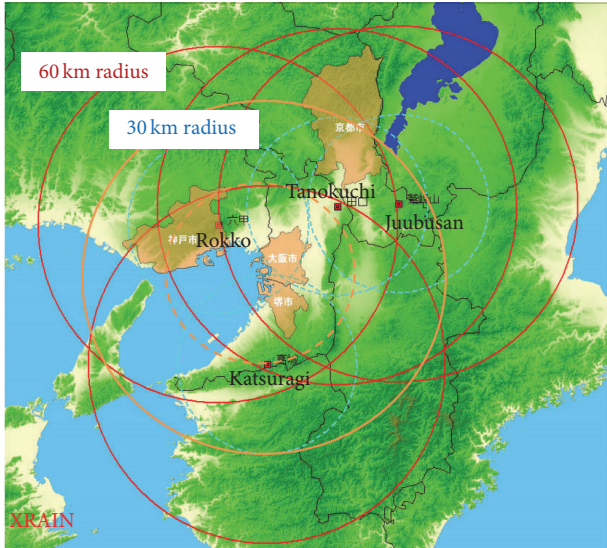


FIGURE 6: Four X-band radars in the Kinki area.

detection and identification of a baby-rain-cell have been described above.

The algorithm identifies rain-cells in three steps and classifies them under five danger levels (L1–L5) in different colors, as is shown in Figure 9. In the first step (1) a volume threshold, ranging from 0.125 km^3 to 62.5 km^3 , is utilized to search baby-rain-cells. In the prediction system, rain-cells with volumes less than 0.125 km^3 or greater than 62.5 km^3 are not considered baby-rain-cells and are excluded.

The second step (2) is to identify initial baby-rain-cells by using a vorticity criterion of 0.03 s^{-1} . Baby-rain-cells that do not include vorticity greater than or equal to the criterion

are considered less dangerous and marked as L1 (blue); otherwise, baby-rain-cells with vorticity greater than or equal to the criterion are potentially dangerous and marked as L2 (yellow).

After identifying baby-rain-cells, the final step is to continually track the generated rain-cells and to identify their danger level of time variation. After being classified into the initial danger levels for baby-rain-cells (L1 and L2), the rain-cells are identified in the next time step using other danger levels, L3 (red), L4 (aqua), and L5 (gray). The vorticity criterion of 0.03 s^{-1} is still utilized to determine the danger level. Rain-cells with vorticities greater than or equal to this criterion are considered very dangerous and marked as L3. Rain-cells that do not include vorticity greater than or equal to the criterion are considered less dangerous and marked as L4. Finally, the remaining rain-cells are not the tracking targets and they are marked as L5.

To track hazardous cells, we propose an algorithm for rain-cell-tracking [14] which is introduced as follows. As the maximum moving speed of a rain-cell is around 60 km/h , the maximum moving range in 5 min is about 5 km . Therefore, for all marked cells, a rain-cell-tracking algorithm, based on the connected component labeling (CCL) scheme [19], is performed to find the nearest cell within the moving range of 5 km in the next time step.

Figure 9 demonstrates one example of prediction. In the three-dimensional figures in the upper part, a new baby-rain-cell is initially detected at 16:10 and marked as L1 (blue) because its vorticity was less than the vorticity criterion. In the next time step, at 16:15, the baby-rain-cell was identified as a dangerous cell and marked as L3 (red). As is shown in Figure 9, the baby-rain-cell was detected before the rainfall reached the ground at 16:10. Furthermore, at 16:15, the prediction system had already identified the baby-rain-cell

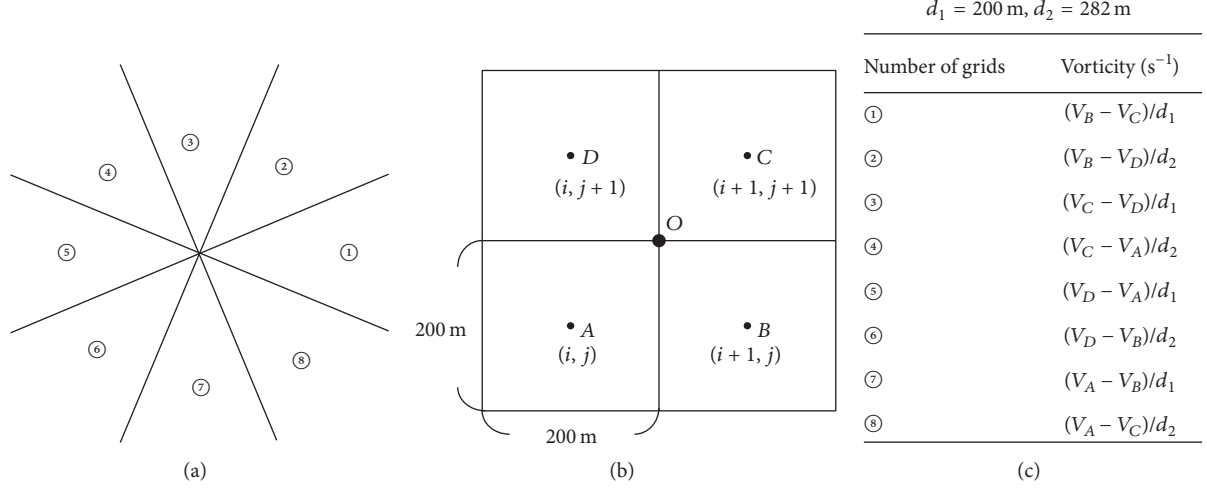


FIGURE 7: (a) Eight-direction map from the radar site, (b) grid number and corresponding formulas for vorticity calculations, and (c) vorticity estimation method for each direction.

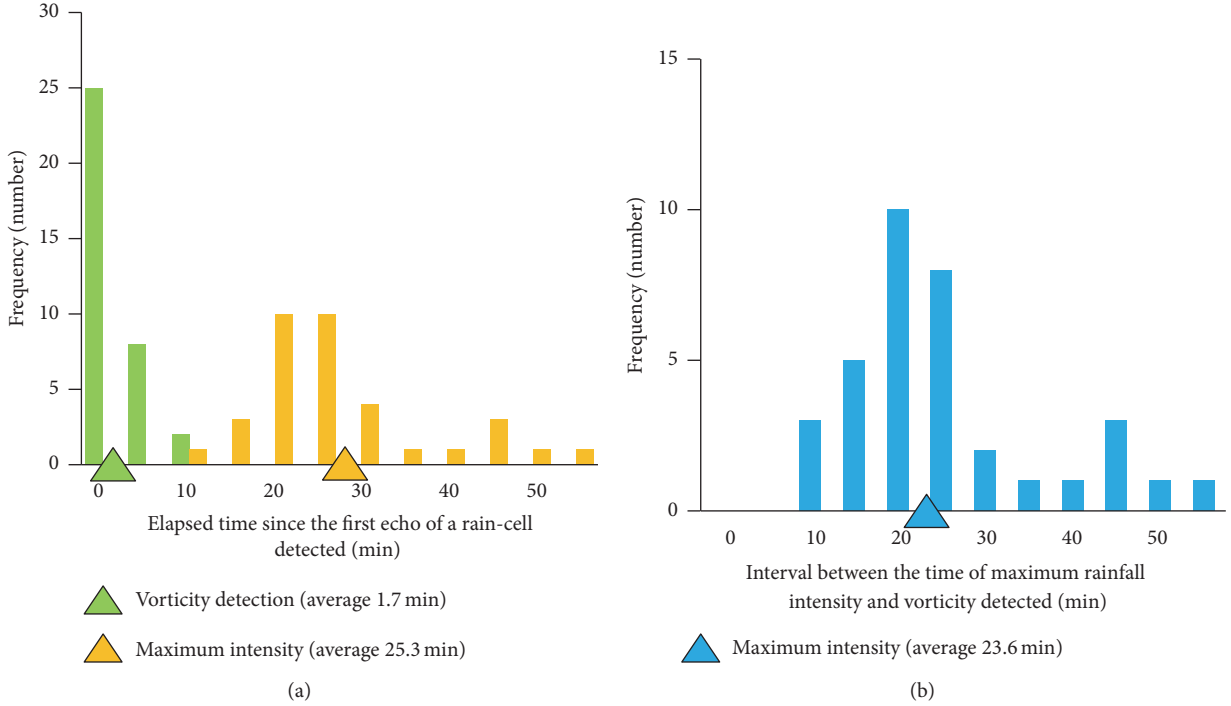


FIGURE 8: The statistics of the elapsed time since the first echo of a rain-cell was detected: (a) green bars: the time interval between the vorticity detection and the first radar echo detection; orange bars: the time interval between the maximum rainfall intensity observation and the first echo detection; (b) blue bars: the time interval between the maximum rainfall intensity observation and the vorticity detection.

as hazardous when slight rainfall appeared on the ground. This example proves that the prediction system can detect and identify a hazardous rain-cell in its early stage before a heavy rainfall reaches the ground.

To sum up, we showed that all rain-cells that caused Guerrilla-heavy rainfall had vertical vorticity values greater than or equal to $0.03 s^{-1}$ from the case study [14]. Based on this result, we developed a Guerrilla-heavy rainfall prediction system that does not miss predicting hazardous rain-cells [14]. As no hazardous rain-cell is missed in the prediction,

the system is quite helpful for disaster prevention. Therefore, this pioneering and practical system has been adapted by the MLIT and implemented at five radar stations of XRAIN in the Kinki area [20]. One example in real practice is illustrated in Figure 10. However, not all baby-cells with large vertical vorticity values develop into severe storms leading to Guerrilla-heavy rainfalls, but in our system, these rain-cells will also be identified as hazardous rain-cells. In the recent research [21], the system has 17.1% false prediction rate over 70 events. For real practice, this rate of false prediction

TABLE 2: List of Guerrilla-heavy rainfall events used for vorticity evaluation. This includes occurrence date, time of first echo detection, first time of detection of vorticity greater than or equal to 0.03 s^{-1} , and time and maximum rainfall intensity on the ground.

Date	Time of rainfall on the ground	Time of baby-cell-detection	Time of vorticity detection	Time of maximum intensity	Maximum intensity (mm/h)
2010/7/7	12:37	12:35	12:35	13:17	97.3
2010/7/16	16:27	16:15	16:15	16:55	97.8
2010/7/17	15:58	15:50	15:50	16:33	113.1
2010/7/24	16:53	16:50	16:50	17:17	116.9
2010/8/6	15:44	15:40	15:40	16:05	70
2010/8/14	12:23	12:20	12:20	12:35	107
2010/8/20	17:55	17:55	17:55	18:13	52.6
2010/8/20	18:28	18:30	18:30	19:15	66.3
2010/8/24	16:31	16:30	16:30	17:21	88.2
2010/8/24	16:59	16:55	16:55	17:17	82.7
2010/8/26	16:52	16:50	16:55	17:17	74.7
2010/8/29	16:10	16:10	16:10	16:42	79.3
2010/8/30	14:57	14:55	14:55	15:43	106.1
2010/8/31	15:21	15:15	15:20	15:45	111.8
2011/7/24	16:24	16:25	16:25	16:39	93.3
2011/7/26	14:33	14:35	14:35	14:55	60.8
2011/7/28	10:18	10:20	10:25	10:41	75.4
2011/7/31	16:42	16:40	16:45	17:04	78.7
2012/7/20	12:36	12:40	12:40	13:03	88.0
2012/7/20	13:03	13:05	13:05	13:25	79.2
2012/7/22	14:26	14:25	14:25	14:45	67.6
2012/7/22	16:06	16:10	16:10	16:35	114.4
2012/7/25	16:08	16:15	16:15	16:35	82.5
2012/7/26	15:50	15:55	15:55	16:14	78.0
2012/8/11	15:58	15:55	16:05	16:17	90.8
2012/8/17	16:44	16:40	16:40	16:59	79.9
2012/8/17	17:23	17:25	17:30	17:44	84.1
2012/8/21	16:01	16:00	16:05	16:22	88.7
2012/8/23	14:54	15:05	15:05	15:31	91.3
2012/8/31	15:20	15:20	15:20	15:30	103.2
2012/8/31	15:32	15:30	15:40	15:47	90.2
2013/8/6	13:10	13:10	13:10	13:33	78.9
2013/8/6	13:45	13:45	13:50	14:05	80.8
2013/8/6	16:12	16:10	16:15	16:23	54.8
2013/8/7	16:45	16:45	16:45	17:10	87.8

is considered to be low and acceptable. Although this is an overestimation of hazardous rain-cells, from the viewpoint of disaster prevention, the fact that there are no missing predictions ensures the safety of people. To the best of our knowledge, this localized torrential rainfall prediction system is the safest in the world.

4. An Analysis of Vortex Tube Structure

As is mentioned in the Section 3, vertical vorticity values can be used to successfully identify hazardous baby-rain-cells aloft before they cause Guerrilla-heavy rainfalls. However, the

reason why the vorticity is effective in identifying hazardous baby-rain-cells is still unclear. Hence, we carried out an analysis of vorticity inside rain-cells that caused Guerrilla-heavy rainfall in order to resolve the relationship between baby-rain-cell growth and corresponding vorticity behavior. Additionally, improved understanding of baby-rain-cell development facilitates quantification of heavy rainfall risk.

As indicated in Section 3.1, vortex tube tilting is the characteristic phenomenon of early stage supercell development. In an analysis of rain-cells in 35 events that did not develop into a supercell, Nakakita et al. [14] found vorticity values greater than or equal to 0.03 s^{-1} . Based on this result, we

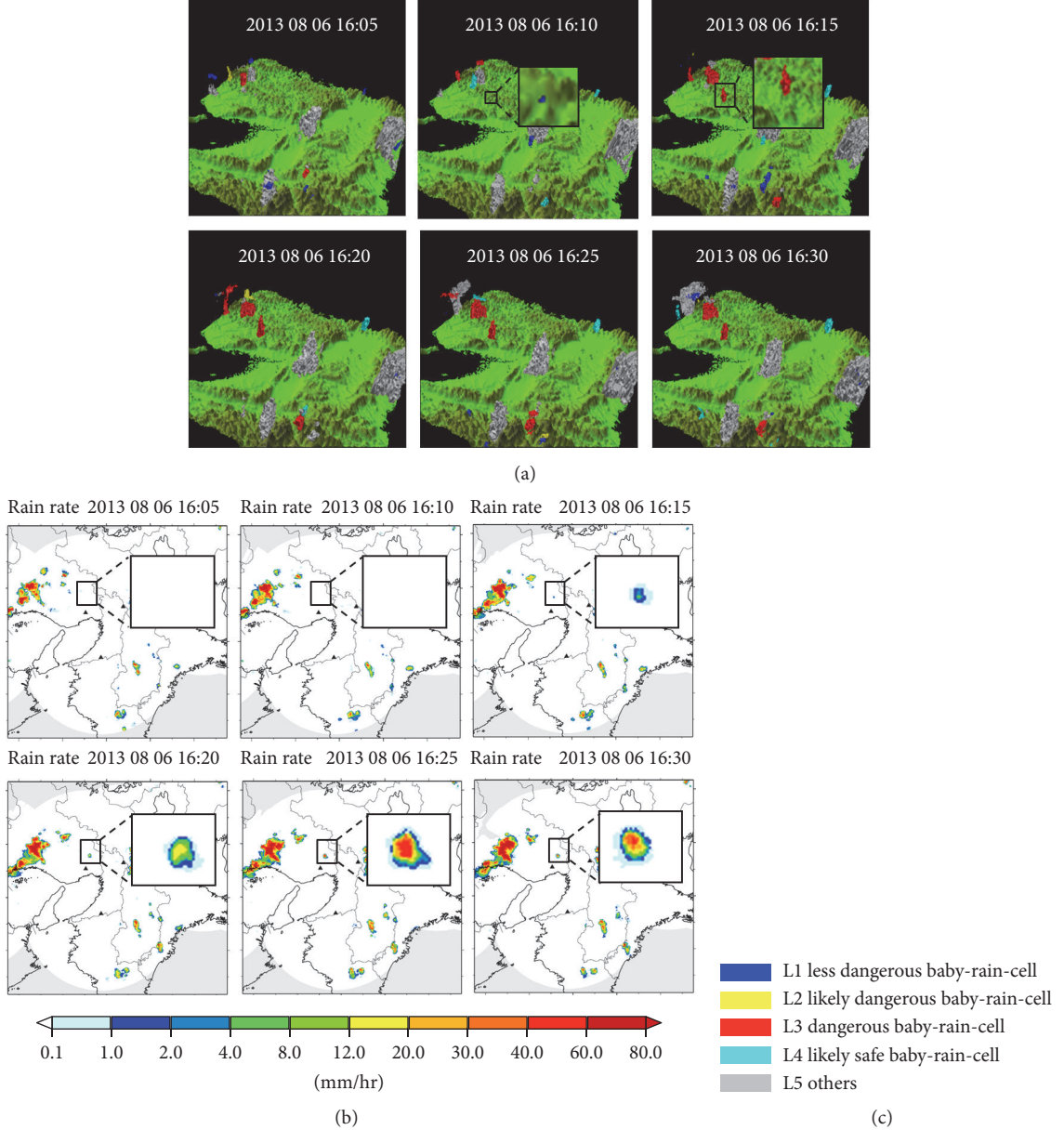


FIGURE 9: Risk prediction of a baby-rain-cell using the Guerrilla-heavy rainfall system: three-dimensional figures (a), two-dimensional rainfall intensity figures (b), and legends of each danger level (c).

assume that the growth of a baby-rain-cell is similar to that of a supercell. To verify this assumption, we analyzed the vorticity distribution inside baby-rain-cells for 16 selected Guerrilla-heavy rainfall events. In the following, we describe the data processing methodology, vorticity distribution analysis, and verification of vortex tube behavior inside baby-rain-cells.

4.1. Methodology of Data Processing. As our focus is on analysis of the vorticity structure in baby-rain-cells, obtaining an accurate vorticity distribution is crucial. In our study, we used observed reflectivity and Doppler velocity. To focus on accurate vorticity distribution, we propose a new data processing methodology. In what follows, we shall present

the new methodology and compare it with conventional methodology [14].

(1) Coordinate System Transformation. In the analysis by Nakakita et al. [18], as the original data is in the polar coordinate system, an interpolation method was utilized to transform the polar coordinate system into the three-dimensional Cartesian coordinate system. For reflectivity and Doppler velocity, the (x, y, z) dimensions of a unit element are $500 \text{ m} \times 500 \text{ m} \times 250 \text{ m}$ and $200 \text{ m} \times 200 \text{ m} \times 200 \text{ m}$, respectively. Meantime, as the duration of one cycle of radar volume scan is five minutes, the analysis time interval was also set to be five minutes. However, we considered this methodology to be applicable to the present study, because

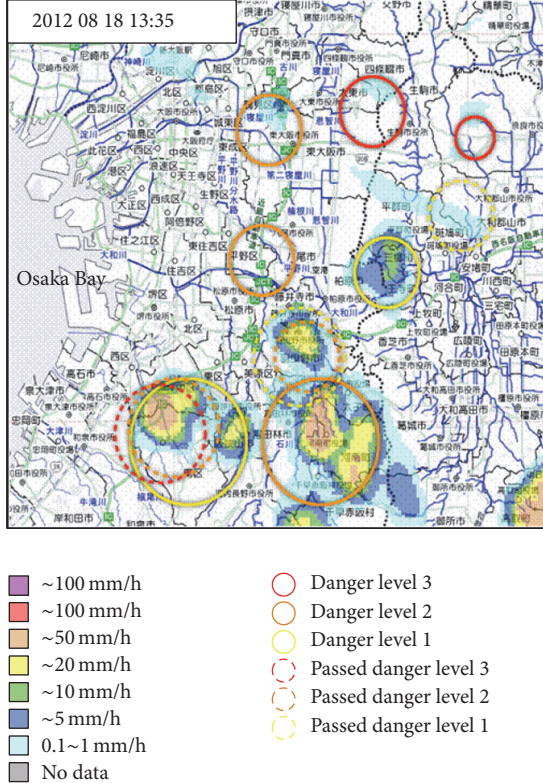


FIGURE 10: One example of the results using the Guerrilla-heavy rainfall prediction system by radars of the MLIT [20]. Circles in different colors denote the dangerous range and the corresponding danger level.

the spatial resolution of data is too low to analyze small and rapidly growing baby-rain-cells, and interpolation may cause artificial distortion of data. Therefore, to obtain precise vorticity distribution, we utilized a new methodology of data processing for extraction of the vorticity distribution from Doppler velocity.

Raw data in the polar coordinate system was directly used for vorticity frequency analysis, without interpolation. Note that, for figure illustrations and vortex tube analysis, we used the plane projection method to convert PPI scan data to planar data in the two-dimensional Cartesian coordinate system. Also for detailed display, the spatial resolution in each plane is 50 m by 50 m. With data in the high spatial resolutions, we can accurately analyze the behavior of a small rain-cell.

(2) *Noise Data Threshold.* The threshold of noise data is critical in radar data processing to avoid interruption from noise echoes. In conventional study, the threshold is set at 20 dBZ for reflectivity data. However, as we focused on the very early stage of small rain-cell development, the reflectivity threshold was set at 5 dBZ, and Doppler velocity was directly used without being filtered by the reflectivity threshold. To distinguish real echoes from noise, we manually collected the first echo data by visual judgment of the reflectivity distribution and Doppler velocity.

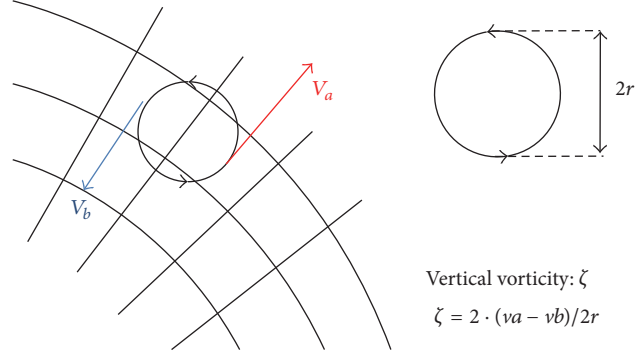


FIGURE 11: Formulas for vorticity calculation, which utilizes adjacent meshes of Doppler velocity data (Nakakita et al., [22]).

(3) *Vorticity Calculation Method.* We introduced an eight-direction classification and used eight different equations for calculating approximate vorticity [18], as shown in Figure 7. If varying vorticity values are obtained from different radar directions, we suggest selecting the largest positive vorticity value at a location to identify hazardous rain-cells of which the vorticity value is greater than or equal to 0.03 s^{-1} . We introduced a new methodology in the present study to obtain a more accurate vorticity distribution. As is shown in Figure 11, vorticity is calculated by the adjacent meshes in Doppler velocity data in the polar coordinate system. It should be noted that our focus was to analyze vortex behavior in three-dimensions, so both positive and negative vorticity were important for analysis. So, in the vorticity distribution we kept all positive and negative values of vorticity at each location without selecting the greatest positive value. Furthermore, the criterion of absolute value of vorticity is set as 0.01 s^{-1} . With this value, which is much smaller than the conventional criterion 0.03 s^{-1} , we were able to analyze the relatively low vorticity of a very early stage rain-cell.

Figure 12 illustrates examples of the data processing output for reflectivity, Doppler velocity, and vorticity distribution. Contour lines show height above the ground, and the interval between major contour lines is 1,000 m.

4.2. *Vorticity Distribution Analysis.* We collected 16 Guerrilla-heavy rainfall events in 2013 and 2014 to analyze the vorticity distribution. Details of the events are tabulated in Table 3, including occurrence date, time of first echo detection, first time of rainfall recorded on the ground, and time of maximum rainfall intensity. For each event, the count of vorticity is calculated using the processed data in the polar coordinate system. By summarizing the count and absolute value of vorticity in all baby-rain-cells, Figure 13 shows the frequency distribution of absolute value of vorticity in the first echo of all collected events. In the baby-rain-cells that did not form supercells, clearly, both positive and negative vorticity existed. And according to this figure, the positive vorticity frequency was greater than negative (Figure 13). This may be due to large-scale positive vorticity in the background affecting small-scale vorticity in the first echoes. However, we focused on only qualitative analysis of the existence

TABLE 3: List of the Guerrilla-heavy rainfall events used for analysis of vorticity and vortex tubes. This includes occurrence date, time of first echo detection, first time of rainfall recorded on the ground, and time of maximum rainfall intensity.

Event	Date	Time of baby-cell-detection	Time of rainfall on the ground	Time of maximum intensity
1	2013/8/6	13:03	13:10	13:33
2	2013/8/6	13:42	13:45	14:05
3	2013/8/6	16:06	16:10	16:23
4	2013/8/7	16:40	16:45	17:10
5	2014/8/17	9:12	9:13	9:39
6	2014/8/17	12:08	12:09	12:23
7	2014/8/17	15:47	15:50	16:04
8	2014/8/18	15:58	16:04	16:18
9	2014/8/23	11:46	11:52	12:08
10	2014/8/23	11:38	11:53	12:05
11	2014/8/23	15:57	16:06	16:29
12	2014/8/23	16:28	16:34	16:57
13	2014/8/24	12:33	12:38	12:53
14	2014/8/25	12:20	12:26	12:49
15	2014/8/25	17:33	17:37	17:51
16	2014/8/27	16:25	16:38	17:13

or absence of negative vorticity in baby-rain-cells. We will analyze the data on different frequencies of positive and negative in further work.

Vertical vortex tubes were identified by connecting vorticity distributions at different altitudes, and we found they were present in all baby-rain-cells that did not evolve into supercells. Figure 14 demonstrates one example of vertical vortex tube structure from a rain-cell in one of the collected events. However, more evidence is needed to support our assumption. Hence, we estimated updraft region and analyzed the relationship between vorticity and updraft by a real event. We shall present the methodology and results in the next section.

4.3. Analysis of the Relationship between Vortex Tubes and Updraft

4.3.1. Theoretical Vortex Tube Behavior in the Early Stage of a Supercell. In recent decades, vortex tube structure has been investigated to clarify the supercell development process, for example, [15–17], but, to our knowledge, systematic analysis of rain-cell vorticity distribution has not been investigated to date, except for supercells. This research is a pioneering study to analyze vortex tube structure at high spatial resolution, associated with a severe Guerrilla-heavy rainfall storm.

Consider a horizontally oriented vortex tube induced by the vertical shear of a horizontal environmental wind which flows perpendicular to the vortex tube, as is shown in Figure 5. Vertically oriented vortex tubes motion can be expressed by the vorticity equation in the z -direction [17] as

$$\frac{d\zeta}{dt} = \xi \cdot \frac{\partial w}{\partial x} + \eta \cdot \frac{\partial w}{\partial y} + \zeta \cdot \frac{\partial w}{\partial z}, \quad (1)$$

where (ξ, η, ζ) are vorticities in the (x, y, z) directions, respectively, and w is the z -component of velocity. In the right hand side (RHS) of (1), the first two terms represent the tilting motion of a horizontal vortex tube by a vertical shear of horizontal wind, and the third term represents the stretching motion of the vertical vortex tube due to variable w in the z -axis direction. Vorticity motion is three-dimensional, and all components are nonlinearly coupled with each other, but for the sake of clear explanation only the vertical vorticity equation is presented here.

One example is given for explanation as follows. In an environment with vertical vorticity $\zeta = 0$ when a vertical shear of horizontal wind occurs $\partial u / \partial z \neq 0$, the horizontal vortex tube of η begins to be tilted by the updraft. Hence, according to (1), vertical vorticity ζ starts to be altered by the tilting motion through the second term in the RHS. In this condition, the z -direction vorticity equation can be rearranged into

$$\frac{d\zeta}{dt} = \eta \cdot \frac{\partial w}{\partial y} = \frac{d\bar{u}(z)}{dz} \cdot \frac{\partial w}{\partial y}, \quad (2)$$

where $\bar{u}(z)$ is the velocity of an environmental wind. As is shown in Figure 5(b), from (2) a positive vorticity is generated in the left side of the updraft relative to the shear flow ($\partial w / \partial y > 0$), and simultaneously a negative vorticity appears in the right side of the updraft relative to the shear flow ($\partial w / \partial y < 0$) instead. Once the pair of vertical vorticities is generated, an updraft feedback mechanism amplifies vertically oriented vortex tube by a stretching motion, as represented by the third term in (1). From this theoretical explanation, we can conclude that a pair of positive and negative vortex tubes exists along the updraft. Further analysis is needed to verify this conclusions as discussed below.

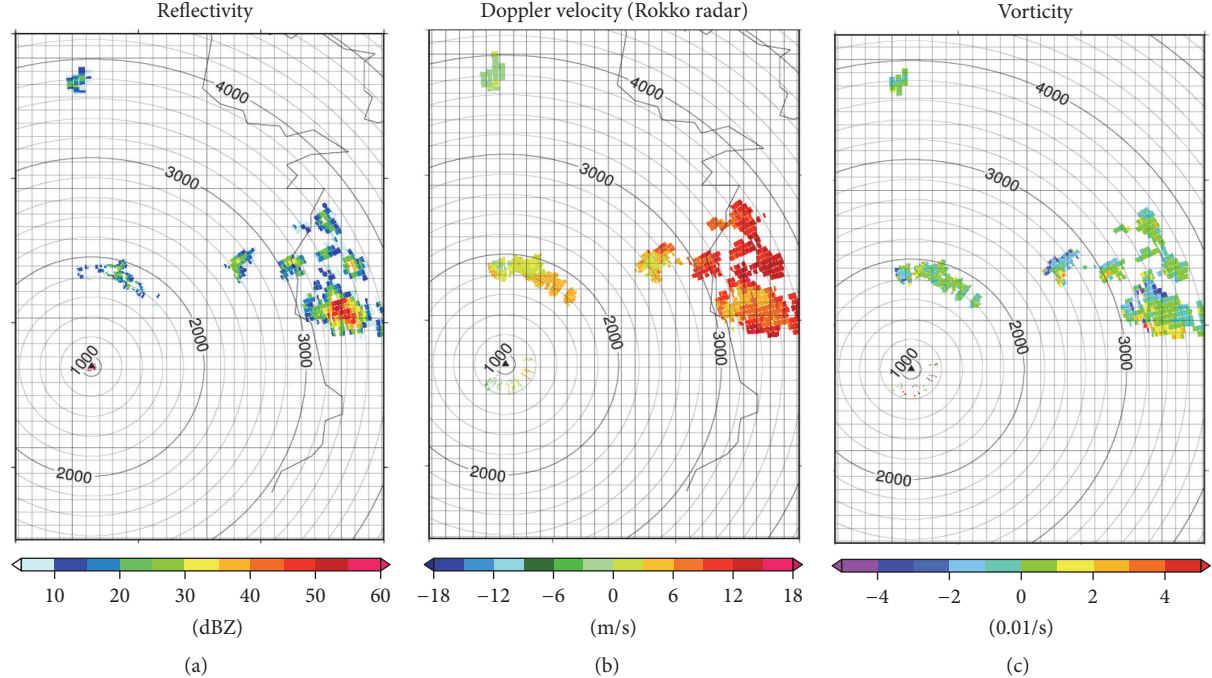


FIGURE 12: One example of distributions of reflectivity (a), Doppler velocity (b), and vorticity (c) after data processing.

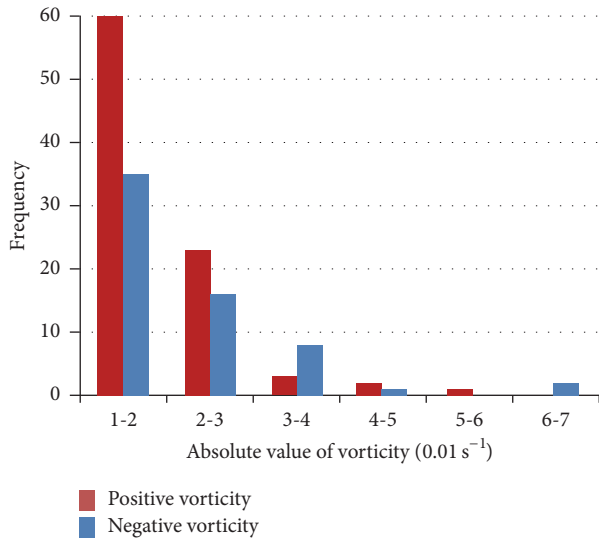


FIGURE 13: The frequency distribution of the absolute values of negative and positive vorticity in baby-rain-cells.

4.3.2. Methodology of Updraft Identification. Hereafter, the relationship between an updraft and corresponding vorticity location is examined in a real event. The importance of an updraft for developing a pair of positive and negative vortex tubes in the vertical direction has been explained in Section 4.3.1. In order to identify updraft location, we utilized differential reflectivity (Z_{DR}) and dual Doppler radar measurement.

(1) *High Z_{DR} Column.* Z_{DR} is one of the polarimetric parameters, and many researchers have focused on Z_{DR} to identify

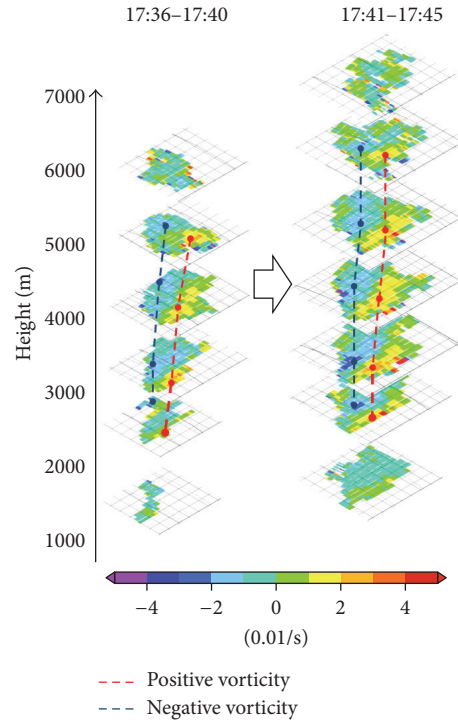


FIGURE 14: One example of structure of vertical vortex tube in the rain-cell of the event 15 in Table 3. The red lines show positive vorticity and the blue lines show negative vorticity.

updraft location in thunderstorms, for example, [23–25]. Z_{DR} depends on the shape and size of hydrometeors; negative values of Z_{DR} can denote vertically oriented scatterers, while positive values denote horizontally oriented scatters, that is,

raindrops. Generally, few raindrops exist above the freezing level, but with updraft some raindrops are lifted up above the freezing level; hence, a high Z_{DR} column can be observed above the freezing level. Thus, this high Z_{DR} column is an effective index to identify an updraft. As is mentioned in Section 2.2, Z_{DR} is corrected to minimize the attenuation problem using K_{DP} by the MLIT [11]. In addition to this, in our study, we carried out additional Z_{DR} correction using reflectivity. The concept of the correction and the calculation method are explained below. Small reflectivity near the ground indicates light rain, and then the raindrop shape must be round. As is mentioned above, Z_{DR} depends on the shape of hydrometeors, so it should show almost 0 dB when the target shape is round. However, actual observed Z_{DR} sometimes show larger (smaller) value than 0 dB when reflectivity is small value (greater than or equal to 5 dBZ and less than 20 dBZ). Thus, we calculated the bias value by a least-square technique so as to minimize the sum of squared errors of Z_{DR} . For further details refer to Nakakita et al. [22].

(2) *Multiple Doppler Radar Analysis.* The radars cannot observe vertical velocity; thus we estimated it with multiple Doppler radar analysis using the variational technique proposed by Shimizu and Maesaka [26]. This variational method minimizes a cost function J , defined as the sum of squared errors, in the entire analysis domain. In this study, the L-BFGS method proposed by Liu and Nocedal [27] was used to optimize the cost function. The cost function is defined as follows:

$$\begin{aligned} J &= J_o + J_d, \\ J_o &= \frac{1}{2} \sum_{i,j,k,m} \lambda_o \\ &\cdot (Vr_m - u \cos A - v \cos B - (w + wt) \cos C)^2, \\ J_d &= \frac{1}{2} \sum_{i,j,k} \lambda_d D^2, \\ A &= \frac{x_m}{r_m}, \\ B &= \frac{y_m}{r_m}, \\ C &= \frac{z_m}{r_m}, \\ D &= \frac{\partial \bar{\rho}u}{\partial x} + \frac{\partial \bar{\rho}v}{\partial y} + \frac{\partial \bar{\rho}w}{\partial z}, \end{aligned} \quad (3)$$

where J_o is the difference between observed and analyzed radial velocity, J_d is continuity equation error, m is the number of radars, u , v , and w are velocity components of wind, x_m , y_m , and z_m are the distance between the target and the radar site, w_t is the target drop velocity, $\bar{\rho}$ is the mean horizontal air density, and λ_o and λ_d are reciprocals of the error variance. Here, the Cartesian coordinate system is used for reflectivity and Doppler velocity, where the dimension of a unit rectangular element is $1 \text{ km} \times 1 \text{ km} \times 500 \text{ m}$. With these

data, we estimated vertical velocity and identified the updraft region.

4.3.3. Analysis of Vortex Tube Tilting in the Rain-Cell. Event 15 of Table 3 was selected for updraft identification based on clear vortex tube shapes and high Z_{DR} above the freezing level. Figure 15 shows the (a) Doppler velocity observed by Tanokuchi radar and schematic diagram of tilting vortex tube, (b) vorticity calculated using Doppler velocity, (c) Z_{DR} , and (d) vertical velocity computed by dual Doppler analysis using Katsuragi and Tanokuchi radar data. In this event, as the stronger west wind occurs at the high altitude, we can reasonably assume a horizontal vortex tube was generated due to vertical shear, as is shown in Figure 15(a).

From the theoretical analysis in Section 4.3.2, the west wind should produce positive vorticity in the south and negative in the north from the theoretical analysis in the previous paragraphs as is shown in Figure 15(a). As is shown in Figure 15(b), the property above is successfully testified by the vorticity distribution using Doppler velocity. And it is noticed that a pair of vorticities was existed in the baby-rain-cell. We consider that an updraft can produce the pair of vortex tubes in the early stage of the rain-cell. The result reinforces the hypothesis that vortex tube development in rain-cells forming a Guerrilla-heavy rainfall is similar to that in the early stage of supercell.

4.3.4. Analysis of Updraft Location. Furthermore, since vortex tube structures have been shown to exist in rain-cells, an updraft must be present between the pair of positive and negative vorticity, as is shown in Figure 15(a). We verify updraft location based on a high Z_{DR} column location and multiple Doppler radar analysis. In this event, the bias value of Z_{DR} was 0.68 dB. Thus, the bias value was subtracted from observed Z_{DR} and we used corrected value for the analysis.

A high Z_{DR} column can be extended above the freezing level by an updraft, for example, [23–25]. Z_{DR} greater than or equal to 2 dB above the freezing level, which was 5,100 m in this event, is used for identification of the updraft location. Zero degree height was estimated using the sonde observation data operated by the Japan Meteorological Agency (JMA) in Shionomisaki in the Kinki area. As a result, a high Z_{DR} column is found between positive and negative vorticities, as is shown in Figure 15(c). For multiple Doppler radar analysis, we used two radar observations' data from Tanokuchi and Katsuragi. As is shown in Figure 15(d), a strong updraft region is found between positive and negative vorticities. These results indicated that a pair of positive and negative vorticities coexists with an updraft in the rain-cell.

To sum up, through verification of vorticity distribution and updraft location with a real event, we have shown that vortex tube tilting, similar to that in a supercell, also exists in a rain-cell which forms a Guerrilla-heavy rainfall.

5. Conclusion

From the serious flood event in Toga River, we have realized that an additional period of more than five to ten minutes

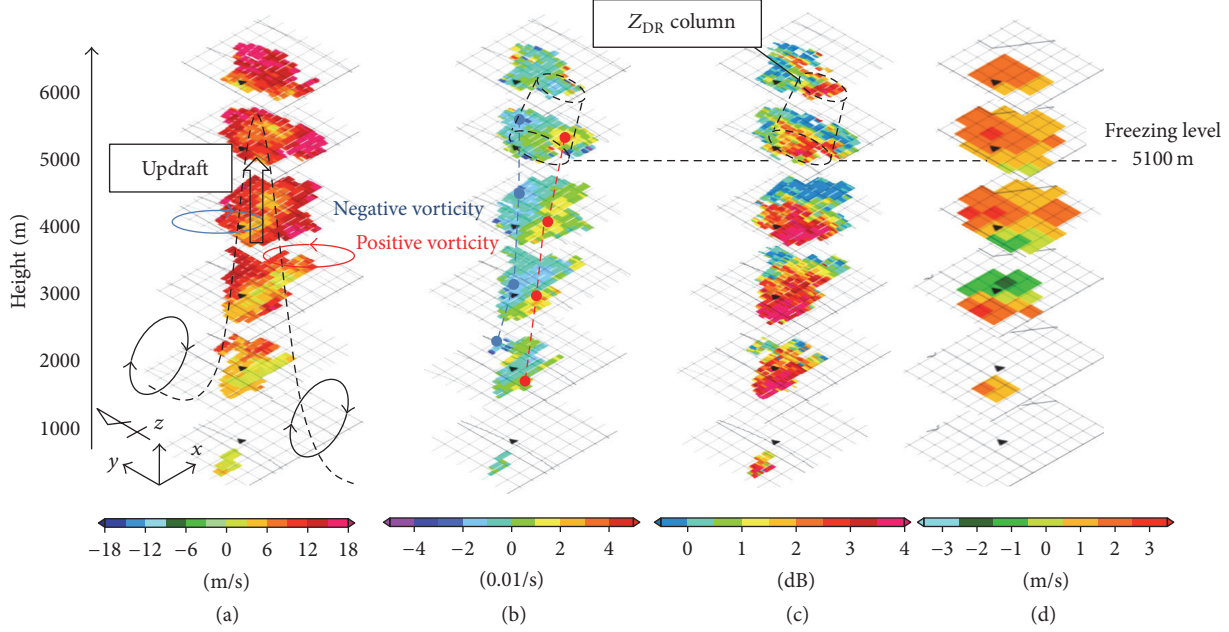


FIGURE 15: The feature of the event 15 observed by Tanokuchi radar; (a) Doppler velocity and schematic diagram of tilting vortex tube, (b) vorticity calculated using Doppler velocity data, (c) Z_{DR} , and (d) vertical velocity computed with dual Doppler analysis using Katsuragi and Tanokuchi radar data. The columns described in black color show the region of the high Z_{DR} column (b, c).

is quite vital and helpful to save precious human lives by evacuating people from a dangerous river before a flood arrival. To obtain this important period, we have developed a system for detection of hazardous rain-cells at an earlier stage.

To protect human life, The most crucial objective for any disaster prevention system is not to miss a disaster prediction. In our analysis, we found that all rain-cells which brought hazardous Guerrilla-heavy rainfalls exhibited vertical vorticity values greater than or equal to 0.03s^{-1} . Therefore, to detect a Guerrilla-heavy rainfall, we utilized this vorticity criterion to develop a prediction system which would not miss prediction of any hazardous rain-cell. Regarding efficiency of real practical rainfall detection, this system has been implemented in five operating radar stations of XRAIN in the Kinki area.

Additionally, as a pioneering attempt, we also performed a brand new vorticity analysis of baby-rain-cells in the events of Guerrilla-heavy rainfalls. As a result, we verified the existence of vertical vortex tubes inside rain-cells which did not develop into supercells. Furthermore, vortex tube tilting motion, similar to that in a supercell, was also proven to exist in the rain-cell which formed a Guerrilla-heavy rainfall. These two results not only make a breakthrough of baby-rain-cell analysis, but also help to clarify the importance of vorticity analysis for efficient identification of hazardous baby-rain-cells.

To better understand the developing mechanism of a baby-rain-cell, it is critical and necessary to analyze flow structure in a cumulonimbus cloud aloft in the atmosphere before raindrop generation. So, analysis of observation data from a cloud radar and a Light Detection and Ranging (Lidar) will be our future task. With better understanding, it is

certain that the precise quantitative risk prediction system of Guerrilla-heavy rainfall could be realized, and perfect protection of human lives from flood disasters can be surely guaranteed in the near future.

Competing Interests

The authors declare that they have no competing interests.

Acknowledgments

The authors greatly acknowledge the financial support of JSPS KAKENHI (Grant nos. 22226010 and 15H05765). The valuable assistance and data from the Kasen-Sabo Research project by the Ministry of Land, Infrastructure, Transport and Tourism (MLIT) of Japan is also deeply appreciated.

References

- [1] I. Fujita, "Disaster investigation of Toga River flood," in *Proceedings of the Japanese Symposium of River Disaster*, 2009 (Japanese).
- [2] E. Nakakita, H. Yamabe, and K. Yamaguchi, "Tragic disaster due to very localized torrential rainfall occurred in Kobe Urban Area in Japan and installation of new radar network system for early detection of the storm system," U-City & Hydroinformatics, World City Forum 2009, Sangdo Convensia, Incheon, Korea 18–21 August, 2009.
- [3] E. Nakakita, H. Yamabe, and K. Yamaguchi, "Earlier detection of the origin of very localized torrential rainfall," *Journal of Hydraulic Engineering, Japan Society of Civil Engineers*, vol. 54, pp. 343–348, 2010 (Japanese).

- [4] C. A. Knight and L. J. Miller, "First radar echoes from cumulus clouds," *Bulletin—American Meteorological Society*, vol. 74, no. 2, pp. 179–188, 1993.
- [5] C. A. Knight, J. Vivekanandan, and S. G. Lasher-Trapp, "First radar echoes and the early ZDR history of Florida cumulus," *Journal of the Atmospheric Sciences*, vol. 59, no. 9, pp. 1454–1472, 2002.
- [6] F. Burnet and J.-L. Brenguier, "The onset of precipitation in warm cumulus clouds: an observational case-study," *Quarterly Journal of the Royal Meteorological Society*, vol. 136, no. 647, pp. 374–381, 2010.
- [7] S. Göke, H. T. Ochs III, and R. M. Rauber, "Radar analysis of precipitation initiation in maritime versus continental clouds near the Florida coast: inferences concerning the role of CCN and giant nuclei," *Journal of the Atmospheric Sciences*, vol. 64, no. 10, pp. 3695–3707, 2007.
- [8] V. Chandrasekar and A. P. Jayasumana, "Radar design and management in a networked environment," in *Proceedings of the ITCOM 2001: International Symposium on the Convergence of IT and Communications*, pp. 142–147, International Society for Optics and Photonics, 2001.
- [9] M. Maki, "X-band polarimetric radar network in the Tokyo metropolitan area—X-NET," in *Proceedings of the 5th European Conference on Radar Meteorology*, 2008.
- [10] D. J. McLaughlin and V. Chandrasekar, "Short wavelength technology and the potential for distributed networks of small radar systems," in *Proceedings of the IEEE Radar Conference*, pp. 1–3, IEEE, Pasadena, Calif, USA, May 2009.
- [11] V. N. Bringi and V. Chandrasekar, *Polarimetric Doppler Weather Radar: Principles and Attenuations*, Cambridge University Press, Cambridge, UK, 2001.
- [12] H. Godo, M. Naito, and S. Tsuchiya, "Improvement of the observation accuracy of X-band dual polarimetric radar by expansion of the condition to use KDP-R relationship," *The Journal of Japan Society of Civil Engineers, Series B1*, vol. 70, no. 4, pp. 505–510, 2014 (Japanese).
- [13] MLIT, 2016, <http://www.river.go.jp/kawabou/ipTopGaikyo.do>.
- [14] E. Nakakita, R. Nishiwaki, and K. Yamaguchi, "Detection of a system for early detection of baby rain cell aloft in a storm and risk projection for urban flash flood," *Advances in River Engineering*, vol. 20, 2014 (Japanese).
- [15] R. Rotunno, "On the evolution of thunderstorm rotation," *Monthly Weather Review*, vol. 109, no. 3, pp. 577–586, 1981.
- [16] J. B. Klemp, "Dynamics of tornadic thunderstorms," *Annual Review of Fluid Mechanics*, vol. 19, no. 1, pp. 369–402, 1987.
- [17] W. R. Cotton, G. Bryan, and S. C. Van den Heever, *Storm and Cloud Dynamics*, vol. 99, Academic Press, 2010.
- [18] E. Nakakita, R. Nishiwaki, H. Yamabe, and K. Yamaguchi, "Research on the prognostic risk of baby cell for guerilla-heavy rainfall considering by vorticity with doppler velocity," *The Journal of Japan Society of Civil Engineers, Series B*, vol. 69, no. 4, pp. 325–330, 2013.
- [19] A. Masuda and E. Nakakita, "Development of a technique to identify the stage of storm life cycle using X-band polarimetric radar," *The Journal of Japan Society of Civil Engineers, Series B*, vol. 70, no. 4, pp. 493–498, 2014 (Japanese).
- [20] M. Katayama, A. Yamaji, F. Nakamura, H. Morita, and E. Nakakita, "Development of a system for early detection of a severe storm," *Advances in River Engineering*, vol. 21, 2015 (Japanese).
- [21] M. Katayama, A. Yamaji, F. Nakamura, H. Morita, and E. Nakakita, "Development of detection system for a local rainstorm," in *Proceedings of the River Engineering Symposium*, 2015 (Japanese).
- [22] E. Nakakita, H. Sato, and K. Yamaguchi, "Fundamental analysis of vortex tubes inside the baby cells of Guerrilla-heavy rainfall," *The Journal of Japan Society of Civil Engineers, Series B*, vol. 72, no. 4, 2016 (Japanese).
- [23] E. A. Brandes, J. Vivekanandan, J. D. Tuttle, and C. J. Kessinger, "A study of thunderstorm microphysics with multiparameter radar and aircraft observations," *Monthly Weather Review*, vol. 123, no. 11, pp. 3129–3143, 1995.
- [24] K. A. Scharfenberg, D. J. Miller, T. J. Schuur et al., "The joint polarization experiment: polarimetric radar in forecasting and warning decision making," *Weather and Forecasting*, vol. 20, no. 5, pp. 775–788, 2005.
- [25] A. Adachi, T. Kobayashi, H. Yamauchi, and S. Onogi, "Detection of potentially hazardous convective clouds with a dual-polarized C-band radar," *Atmospheric Measurement Techniques*, vol. 6, no. 10, pp. 2741–2760, 2013.
- [26] S. Shimizu and Y. Maesaka, "Multiple doppler radar analysis using variational technique to retrievete three-dimensional wind field," *NIED Report*, vol. 70, pp. 1–8, 2007 (Japanese).
- [27] D. C. Liu and J. Nocedal, "On the limited memory BFGS method for large scale optimization," *Mathematical Programming*, vol. 45, no. 1, pp. 503–528, 1989.

Research Article

Evaluation of TRMM Multisatellite Precipitation Analysis in the Yangtze River Basin with a Typical Monsoon Climate

Zengxin Zhang,^{1,2} Qiu Jin,¹ Xi Chen,³ Chong-Yu Xu,^{4,5} Sheng Chen,⁶
Elica M. Moss,⁷ and Yuhan Huang¹

¹*Joint Innovation Center for Modern Forestry Studies, College of Biology and the Environment, Nanjing Forestry University, Nanjing 210037, China*

²*State Key Laboratory of Satellite Ocean Environment Dynamics, Second Institute of State Oceanic Administration, Hangzhou 310012, China*

³*State Key Laboratory of Hydrology-Water Resources and Hydraulics Engineering, Hohai University, Nanjing 210098, China*

⁴*State Key Laboratory of Water Resources and Hydropower Engineering Science, Wuhan University, Wuhan 430072, China*

⁵*Department of Geosciences, University of Oslo, 0316 Oslo, Norway*

⁶*Hydrometeorology and Remote Sensing Laboratory and School of Civil Engineering and Environmental Science, University of Oklahoma, Norman, OK 73072, USA*

⁷*Department of Biological and Environmental Sciences, Alabama A&M University, Normal, AL 35762, USA*

Correspondence should be addressed to Zengxin Zhang; nfuzhang@163.com

Received 15 March 2016; Revised 29 July 2016; Accepted 25 October 2016

Academic Editor: Roberto Fraile

Copyright © 2016 Zengxin Zhang et al. This is an open access article distributed under the Creative Commons Attribution License, which permits unrestricted use, distribution, and reproduction in any medium, provided the original work is properly cited.

Satellite-based precipitation products are expected to offer an alternative to ground-based rainfall estimates in the present and the foreseeable future. In this paper, we evaluate the performance of TRMM 3B42 precipitation products in the Yangtze River basin for the period of 2003~2010. The results are as follows: (1) the performance of RTV7 (V7) products is generally better than that of RTV6 (V6) in the Yangtze River basin, and the percentage of best performance (bias ranging within -10%~10%) for the annual mean precipitation increases from 21.72% (54.79%) to 36.70% (59.85%) as the RTV6 (V6) improved to the RTV7 (V7); (2) the TMPA products have better performance in the wet period than that in the dry period in the Yangtze River basin; (3) the performance of TMPA precipitation has been affected by the elevation and a downward trend can be found with the increasing elevation in the Yangtze River basin. The average CC between the V7 and observed precipitation in July decreases from 0.71 to 0.40 with the elevation of gauge stations increasing from 500 m below to 4000 m above in the Yangtze River basin. More attention should be paid to the influence of complex climate and topography.

1. Introduction

Seasonal and interannual climate variability in the subtropical humid monsoon region is mainly determined by changes in precipitation [1]. Accurate precipitation data with high spatial and temporal resolution are deemed necessary for various fields of research, such as climate change, water resources management, and meteorological disaster prevention [2–5]. Although rain gauges are considered as the standard for measuring precipitation, the rain gauge network is still insufficient across large areas worldwide, and the remotely sensed information about precipitation becomes one of the

main sources of reliable and continuous data [6, 7]. Thus satellite-based precipitation products are expected to offer an alternative to ground-based precipitation estimates in the present and the foreseeable future [8]. For this purpose, the quality and applicability of satellite-based precipitation products need to be evaluated [9].

Satellite-based precipitation products offer a potential alternative or supplement to ground-based rainfall estimates over sparsely gauged or ungauged basins [6, 7, 10–13]. As the Tropical Rainfall Measuring Mission (TRMM) satellite completes more than a decade of operation, it has provided researchers throughout the world with a large volume of

rainfall data for the validation of atmospheric and climate models [14]. The TRMM products include the near-real-time products, that is, 3B42RT Version 6 and Version 7 (hereafter RTV6 and RTV7) estimates and the research products of 3B42 Version 6 and Version 7 (hereafter V6 and V7) estimates [15, 16]. TRMM rainfall products have been widely used in the fields of hydrology, meteorology, and agricultural science [17–19].

In recent years, comparisons between the TRMM rainfall products and rain gauge observations have been made in different climate regions in the world [20–25]. Tong et al. [26] revealed that the TRMM 3B42V7 precipitation data have a better performance than that of RTV7 and PERSIANN in different climate zones. Collischonn et al. [27] found that the TRMM 3B42 rainfall data could be considered reliable in the Tapajo's basin and Amazon basin, Brazil. For the RTV6 and RTV7 products, Chen et al. [14] showed that the TRMM 3B42RT rainfall data had a high precision and a good correlation with the observed precipitation in the humid subtropical Pearl River basin, China, at the basin scale. For the V6 and V7 products, Gu et al. [28] found that the V6 rainfall product was reliable and had good precision in the Yangtze River basin, China, and the TRMM rainfall data estimates could well represent the seasonal changes between wet and dry periods. Chen et al. [29] reported that V7 was adequate at detecting intense tropical cyclone rainfall in the tropic Pacific basin. Zhao et al. [30] also found that there were good linear relationships between V7 and rain gauge data in the arid and humid transition region-Weihe River catchment, Yellow River basin.

Differences between the near-real-time products (RTV6 and RTV7) and research products (V6 and V7) have been reported. Qiao et al. [31] assessed the successive V6 and V7 TMPA (TRMM multisatellite precipitation analysis) rainfall products over the climate-transitional zone in the southern Great Plains, USA. As the V7 products are likely to be the last ones for TMPA data released in early 2013, V7 corrects the widespread rainfall underestimation from V6, and this improvement was more pronounced in the relatively dry basin. Yong et al. [32] reported that V7 product generally performs better than the original V6 over the high-latitude Laohehe basin and the low-latitude Mishui basin at both daily and monthly scales. Xue et al. [19] revealed that the V7 algorithm had significantly upgraded from V6 in precipitation accuracy.

However, accuracy of the TRMM precipitation data varies in different areas and seasons and across different spatiotemporal scales. Khan et al. [33] suggested that the best agreement between the V7 and gauge observations with correlation coefficient values ranged from moderate (0.4) to high (0.8) over the spatial domain of Pakistan, and the seasonal variation of rainfall frequency had large biases (100%~140%) over high latitudes (36° N) with complex terrain for daily, monsoon, and premonsoon comparisons. Habib et al. [34] reported that the TMPA products tended to overestimate small rain rates and underestimate large rain rates over Louisiana, USA. Islam and Uyeda [35] found that 3B42 rainfall data overestimated the rainfall during the premonsoon period in dry regions but underestimated it during the monsoon period in wet regions

over Bangladesh. Li et al. [36] stated that daily TRMM rainfall data could not describe the occurrence and contribution rates of precipitation accurately in Poyang Lake basin, China. Almazroui [37] highlighted a general overestimation in the satellite products over Saudi Arabia. Liu [38] examined the differences between V6 and V7 on a global scale and found that although both V6 and V7 showed a good agreement in moderate and heavy rain regimes, there existed systematic differences between them. Thus, more studies are of importance in further understanding the impacts of climate and topography on the evaluation of TMPA products in the world.

The Yangtze River originates from the Qinghai-Tibet Plateau and flows across three distinct terrains from the headwater region to the East China Sea at Shanghai city, with a 7000 m elevation drop [39]. Most of the Yangtze River basin is dominated by the subtropical monsoon climate [39]. The Yangtze, the longest river in China, has been subjected to flooding throughout history [40]. Although there are hundreds of gauge stations in the Yangtze River basin, the gauge network is still insufficient in the basin especially in the upper Yangtze reaches due to its high elevation and complex terrain [41]. Additionally, the most widely used rain gauge stations are distributed sparsely and unevenly [42, 43]. Several studies have been made in the Yangtze River basin in evaluating the performance of the TMPA products. For example, Hao et al. [41] reported that TRMM RTV7 significantly overestimates the precipitation over the upper Yellow and Yangtze River basins. Gao and Liu [40] also found that the TMPA products had better agreement with gauge measurements over humid regions than that over arid regions in the Tibetan Plateau. Moreover, biases of TMPA present weak dependence on topography, while biases of TMPA RT present dependence on topography which indicated that topography and variability of elevation and surface roughness played important roles in explaining the bias of TMPA products.

Although the TRMM multisatellite precipitation data have been extensively evaluated in many areas in recent years, the knowledge of the impacts of complex topography on the precipitation in a humid monsoon area is limited [8]. The scientific questions to be investigated in this paper include the following: (1) does the V7 improve the precipitation evaluation in the Yangtze River basin compared to V6? (2) do the different monsoon climates impact the precipitation precision in the upper and mid-lower Yangtze reaches? (3) do the different topographies between plateau region and the East China plains have significant influence on the precipitation precision of the TMPA products in the Yangtze River basin? In this study, we attempt to address these problems based on thorough analysis of observed and TMPA precipitation datasets over the Yangtze River basin. This study is of importance in further understanding the impacts of monsoon and complex topography on the precipitation assessment in a large river basin scale.

2. Data and Methods

2.1. Study Area. The Yangtze River is the longest river in China and the third longest river in the world. The river is about 6300 km long and the basin lies between latitudes

24°N and 36°N and longitudes 90°E and 122.5°E with an area of 1,800,000 km² that accounts for about one-fifth of China's territory [28]. The annual mean gross amount of water resources of the Yangtze River basin is 976 km³ [44]. The importance of the Yangtze River lies not only in its geographical position, sheer size, and complex geomorphology, but also in the way that the river plays an important role in the regional water cycle, energy balance, climate change, and ecosystems as well as in China's economic and social development [39]. Three types of monsoon prevail in the Yangtze River basin. In winter, the entire Yangtze River basin is under the control of the Siberian northwest monsoon. In summer, the East Asia monsoon predominantly influences the middle and lower reaches, while the Indian southwest monsoon mainly influences the upper reaches. The Indian and the East Asian monsoon systems are independent of each other and, at the same time, interact with each other [45, 46]. Climatically, the southern part of the basin is adjacent to the tropical zone and the northern part is close to the temperate zone, across the low-latitude region and mid-latitude region.

2.2. Precipitation Data. The TMPA precipitation estimates are based primarily on a combination of microwave (MW) and merging infrared (IR) estimates from multiple satellites [34]. The 3B42 TMPA datasets used in this study were downloaded from the NASA website (<https://trmm.gsfc.nasa.gov/>). It has a high temporal (3 h) and spatial (0.25° × 0.25°) resolution. The 3B42 TMPA dataset is available in two versions: a research-quality product (3B42) released 10~15 days after each month, covering the global latitude belt from 60°N to 60°S, and a near-real-time product (3B42RT), which is released approximately 9 h after real-time with the coverage of the latitude belt from 50°N to 50°S. The main differences between the two versions are the use of the rain gauge data for bias reduction, which are unavailable in the real-time products [34, 47].

Daily rainfall data of eight years (2003~2010) from 224 rain gauge stations in the Yangtze River basin shown in Figure 1 is compared with the TRMM rainfall data to evaluate the quality of TRMM rainfall estimates at different spatial and temporal scales. The readers should bear in mind that the gauges used in the observed precipitation might not be completely independent of those used in V6/V7 since data from some rain gauge stations could be in both of datasets according to the China Meteorological Administration.

2.3. Statistical Indices. Statistical indices are widely used to evaluate the performance of TMPA precipitation products against the rain gauges; four validation statistical indices are selected in this study. These are the relative bias (Bias), correlation coefficient (CC), root mean square error (RMSE), and Error, defined, respectively, by the following equations:

$$\text{Bias} = \left[\frac{\sum_{i=1}^n \text{SIM}_i - \sum_{i=1}^n \text{OBS}_i}{\sum_{i=1}^n \text{OBS}_i} \right] \times 100\%,$$

$$\text{CC} = \frac{\sum_{i=1}^n (\text{OBS}_i - \bar{\text{OBS}}) \sum_{i=1}^n (\text{SIM}_i - \bar{\text{SIM}})}{\sqrt{\sum_{i=1}^n (\text{OBS}_i - \bar{\text{OBS}})^2 \sum_{i=1}^n (\text{SIM}_i - \bar{\text{SIM}})^2}},$$

$$\text{RMSE} = \sqrt{\frac{\sum_{i=1}^n (\text{OBS}_i - \text{SIM}_i)^2}{n}},$$

$$\text{Error} = \text{OBS}_i - \text{SIM}_i,$$
(1)

where OBS_i is the observed precipitation; SIM_i is the TMPA precipitation; $\bar{\text{OBS}}$ denotes the mean of the gauge station precipitation; $\bar{\text{SIM}}$ denotes the mean of the TMPA precipitation; and n is the amount of daily precipitation in the analysis.

3. Results

3.1. Spatial and Temporal Variation of TMPA Products in the Yangtze River Basin. Figure 2 shows the spatial distribution of annual mean precipitation in Yangtze River basin from observed and TMPA data during the period of 2003~2010. Observed annual mean precipitation decreases from southeast (>2000 mm/a) to northwest (<400 mm/a) (Figure 2(e)). Comparatively, the spatial distributions of precipitation of the V6 and V7 (Figures 2(b) and 2(d)) are similar to that of observed precipitation (Figure 2(e)) and the percentage of best performance (bias ranges from -10% to 10%) reaches 54.79% and 59.85% for V6 and V7, respectively (Table 1). However, both of the RTV6 and RTV7 tend to overestimate precipitation over the upper Yangtze River basin and the percentage of overestimating (bias > 50%) reaches 29.74% and 33.51% for the RTV6 and RTV7, respectively. While they underestimate precipitation in the middle and lower Yangtze River basin, the percentage of underestimating (bias < -10%) for the RTV7 in the middle and lower Yangtze River basin is 12.14% while it sums up to 79.11% for the RTV6.

The relative precipitation bias of the TMPA estimates against the interpolated observed data for the average annual precipitation is shown in Figure 3. The larger positive precipitation bias can be found in the upper Yangtze reaches and negative precipitation bias appears in the mid-lower Yangtze reaches for the RTV6 product (Figure 3(a)), and the performance of the RTV7 has been significantly improved in comparison with that of RTV6 in terms of magnitude of the bias (Figure 3(c)). For example, the percentage of best performance (ranging within -10% ~10%) for the RTV7 product is 36.70%, which is higher than that of the RTV6 with the percentage of 21.72% over the entire Yangtze River basin (Table 1). It also shows that, in the mid-lower Yangtze reaches, the best performance for the RTV7 is much better than that of the upper Yangtze reaches. In other words, there has been a marked improvement for the RTV7 in the mid-lower Yangtze reaches and an improvement for the evaluation of the RTV7 in the upper Yangtze reaches compared with that of the RTV6 products. Not surprisingly, both the V6 and V7 (Figures 3(b) and 3(d)) have similar spatial patterns of precipitation biases in the Yangtze River basin and most of the precipitation bias ranges from -10% to 10% for both of them (Table 1).

Figure 4 shows the changes of monthly mean precipitation for the observed and TMPA products in the Yangtze River basin from 2003 to 2010. It can be seen that both the V6 and V7 products capture the seasonal variabilities of the observed precipitation better than that of the RTV7

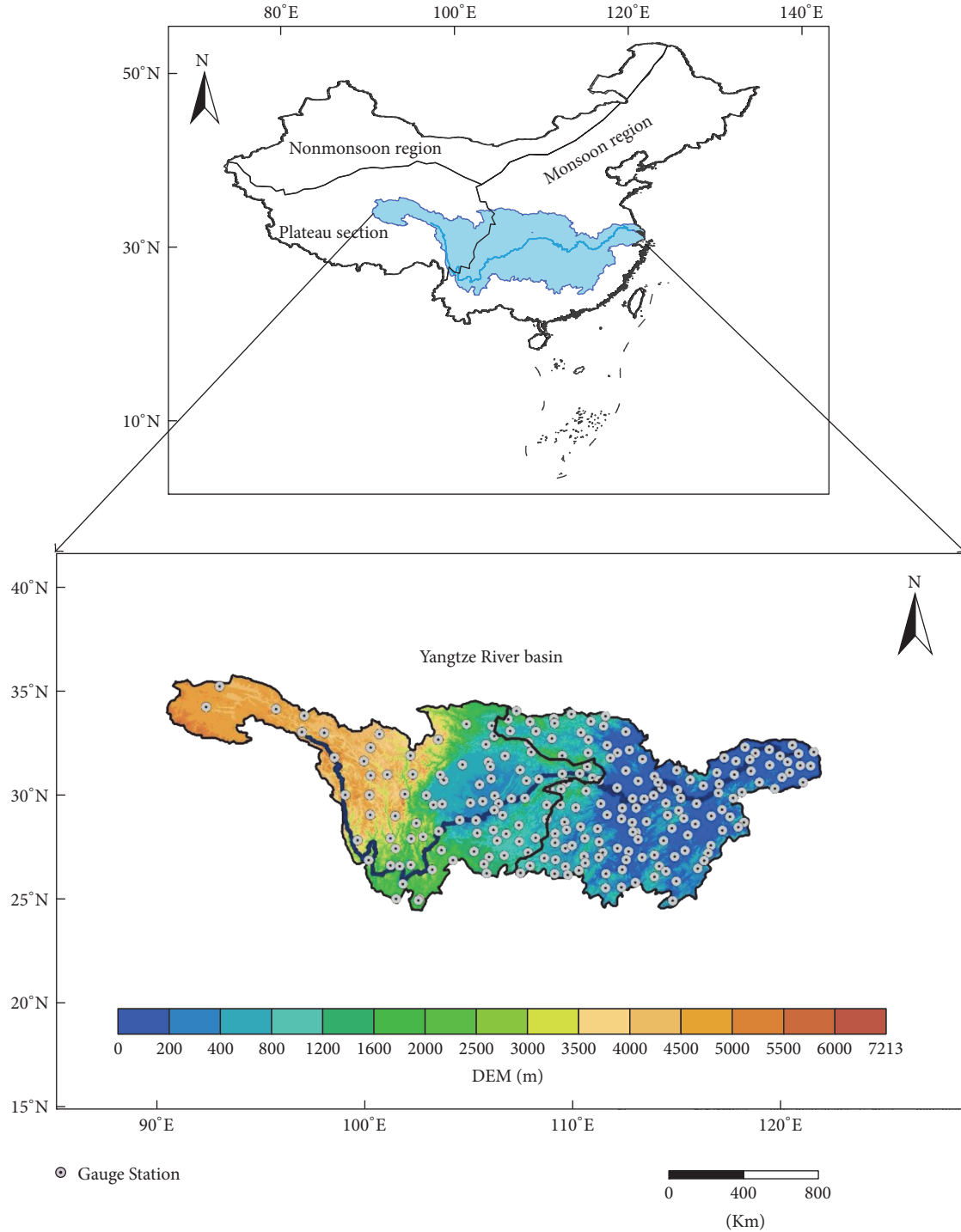


FIGURE 1: Location of the Yangtze River basin and gauge stations.

and RTV6 products do. The RTV7 and the RTV6 products overestimate the precipitation in the upper Yangtze reaches especially in the dry period, while underestimating the precipitation in the mid-lower Yangtze reaches.

For the monthly mean precipitation between the observed and TMPA products (Figure 5), it is clear that the observed monthly precipitation maximum appears in June

in the mid-lower Yangtze reaches and one month earlier than that in the upper Yangtze reaches. All of the TMPA products agree well with the monthly changes of the observed precipitation in the Yangtze River basin. However, the RTV6 product overestimates precipitation in winter and spring in the upper Yangtze reaches and the RTV7 overestimates precipitation in summer in the mid-lower Yangtze reaches.

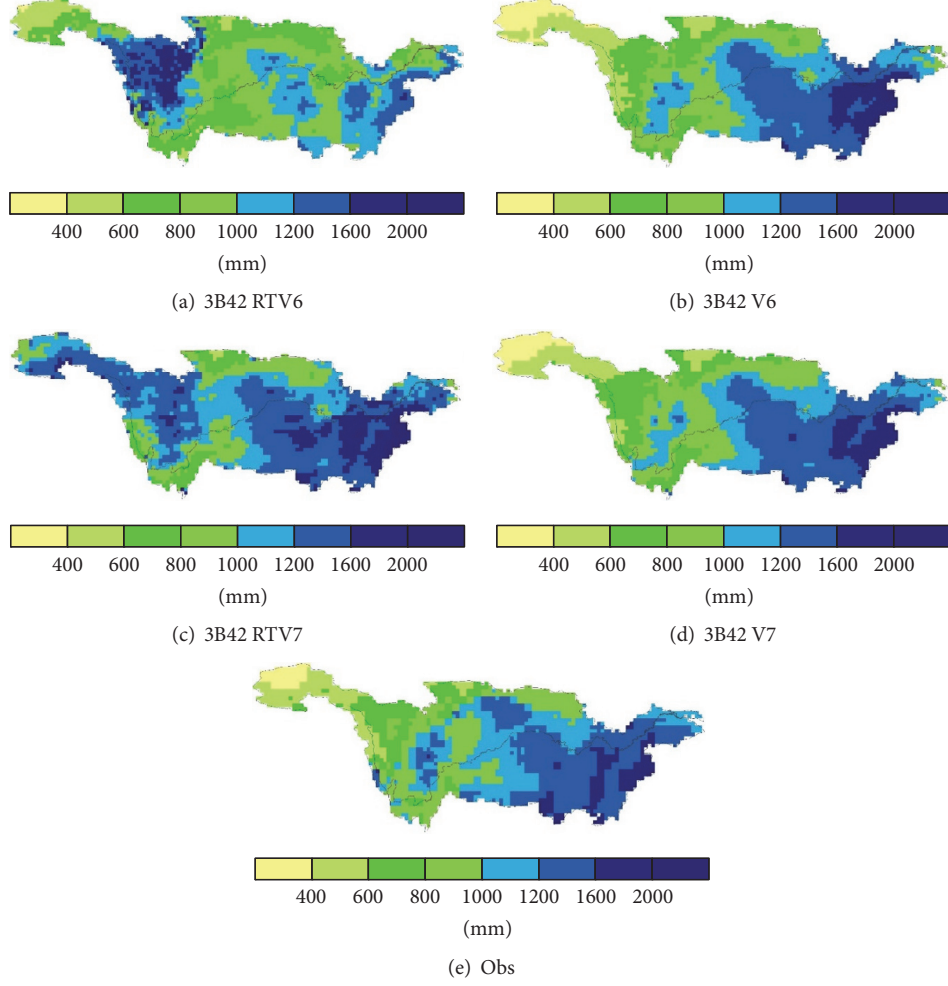


FIGURE 2: Spatial distribution of average annual precipitation in Yangtze River basin for the TMPA and observed data from 2003 to 2010.

TABLE 1: Distributions of Bias for rainfall estimates from TMPA in the upper Yangtze, mid-lower Yangtze, and the entire Yangtze (Unit: %).

Area	TMPA	<-50	-50~ -31	-30~ -11	-10~ 10	11~30	31~50	>50
The upper Yangtze	RTV6	0	3.44	25.56	23.60	9.91	7.75	29.74
	V6	0.27	5.39	36.88	47.54	9.58	0.34	0
	RTV7	0.13	0.40	12.81	24.88	20.50	7.75	33.51
	V7	0.13	2.90	31.09	52.66	12.88	0.27	0.07
The mid-lower Yangtze	RTV6	0	16.85	62.26	19.38	1.52	0	0
	V6	0	0.17	18.28	63.86	17.69	0	0
	RTV7	0	0.51	11.63	51.47	30.50	5.64	0.25
	V7	0	0.17	12.89	68.83	18.03	0.08	0
The entire Yangtze	RTV6	0	9.40	41.87	21.72	6.18	4.31	16.52
	V6	0.15	3.07	28.61	54.79	13.18	0.19	0
	RTV7	0.07	0.45	12.28	36.70	24.94	6.82	18.73
	V7	0.07	1.69	23.00	59.85	15.17	0.19	0.04

3.2. Variation of the Precipitation under the Influence of Monsoon Climate. East Asian monsoon is difficult to arrive in the upper Yangtze reaches, especially the headwater areas in the Yangtze River [46]. However, the upper Yangtze reaches are adjacent to the India monsoon regions where

the precipitation could be affected by the India monsoon [39, 48]. Some areas in the upper Yangtze reaches are located in the Tibet Plateau which is affected by the plateau climate. Therefore, the Yangtze River basin is affected by three types of monsoon, winter monsoon, East Asian summer monsoon,

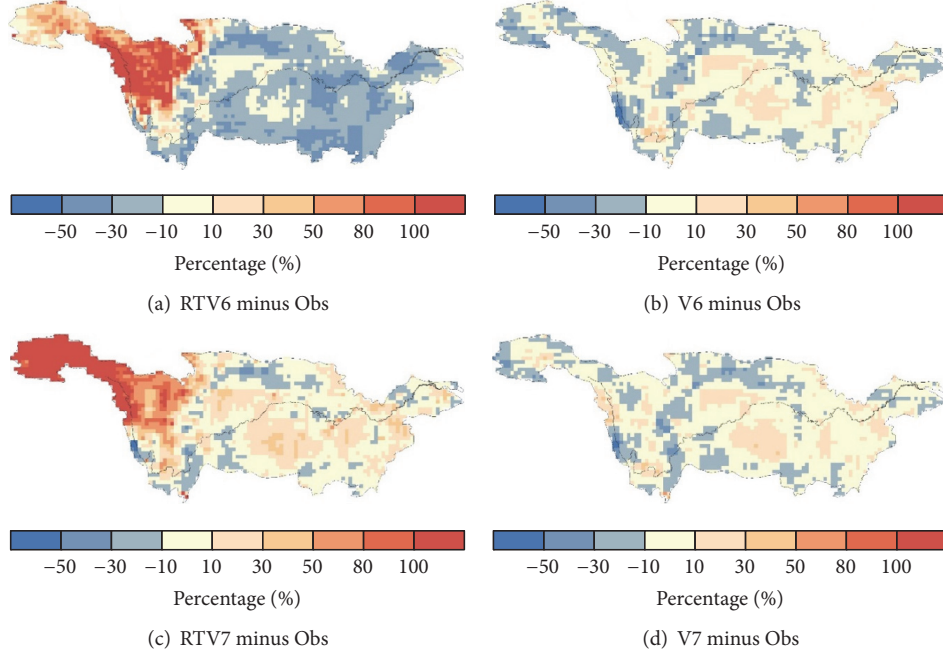


FIGURE 3: The relative bias of the TMPA precipitation estimates against the interpolated observed precipitation data for the average annual precipitation in the Yangtze River basin.

and Indian summer monsoon [49, 50]. In winter, the entire Yangtze River basin is mainly controlled by the Siberian northwest monsoon, while in summer the upper Yangtze reaches are mainly affected by India monsoon, and the mid-lower Yangtze reaches are usually dominated by the East Asian monsoon. The temporal and spatial distributions of the rain zone in the Yangtze River basin are closely related to monsoon activities and seasonal motion of subtropical highs [51]. Normally, the summer monsoon starts to influence the Yangtze River Basin in April and retreats in October [46]. According to the monthly mean precipitation in the Yangtze River basin during the period of 2003~2010, dry period (from November to March) and wet period (from May to September) were defined in this paper.

Since the Asia monsoon has obviously seasonal variation characteristics, the correlations between TMPA products and observed precipitation in different seasons have been calculated. Figure 6 shows the density-colored scatter plots of TMPA versus observed daily precipitation data for the dry period and wet period in the Yangtze River basin. There are significant correlations between the TMPA products and observed precipitation in the Yangtze River basin (statistically significant at the 99% confidence level). Higher CC values can be found between the TMPA products and the observed precipitation for each of the TMPA products in the wet periods than that of dry periods in the Yangtze River basin. However, the RSME of the TMPA precipitation estimates against the observed precipitation is generally smaller for the dry periods than that of the wet periods in the Yangtze River basin. It can be found that an obvious improvement of the RTV7 product has been made over the RTV6 product. The correlations between the RTV7 and observed precipitation

are higher than that of RTV6 in both the wet periods and dry periods in the upper and mid-lower Yangtze reaches, respectively. Overall, the V7 products have the higher CC value and smaller Bias and RMSE in the wet periods and dry periods than that of V6 product over the Yangtze River basin. Nevertheless, there is still systematic bias for the V7 products as the fitted lines (red lines in Figure 6) deviated from the lines in 45° angle (blue lines in Figure 6), especially in the upper Yangtze reaches for the dry period.

Figure 7 can be used to further identify the precision of different monsoon precipitation estimates from the TMPA precipitation products, for example, East Asian summer monsoon precipitation seen from Figure 7 in July and located in the lower elevation area (at 500 m above sea level), Indian summer monsoon seen from Figure 7 in July and located in the Tibet Plateau over 4000 m above sea level, and the Siberian northwest monsoon seen from Figure 7 in January. Generally, all the TMPA precipitation products give a more reliable estimation of East Asian summer monsoon precipitation (CC ranges 0.39~0.90 as for V7) than that of the Indian summer monsoon precipitation (CC ranges 0.27~0.89 as for V7), and the reliability of the TMPA precipitation products in estimation of the Siberian northwest monsoon precipitation decreases as the elevation increases.

3.3. Variation of the Precipitation with Elevation. Evaluation of the TMPA precipitation products with the changes of elevation is also shown in Figure 7. Overall, the performance of TMPA precipitation estimation shows a downward trend with the increasing elevation in the Yangtze River basin in different seasons. Higher correlations between the TMPA products and observed precipitation can be found in the

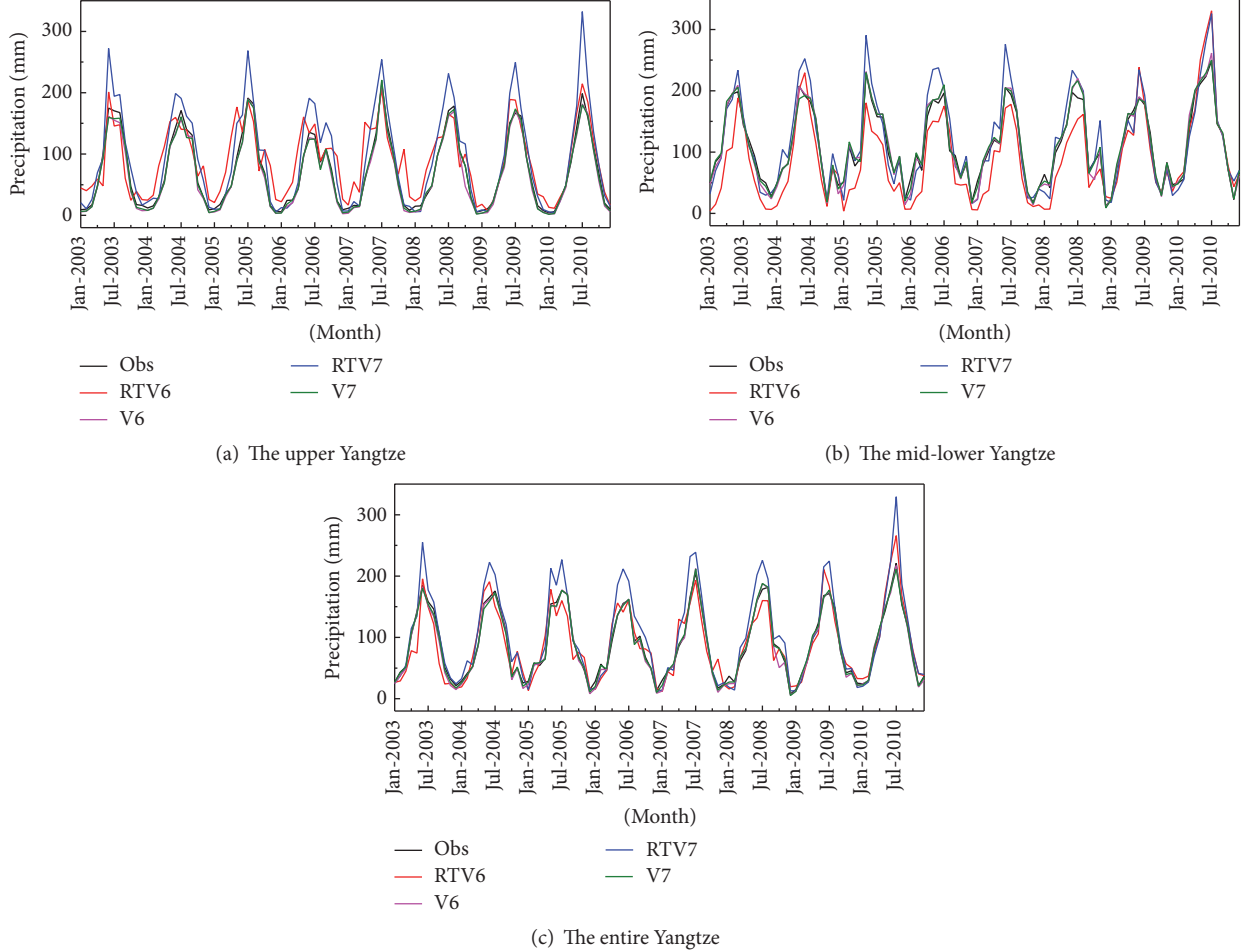


FIGURE 4: The comparison between the monthly observed and TMPA products precipitation from 2003 to 2010. ((a), the upper Yangtze; (b), the mid-lower Yangtze; (c), the entire Yangtze).

lower elevation areas, while lower correlations appear in the higher elevation areas in April, July, and October. Highest correlations between V7 product and observed precipitation can be found in the lower elevation areas in July and its CC value is as high as 0.90. As for V7 product, there are 114 stations located in the middle and lower Yangtze River basin within 500 m above sea level and the CC (V7 versus Obs) ranges 0.48~0.90, while 22 stations scatter in this area 500 m high and the CC ranges 0.39~0.86 in July. However, there are 26 stations located in the upper Yangtze River basin 500 m below with the CC ranging from 0.41 to 0.93; 61 stations scatter in this area 500~4000 m high and the CC ranges 0.27~0.89, while 6 stations are located 4000 m high with the CC ranging within 0.27~0.50.

Figure 8 shows the changing of correlation coefficient of daily mean TMPA products and observed precipitation data with elevation. It seems that the downward trend of the correlation coefficient is found with the increasing elevation. The most rapid decline is found for RTV6 and the slowest downward trend can be found for V7.

To better understand the changes of CC between the TMPA products and observed precipitation with elevation,

the correlations between the TMPA products and observed precipitation of 8 tributaries of the Yangtze River basin were summarized in Table 2. We can find that the correlations appear higher in the lower river basin and then decrease from the lower river basin to the higher river basin as a whole. The lowest correlations appear in the Jinsha River basin with the highest average elevation of 2700 m above sea level. Moreover, higher correlations can be found in the Jialing River basin with lower elevations, which are also located in the upper Yangtze reaches. It was also found that the performance of TRV7 (V7) is better than that of TRV6 (V6) in both the lower and higher river basins. The results reveal that the impacts of elevation should be considered when using TMPA products.

4. Discussion

Precipitation variability becomes essential to reveal the changing features of the monsoon climate as satellite-based precipitation products are highly valued along with the development of the remote sensing technology in recent years [6, 7]. With the previous analysis results, the TMPA products have become more reliable in estimating the precipitation in

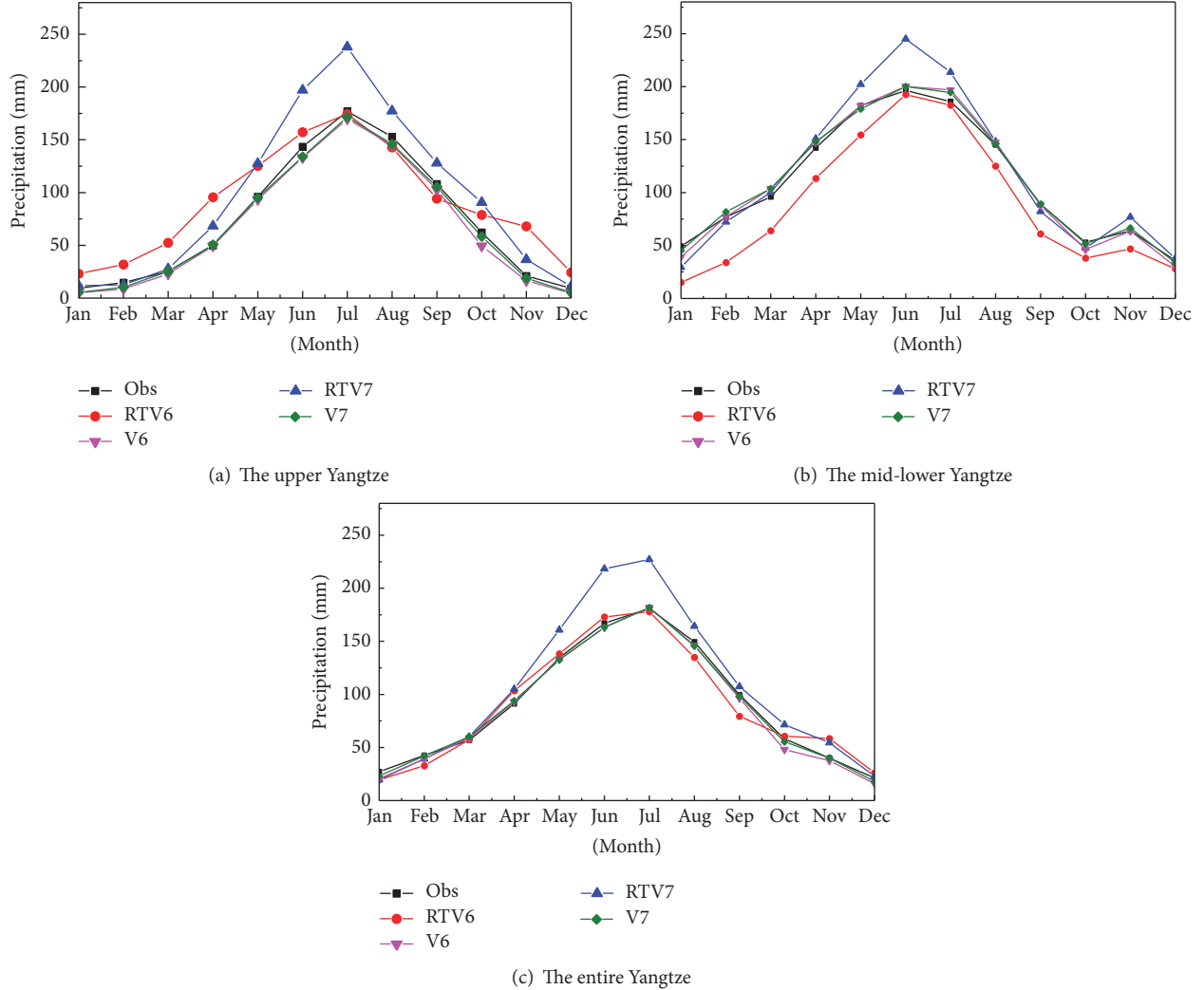


FIGURE 5: The same as Figure 4, but for the average monthly mean precipitation.

TABLE 2: The correlation coefficient between the TMPA products and observed precipitation of 8 tributaries of the Yangtze River.

Tributaries (elevation, m)	Taihu Lake (22)	Poyang Lake (137)	Dongting Lake (287)	Han River (480)	Jialing River (484)	Wujiang River (1011)	Mintuo River (1670)	Jinsha River (2713)
RTV6	0.51	0.62	0.60	0.61	0.63	0.61	0.54	0.48
V6	0.63	0.68	0.69	0.68	0.70	0.69	0.64	0.61
RTV7	0.61	0.70	0.69	0.66	0.69	0.68	0.61	0.57
V7	0.65	0.69	0.70	0.70	0.72	0.71	0.65	0.63

the Yangtze River basin as the RTV6 improved to the RTV7 and the V6 to V7. The performance of the RTV7 (V7) precipitation products is generally better than that of RTV6 (V6), which is in agreement with previous studies. However, there exist systematic differences between TMPA products and observed precipitation. Both of the RTV6 and RTV7 overestimate the annual mean precipitation in the upper Yangtze reaches and they underestimate the precipitation in the mid-lower Yangtze reaches. However, the percentage of underestimating (bias < -10%) for the RTV7 in the middle and lower Yangtze River basin is significantly less than that of RTV6.

The monsoon climate might have significant impacts on the precipitation evaluation in the Yangtze River basin. The TMPA products have better performance to reveal the features of summer monsoon precipitation than that of winter monsoon in the Yangtze River basin. Higher CC values can be found between the TMPA products and the observed precipitation for each of the TMPA products in the wet periods than that of dry periods in the Yangtze River basin. The V7 product has the higher CC value in the wet period than that of dry period in the Yangtze River basin. Nevertheless, there is still systematic bias for

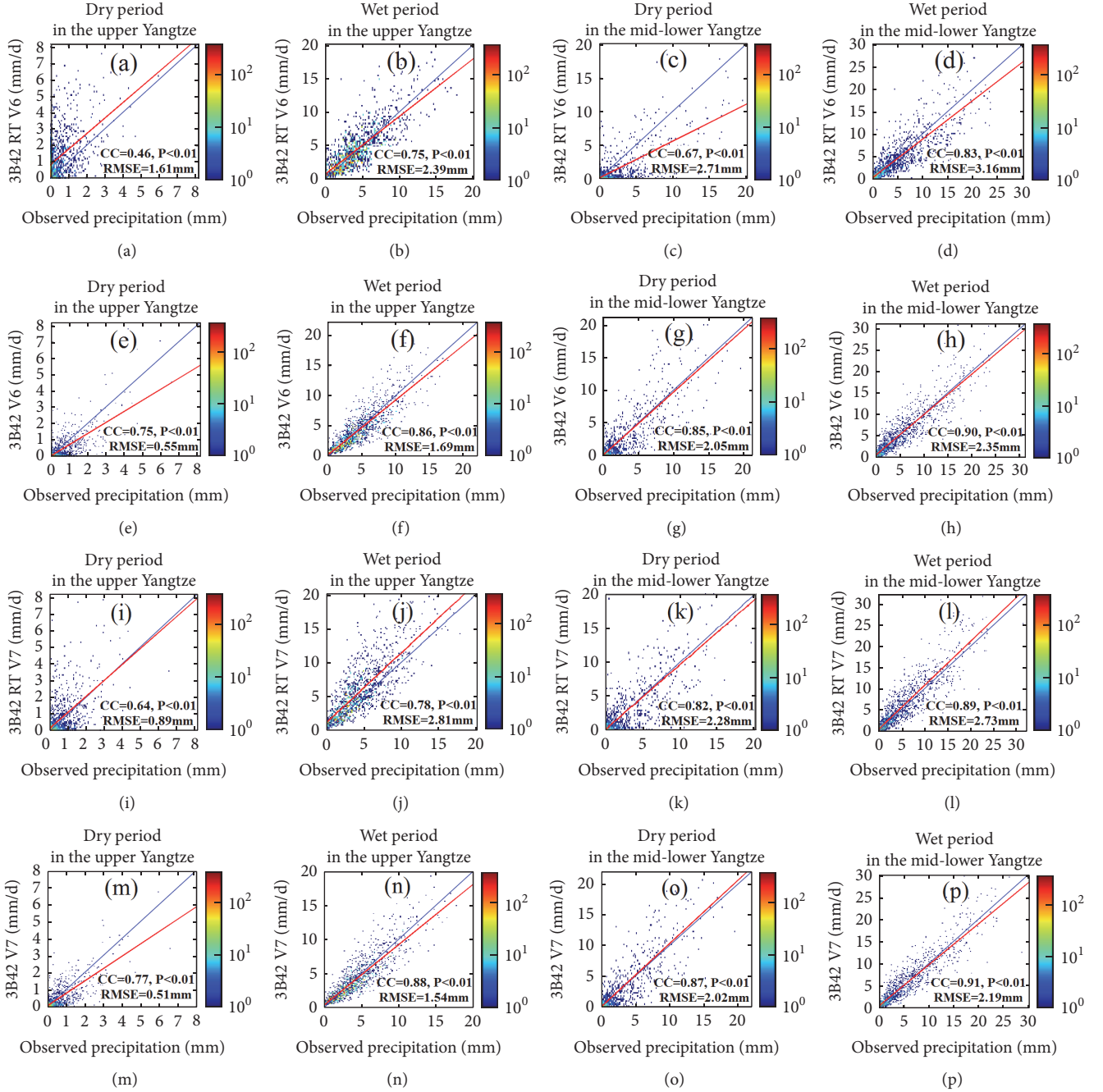


FIGURE 6: Scatter plots of TMPA versus observed daily mean precipitation for the dry period and wet period in the Yangtze River basin.

the V7 product, especially in the upper Yangtze reaches for the dry period. Similar results also can be found in previous studies; for example, Gao and Liu [40] revealed better agreement with gauge measurements over humid regions than that over arid regions in the Tibetan Plateau. Gu et al. [28] reported that the TRMM V6 data slightly overestimated rainfall during the wet season and underestimated rainfall during the dry season in the Yangtze River basin. Islam and Uyeda [35] indicated that the V5 data overestimated the rainfall during the premonsoon period and in

dry regions but underestimated it during the monsoon period and in wet regions.

A noticeable improvement in satellite-based precipitation products has been made. Montero-Martínez et al. [52] conducted an evaluation of precipitation estimations in a complex topography and high elevation and they found that 2B31 TRMM data could be used in weather applications for the area with complex topographical characteristics and also as a tool in the diagnosis of individual rain events in other regions where there were no other data sources available.

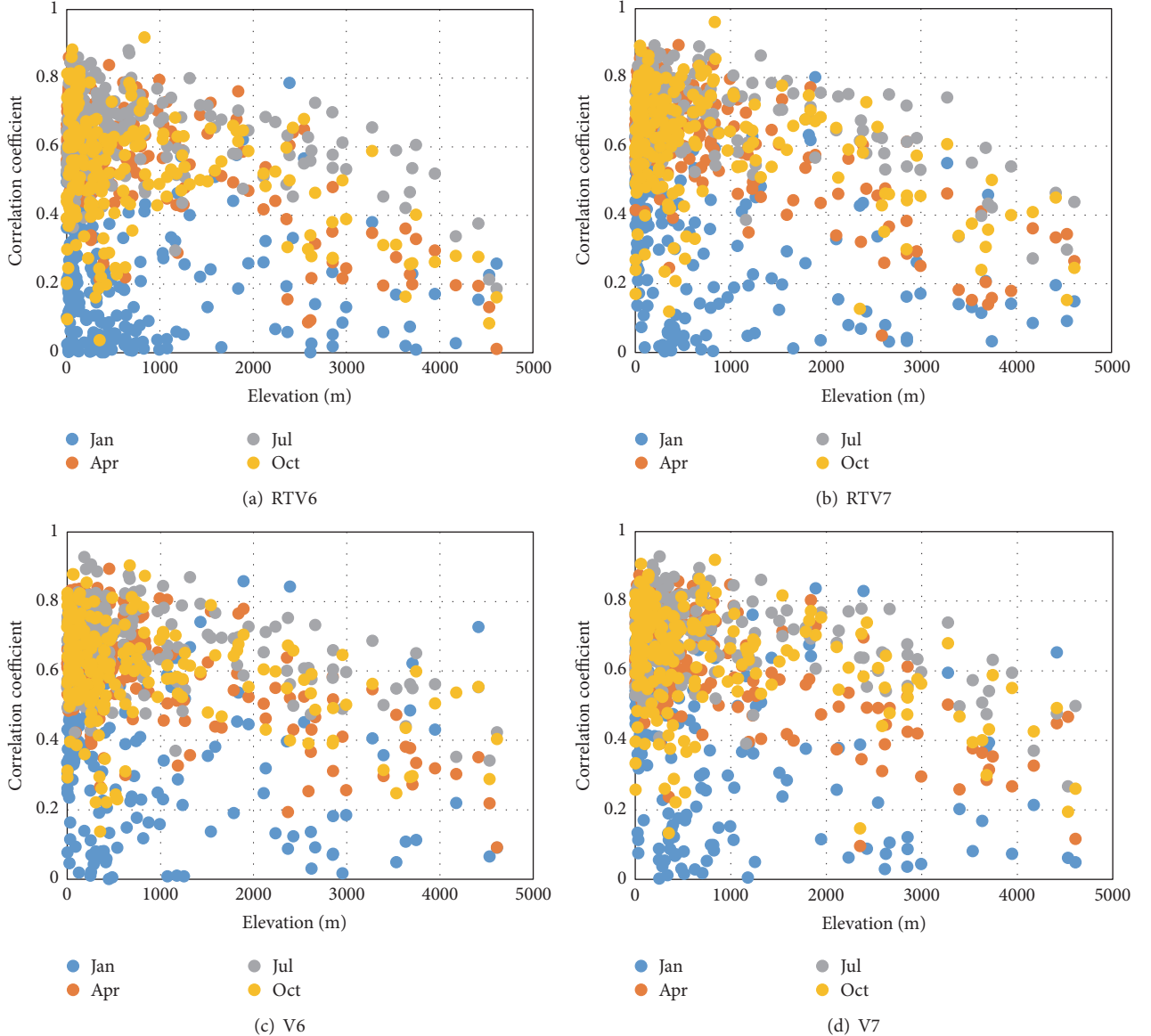


FIGURE 7: Seasonal distribution of correlation coefficient of TRMM precipitation and observed data with elevation.

While Yong et al. [32] thought the RTV7 represented a substantial improvement over the RTV6 in the low-latitude Mishui basin, such improvement was not found in the high-latitude Laohahe basin, which suggested that the RTV7 precipitation estimates still have much room for improvement at high latitudes.

The performance of TMPA precipitation estimation shows a downward trend with the increasing elevation in the Yangtze River basin in different seasons. The CC values vary from 0.41~0.93 (500 m below) to 0.27~0.89 (500~4000 m high) and 0.27~0.50 (4000 m high) in July in the upper Yangtze reaches. Many studies indicated that the satellite-based precipitation has larger measurement uncertainties over complex terrains, inland water bodies, and high-latitude areas [40, 42], as the analysis by Gao and Liu [40] found that biases of TMPA and CMORPH present weak dependence on topography in the Tibetan Plateau, while Dinku et al.

[53] stated that satellite-based precipitation estimation is controlled by the orography. Gao and Liu [40] inferred that positive bias in TMPA RT products over the Tibetan Plateau may be attributable to the impact of topography on IR observations. Moreover, Gebregiorgis and Hossain [54] indicated that satellite rainfall uncertainty is dependent more on topography than the climate of the region in some areas.

5. Conclusions

The main objective of this study is to quantify evaluation of different TMPA precipitation products by using rain gauge data for the years of 2003~2010. We evaluated and compared the statistical characteristics of RTV6 (V6) and RTV7 (V7) over the Yangtze River basin. The main findings are summarized as follows.

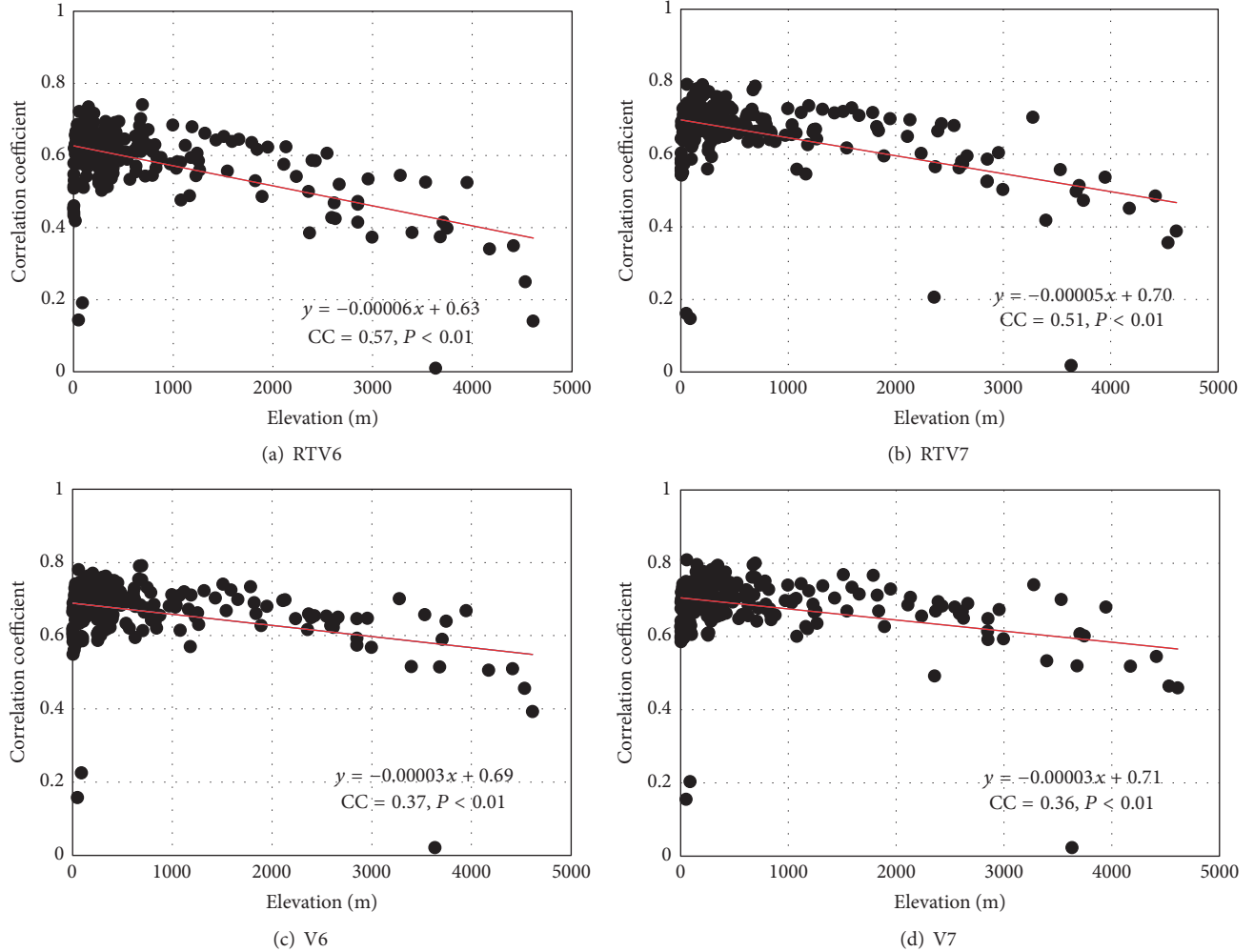


FIGURE 8: The correlativity between elevation and correlation coefficient of TRMM precipitation and observed data.

Both V6 and V7 have similar spatial patterns of precipitation biases in the Yangtze River basin and most of the precipitation bias ranges from -10% to 10% . The performance of the RTV7 (V7) precipitation products is generally better than that of RTV6 (V6) and the percentage of best performance for the RTV7 (V7) products is 36.70% (59.85%), while it is 21.72% (54.79%) for the RTV6 (V6) over the entire Yangtze River basin.

The monsoon climate might have significant impacts on the precipitation evaluation in the Yangtze River basin. Higher CC values can be found between the TMPA products and the observed precipitation during the wet period (CC ranges $0.75\sim0.91$) than that of the dry period (CC ranges $0.46\sim0.87$) in the Yangtze River basin, and average CC value between TMPA products and observed precipitation is 0.67 in July and it is 0.32 in January for the entire Yangtze River basin.

The performance of TMPA precipitation might be affected by the elevation in the Yangtze River basin. A downward trend for performance of the TMPA products with the increasing elevation can be found in the Yangtze River basin in different seasons. The correlation coefficient (CC)

between the V7 and observed precipitation ranges $0.41\sim0.93$ and $0.27\sim0.89$ in the upper Yangtze reaches 500 m below and $500\sim4000\text{ m}$ high, respectively, while the CC decreases to $0.27\sim0.50$ when the stations are located 4000 m high.

This paper addresses knowledge gaps from previous studies by assessing the impacts of monsoon climate and elevation on the evaluation of TMPA precipitation products in the Yangtze River basin. The results quantify the evaluation of TMPA precipitation products based on different time scale in different areas in the Yangtze River basin. Outcomes of this work are expected to assist in answering the question regarding the performance of satellite precipitation in a complex climate and topography area.

Competing Interests

The authors declare that they have no competing interests.

Acknowledgments

This paper is financially supported by the State Key Development Program for Basic Research of China (Grant no.

2012CB417006) and by National Natural Science Foundation of China (Grant nos. 51190090 and 41171020). Project was supported by Distinguished Young Scholars Fund of Nanjing Forestry University and by Open Research Fund Program of State Key Laboratory of Water Resources and Hydropower Engineering Science (Grant no. 2011B079), Key Laboratory of Watershed Geographic Sciences, Chinese Academy of Sciences (Grant no. WSGS2015005), the State Key Laboratory of Satellite Ocean Environment Dynamics, Second Institute of State Oceanic Administration, Six Talent Peaks Project in Jiangsu Province (Grant no. 2015-JY-017), and the Priority Academic Program Development of Jiangsu Higher Education Institutions (PAPD). The authors would like to thank the National Climate Centre in Beijing for providing valuable climate datasets.

References

- [1] R. F. Adler, J.-J. Wang, G. Gu, and G. J. Huffman, "A ten-year tropical rainfall climatology based on a composite of TRMM products," *Journal of the Meteorological Society of Japan*, vol. 87, pp. 281–293, 2009.
- [2] Z. Duan and W. G. M. Bastiaanssen, "First results from Version 7 TRMM 3B43 precipitation product in combination with a new downscaling-calibration procedure," *Remote Sensing of Environment*, vol. 131, pp. 1–13, 2013.
- [3] S. Pombo and R. P. de Oliveira, "Evaluation of extreme precipitation estimates from TRMM in Angola," *Journal of Hydrology*, vol. 523, pp. 663–679, 2015.
- [4] M. M. Rahman, D. S. Arya, N. K. Goel, and A. K. Mitra, "Rainfall statistics evaluation of ECMWF model and TRMM data over Bangladesh for flood related studies," *Meteorological Applications*, vol. 19, no. 4, pp. 501–512, 2012.
- [5] M. Zhang, Y. C. Qi, and X. M. Hu, "Impact of East Asian winter monsoon on the Pacific storm track," *Meteorological Applications*, vol. 21, no. 4, pp. 873–878, 2014.
- [6] V. M. Mantas, Z. Liu, C. Caro, and A. J. S. C. Pereira, "Validation of TRMM multi-satellite precipitation analysis (TMPA) products in the Peruvian Andes," *Atmospheric Research*, vol. 163, pp. 132–145, 2015.
- [7] R. Shrivastava, S. K. Dash, M. N. Hegde, K. S. Pradeepkumar, and D. N. Sharma, "Validation of the TRMM multi satellite rainfall product 3B42 and estimation of scavenging coefficients for 131I and 137Cs using TRMM 3B42 rainfall data," *Journal of Environmental Radioactivity*, vol. 138, pp. 132–136, 2014.
- [8] X.-H. Li, Q. Zhang, and C.-Y. Xu, "Suitability of the TRMM satellite rainfalls in driving a distributed hydrological model for water balance computations in Xinjiang catchment, Poyang lake basin," *Journal of Hydrology*, vol. 426–427, pp. 28–38, 2012.
- [9] Q. Cao and Y. C. Qi, "The variability of vertical structure of precipitation in Huaihe River Basin of China: implications from long-term spaceborne observations with TRMM precipitation radar," *Water Resources Research*, vol. 50, no. 5, pp. 3690–3705, 2014.
- [10] S.-J. Wu, H.-C. Lien, C.-T. Hsu, C.-H. Chang, and J.-C. Shen, "Modeling probabilistic radar rainfall estimation at ungauged locations based on spatiotemporal errors which correspond to gauged data," *Hydrology Research*, vol. 46, no. 1, pp. 39–59, 2015.
- [11] K. Asghari and M. Nasseri, "Spatial rainfall prediction using optimal features selection approaches," *Hydrology Research*, vol. 46, no. 3, pp. 343–355, 2015.
- [12] M. Shafiei, B. Ghahraman, B. Saghaian, S. Pande, S. Gharari, and K. Davary, "Assessment of rain-gauge networks using a probabilistic GIS based approach," *Hydrology Research*, vol. 45, no. 4–5, pp. 551–562, 2014.
- [13] S. J. Wu, C. H. Chang, C. T. Hsu, and J. C. Shen, "An evaluation framework for identifying the optimal rain-gauge network based on spatiotemporal variation in quantitative precipitation estimation," *Hydrology Research*, 2016.
- [14] C. Chen, Z. Yu, L. Li, and C. Yang, "Adaptability evaluation of TRMM satellite rainfall and its application in the dongjiang river basin," *Procedia Environmental Sciences A*, vol. 10, pp. 396–402, 2011.
- [15] J. Meng, L. Li, Z. Hao, J. Wang, and Q. Shao, "Suitability of TRMM satellite rainfall in driving a distributed hydrological model in the source region of Yellow River," *Journal of Hydrology*, vol. 509, pp. 320–332, 2014.
- [16] P. D. Wagner, P. Fiener, F. Wilken, S. Kumar, and K. Schneider, "Comparison and evaluation of spatial interpolation schemes for daily rainfall in data scarce regions," *Journal of Hydrology*, vol. 464–465, pp. 388–400, 2012.
- [17] C. B. Moffitt, F. Hossain, R. F. Adler, K. K. Yilmaz, and H. F. Pierce, "Validation of a TRMM-based global flood detection system in Bangladesh," *International Journal of Applied Earth Observation and Geoinformation*, vol. 13, no. 2, pp. 165–177, 2011.
- [18] A. K. Sahoo, J. Sheffield, M. Pan, and E. F. Wood, "Evaluation of the Tropical Rainfall Measuring Mission Multi-Satellite Precipitation Analysis (TMPA) for assessment of large-scale meteorological drought," *Remote Sensing of Environment*, vol. 159, pp. 181–193, 2015.
- [19] X. Xue, Y. Hong, A. S. Limaye et al., "Statistical and hydrological evaluation of TRMM-based Multi-satellite Precipitation Analysis over the Wangchu Basin of Bhutan: are the latest satellite precipitation products 3B42V7 ready for use in ungauged basins?" *Journal of Hydrology*, vol. 499, pp. 91–99, 2013.
- [20] D. C. Buarque, R. C. D. De Paiva, R. T. Clarke, and C. A. B. Mendes, "A comparison of Amazon rainfall characteristics derived from TRMM, CMORPH and the Brazilian national rain gauge network," *Journal of Geophysical Research Atmospheres*, vol. 116, no. 19, Article ID D19105, 2011.
- [21] L. Li, C. S. Ngongondo, C.-Y. Xu, and L. Gong, "Comparison of the global TRMM and WFD precipitation datasets in driving a large-scale hydrological model in southern Africa," *Hydrology Research*, vol. 44, no. 5, pp. 770–788, 2013.
- [22] A. Sealy, G. S. Jenkins, and S. C. Walford, "Seasonal/regional comparisons of rain rates and rain characteristics in West Africa using TRMM observations," *Journal of Geophysical Research-Atmospheres*, vol. 108, no. 10, 2003.
- [23] D. B. Wolff and B. L. Fisher, "Comparisons of instantaneous TRMM ground validation and satellite rain-rate estimates at different spatial scales," *Journal of Applied Meteorology and Climatology*, vol. 47, no. 8, pp. 2215–2237, 2008.
- [24] H. Xu, C.-Y. Xu, N. R. Sælthun, B. Zhou, and Y. Xu, "Evaluation of reanalysis and satellite-based precipitation datasets in driving hydrological models in a humid region of Southern China," *Stochastic Environmental Research and Risk Assessment*, vol. 29, no. 8, pp. 2003–2020, 2015.
- [25] H. Xu, C.-Y. Xu, N. R. Sælthun, Y. Xu, B. Zhou, and H. Chen, "Entropy theory based multi-criteria resampling of rain gauge networks for hydrological modelling—a case study of humid area in southern China," *Journal of Hydrology*, vol. 525, pp. 138–151, 2015.

- [26] K. Tong, F. Su, D. Yang, and Z. Hao, "Evaluation of satellite precipitation retrievals and their potential utilities in hydrologic modeling over the Tibetan Plateau," *Journal of Hydrology*, vol. 519, pp. 423–437, 2014.
- [27] B. Collischonn, W. Collischonn, and C. E. M. Tucci, "Daily hydrological modeling in the Amazon basin using TRMM rainfall estimates," *Journal of Hydrology*, vol. 360, no. 1–4, pp. 207–216, 2008.
- [28] H.-H. Gu, Z.-B. Yu, C.-G. Yang, Q. Ju, B.-H. Lu, and C. Liang, "Hydrological assessment of TRMM rainfall data over Yangtze River Basin," *Water Science and Engineering*, vol. 3, no. 4, pp. 418–430, 2010.
- [29] Y. Chen, E. E. Ebert, K. J. E. Walsh, and N. E. Davidson, "Evaluation of TRMM 3B42 precipitation estimates of tropical cyclone rainfall using PACRAIN data," *Journal of Geophysical Research-Atmospheres*, vol. 118, no. 5, pp. 2184–2196, 2013.
- [30] H. Zhao, S. Yang, Z. Wang, X. Zhou, Y. Luo, and L. Wu, "Evaluating the suitability of TRMM satellite rainfall data for hydrological simulation using a distributed hydrological model in the Weihe River catchment in China," *Journal of Geographical Sciences*, vol. 25, no. 2, pp. 177–195, 2015.
- [31] L. Qiao, Y. Hong, S. Chen, C. B. Zou, J. J. Gourley, and B. Yong, "Performance assessment of the successive Version 6 and Version 7 TMPA products over the climate-transitional zone in the southern Great Plains, USA," *Journal of Hydrology*, vol. 513, pp. 446–456, 2014.
- [32] B. Yong, B. Chen, J. J. Gourley et al., "Intercomparison of the Version-6 and Version-7 TMPA precipitation products over high and low latitudes basins with independent gauge networks: is the newer version better in both real-time and post-real-time analysis for water resources and hydrologic extremes?" *Journal of Hydrology*, vol. 508, pp. 77–87, 2014.
- [33] S. I. Khan, Y. Hong, J. J. Gourley, M. U. K. Khattak, B. Yong, and H. J. Vergara, "Evaluation of three high-resolution satellite precipitation estimates: potential for monsoon monitoring over Pakistan," *Advances in Space Research*, vol. 54, no. 4, pp. 670–684, 2014.
- [34] E. Habib, A. Henschke, and R. F. Adler, "Evaluation of TMPA satellite-based research and real-time rainfall estimates during six tropical-related heavy rainfall events over Louisiana, USA," *Atmospheric Research*, vol. 94, no. 3, pp. 373–388, 2009.
- [35] M. N. Islam and H. Uyeda, "Use of TRMM in determining the climatic characteristics of rainfall over Bangladesh," *Remote Sensing of Environment*, vol. 108, no. 3, pp. 264–276, 2007.
- [36] X. Li, Q. Zhang, and X. Ye, "Dry/wet conditions monitoring based on TRMM rainfall data and its reliability validation over poyang lake basin, China," *Water*, vol. 5, no. 4, pp. 1848–1864, 2013.
- [37] M. Almazroui, "Calibration of TRMM rainfall climatology over Saudi Arabia during 1998–2009," *Atmospheric Research*, vol. 99, no. 3–4, pp. 400–414, 2011.
- [38] Z. Liu, "Comparison of versions 6 and 7 3-hourly TRMM multi-satellite precipitation analysis (TMPA) research products," *Atmospheric Research*, vol. 163, pp. 91–101, 2015.
- [39] Y. Guan, X. Zhang, F. Zheng, and B. Wang, "Trends and variability of daily temperature extremes during 1960–2012 in the Yangtze River Basin, China," *Global and Planetary Change*, vol. 124, pp. 79–94, 2015.
- [40] Y. C. Gao and M. F. Liu, "Evaluation of high-resolution satellite precipitation products using rain gauge observations over the Tibetan Plateau," *Hydrology and Earth System Sciences*, vol. 17, no. 2, pp. 837–849, 2013.
- [41] Z.-C. Hao, K. Tong, X.-L. Liu, and L.-L. Zhang, "Capability of TMPA products to simulate streamflow in upper Yellow and Yangtze River basins on Tibetan Plateau," *Water Science and Engineering*, vol. 7, no. 3, pp. 237–249, 2014.
- [42] Z. Li, D. Yang, and Y. Hong, "Multi-scale evaluation of high-resolution multi-sensor blended global precipitation products over the Yangtze River," *Journal of Hydrology*, vol. 500, pp. 157–169, 2013.
- [43] W. Xie, Y. Fu, Y. Li, J. Li, Y. Li, and Q. Yue, "Cryogenic THGEM-GPM for the readout of scintillation light from liquid argon," *Nuclear Instruments and Methods in Physics Research Section A: Accelerators, Spectrometers, Detectors and Associated Equipment*, vol. 774, pp. 120–126, 2015.
- [44] D. Long, Y. Yang, Y. Wada et al., "Deriving scaling factors using a global hydrological model to restore GRACE total water storage changes for China's Yangtze River Basin," *Remote Sensing of Environment*, vol. 168, pp. 177–193, 2015.
- [45] T. Islam, M. A. Rico-Ramirez, D. Han, P. K. Srivastava, and A. M. Ishak, "Performance evaluation of the TRMM precipitation estimation using ground-based radars from the GPM validation network," *Journal of Atmospheric and Solar-Terrestrial Physics*, vol. 77, pp. 194–208, 2012.
- [46] G.-J. Zhao, G. Hörmann, N. Fohrer, J.-F. Gao, J.-Q. Zhai, and Z.-X. Zhang, "Spatial and temporal characteristics of wet spells in the Yangtze River Basin from 1961 to 2003," *Theoretical and Applied Climatology*, vol. 98, no. 1–2, pp. 107–117, 2009.
- [47] S. Chen, Y. Hong, Q. Cao et al., "Similarity and difference of the two successive V6 and V7 TRMM multisatellite precipitation analysis performance over China," *Journal of Geophysical Research Atmospheres*, vol. 118, no. 23, pp. 13060–13074, 2013.
- [48] B. D. Su, T. Jiang, and W. B. Jin, "Recent trends in observed temperature and precipitation extremes in the Yangtze River basin, China," *Theoretical and Applied Climatology*, vol. 83, no. 1–4, pp. 139–151, 2006.
- [49] J. He, J. Ju, Z. Wen, J. Lü, and Q. Jin, "A review of recent advances in research on Asian monsoon in China," *Advances in Atmospheric Sciences*, vol. 24, no. 6, pp. 972–992, 2007.
- [50] R. Huang, J. Chen, and G. Huang, "Characteristics and variations of the East Asian monsoon system and its impacts on climate disasters in China," *Advances in Atmospheric Sciences*, vol. 24, no. 6, pp. 993–1023, 2007.
- [51] Q. Zhang, C.-Y. Xu, T. Jiang, and Y. Wu, "Possible influence of ENSO on annual maximum streamflow of the Yangtze River, China," *Journal of Hydrology*, vol. 333, no. 2–4, pp. 265–274, 2007.
- [52] G. Montero-Martínez, V. Zarraluqui-Such, and F. García-García, "Evaluation of 2B31 TRMM-product rain estimates for single precipitation events over a region with complex topographic features," *Journal of Geophysical Research Atmospheres*, vol. 117, no. 2, Article ID D02101, 2012.
- [53] T. Dinku, S. Chidzambwa, P. Ceccato, S. J. Connor, and C. F. Ropelewski, "Validation of high-resolution satellite rainfall products over complex terrain," *International Journal of Remote Sensing*, vol. 29, no. 14, pp. 4097–4110, 2008.
- [54] A. S. Gebregiorgis and F. Hossain, "Understanding the dependence of satellite rainfall uncertainty on topography and climate for hydrologic model simulation," *IEEE Transactions on Geoscience and Remote Sensing*, vol. 51, no. 1, pp. 704–718, 2013.

Research Article

Flood Forecasting Based on TIGGE Precipitation Ensemble Forecast

Jinyin Ye,¹ Yuehong Shao,² and Zhijia Li³

¹Huaihe Meteorological Center, Hefei 230031, China

²Nanjing University of Information Science and Technology, Nanjing 210044, China

³College of Hydrology and Water Resources, Hohai University, Nanjing 210098, China

Correspondence should be addressed to Jinyin Ye; yejinyin@sina.com

Received 17 July 2016; Revised 16 October 2016; Accepted 6 November 2016

Academic Editor: Anthony R. Lupo

Copyright © 2016 Jinyin Ye et al. This is an open access article distributed under the Creative Commons Attribution License, which permits unrestricted use, distribution, and reproduction in any medium, provided the original work is properly cited.

TIGGE (THORPEX International Grand Global Ensemble) was a major part of the THORPEX (Observing System Research and Predictability Experiment). It integrates ensemble precipitation products from all the major forecast centers in the world and provides systematic evaluation on the multimodel ensemble prediction system. Development of meteorologic-hydrologic coupled flood forecasting model and early warning model based on the TIGGE precipitation ensemble forecast can provide flood probability forecast, extend the lead time of the flood forecast, and gain more time for decision-makers to make the right decision. In this study, precipitation ensemble forecast products from ECMWF, NCEP, and CMA are used to drive distributed hydrologic model TOPX. We focus on Yi River catchment and aim to build a flood forecast and early warning system. The results show that the meteorologic-hydrologic coupled model can satisfactorily predict the flow-process of four flood events. The predicted occurrence time of peak discharges is close to the observations. However, the magnitude of the peak discharges is significantly different due to various performances of the ensemble prediction systems. The coupled forecasting model can accurately predict occurrence of the peak time and the corresponding risk probability of peak discharge based on the probability distribution of peak time and flood warning, which can provide users a strong theoretical foundation and valuable information as a promising new approach.

1. Introduction

Flood forecasting is one of the major bases for decision-makers to deal with an emergency situation associated with heavy rainfall. Precipitation is the most important information required for flood forecasting. The accuracy and the lead time are two major factors influencing the performance of the flood forecasting [1]. Application of precipitation forecast products from numerical weather prediction (NWP) on flood forecasting is one of the primary ways to extend the lead time of a flood forecast. The NWP makes it possible to generate useful flood information and issue an early warning of flood. However, due to the errors associated with initial condition and model, the chaos of the atmosphere, and the uncertainties of parameterization as well as the heterogeneousness of the underlying surface, there are large discrepancies between the “single” deterministic flood forecast and the observations, especially for the outburst of local meteorological and

hydrological events [2]. To overcome the limit of the deterministic forecast, people start to focus on the uncertainty of the meteorological and hydrological processes. The traditional “single” deterministic forecast is gradually replaced by the probability forecast which represents the uncertainty of the forecast, that is, a transition from deterministic forecast to ensemble forecast. As a new technique of NWP, ensemble forecast considers the influences from the imperfect boundary conditions and data assimilation, turning the deterministic forecast to complete probability forecast of atmospheric variables [3]. It is a new approach for precipitation forecast and runoff forecast [4].

To account for the uncertainties of the forecasts from multiple global models, an interactive grand global ensemble system was proposed. TIGGE (THORPEX International Grand Global Ensemble) is an international scientific project collecting forecast products from all the major forecast centers in the world and evaluating the multiple model

ensemble system [5]. TIGGE ensemble forecast combines the uncertainties from multiple sources and represents those uncertainties with probability distribution. It has already been applied on flood forecasting and early warning of flood with successful results. Pappenberger et al. [6] coupled TIGGE ensemble data with 5 km distributed hydrologic model and successfully produced early warning for flood with a lead time of 10 days. He et al. [7, 8] used TIGGE ensemble forecasts to drive an atmospheric-hydrologic-hydraulic cascade system to produce a probabilistic discharge forecast and early flood warning. Peng et al. [9] used ECMWF ensemble forecast to drive Xinanjiang hydrologic model (hereafter XAJ model) and, by forecasting range of the runoff, provided useful risk information to decision-maker. However, the last research work only considered ECMWF model; uncertainties from multiple models and multiple forecast centers are not involved. Precipitation ensemble forecasts from four major forecast centers were used to make superensemble forecast and early flood warning; the results are encouraging [10, 11]. For most studies in China, they adopted aggregated approach with XAJ model and did not consider the influence from heterogeneous underlying surface. On the basis of the improved SIMTOP (a simple TOPMODEL) runoff parameterization scheme and the calculating method of three-layer soil moisture balance in Xinanjiang model, Yong (2008) developed a simple but highly-efficient large-scale hydrological model (TOPX). The offline test performed at Youshui River catchment (a small branch of Yangtze River) indicated that the TOPX model produced better simulation effect of daily runoff in small sized catchments and it can describe the various hydrological processes of watershed [12]. In this study, we focus on Yishu River catchment (upstream catchment of Linyi hydrologic station). ECMWF (50 ensemble members), NCEP (20 ensemble members), and CMA (15 ensemble members) ensemble precipitation data were used to drive the distributed hydrologic model TOPX to make flood forecast and early flood warning.

2. About the Catchment

The research area in this study includes the upstream catchment of Yishu River (i.e., Linyi subsystem) with a catchment size of 10152 km². It has a typical continent monsoon climate with four distinct seasons. It is hot in summer with a lot of rainy days and cold and windy in winter. There is an uneventful terrain with elevation ranging from 57 m to 1125 m. The mean annual temperature is 11.8°C–13.3°C and mean annual precipitation/evaporation amount is 830 mm/839 mm with most of precipitation fall in summer in a form of heavy rainfall. There is also significant interannual variation of the precipitation.

3. Construction of Flood Forecast Model Based on TIGGE Ensemble Precipitation Forecast

3.1. Introduction to TOPX. TOPX is a land-surface model developed based on improved SIMTOP (a simple TOPMODEL) and XAJ model. It incorporates both the

topographic index concept from TOPMODEL and the water budget balance principle and is able to capture the land-surface hydrologic processes with a linear scaling transformation scheme for topographic index [12].

The model has seven major components including storage capacity curve, dynamic change of soil moisture, simulated surface runoff and subsurface runoff, simulated discharge, base discharge, Muskingum merge flow, and evaluation factor. TOPX can provide the function of scaling transformation on topographic index. Although the TOPX model has less data input and minimum parameters for calibrating, it can better describe the two-dimensional hydrological processes. The detailed introduction about the model can be found in Yong (2008) and Shao [13]. In the following, we will only introduce the generation and concentration of the runoff as well as the dynamic changes of soil water.

(1) Runoff Generation Formula. A revised SIMTOP runoff generation scheme including the generation of both surface runoff and subsurface runoff is adopted in this study. The formula is shown below:

$$\begin{aligned} R_s &= F_{\max} e^{-C_s z_\nabla} Q_{\text{wat}}, \\ R_{sb} &= R_{sb,\max} e^{-f z_\nabla}, \end{aligned} \quad (1)$$

where R_s is surface runoff, R_{sb} is subsurface runoff, F_{\max} is percentage of the maximum saturated area, $R_{sb,\max}$ is the maximum subsurface runoff when the soil moisture deficit depth is 0, Q_{wat} is net precipitation, z_∇ is average water depth, f is decaying parameter of soil, and C_s is a coefficient that can be derived by fitting the exponential function to the discrete cumulative distribution function (CDF) of the topographic index λ_m . The computational approach to C_s and λ_m can be found in the work of Niu et al. [14]. The revised SIMTOP scheme can represent the topographic information more accurately and produce more realistic temporal-spatial distribution of variables and parameters.

(2) Calculation of Soil Moisture. Soil moisture deficit is a crucial variable connecting surface runoff and subsurface runoff, and it is closely related to the budget of the soil moisture. This formula is developed based on three-layer soil evapotranspiration scheme from XAJ model, and it can significantly simplify the calculation of the soil moisture deficit without reducing the accuracy required by the model [15]. After the temporal-spatial distribution of soil moisture is obtained from the three-layer evapotranspiration formula, the soil moisture deficit thus can be estimated from the difference of the average storage capacity and soil moisture, and finally the surface runoff and subsurface runoff will be calculated. The formula is shown below:

$$z_\nabla = WM - W[i], \quad (2)$$

where WM is the areal mean tension water capacity which has three components WU, WL, and WD in the upper, lower, and

TABLE 1: Some major parameters in TOPX model with calibration results.

Parameter name	Physical meaning	Parameter type	Calibration (20010729)	Calibration (20020722)
f	Decaying parameter	<i>Runoff generation parameters</i>	180	180
G_{\max}	Maximum underground runoff		50	50
KSS	Outflow coefficient of free water storage to interflow relationship		0.012	0.012
B	Exponential of the distribution to tension water capacity		0.40	0.35
K	Ratio of potential evapotranspiration to pan evaporation		0.85	0.85
WM	Averaged soil moisture storage capacity		125.0	125.0
WUM	Averaged soil moisture storage capacity of upper layer	<i>Soil moisture calculation</i>	30.0	30.0
WLM	Averaged soil moisture storage capacity of lower layer		90.0	90.0
C	Evapotranspiration coefficient of deep layer		0.12	0.12
KKG	Recession constants of the ground water storage	<i>Runoff concentration parameters</i>	0.988	0.988
UH	Initial value of unit hydrograph		/0, 44.6, 156, 86.7, 39, 22.3, 15.6/	/0, 12, 42, 23, 3, 10.5, 6.0, 4.2/

deep layer, respectively, and $W[i]$ is the sum of three-layer soil moisture of the i th day.

(3) *Runoff Concentration*. There are three components in TOPX model: overland flow concentration, river network flow, and subsurface flow concentration. Three different methods including empirical unit hydrograph method, Muskingum channel routing method, and linear reservoir parameter method are applied to calculate these three components, respectively, and finally the outlet runoff is obtained.

3.2. TIGGE Precipitation Ensemble Coupled with TOPX. As one of the primary international scientific projects, THORPEX aims to contribute to our society, economics, and environment by advancing a unified observation-forecast system and improving the accuracy of 1–14 days' high impact weather forecast. TIGGE, as the core component of the THORPEX, aggregates the forecast products from all major forecast centers in the world and provides further analyzing, processing, and evaluation support to users. All the forecast centers started to receive and share the corresponding TIGGE data, which provides an opportunity for developing a flood forecast model based on coupling TIGGE data and hydrologic model. NCEP, ECMWF, and CMA ensemble forecast data from TIGGE project are used in this study; the horizontal resolutions for these forecast data are $1^\circ \times 1^\circ$, $0.5^\circ \times 0.5^\circ$, and $0.5625^\circ \times 0.5625^\circ$, respectively. Because of different resolution for these three forecast data, 12, 25, and 20 grid points are used to cover the area we are interested in (Figure 1). Also inverse distance weighting (IDW) method and Kriging method are adopted to downscale the 6-hour accumulated precipitation forecast from different ensemble dataset into 1 km to drive the hydrologic model. Hereafter, the TOPX coupled with ECMWF, NCEP, and CMA ensemble precipitation

forecast is called ECMWF-TOPX, NCEP-TOPX, and CMA-TOPX, respectively.

According to the hydrological and metrological data, 12 flood events are selected for this study. The simulation starts from the time when the precipitation occurred and ends after the flood retreated with a time step of 6 hours. The model parameters are calibrated with 6 flood events during 2001–2004. The calibrated parameters from two of these typical events are then used in simulation of another 6 flood events during 2005–2008. Some major parameters in TOPX hydrologic model as well as their physical meanings are showed in Table 1. The calibrated model parameters from 20010729 event are used to verify three predicted floods with TIGGE data during 2007–2008. Due to similarity of the discharge magnitude between 2010 and 2002, one of the flood forecast in 2010 is verified with calibrated model parameters from 20020722 event.

4. Verification of Flood Forecast in Yi River Catchment

4.1. Results of TIGGE Precipitation Ensemble Forecast. Accuracy of the precipitation forecast directly influences the performance of the model forecast. Therefore, it is necessary to evaluate the TIGGE precipitation ensemble forecast first. We compared ECMWF, NCEP, and CMA ensemble forecasts, and the multimodel precipitation ensemble is also verified with observations. Four heavy rainfall events including 20070809, 20070815, 20080720, and 20100716 are selected to evaluate TIGGE precipitation forecast. Figure 2 shows the precipitation forecast from ECMWF, NCEP, and CMA ensemble forecasts as well as the verification against observations. Non-real-time update means only the 10-day

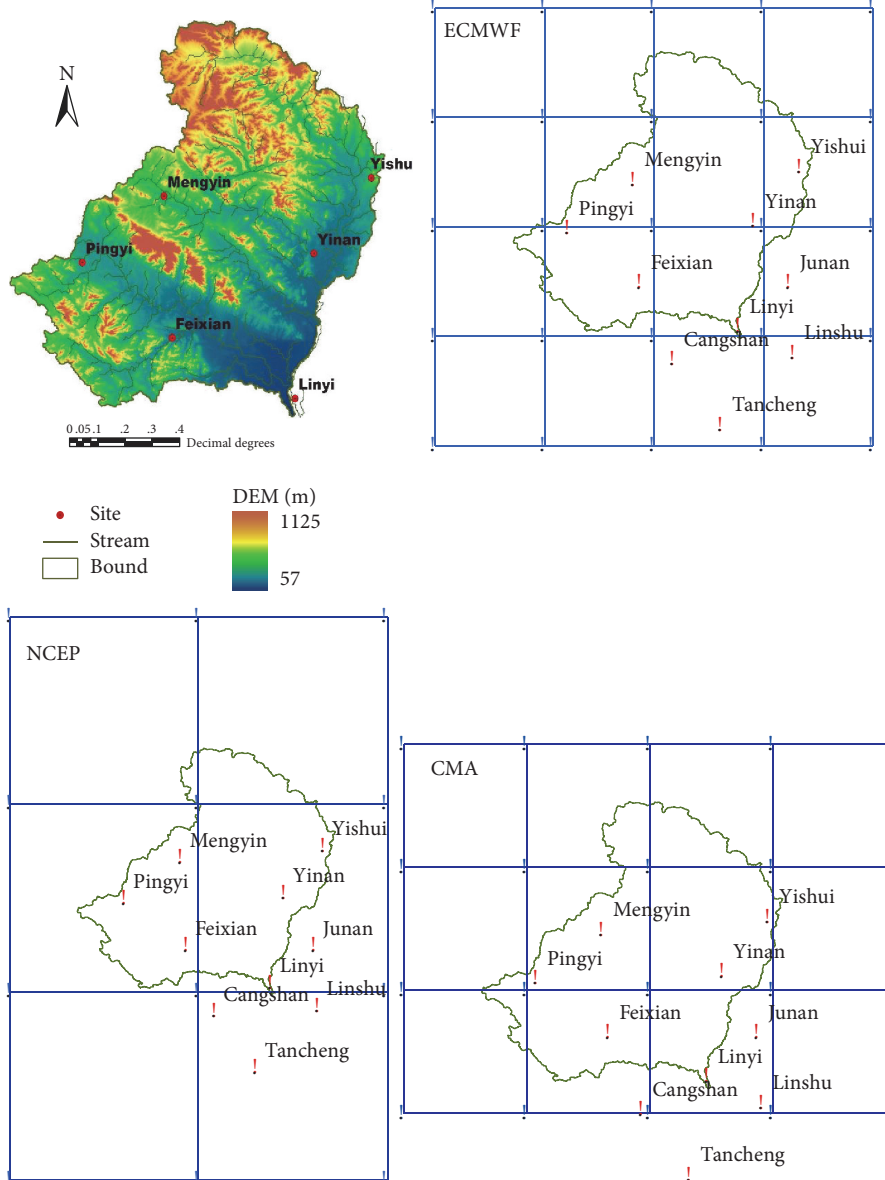


FIGURE 1: Distribution of stations, catchments, and the selected grid points in ECMWF, NCEP, and CMA ensemble models.

precipitation forecast is used, and real-time update means daily precipitation forecast is used. Figure 2 shows clearly the remarkable differences among those three ensemble forecasts. NCEP forecasted less precipitation than observations with substantial smaller maximum precipitation. The precipitation forecast in CMA ensemble products is much larger than observations, with large discrepancy in forecasted time of occurrence of heavy rainfall. Also, the spread of ensemble members is also much larger than that in other ensemble forecasts.

4.2. Discharge Forecasts over Yi River Catchment. Figure 3 shows the forecasted discharges based on three different precipitation ensemble forecasts for 20070809 event. It can be noticed that the peak discharge as well as the time of

occurrence can be well predicted by all the three ensemble forecasts. However, there are large errors for the magnitude of forecasted discharges. CMA-TOPX obviously forecasted much larger amount of discharges, while NCEP-TOPX forecasted much smaller amount instead. Only ECMWF-TOPX forecasted discharges are relatively close to the observations. The results for the other three events are similar; ECMWF-TOPX forecasted discharges are always the best among them. Because the runoff generation scheme is better for humid area, for those events (e.g., 20100706 event) with less amount of runoff, the simulation results are not good. There are large discrepancies among the three ensembles; the forecasted discharges as well as time of occurrence all significantly deviate from the observations. Nevertheless, if we use all the 85 ensemble members to drive the TOPX, we can obtain

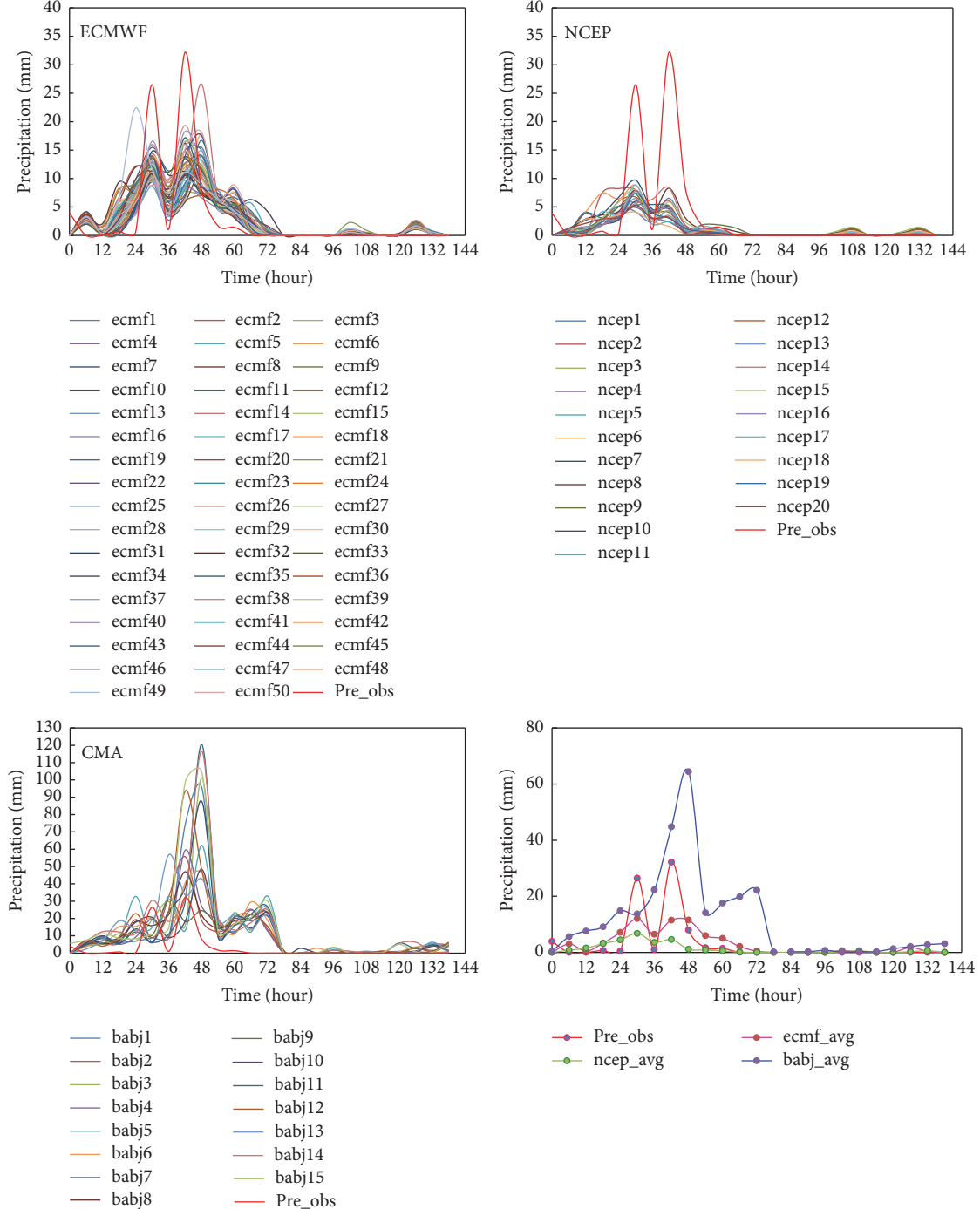


FIGURE 2: Comparison of the predicted precipitation (20070809 event) from ECMWF, NCEP, and CMA ensemble models.

superensemble forecasts (figure not shown). Superensemble forecasts can provide comprehensive information including the range and the probability distribution of forecasted discharges, as well as the superensemble mean of all 85 members. For example, for the 20070809 event, the probability of discharge larger than $2000 \text{ m}^3/\text{s}$ and $1000 \text{ m}^3/\text{s}$ is 35.3% and 69.4%, respectively. The users can respond to the forecasted probability accordingly.

Figure 4 shows the ensemble mean discharges from ECMWF-TOPX, NCEP-TOPX, and CMA-TOPX models. It is obvious that the forecasted peak discharges and the time of occurrence are close to the observations. However, large variabilities exist for the forecasted magnitudes of the peak discharges. It can be seen that the ECMWF-TOPX has the closest magnitude to the observations for the 20070809 event, which is probably related to the fact that it has

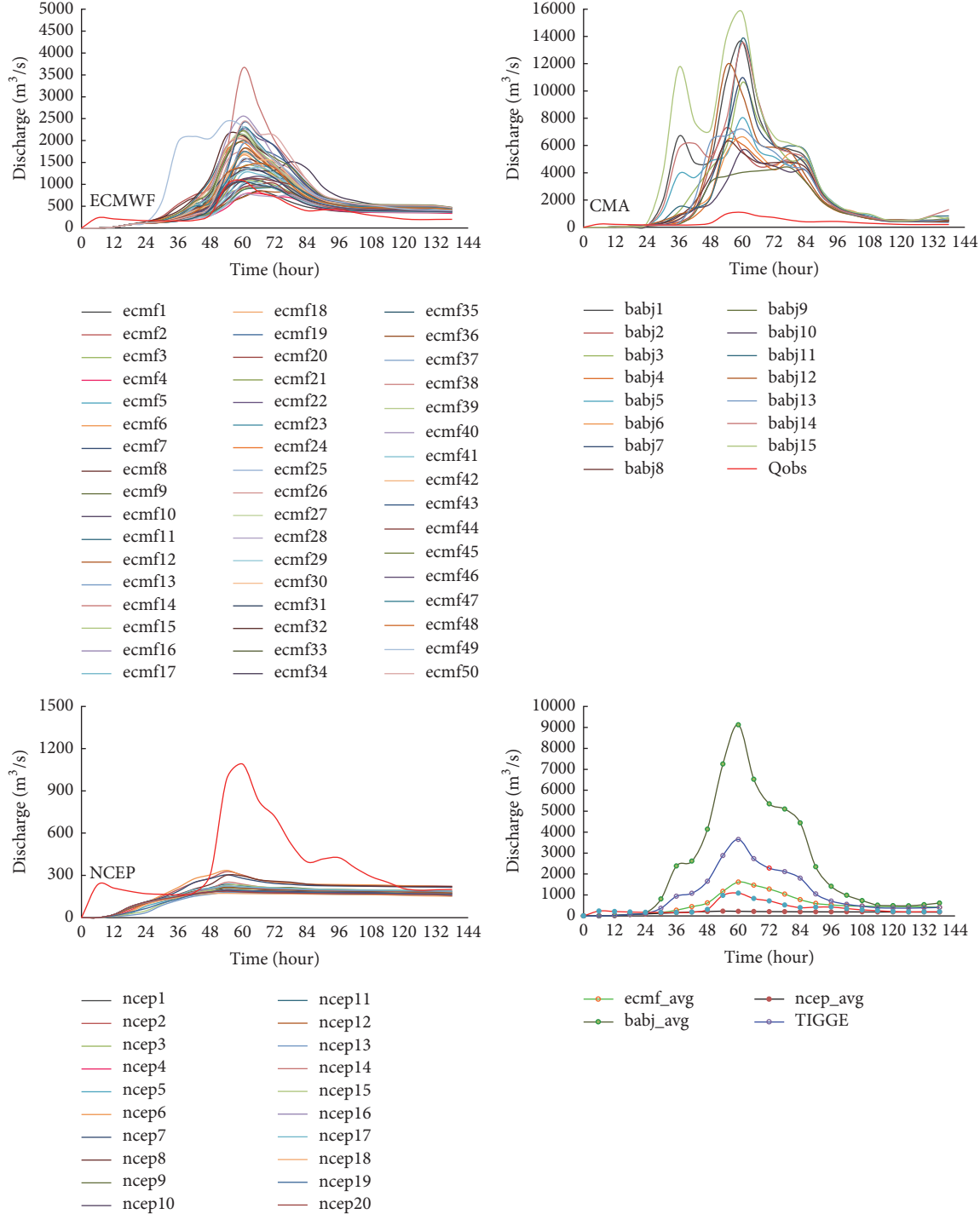


FIGURE 3: Same with Figure 2 except for forecasted discharges.

the most ensemble members (50). For all the other three events, the superensemble is the best. The NCEP-TOPX has the minimum ensemble mean discharge, while the CMA-TOPX ensemble mean discharge has the maximum ensemble mean discharge due to the largest amount of forecasted precipitation. In general, these three coupled systems can all predict the occurrence time of peak discharge, but significant forecast errors still exist for the magnitude of discharge,

especially for NCEP-TOPX and CMA-TOPX, which is due to less/more forecasted precipitation. The challenges for later research are how we can improve the accuracy of peak discharge by calibrating the ensemble precipitation forecasts from different forecast centers and how we set different weights for different ensemble systems.

Figure 5 shows the occurrence of peak discharge probability distribution for the 20070809, 20070815, 20080720, and

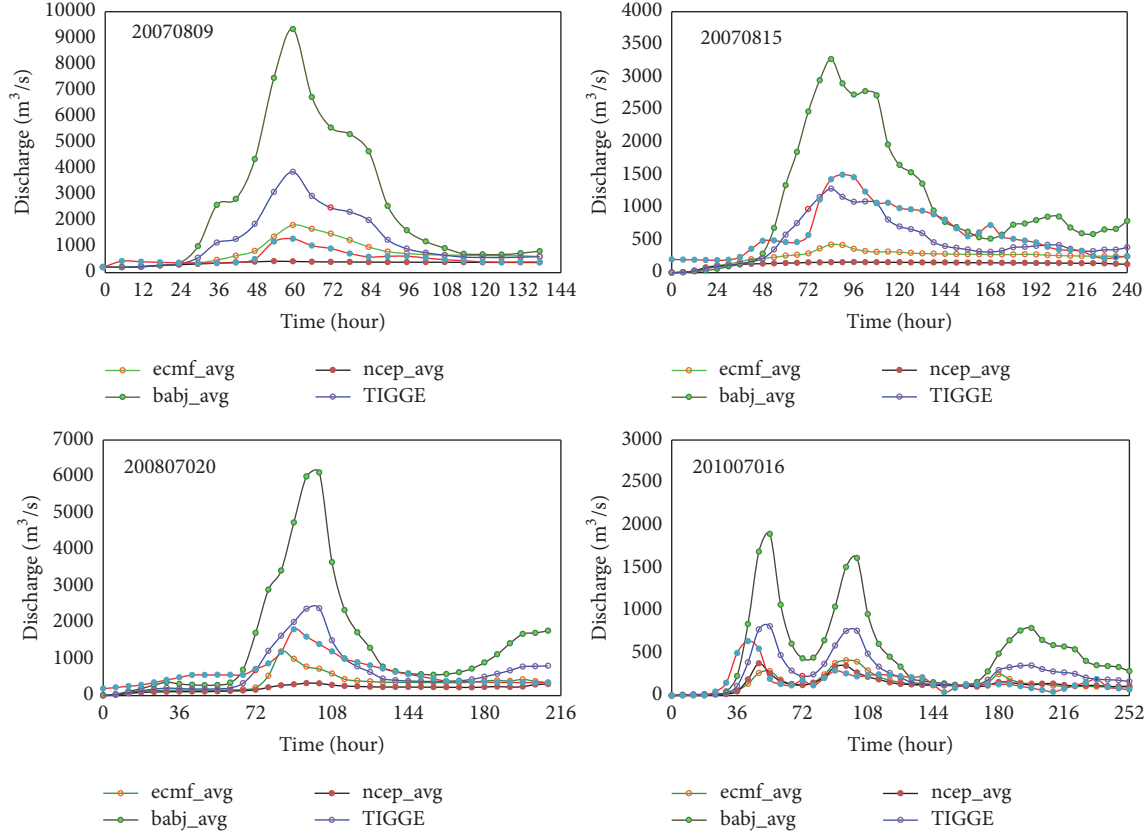


FIGURE 4: Comparison of the superensemble forecasted discharges from equal weight superensemble with observations (red lines with dots).

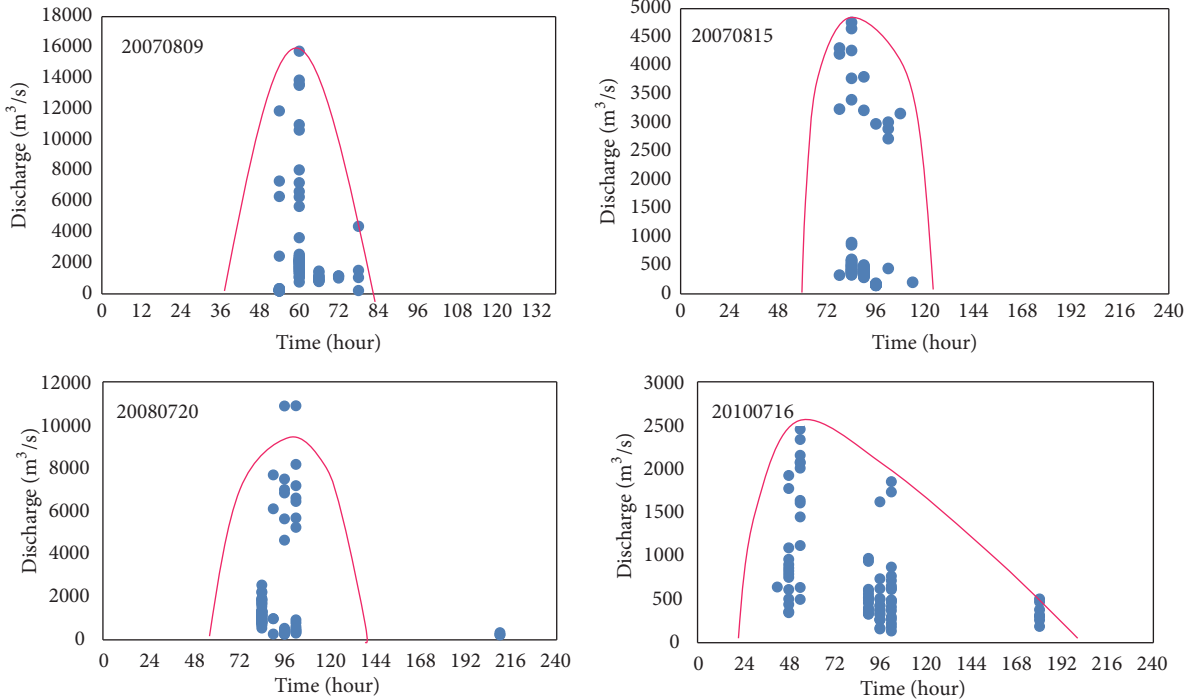


FIGURE 5: The scatter plot between the peak discharge (vertical coordinate) and its occurrence (horizontal coordinate) forecasts from superensemble members. The inverse U-shaped envelope curve reflects the joint probability distribution of the peak discharge and its occurrence forecasts.

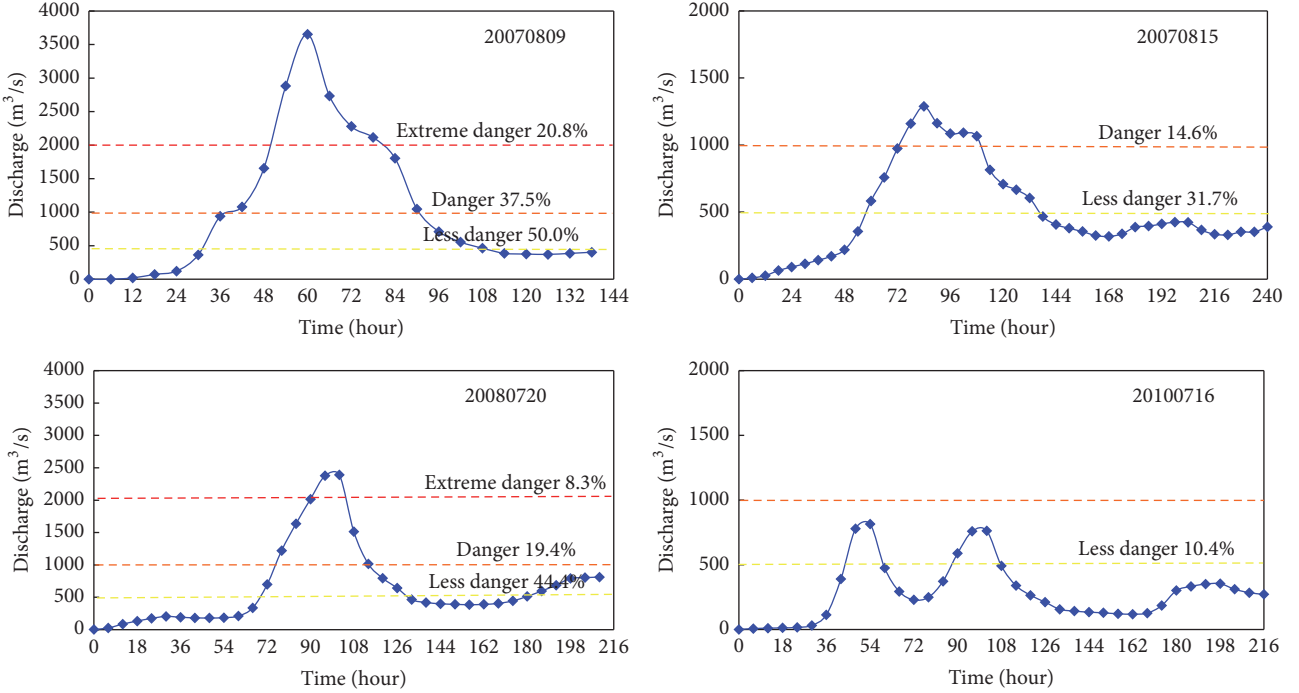


FIGURE 6: Flood warning probability from superensemble system.

20100716 events from superensemble forecast. All the events show an inverse “U” probability distribution or approximately a normal distribution except the 20100716 event. It can easily be obtained from Figure 5 that the occurrence of peak discharge mainly locates within the window zone/interval, and the probability is further calculated by the proportion of the members with peak discharge from all ensemble members. All the ensemble members forecasted similar occurrence of peak discharge; there is little difference among these three ensemble systems. The forecasted occurrence of peak discharge is close to the observations with forecast error less than 12 hours. For the 20100716 event, the peak discharge is relatively less than others, and there is more than one peak discharge. The precipitation for this event is not well predicted in all the ensemble systems, which causes large errors in forecasted discharge. Two main reasons are responsible for this: one is the large forecast errors of precipitation and the other one is hydrologic model itself which has unsatisfied performance for flood with a small discharge. For this event, the spread of the ensemble members in each model is relatively small, but large discrepancies exist among the models. The forecasted occurrence window of peak discharge differs, which makes it difficult for users to make decisions. For all these four events, the forecasts for large discharge are much better than that for small discharge. The superensemble of forecasted occurrence of peak discharge can easily be obtained from the probability distribution map of the peak discharge, which is one of the advantages of the superensemble.

Figure 6 shows the flood warning probability from superensemble system. X-axis represents the forecast time, and Y-axis represents the mean discharge of 85 members. The

probability for three flood ratings (“less danger,” “danger,” and “extreme danger”) is, respectively, calculated and considered by the ratio of the corresponding duration to total duration, which is from 0 h to the longest lead time at 6 h intervals. The 20070809 and 20080720 events have higher discharges, followed by the 20070815 event. The 20100716 event has the lowest discharges. For the 20070809 event, the superensemble forecasted probability for “less danger” (discharges greater than $500 \text{ m}^3/\text{s}$) is 50.0%, for “danger” (discharges greater than $1000 \text{ m}^3/\text{s}$) is 37.5%, and for “extreme danger” (discharges greater than $2000 \text{ m}^3/\text{s}$) is 20.8%. It means, for more than 1/3 of the time during this event, the discharges passing the outlet of Linyi catchment are over “danger” threshold. For more than 1/5 of the time during this event, the discharges passing the Linyi catchment are over “extreme danger” threshold. The discharges in 20070815 event are lower, and the probability of reaching “extreme danger” threshold is only 14.6%. The discharges in 20100716 event are the lowest, and the probability of reaching “less danger” threshold is only 10.4% and yet did not reach “danger” threshold. All above information are very useful references for decision-makers in local government and hydrological, meteorological, and agricultural offices. Due to various configuration of the models, the forecasted precipitation is significantly different, which further leads to tremendous discrepancies on forecasted discharges. However, the occurrence of the peak discharge and the probability of flood are well predicted. Compared with deterministic forecast, flood forecasting based on TIGGE and TOPX is able to provide more valuable information and probability of risk and is a promising approach.

5. Summary and Discussions

In this paper, flood forecasting using distributed hydrologic model TOPX coupled with TIGGE ensemble precipitation data is documented. TIGGE data from ensemble forecast products at ECMWF, NCEP, and CMA are used to drive TOPX to make flood forecast for 20070809, 20070815, 20080720, and 20100716 events over Yishu River catchment. The results show the coupled model can successfully simulate the discharges during the events. The peak discharges as well as the occurrence of the peak discharge can be well predicted, but large discrepancies exist between the models. The CMA-TOPX forecasted higher discharges, while the NCEP-TOPX forecasted lower discharges. The ECMWF-TOPX forecasts are in between the other two models and are closest to the observation. According to the superensemble forecast of the occurrence of the peak discharge and the probability of flood, the TIGGE-TOPX coupled model can successfully predict the occurrence time of the peak discharge and probability of flood, which is the primary basis for decision-makers to make a decision.

This initial approach aims to build a basic framework of flood forecast model using TOPX model coupled with TIGGE precipitation data. The preliminary results are encouraging, but some issues need further investigation and research. Firstly, TIGGE dataset starts from year 2007, and only discharges data during years 2007–2010 are used in this study. Because of the limited data, only four flood events are simulated with TIGGE data as input. Though the results are encouraging, more flood events are needed to verify the performance of the coupled model, especially for the event in dry year. The hydrologic processes over nonhumid area are also not well simulated in TOPX. Second, accuracy of the precipitation forecast directly impacts the accuracy of the flood forecast. There are large forecast errors in all the global ensemble forecast models. Third, ensemble precipitation forecasts from three global NWP centers (ECMWF, NCEP, and CMA) are used in this study. The forecasted precipitation from these three NWP centers varies significantly. Currently, equal weight averaging is adopted to obtain the superensemble mean. To attribute different weight to each forecast center according to their forecasts biases is the next topic we should focus on and put efforts into.

Competing Interests

The authors declare that there is no conflict of interests regarding the publication of this paper.

Acknowledgments

The current research is supported financially by the Basic Research Program of Youth Fund Project of Jiangsu Province (BK20141001), China Special Fund for Meteorological Research in the Public Interest (GYHY201406021), Huaihe River Basin Meteorological Open Research Fund (HRM201205), National Natural Science Foundation of China (41275030), and Anhui Provincial Natural Science Foundation (1508085MD64).

References

- [1] Q. Wu, "Review of 20th century floods," *Journal of Catastrophology*, no. 2, pp. 62–69, 2002 (Chinese).
- [2] E. Roulin and S. Vannitsem, "Skill of medium-range hydrological ensemble predictions," *Journal of Hydrometeorology*, vol. 6, no. 5, pp. 729–744, 2005.
- [3] E. Roulin, "Skill and relative economic value of medium-range hydrological ensemble predictions," *Hydrology and Earth System Sciences*, vol. 11, no. 2, pp. 725–737, 2007.
- [4] J. Komma, C. Reszler, G. Blöschl et al., "Ensemble prediction of floods-catchment non-linearity and forecast probabilities," *Natural Hazards Earth System Sciences*, no. 7, pp. 431–444, 2007.
- [5] J. Thielen, J. Bartholmes, M. H. Ramos et al., "The European Flood Alert System-part 1: concept and development," *Hydrology and Earth System Science Discussions*, no. 5, pp. 257–287, 2008.
- [6] F. Pappenberger, J. Bartholmes, J. Thielen, H. L. Cloke, R. Buizza, and A. de Roo, "New dimensions in early flood warning across the globe using grand-ensemble weather predictions," *Geophysical Research Letters*, vol. 35, no. 10, Article ID L10404, 2008.
- [7] Y. He, F. Wetterhall, H. L. Cloke et al., "Tracking the uncertainty in flood alerts driven by grand ensemble weather predictions," *Meteorological Applications*, vol. 16, no. 1, pp. 91–101, 2009.
- [8] Y. He, F. Wetterhall, H. Bao et al., "Ensemble forecasting using TIGGE for the July–September 2008 floods in the Upper Huai catchment: A Case Study," *Atmospheric Science Letters*, vol. 11, no. 2, pp. 132–138, 2010.
- [9] Y. Peng, W. Xu, P. Wang, and F. F. You, "Food forecasting by coupling TIGGE ensemble precipitation forecast," *Journal of Tianjin University*, vol. 48, no. 2, pp. 177–184, 2015 (Chinese).
- [10] H.-J. Bao, L.-N. Zhao, Y. He et al., "Coupling ensemble weather predictions based on TIGGE database with Grid-Xinanjiang model for flood forecast," *Advances in Geosciences*, vol. 29, pp. 61–67, 2011.
- [11] H. Bao and L. Zhao, "Flood forecasting over Huai River catchment based on ensemble forecast," *Journal of Hydraulic Engineering*, vol. 43, no. 2, pp. 216–225, 2012 (Chinese).
- [12] B. Yong, *Development of a land-surface hydrologic model TOPX and its coupling study with regional climate model RIEMS* [Ph.D. thesis], School of Geographic and Oceanic Science, Nanjing University, Nanjing, China, 2008 (Chinese).
- [13] Y. Shao, *Assimilation of doppler radar precipitation with the improved regional climate model RIEMS* [Ph.D. thesis], School of Geographic and Oceanic Science, Nanjing University, Nanjing, China, 2010 (Chinese).
- [14] G.-Y. Niu, Z.-L. Yang, R. E. Dickinson, and L. E. Gulden, "A simple TOPMODEL-based runoff parameterization(SIMTOP) for use in global climate models," *Journal of Geophysical Research Atmospheres*, vol. 110, no. 21, Article ID D21106, 2005.
- [15] R. Zhao, *Hydrologic Models: Xinanjiang Model and Shanbei Model*, Hydraulic and Electric Power Press, Beijing, China, 1984 (Chinese).

Research Article

Radar-Derived Quantitative Precipitation Estimation Based on Precipitation Classification

Lili Yang,^{1,2} Yi Yang,¹ Peng Liu,¹ and Lina Wang²

¹Key Laboratory for Semi-Arid Climate Change of the Ministry of Education, Key Laboratory of Arid Climatic Changing and Reducing Disaster of Gansu Province, College of Atmospheric Sciences, Lanzhou University, Lanzhou 730000, China

²Gansu Province Environmental Monitoring Center, Lanzhou 730020, China

Correspondence should be addressed to Yi Yang; yangyi@lzu.edu.cn

Received 30 June 2016; Accepted 13 October 2016

Academic Editor: Zhe Li

Copyright © 2016 Lili Yang et al. This is an open access article distributed under the Creative Commons Attribution License, which permits unrestricted use, distribution, and reproduction in any medium, provided the original work is properly cited.

A method for improving radar-derived quantitative precipitation estimation is proposed. Tropical vertical profiles of reflectivity (VPRs) are first determined from multiple VPRs. Upon identifying a tropical VPR, the event can be further classified as either tropical-stratiform or tropical-convective rainfall by a fuzzy logic (FL) algorithm. Based on the precipitation-type fields, the reflectivity values are converted into rainfall rate using a Z-R relationship. In order to evaluate the performance of this rainfall classification scheme, three experiments were conducted using three months of data and two study cases. In Experiment I, the Weather Surveillance Radar-1988 Doppler (WSR-88D) default Z-R relationship was applied. In Experiment II, the precipitation regime was separated into convective and stratiform rainfall using the FL algorithm, and corresponding Z-R relationships were used. In Experiment III, the precipitation regime was separated into convective, stratiform, and tropical rainfall, and the corresponding Z-R relationships were applied. The results show that the rainfall rates obtained from all three experiments match closely with the gauge observations, although Experiment II could solve the underestimation, when compared to Experiment I. Experiment III significantly reduced this underestimation and generated the most accurate radar estimates of rain rate among the three experiments.

1. Introduction

Owing to its significant impacts on human activities, precipitation is one of the most important factors in meteorological analysis; accordingly, its study has attracted considerable attention. Quantitative precipitation estimation (QPE) plays a very important role in generating warnings of meteorological, hydrological, and geological disasters. The accuracy of numerical weather predictions can be significantly improved when the precipitation rate is assimilated into the weather prediction models [1, 2]. Currently, precipitation rate data is obtained primarily from rain gauge networks, which can provide real-time rainfall estimates. However, the spatial distribution of rain gauges is sparse in remote regions, particularly in mountainous areas, which can result in insufficient spatial resolution for accurate mapping of the rainfall patterns. Consequently, obtaining QPE products with high spatial and temporal resolution is currently one of the main tasks in conducting hydrometeorological studies [3, 4].

Weather radars, in particular, can provide precipitation estimates with high spatial and temporal resolution over a large area [5]. Radar reflectivity, Z (mm^6/m^3), is related to rainfall rate, R (mm/h), through a variable power law relationship (Z-R relationship), which can be used to obtain QPE products.

Numerous Z-R relationships based on raindrop size distribution observations have been proposed [6–8]. Z-R relationships of the form $Z = AR^B$ can be derived from pairs of Z and R observations, assuming that sufficient corresponding paired Z-R data samples are available. The default WSR-88D Z-R relationship, $Z = 300R^{1.4}$ [9–11], was derived based on summer convective events in Florida, USA. However, this default Z-R relationship cannot fully address the complicated characteristics of rain in, for example, China [12–14]. It is known that different types of precipitation correspond to different raindrop size distributions (DSDs), and precipitation types can also be classified based on the formation mechanism, duration, and internal structure. The precipitation regime can therefore be divided into different rainfall types.

Convective rainfall systems are associated with strong vertical velocity fields, small areal coverage, and high rainfall intensities, and an echo that can be extended to a relatively high altitude and with a high center of mass. Conversely, stratiform rainfall systems have relatively weak vertical velocity fields, great horizontal homogeneity, and low rainfall intensity. Although the intensity of stratiform rainfall is much weaker than that in adjacent convective cells, stratiform rain typically covers a larger area and always contributes with a significant portion (40–50%) of the total rainfall, even in convective-dominant systems [15]. Tropical rain systems generally occur in lower altitudes and very humid air, with condensation occurring continuously throughout the air descent. The main feature of tropical rain systems is that their reflectivity increases monotonically as height decreases, yielding a maximum reflectivity at the lowest levels of the vertical profile of reflectivity (VPR), resulting in considerable error when conducting precipitation estimation using the default Z - R relationship of WSR-88D. Moreover, multiple types of precipitation may coexist within a wide range of rainfall events.

Radar research scientists worldwide have undertaken extensive studies to improve the accuracy of radar QPE [16–23]. Typically, precipitation is first classified into various types, and corresponding multiple Z - R relationships are then used [19, 24–26]. Precipitation can generally be classified into either convective or stratiform regimes, which has been a particular focus of many studies [27–29]. Such basic classifications typically adopt a fixed threshold or set of boundary conditions for rainfall recognition. However, these methods are known to be sensitive to the used threshold values and because there is a considerable overlap between stratiform and convective regimes in many respects, using fixed boundary conditions or thresholds often leads to false positives. Moreover, it is often difficult to directly identify the boundary between stratiform and convective regimes [30]. Yang et al. [30] used the reference values of Steiner et al. [29] to derive a statistical relationship between four characteristic parameters and two rain types, in order to develop the probability distribution of convective and stratiform rainfall based on a fuzzy-logic (FL) algorithm, which was able to improve the accuracy of QPE [31]. Despite efforts such as these, many techniques can still underestimate rainfall to some extent. Based on the stratiform and convective precipitation classification, many researchers have suggested focusing on tropical rain as an avenue to mitigate the underestimation of QPE, and some studies have been able to reduce QPE underestimation by employing an automated radar technique to identify tropical precipitation, in order to divide precipitation into tropical rain and stratiform and convective types [32, 33]. Qi et al. [34] converted reflectivity into precipitation utilizing the tropical rain Z - R relationship instead of the default WSR-88D Z - R relationship, which improved the accuracy to some extent. Similarly, Zhang et al. [35] improved the accuracy of radar-derived QPE by using an automatic identification method to identify tropical, stratiform, and convective precipitation types based on radar observations and model outputs. They then applied various Z - R relationships in order to convert reflectivity into rain rates, based on precipitation types. The

results showed that their method improved the accuracy of radar-derived QPE.

In this study, precipitation is first divided into stratiform and convective precipitation types using the FL algorithms proposed by Yang et al. [30], and then tropical rain is identified based on the VPR characteristics [36, 37], as discussed by Xu et al. [33]. Tropical rainfall is further divided into tropical-stratiform and tropical-convective rainfall, and the respective adaptive Z - R relationships are then applied for QPE. A three-month dataset is used to compare the newly proposed tropical rain identification scheme with the results obtained with the default WSR-88D Z - R relationship and a convective/stratiform rain identification scheme. Section 2 describes the precipitation classification method and the corresponding Z - R relationships and discusses the benefits of precipitation classification. Section 3 illustrates the evaluation results of using long-term datasets using descriptive statistics. Two case studies are also provided in Section 4 to evaluate the performance of the proposed precipitation classification method. Finally, Section 5 presents the main results of the study.

2. Algorithm Description

Underestimation of rainfall can occur when precipitation is divided into general stratiform and convective types. This study aims to improve the accuracy of radar QPE by building upon the convective, stratiform, and tropical precipitation technique described by Xu et al. [33]. The proposed method uses volume scan reflectivity data from a Doppler radar to recognize tropical VPRs, by first dividing rain data into stratiform and convective precipitation (using an FL algorithm) and then classifying tropical rain events as stratiform, convective, or tropical precipitation. Figure 1 shows a flow chart illustrating this process of precipitation classification.

2.1. Identification of Tropical VPRs. This study uses VPRs to identify the potential presence of tropical rain. As a first step, volume scan reflectivity data from Doppler radar are simply classified into assumed stratiform or convective types, based on the vertically integrated liquid (VIL) water content. In particular, the data are classified as belonging to the stratiform type when the VIL value is below 6.5 kg/m^3 [38]; otherwise, they are classified as convective. Stratiform reflectivity observations larger than 10 dBZ from all tilts in an annular region between two predefined ranges, r_1 and r_2 (with the empirical values of 20 and 80 km, resp.), are used to obtain an averaged VPR [39]. The number of data samples within a 20-km radius of the radar is limited, owing to a terrain clearance rule incorporated into a quality control (QC) scheme [40], whereby any radar bin whose bottom is within 50 m of the ground is removed. Furthermore, the region of interest has to be far enough from the radar receiver, to avoid the cone of silence in the receiver's immediate vicinity. The accuracy of precipitation classification is also limited by the decrease in vertical resolution beyond an 80-km radius.

The second step combines the output of the first step with the method of bright band identification proposed by Zhang

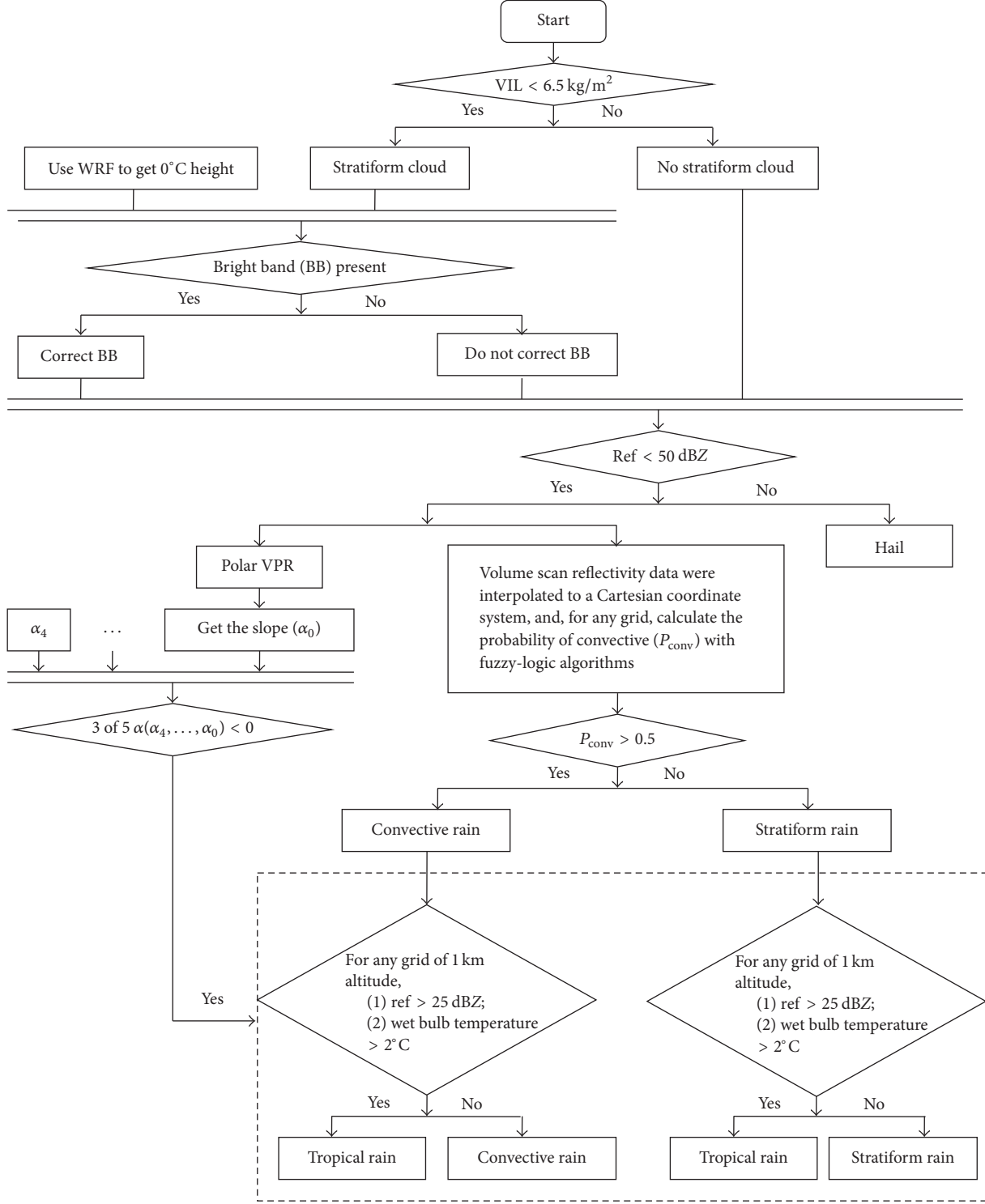


FIGURE 1: Flow chart of the precipitation classification method devised in this study.

et al. [39], to determine whether a bright band is present. The specific method adopted for this step can be summarized as follows:

- (1) The local maximum reflectivity (Z_{peak}) and its height (h_{peak}) in the VPR are found. The search for the

local maximum in the VPR starts at 500 m above the 0°C isotherm altitude ($h_{0^\circ\text{C}}$) obtained from the Weather Research and Forecasting (WRF) model and continues downward. A 500-m cushion is used to account for uncertainties in the model's 0°C height.

- (2) Once the local maximum is found, the height h_{top} (h_{bottom}) above (below) the maximum level at which reflectivity decreases monotonically by a given percentage (default = 10%) [39] of the maximum reflectivity (in dBZ) is determined, along with its corresponding reflectivity Z_{top} (Z_{bottom}).
- (3) If the following three criteria are met, a bright band is considered to exist:

$$\begin{aligned} h_{\text{top}} - h_{\text{bottom}} &\leq D_0, \\ h_{\text{top}} - h_{\text{peak}} &\leq D_1, \\ h_{\text{peak}} - h_{\text{bottom}} &\leq D_1. \end{aligned} \quad (1)$$

The parameters D_0 and D_1 are assumed to be dependent on both the vertical resolution of the reflectivity observations and the radar scan strategy. Here, D_0 and D_1 are set to 1.5 and 1 km, respectively.

- (4) If a bright band exists, its top (BB_t) and bottom (BB_b) heights are defined as follows:

$$\begin{aligned} \text{BB}_t &= \begin{cases} h_{\text{top}}, & h_{\text{top}} - h_{\text{peak}} \leq D_t, \\ h_{\text{peak}} + D_t, & h_{\text{top}} - h_{\text{peak}} > D_t, \end{cases} \\ \text{BB}_b &= \begin{cases} h_{\text{bottom}}, & h_{\text{peak}} - h_{\text{bottom}} \leq D_b, \\ h_{\text{peak}} - D_b, & h_{\text{peak}} - h_{\text{bottom}} > D_b. \end{cases} \end{aligned} \quad (2)$$

Here, D_t and D_b serve as top and bottom caps of the bright band (BB), with default values of 500 and 700 m, respectively [39].

To avoid excessive corrections of the bright band, the height of the local maximum reflectivity is searched again if the minimum reflectivity is lower than a preset threshold (default = 28 dBZ). This height is defined as the lowest height at which the reflectivity is larger than or equal to the threshold [38]. This parameter can sometimes lead to insufficient or excessive bright band correction, an issue that will be solved in the future using observations from a dual-polarization radar [41].

The third step involves the correction of any existing bright bands [42]. If the values of BB_t , BB_b and their corresponding reflectivities (Z_{Bt} and Z_{Bb} , resp.) are valid, $\text{BB}_b < h_{\text{peak}}$, and $\text{BB}_t > h_{\text{peak}}$, and then the slope (S) of reflectivity between BB_t and BB_b is calculated as follows:

$$S = \frac{(Z_{\text{Bt}} - Z_{\text{Bb}})}{(\text{BB}_t - \text{BB}_b)}. \quad (3)$$

If the reflectivity height h_i is located between BB_t and BB_b , the reflectivity is reassigned as

$$Z_i = Z_{\text{Bt}} - S \times (\text{BB}_t - h_i). \quad (4)$$

If BB_t does not exist, the value of BB_b is valid, and $\text{BB}_b < h_{\text{peak}}$, and the reflectivities located above BB_b (with value larger than Z_{Bb}) are reassigned to Z_{Bb} .

The fourth step, which involves reflectivity observations from all tilts in an annular region between 20 and 80 km, involves recalculation of the average stratiform VPR after bright band correction.

The fifth step involves determining whether a tropical VPR has been captured. Following Xu et al. [33], the identification (or diagnosis) of tropical VPR is made with a least-squares fit from the bottom of the bright band to the bottom of the VPR, in cases where a bright band exists; otherwise, the fit is made from $h_{-0^\circ\text{C}}$ to the bottom of the VPR. The slope (α) of the VPR is then calculated. The resulting VPR is considered as tropical if three out of five values of α (for the present and the four previous moments) are lower than or equal to 0; otherwise, it is regarded as a nontropical VPR.

2.2. Convective and Stratiform Rainfall Classification. To improve the accuracy of radar QPE, this study adopted the FL algorithm developed by Yang et al. [30] to classify convective and stratiform rainfall. Brief details of the FL algorithm are given below.

First, the volume scan reflectivity data from the Doppler radar are interpolated to a Cartesian coordinate system with the same latitude and longitude range (0.01°) of the original data. Four features, denoted as F_1 – F_4 , are calculated based on the reflectivity data. These features are, respectively, (a) the reflectivity at 2 km, (b) the reflectivity standard deviation in the horizontal direction, (c) the product of the radar top height and the reflectivity value at 2 km, and (d) the vertically integrated liquid water content [30].

As a second step, membership functions are used to determine the degree to which each feature belongs to each rain type, using a fuzzification process. Linear functions are used as membership functions for convection:

$$\mu_{k,C}(x, a, b) = \begin{cases} 0, & x \leq a, \\ \frac{(x-a)}{(b-a)}, & a < x < b, \\ 1, & x \geq b, \end{cases} \quad (5)$$

$$(k = 1, 2, \dots, N)$$

and stratification:

$$\mu_{k,S}(x, a, b) = \begin{cases} 1, & x \leq a, \\ \frac{(b-x)}{(b-a)}, & a < x < b, \\ 0, & x \geq b, \end{cases} \quad (6)$$

$$(k = 1, 2, \dots, N),$$

where N is the input feature parameter, subscript k is set to 1, 2, 3, or 4, C and S identify the convective and stratiform cases, respectively, x is the feature value, a is the left breaking point, and b is the right breaking point. Different feature parameters are assigned different breaking points. For F_1 , the parameters are set to $a = 20$ dBZ and $b = 45$ dBZ; for F_2 , they are $a = 1$ dBZ and $b = 14$ dBZ; for F_3 , they are $a = 100$ km·dBZ and

$b = 500 \text{ km}\cdot\text{dBZ}$; and, for F_4 , they are $a = 0.5 \text{ kg}/\text{km}^2$ and $b = 5.0 \text{ kg}/\text{km}^2$ [30]. From (5) and (6), it is clear that

$$\mu_{k,S}(x, a, b) = 1 - \mu_{k,C}(x, a, b). \quad (7)$$

Third, the weighted average values of the measurement belonging to each specific class are obtained as follows:

$$P_e = \frac{\left(\sum_{k=1}^N W_k \cdot P_{k,e}\right)}{\left(\sum_{k=1}^N W_k\right)}, \quad (8)$$

where $P_{k,e} = \mu_{k,e}(X_k)$, e identifies the convective or stratiform case, W_k is the weighting factor (with equal weighting assigned in this study for simplicity), N is the number of input feature parameters, and P_c and P_s indicate the weighted average values of the convective and stratiform classes, respectively. As the sum of P_c and P_s is 1, the value of P_c can be used to express classifications for convection in a probabilistic manner. Grid points for which $P_c \geq 0.5$ are classified as convective rainfall; all other grid points are classified as stratiform rainfall.

2.3. Identification of Tropical Rainfall Regions. To improve the accuracy of the radar QPE, tropical rainfall is considered to be present if tropical VPR is present and the grid at 1 km altitude meets the following two criteria [33]: (1) the reflectivity is greater than 25 dBZ and (2) the surface wet bulb temperature is greater than 2°C. The surface wet bulb temperature is calculated as follows:

$$E = 6.11 \times 10^{7.5 \times T_{dc}/(237.7 + T_{dc})}$$

$$W_{Bc} = \frac{(0.00066 \times P \times T_c + 4098 \times E/T_{dc} \times (237.7 + T_{dc})^2)}{(0.00066 \times P + 4089 \times E / (237.7 + T_{dc})^2)}, \quad (9)$$

where T_{dc} is the dew point temperature (in °C), E is the vapor pressure from dew point (in mb), W_{Bc} is the surface wet bulb temperature (in °C), P is the pressure (in mb), and T_c is the air temperature (in °C). The above parameters are simulated using the WRF model or from other data.

In this way, stratiform rainfall is further divided into stratiform and tropical-stratiform rainfall, and convective rainfall is further divided into convective and tropical-convective rainfall.

2.4. Radar QPE Calculation. Three sets of experiments were conducted to test the proposed method. In Experiment I, only the WSR-88D default Z - R relationship ($Z = 300R^{1.4}$) was used. In Experiment II, as the rain type is identified by a FL algorithm, the corresponding Z - R relationships were applied to the rain rate calculation at each grid point. For each grid point, the relationship $Z = 300R^{1.4}$ was applied for the convective rainfall calculation if $P_c \geq 0.5$. Otherwise, the relationship $Z = 200R^{1.6}$ [6] was applied, for stratiform rainfall calculation. In Experiment III, stratiform and convective rainfall in tropical rainfall events were further

divided into stratiform and tropical-stratiform rainfall and convective and tropical-convective rainfall, respectively. The relationships were the same as those used in Experiment II, except that the tropical rainfall relationship $Z = 30.7R^{1.66}$ was adopted (Yadong Wang, personal communication). In an attempt to exclude the impact of nonprecipitation echoes and hail, quality control was conducted prior to precipitation classification. Additionally, reflectivity at 1 km was used to reduce the errors caused by spatial inconsistencies and the effects of bright band measurements not yet properly revised.

2.5. Performance Evaluation. The mean deviation error (BIAS), relative absolute error (RAE) rate, and root mean square error (RMSE) are selected as statistical indicators for quantitatively assessing the quality of radar QPE in the different experiments [43]. The mean deviation error is defined as follows:

$$\text{BIAS} = \frac{1}{n} \sum_{i=1}^n (R_a(i) - R_g(i)), \quad (10)$$

where $R_a(i)$ is the radar QPE of the i th station, $R_g(i)$ is the observed precipitation of the i th site, and n is the total number of samples involved in the performance assessment.

The radar QPE error may be positive or negative; therefore, its mean will not reflect the radar QPE performance. To objectively reflect performance, the mean absolute error rate is used and is defined as follows:

$$\text{RAE} = \frac{\sum_{i=1}^n |R_a(i) - R_g(i)|}{\sum_{i=1}^n R_g(i)} \times 100\%. \quad (11)$$

In addition, downpour and drizzle may coexist during a precipitation process; as the RAE of downpour is larger than that of drizzle, the root mean square error primarily represents the performance of the downpour component of the rainfall:

$$\text{RMSE} = \left(\frac{\sum_{i=1}^n (R_a(i) - R_g(i))^2}{n} \right)^{1/2}. \quad (12)$$

As the above three equations imply, a BIAS closer to 0 corresponds to more similar (in the average) QPE and observed rain types, whereas a smaller RAE corresponds to a higher radar QPE accuracy for the entire precipitation process. Similarly, a smaller RMSE indicates a more accurate radar QPE for the heavy precipitation portion of the process.

3. Long-Term Data Statistics

Many previous studies have shown that extreme precipitation is likely to take place in the Yangtze River–Huaihe River valley, the Yangtze River valley, and on the southeast coast of China, with persistent, heavy rainfall events being more abundant in June and July [44–46]. Tropical rain has been found in these regions, although underestimation occurs when conventional QPE is utilized. We evaluated three months of data obtained from the Yangtze River–Huaihe River valley, in order to assess the degree to which

TABLE 1: Hefei CINRAD radar parameters.

Wavelength	Beam width	Scan mode	Elevation angle	Bin spacing	Obtained data	Time resolution
10 cm	1° half-power beam width	360° azimuthal volume	0.5°–19.5°	250 m for velocity and spectral width; 1000 m for reflectivity	Reflectivity, radial velocity, spectral width	Approximately 6 min

the proposed identification process improves estimation accuracy when compared with analyses conducted using the default WSR-88D Z - R relationship and convective-stratiform precipitation segmentation rain identification scheme. Doppler radar data for this study were taken from the Hefei Doppler radar (117.258° E, 31.867° N, 165.5 m), a Chinese New Generation Radar S-band radar instrument (CINRAD WSR-98D/SA). The WSR-98D/SA is a 10-cm wavelength Doppler radar with a 1° half-power beam width. The data obtained consisted of volume scans of radar reflectivity, radial velocity, and spectrum width collected in a polar coordinate system, at increasing elevation angles. During periods of precipitation, the radar operates in a 360° azimuthal volume scan mode, with the elevation angle increasing from 0.5° to 19.5° and the temporal resolution of the data depending on the operational mode of the radar. Bin spacing is 250 m in the radial direction, with reflectivity values averaged over four bins, to increase the number of independent measurements collected for each recorded value. Accordingly, reflectivity values are recorded at 1-km intervals along the radar beam, whereas velocity parameters are recorded at 250 m intervals. Each volume scan takes approximately 6 min. The radar parameters are shown in Table 1.

3.1. Data and Domain. The data from the Hefei Doppler radar and gauge of Anhui Province were collected from June to August in 2010. The horizontal domain (115.758° E– 118.758° E, 30.367° N– 33.367° N) in this study was a 300×300 km grid centered at the radar with a 1 km horizontal resolution (a 301×301 grid). The vertical domain consisted of 73 layers and had an altitude of 18 km (0.25-km resolution). The center of the horizontal domain is the site of Hefei radar. The domain is shown in Figure 2.

3.2. Statistical Results for Three Months of Data. To compare the estimates obtained with different schemes, some statistical indicators were obtained for the June–August, 2010, period, and are presented in Table 2. As shown, Experiment II performed consistently better than Experiment I, but Experiment III produced the results closest to the observed precipitation and with the greatest precision. It should be mentioned that there is a significant difference between the observed precipitation and the radar estimated rainfall when the intensity of the observed precipitation is less than 2 mm/h; therefore, rainfall with intensity below 2 mm/h was excluded.

The statistical indicators in Table 2 were obtained from all precipitation types; to further understand the particular effects of tropical rain, the statistical indicators specific of tropical rain events that occurred in the June–August, 2010, period are presented in Table 3. In other words, in contrast

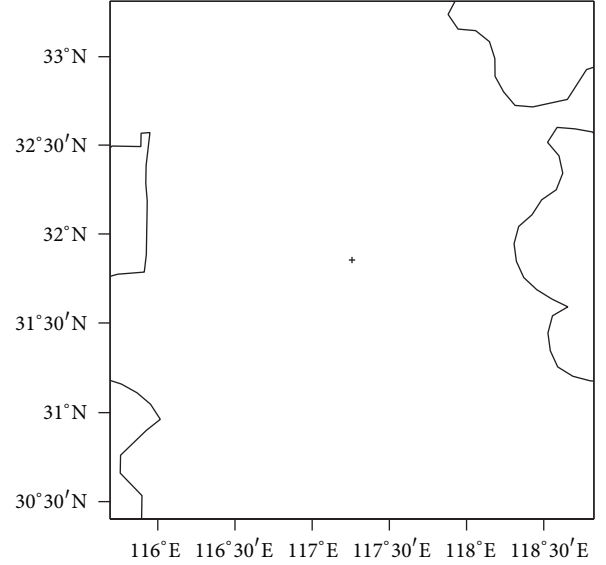


FIGURE 2: Study domain (the “+” represents the Hefei radar location).

TABLE 2: Error analysis of the June–August, 2010, data.

Error	Exp. I	Exp. II	Exp. III
BIAS (mm)	-1.299	-1.124	-0.219
RAE (%)	31.0	28.3	27.1
RMSE (mm)	2.191	2.100	1.877

TABLE 3: Error analysis of stations with tropical rain in the June–August 2010 period.

Error	Exp. I	Exp. II	Exp. III
BIAS (mm)	-1.912	-1.791	0.041
RAE (%)	32.3	31.0	22.7
RMSE (mm)	3.354	3.314	2.327

with Table 2, the statistical indicators in Table 3 do not consider data from grid points not experiencing tropical rainfall. The results in Table 3 match those of Table 2 in that radar QPE is noticeably improved using the FL method proposed here. This improvement becomes even more significant when in the presence of tropical rainfall events.

To further understand the various precipitation events that took place in June–August, 2010, and better describe how QPE is affected under three rainfall conditions (stratiform, convective, and a hybrid precipitation case in which convective and stratiform precipitation are present at the same time), the three-month period was divided into 12 precipitation

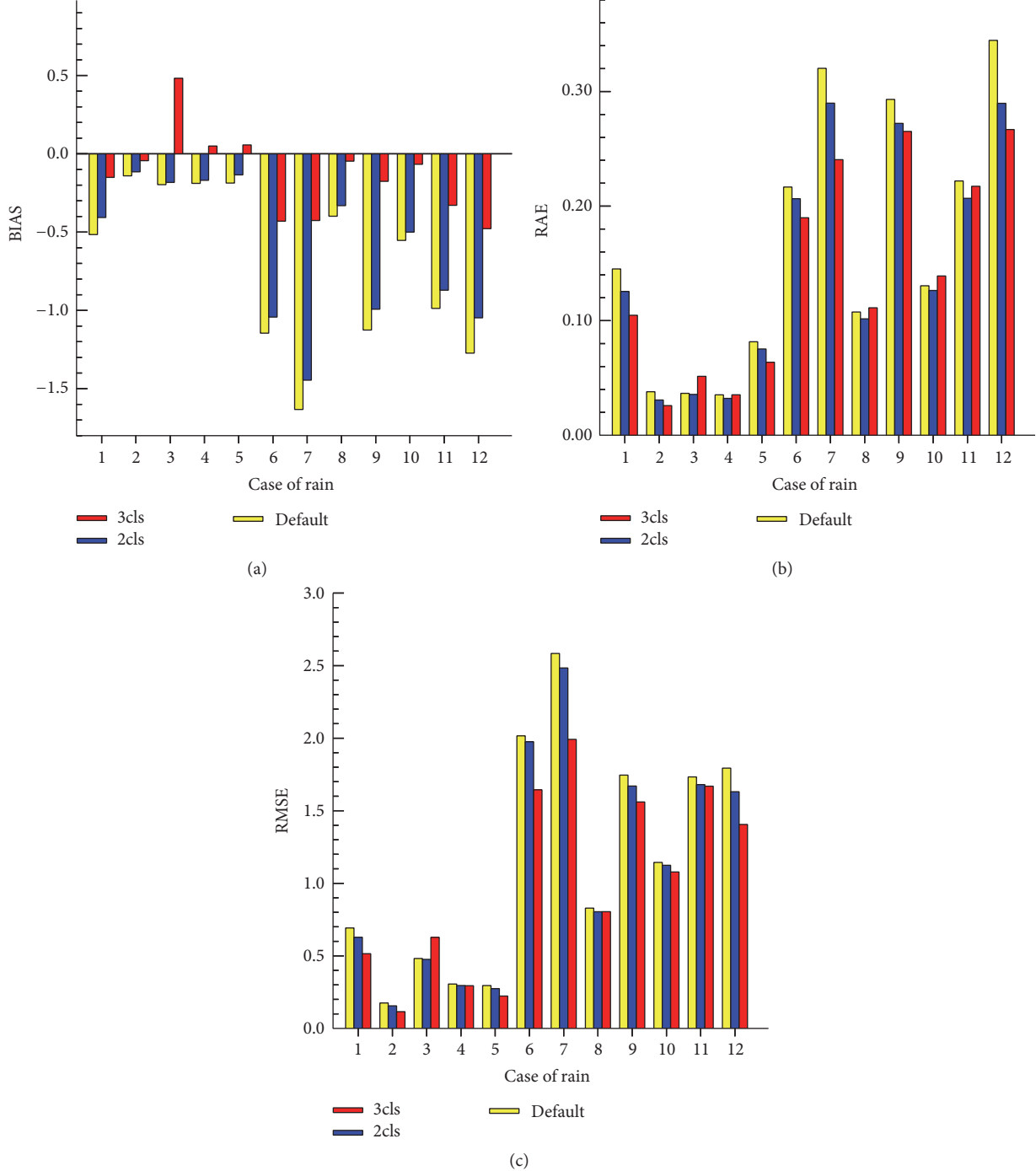


FIGURE 3: Error statistics considering all stations, for each precipitation process. Label “2cls” represents classification in two precipitation classes (Experiment II), and “3cls” represents classification in three precipitation classes (Experiment III). The units of BIAS and RMSE are mm; RAE is dimensionless.

cases (Table 4). The analysis of the several events is shown in Figure 5, which presents the error curves for each case. As shown, Experiment III consistently produced the lowest error values (with the exception of case 3), particularly in cases 1, 6, and 7.

Figure 4 shows the same type of information in Figure 3, but this time considering only tropical rainfall events. Thus, as shown, separating precipitation into convective and

stratiform using the FL algorithm produces better results than simply using the default Z-R relationship, although separating the precipitation into convective, stratiform, and tropical rain produces results even closer to the observed precipitation, not only for the overall precipitation process but also for the heavy precipitation portion only.

In cases 1, 6, and 7, Experiment III produced the best results; however, its results for case 3 are not very good.

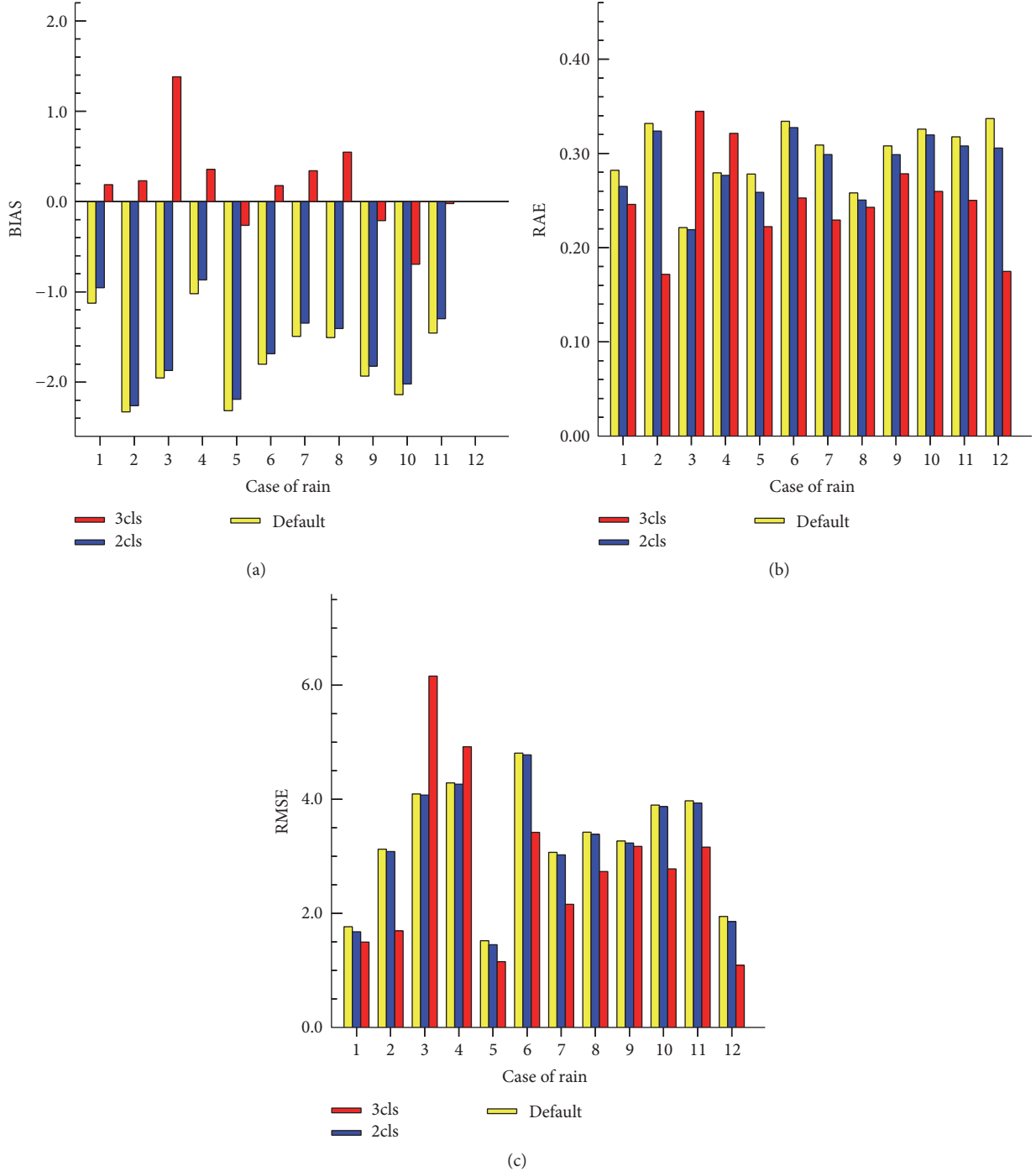


FIGURE 4: Error statistics considering only tropical rain events. Label “2cls” represents classification in two precipitation classes (Experiment II), and “3cls” represents classification in three precipitation classes (Experiment III). The units of BIAS and RMSE are mm; RAE is dimensionless.

These four cases were therefore selected to further study the different results of the three sets of experiments. The corresponding errors for each station are shown in Figure 5, as a function of time; cases 1, 3, 6, and 7 are represented from the top to the bottom row, respectively, and the BIAS, RAE, and RMSE values are represented in columns, from left to right, respectively. It should be noted that these results are

the same ones presented in Figure 3; as shown, in cases 1, 6, and 7, Experiment III not only produced the smallest total errors but also consistently exhibited the lowest errors on an hourly basis. However, the results of Experiment III are not better than those of II or I in case 3. Further analysis revealed that case 3 represents an intermittent rainfall event that was primarily formed by scattered convective cells in

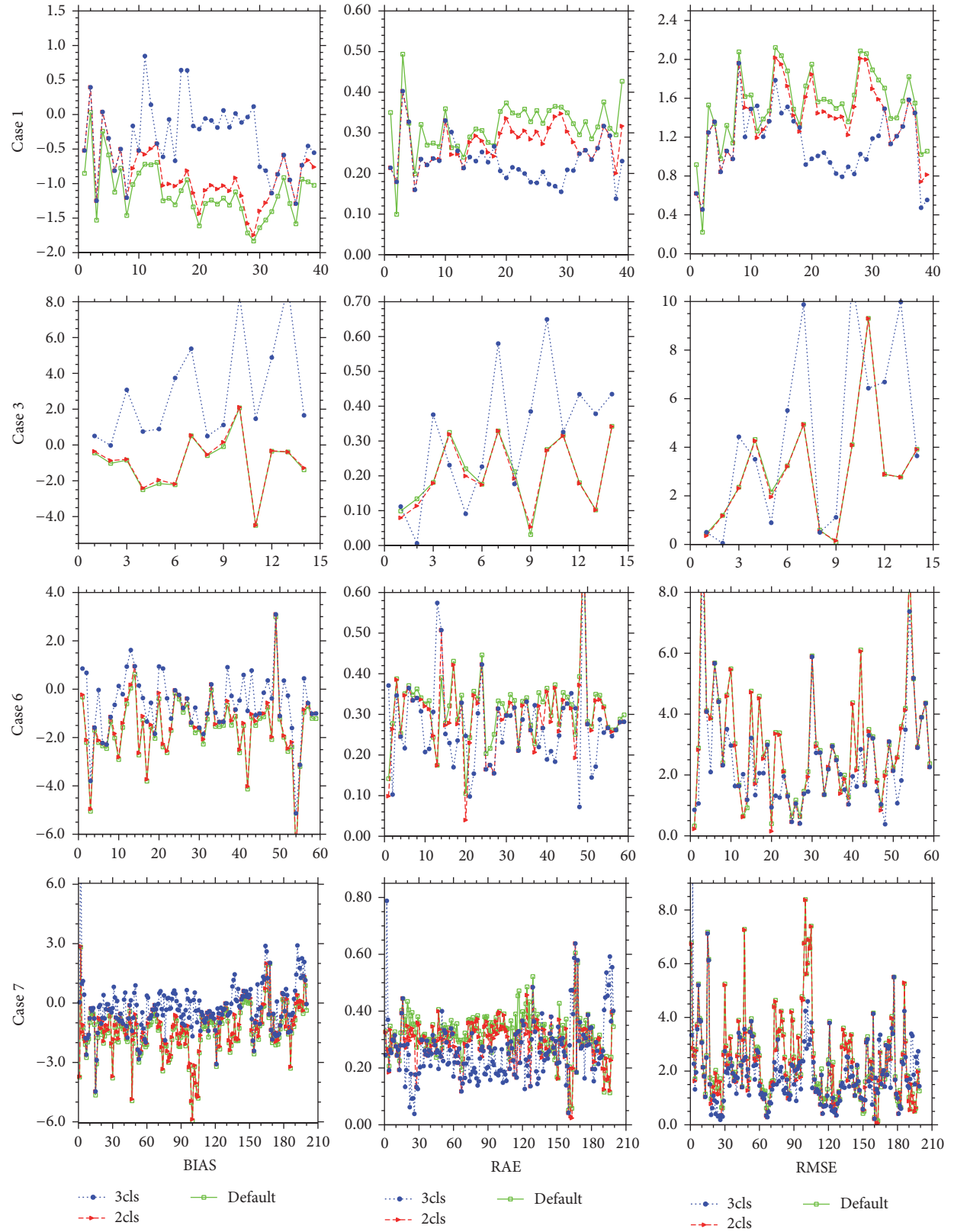


FIGURE 5: Hourly errors for all stations. Cases 1, 3, 6, and 7. The abscissas represent rainfall duration (unit: h).

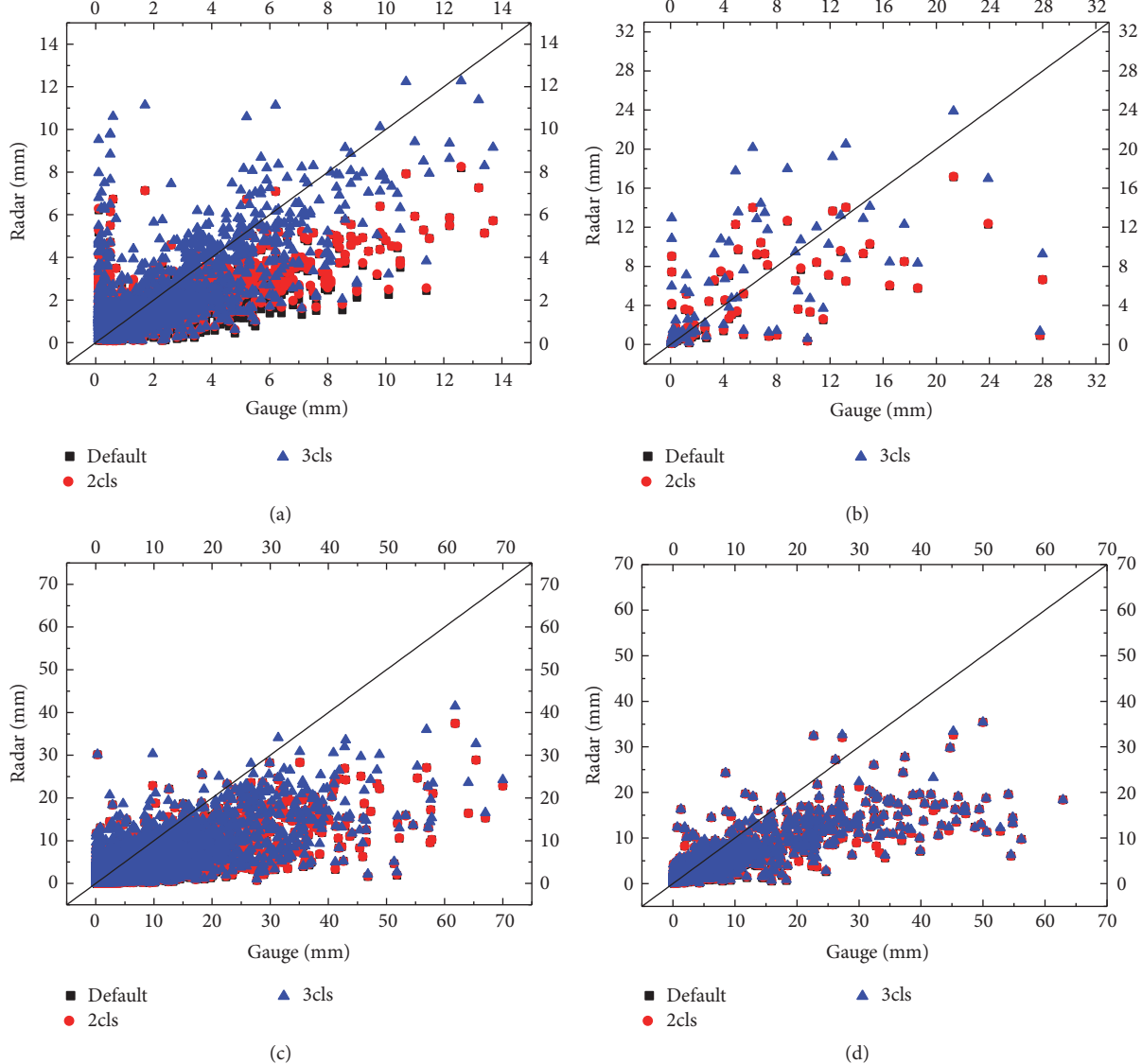


FIGURE 6: Scatter plot of gauge versus radar-derived 6-h accumulated precipitation estimates (case 3 uses 4-h accumulated precipitation values). (a) Case 1. (b) Case 3. (c) Case 6. (d) Case 7. (The diagonal line represents the ideal line, corresponding to an equality between the radar and gauge estimates.)

which either the precipitation ranges or the rainfall durations were scattered, with each rainfall lasting less than 6 h and with limited rainfall per hour. The shortcomings in case 3 may also relate to the selected reflectivity-rainfall rate ($Z-R$) relationships, as these were obtained by statistics related to seasonal climate and geography. Therefore, further work will have to be performed to better capture local real-time dynamic $Z-R$ relationships in the future.

To better understand the differences between gauge measurements and QPE in terms of the amount of precipitation, scatter plots of gauge versus radar-derived 6-h accumulated precipitation estimates except for case 3, for which 4-h accumulated precipitation values are used, because in this case the rainfall lasted less than 6 h are shown in Figure 6. Figure 6(a) shows the results of case 1, in which

the strongest precipitation process intensity is 14 mm/h. It is seen that the precipitation produced by all three experiments corresponds well with observations, in particular the rainfall estimate from Experiment III, and that most of the results approximate the ideal line. In addition, smaller rainfall intensities correspond to bigger errors, particularly at rainfall intensities less than 2 mm/h. Figure 6(b) shows the results for case 3, in which either the precipitation ranges or rainfall durations were scattered. It is clear that the radar-retrieved accumulation precipitation estimations produced in Experiment III mostly improved the problem of underestimation, although overestimation is demonstrated in some stations. Moreover, the results from Experiment II and Experiment I are similar in that convective rainfall precipitation processes are mainly obtained from the FL method classification, a

TABLE 4: Twelve precipitation events selected for performance evaluation.

Event	Precipitation duration	Binary classification	Tropical rain present?
1	June 07–09	Stratiform	Yes
2	June 13–14	Stratiform	Yes
3	June 17–20	Convective	Yes
4	June 23–24	Stratiform	Yes
5	June 27–30	Stratiform	Yes
6	July 02–04	Convective and stratiform	Yes
7	July 06–19	Convective and stratiform	Yes
8	July 21–22	Convective and stratiform	Yes
9	July 24–August 02	Convective and stratiform	Yes
10	August 04–11	Convective and stratiform	Yes
11	August 14–20	Convective and stratiform	Yes
12	August 21–31	Convective and stratiform	Yes

result consistent with Table 4. Figure 6(c) shows the results for case 6, in which the precipitation area is broader and the strongest intensity is 70 mm/h. The correspondence between gauge and QPE improves from Experiment I to Experiment III. Figure 6(d) shows the results for case 7, in which the strongest intensity is 60 mm/h. It is clear that the precipitation for all three experiments corresponds well with observations, especially in the case of Experiment III, which shows a significantly reduced underestimation when compared with Experiments I and II.

4. Case Studies

The cases of heavy rainfall events in Hefei (valid at 0800 UTC, July 22, 2009) and Liuzhou (valid at 1300 UTC, June 12, 2008) were analyzed, to test how easily the proposed method could be applied in different places and times. The Liuzhou Doppler radar (109.456°E, 24.357°N, 346.8 m) is of the same type as the Hefei Doppler radar.

4.1. Heavy Rainfall in Hefei on July 21–23, 2009. Most parts of the Yangtze River–Huaihe River valley and the southern part of the Yangtze River experienced heavy rainfall on July 21–23, 2009 [25], with local downpours of approximately 150 mm of rain. During this period, there was a wide range of precipitation, including heavy rain that was distributed primarily in the north of Anhui Province, with the precipitation intensity reaching 40 mm/h.

The distributions of convective and stratiform rainfall based on the classification of the FL algorithm are shown in Figure 7(a), which shows a rainfall process overall dominated by widespread stratiform rainfall embedded with convective rainfall. A stratiform cloud covering a large area appeared throughout the entire precipitation process and was relatively stable. Only a few parts of Hefei could be identified as convective rainfall regions, embedded in a wide region of stratiform rainfall. The convective rainfall regions changed frequently, and their coverage area was very limited. Thus, the range of estimated precipitation is relatively large.

Although the problem of underestimation is mitigated, to some extent, by classifying the precipitation into convective

and stratiform precipitation, significant differences between observation and estimation remain; the primary objective of classifying precipitation into convective, stratiform, and tropical precipitation is the improvement of QPE accuracy. Figure 7(b) shows the results obtained for the three types of cloud classification. It is clear that some convective and stratiform precipitation obtained from the FL algorithms are again identified as tropical precipitation, with the corresponding cases redefined as a stratiform, convective, or tropical mixed precipitation.

As can be seen from Figure 7(c), the characteristics of the precipitation event in Hefei on July 21–23, 2009, include the presence of a bright band; it was identified as convective and stratiform mixed precipitation using the FL algorithm, and the VPR slope after bright band correction was found to be negative; in other words, tropical rainfall may have been present in this case.

To demonstrate the differences between the three experiments' results, a scatter plot of gauge versus radar-derived 1-h accumulated precipitation is shown in Figure 7(d). Even though all three experiments produce some degree of underestimation, the correspondence between gauge and radar-derived 1-h accumulated precipitation is improved from Experiment I (greatest underestimation) to Experiment III (least underestimation). Thus, Experiment III produces a significantly more accurate estimation of rainfall compared to the other two experiments, particularly when the rainfall intensity is high.

4.2. Liuzhou Rainfall Event during June 11–12, 2008. The primary difference between the Liuzhou precipitation event and the Hefei event is that the Liuzhou precipitation case took place at a different location.

Liuzhou, in the Guangxi Province, received heavy rain at 0800 UTC on June 11, 2008. The 12-h rainfall accumulation from 0400 to 1600 UTC on June 12 reached 233 mm, with heavy rainfall (307 mm) also occurring in Liujiang County. The water level in Liujiang exceeded the warning level of 2.86 m until 1900 UTC on June 12. The heavy rainfall caused waterlogging in some areas and a number of road traffic interruptions until June 13, when the rain began to ease.

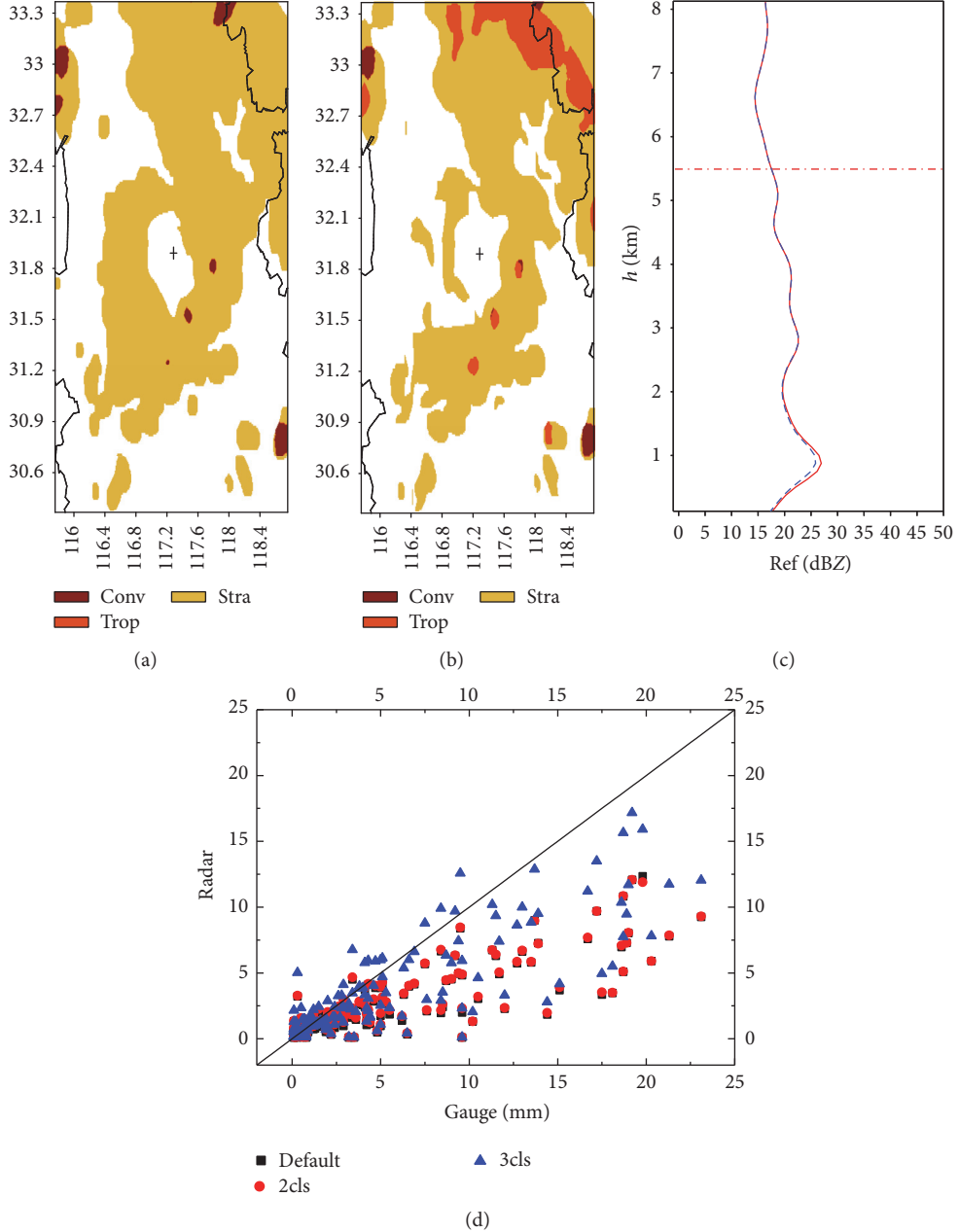


FIGURE 7: Hefei heavy rain (valid at 0800 UTC, July 22, 2009). (a) Results of the FL algorithm (the abscissas represent longitude, the vertical axis represents latitude, the “+” sign represents the radar location, and the colors of “Conv” and “Stra” represent convective and stratiform rainfall regions, resp.). (b) Distribution of the convective, stratiform, and tropical rainfall. (c) Averaged stratiform VPR (the abscissas represent the value of reflectivity in dBZ, the vertical axis represents the altitude in km, the long dashed line is the 0°C isotherm altitude, the red solid line is the VPR before bright band correction, and the blue short dashed line is the VPR after bright band correction). (d) Scatter plot of gauge versus radar-derived 1-h accumulated precipitation (the abscissas represent gauge results in mm, the vertical axis represents radar-derived 1-h accumulated precipitation in mm, and the diagonal line represents the ideal line).

Figure 8 shows an analysis of the heavy rainfall in Liuzhou during June 11-12, 2008, valid at 1300 UTC on June 12. Comparing the 1-h rainfall accumulation from the gauges with the convective and stratiform distribution obtained from the FL algorithm (Figure 8(a)), it is clear that the entire process was based primarily on convective rainfall that did not aggregate but was found in the vicinity of the radar. Heavy rainfall reached 25 mm/h just next to the radar.

The distributions of the three types of rainfall are illustrated in Figure 8(b), which shows that the Liuzhou event was a mixed stratiform, convective, and tropical precipitation case. Most of the convective and stratiform precipitation obtained from the FL algorithm is again distinguishable as tropical rain, although there is some convective precipitation near the radar, which recognized the area as being dominated by convective precipitation.

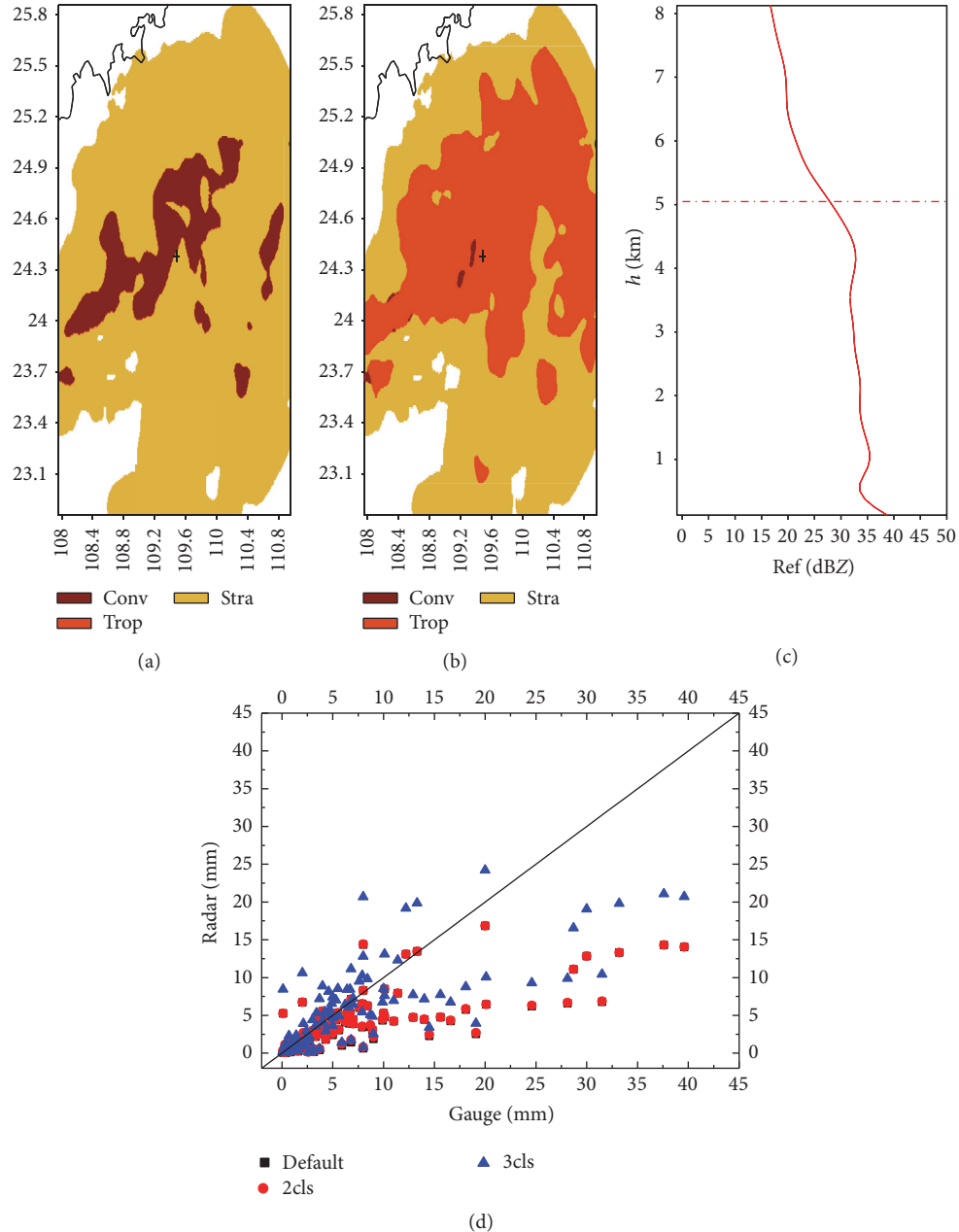


FIGURE 8: Heavy rainfall in Liuzhou during June 11-12, 2008, as recorded at (or analyzed for) 1300 UTC on June 12: (a) results of the FL algorithm (the abscissas represent longitude, the vertical axis represents latitude, the “+” sign represents the radar location, and colors of “Conv” and “Stra” represent convective and stratiform rainfall, resp.). (b) Distribution of convective, stratiform, and tropical rainfall. (c) Averaged stratiform VPR (the abscissas represent the value of reflectivity in dBZ, the vertical axis represents the altitude in km, the long dashed line is the 0°C isotherm altitude, the red solid line is the VPR before bright band correction. (d) Scatter plot of gauge versus radar-derived 1-h accumulated precipitation (the abscissas represent gauge results in mm, the vertical axis represents radar-derived 1-h accumulated precipitation in mm, and the diagonal line represents the ideal line).

As the VPR shown in Figure 8(c) implies, no bright band is observed for this event. The value of $h_{-0^{\circ}\text{C}}$ is 5042.6 m, the VPR slope is negative, and tropical precipitation is possibly present.

For comparison between the three experiments, a scatter plot of gauge versus radar-derived 1-h accumulated precipitation is provided in Figure 8(d). It is clear that the precipitation of all three experiments corresponds well with observations.

Experiment II performs better than Experiment I, and Experiment III performs the best of all, particularly for large rainfall intensity. Thus, the rainfall estimated by Experiment III is found to correspond most closely to the observed rainfall.

5. Conclusions

This paper introduced a method for improving the precision of radar QPE by using an FL algorithm to divide events

into stratiform and convective precipitation types and then further identifying tropical rain based on the VPR characteristics. First, the proposed method corrects any bright bands that are present. Volume scan reflectivity data from Doppler radar are used to recognize tropical VPRs, using the precipitation classification technique of Xu et al. [33]. Volume scan reflectivity data from Doppler radar are then interpolated to the Cartesian coordinate system over the same latitude and longitude range (0.01°), and the rain is divided into stratiform precipitation and convective precipitation using an FL algorithm [30]. The precipitation is then considered to be tropical rainfall if it has a tropical VPR and the grid at an altitude of 1 km meets the following criteria: (1) the reflectivity is greater than 25 dBZ and (2) the surface wet bulb temperature is greater than 2°C . The reflectivity at 1 km is used to assign an adaptive $Z-R$ relationship. Three sets of experiments were presented in this paper. In Experiment I, for each weather event only the default WSR-88D $Z-R$ relationship ($Z = 300R^{1.4}$) was used. In Experiment II, the rain type was identified as convective or stratiform using an FL algorithm; then, the relationships $Z = 300R^{1.4}$ and $Z = 200R^{1.6}$ were applied for convective and stratiform rainfall calculations, respectively. In Experiment III, stratiform and convective rainfall in tropical rainfall events were further divided into stratiform and tropical-stratiform rainfall and convective and tropical-convective rainfall, respectively. The relationships adopted were the same as those used in Experiment II, except that the tropical rainfall relationship was $Z = 30.7R^{1.66}$. A long sequence (three months) of data and two additional study cases were conducted, in order to determine the impact on QPE of the method devised for this study. The conclusions of the study can be summarized as follows:

- (1) Although most radar QPEs were lower than the directly observed precipitation for all the rainfall events analyzed in this study, the results of all three experiments corresponded closely to the observed precipitation. Separating the precipitation into convective and stratiform types using the FL algorithm enabled better performances compared to simply using the default $Z-R$ relationship. Separating the precipitation into convective, stratiform, and tropical rain produced results that were the closest to the observed precipitation, not only during the whole precipitation processes but also individually within the heavy precipitation portions of these events.
- (2) Given that a large-scale precipitation event usually contains multiple types of precipitation, large estimation errors can be introduced if a single $Z-R$ relationship is used for the entire process. The FL algorithm used here can skillfully separate convective precipitation from stratiform precipitation and thus improve the accuracy of radar QPE to some extent. Nevertheless, the problem of underestimation remains. This study built upon the characteristics of tropical precipitation and the convective, stratiform precipitation classification techniques using an FL algorithm; the resulting method was shown to have

improved accuracy, not only during the whole precipitation processes but also individually within the heavy precipitation portions of these events.

- (3) The proposed tropical rain identification scheme produced similar results when applied to the cases of heavy rainfall in Hefei (valid at 0800 UTC on July 22, 2009) and in Liuzhou (valid at 1300 UTC on June 12, 2008). In future work, the newly proposed scheme will be further tested, to evaluate its general applicability to different times and locations.

Competing Interests

The authors declare that there is no conflict of interests regarding the publication of this paper.

Acknowledgments

This research was supported by the National Science Foundation of China (nos. 41175092 and 41375109).

References

- [1] K. P. Georgakatos, "Covariance propagation and updating in the context of real-time radar data assimilation by quantitative precipitation forecast models," *Journal of Hydrology*, vol. 239, no. 1–4, pp. 115–129, 2000.
- [2] Z. Pu and W.-K. Tao, "Mesoscale assimilation of TMI rainfall data with 4DVAR: sensitivity studies," *Journal of the Meteorological Society of Japan*, vol. 82, no. 5, pp. 1389–1397, 2004.
- [3] C. S. Gardner and W. Yang, "Operational C-band dual-polarization radar QPE for the subtropical complex terrain of Taiwan," *Advances in Meteorology*, no. 11, pp. 1–15, 2016.
- [4] M. Gocic, S. Shamshirband, Z. Razak, D. Petković, S. Ch, and S. Trajkovic, "Long-term precipitation analysis and estimation of precipitation concentration index using three support vector machine method," *Advances in Meteorology*, vol. 2016, Article ID 7912357, 11 pages, 2016.
- [5] J. Kalogiros, M. Anagnostou, F. S. Marzano et al., "Mobile radar network measurements for flood applications during the field Campaign of HydroRad Project," in *Advances in Meteorology, Climatology and Atmospheric Physics*, pp. 137–143, Springer, 2013.
- [6] J. S. Marshall and W. M. K. Palmer, "The distribution of raindrops with size," *Journal of the Atmospheric Sciences*, vol. 5, no. 4, pp. 165–166, 1948.
- [7] D. P. Jorgensen and P. T. Willis, "A $Z-R$ relationship for hurricanes," *Journal of Applied Meteorology*, vol. 21, no. 3, pp. 356–366, 1982.
- [8] P. Tabary, A.-A. Boumahmoud, H. Andrieu et al., "Evaluation of two 'integrated' polarimetric Quantitative Precipitation Estimation (QPE) algorithms at C-band," *Journal of Hydrology*, vol. 405, no. 3–4, pp. 248–260, 2011.
- [9] S. M. Hunter, "WSR-88D radar rainfall estimation: capabilities, limitations and potential improvements," *National Weather Digest*, vol. 20, no. 4, pp. 26–38, 1996.
- [10] C. W. Ulbrich and L. G. Lee, "Rainfall measurement error by WSR-88D radars due to variations in $Z-R$ law parameters and the radar constant," *Journal of Atmospheric and Oceanic Technology*, vol. 16, no. 8, pp. 1017–1024, 1999.

- [11] B. E. Vieux and P. B. Bedient, "Estimation of rainfall for flood prediction from WSR-88D reflectivity: a case study, 17–18 October 1994," *Weather and Forecasting*, vol. 13, no. 2, pp. 407–415, 1998.
- [12] F. Tian, M. Cheng, Y. Zhang et al., "An investigation into the effect of rain gauge density on estimating the areal rainfall using a radar-gauge calibration algorithm," *Acta Meteorological Sinica*, vol. 68, no. 5, pp. 717–730, 2010.
- [13] X. Wei, *Research on self-adaptive optimized algorithm for radar quantificationally estimating precipitation [Ph.D. dissertation]*, Nanjing University of Information Science & Technology, 2015.
- [14] Q. Zeng, H. He, Y. Zhang et al., "Parameterizations for the raindrop size distribution and its application in radar rainfall estimation," *Meteorology and Disaster Reduction Research*, vol. 38, no. 4, pp. 46–53, 2015.
- [15] E. N. Anagnostou, "A convective/stratiform precipitation classification algorithm for volume scanning weather radar observations," *Meteorological Applications*, vol. 11, no. 4, pp. 291–300, 2004.
- [16] J. Gao and D. J. Stensrud, "Assimilation of reflectivity data in a convective-scale, cycled 3DVAR framework with hydrometeor classification," *Journal of the Atmospheric Sciences*, vol. 69, no. 3, pp. 1054–1065, 2012.
- [17] M. Xue, F. Kong, K. W. Thomas et al., "Prediction of convective storms at convection-resolving 1 km resolution over continental united states with radar data assimilation: an example case of 26 May 2008 and precipitation forecasts from spring 2009," *Advances in Meteorology*, vol. 2013, Article ID 259052, 9 pages, 2013.
- [18] J. Sun, "Convective-scale assimilation of radar data: progress and challenges," *Quarterly Journal of the Royal Meteorological Society*, vol. 131, no. 613, pp. 3439–3463, 2006.
- [19] Y. Qi, J. Zhang, and P. Zhang, "A real-time automated convective and stratiform precipitation segregation algorithm in native radar coordinates," *Quarterly Journal of the Royal Meteorological Society*, vol. 139, no. 677, pp. 2233–2240, 2013.
- [20] Y. Qi, J. Zhang, Q. Cao, Y. Hong, and X.-M. Hu, "Correction of radar QPE errors for nonuniform VPRs in mesoscale convective systems using TRMM observations," *Journal of Hydrometeorology*, vol. 14, no. 5, pp. 1672–1682, 2013.
- [21] Y. Qi and J. Zhang, "Correction of radar QPE errors associated with low and partially observed brightband layers," *Journal of Hydrometeorology*, vol. 14, no. 6, pp. 1933–1943, 2013.
- [22] Y. Qi, J. Zhang, B. Kaney, C. Langston, and K. Howard, "Improving WSR-88D radar QPE for orographic precipitation using profiler observations," *Journal of Hydrometeorology*, vol. 15, no. 3, pp. 1135–1151, 2014.
- [23] J. Zhang, K. Howard, C. Langston et al., "Multi-Radar Multi-Sensor (MRMS) quantitative precipitation estimation: initial operating capabilities," *Bulletin of the American Meteorological Society*, vol. 97, no. 4, pp. 621–638, 2016.
- [24] S. Chumchean, A. Seed, and A. Sharma, "An operational approach for classifying storms in real-time radar rainfall estimation," *Journal of Hydrology*, vol. 363, no. 1–4, pp. 1–17, 2008.
- [25] P. P. Mapiam and N. Sriwongsitanon, "Climatological Z-R relationship for radar rainfall estimation in the upper Ping river basin," *ScienceAsia*, vol. 34, no. 2, pp. 215–222, 2008.
- [26] T. N. Rao, D. N. Rao, K. Mohan, and S. Raghavan, "Classification of tropical precipitating systems and associated Z-R, relationships," *Journal of Geophysical Research Atmospheres*, vol. 106, no. 16, pp. 17699–17711, 2001.
- [27] M. I. Biggerstaff and S. A. Listema, "An improved scheme for convective/stratiform echo classification using radar reflectivity," *Journal of Applied Meteorology*, vol. 39, no. 12, pp. 2129–2150, 2000.
- [28] D. D. Churchill and R. A. Houze Jr., "Development and structure of winter monsoon cloud clusters on 10 December 1978," *Journal of the Atmospheric Sciences*, vol. 41, no. 6, pp. 933–960, 1984.
- [29] M. Steiner, R. A. Houze, and S. E. Yuter, "Climatological characterization of three-dimensional storm structure from operational radar and rain gauge data," *Journal of Applied Meteorology*, vol. 34, no. 9, pp. 1978–2007, 1995.
- [30] Y. Yang, X. Chen, and Y. Qi, "Classification of convective/stratiform echoes in radar reflectivity observations using a fuzzy logic algorithm," *Journal of Geophysical Research Atmospheres*, vol. 118, no. 4, pp. 1896–1905, 2013.
- [31] L. L. Yang, Y. Yang, Y. C. Qi, X. X. Qiu, and Z. Q. Gong, "A case study of radar-derived quantitative precipitation estimation," *Advanced Materials Research*, vol. 726–731, pp. 4541–4546, 2013.
- [32] B. Wang, J. Zhang, W. Xia et al., "Analysis of radar and gauge rainfall during the warm season in Oklahoma," in *Proceedings of the 22nd Conference on Hydrology*, New Orleans, La, USA, 2008.
- [33] X. Xu, K. Howard, and J. Zhang, "An automated radar technique for the identification of tropical precipitation," *Journal of Hydrometeorology*, vol. 9, no. 5, pp. 885–902, 2008.
- [34] Y. Qi, J. Min, J. Zhang et al., "Study of radar quantitative precipitation estimation in summer of the Yangtze River-Huaihe River valley," in *Proceedings of the 27th Annual Meeting of Chinese Meteorological Society on Practice of Radar Technology Development and Application*, 2010.
- [35] L. Zhang, L. Chu, F. Ye et al., "The automatic identification of rainfall type by using radar data," *Transactions of Atmospheric Sciences*, vol. 35, no. 1, pp. 95–102, 2012.
- [36] Q. Cao, Y. Hong, J. J. Gourley et al., "Statistical and physical analysis of the vertical structure of precipitation in the mountainous west region of the united states using 11+ years of spaceborne observations from TRMM precipitation radar," *Journal of Applied Meteorology and Climatology*, vol. 52, no. 2, pp. 408–424, 2013.
- [37] Q. Cao and Y. Qi, "The variability of vertical structure of precipitation in Huaihe River Basin of China: implications from long-term spaceborne observations with TRMM precipitation radar," *Water Resources Research*, vol. 50, no. 5, pp. 3690–3705, 2014.
- [38] J. Zhang and Y. Qi, "A real-time algorithm for the correction of brightband effects in radar-derived QPE," *Journal of Hydrometeorology*, vol. 11, no. 5, pp. 1157–1171, 2010.
- [39] J. Zhang, C. Langston, and K. Howard, "Brightband identification based on vertical profiles of reflectivity from the WSR-88D," *Journal of Atmospheric & Oceanic Technology*, vol. 25, no. 10, pp. 1859–1872, 2008.
- [40] L. Tang, J. Zhang, C. Langston, J. Krause, K. Howard, and V. Lakshmanan, "A physically based precipitation-nonprecipitation radar echo classifier using polarimetric and environmental data in a real-time national system," *Weather and Forecasting*, vol. 29, no. 5, pp. 1106–1119, 2014.
- [41] Y. Qi, J. Zhang, P. Zhang, and Q. Cao, "VPR correction of bright band effects in radar QPEs using polarimetric radar observations," *Journal of Geophysical Research Atmospheres*, vol. 118, no. 9, pp. 3627–3633, 2013.

- [42] Y. Xiao, L. Liu, Z. Li et al., "Automatic recognition and removal of the bright band using radar reflectivity data," *Plateau Meteorology*, vol. 29, no. 1, pp. 197–205, 2010.
- [43] X. Gao, J. Liang, and C. Li, "Radar quantitative precipitation estimation techniques and effect evaluation," *Journal of Tropical Meteorology*, vol. 28, no. 1, pp. 77–88, 2012.
- [44] Y. Tang, J. Gan, L. Zhao, and K. Gao, "On the climatology of persistent heavy rainfall events in China," *Advances in Atmospheric Sciences*, vol. 23, no. 5, pp. 678–692, 2006.
- [45] Q. Zhang, C. Liu, C.-Y. Xu, Y. Xu, and T. Jiang, "Observed trends of annual maximum water level and streamflow during past 130 years in the Yangtze River basin, China," *Journal of Hydrology*, vol. 324, no. 1–4, pp. 255–265, 2006.
- [46] Q. Zhang, C.-Y. Xu, Z. Zhang, Y. D. Chen, C.-L. Liu, and H. Lin, "Spatial and temporal variability of precipitation maxima during 1960–2005 in the Yangtze River basin and possible association with large-scale circulation," *Journal of Hydrology*, vol. 353, no. 3–4, pp. 215–227, 2008.

Research Article

Mesoscale and Local Scale Evaluations of Quantitative Precipitation Estimates by Weather Radar Products during a Heavy Rainfall Event

Basile Pauthier,¹ Benjamin Bois,¹ Thierry Castel,¹ D. Thévenin,² Carmela Chateau Smith,³ and Yves Richard¹

¹*Centre de Recherche de Climatologie, Biogéosciences UMR 6282 CNRS, Université Bourgogne Franche-Comté, 6 bd Gabriel, 21000 Dijon, France*

²*Météo-France Direction Régionale Centre-Est, 22 rue Louis de Broglie, 21000 Dijon, France*

³*UFR SVTE, Université Bourgogne Franche-Comté, 6 bd Gabriel, 21000 Dijon, France*

Correspondence should be addressed to Basile Pauthier; basile.pauthier@u-bourgogne.fr

Received 8 June 2016; Revised 9 September 2016; Accepted 19 September 2016

Academic Editor: Bin Yong

Copyright © 2016 Basile Pauthier et al. This is an open access article distributed under the Creative Commons Attribution License, which permits unrestricted use, distribution, and reproduction in any medium, provided the original work is properly cited.

A 24-hour heavy rainfall event occurred in northeastern France from November 3 to 4, 2014. The accuracy of the quantitative precipitation estimation (QPE) by PANTHERE and ANTILOPE radar-based gridded products during this particular event, is examined at both mesoscale and local scale, in comparison with two reference rain-gauge networks. Mesoscale accuracy was assessed for the total rainfall accumulated during the 24-hour event, using the Météo France operational rain-gauge network. Local scale accuracy was assessed for both total event rainfall and hourly rainfall accumulations, using the recently developed HydraVitis high-resolution rain gauge network Evaluation shows that (1) PANTHERE radar-based QPE underestimates rainfall fields at mesoscale and local scale; (2) both PANTHERE and ANTILOPE successfully reproduced the spatial variability of rainfall at local scale; (3) PANTHERE underestimates can be significantly improved at local scale by merging these data with rain gauge data interpolation (i.e., ANTILOPE). This study provides a preliminary evaluation of radar-based QPE at local scale, suggesting that merged products are invaluable for applications at very high resolution. The results obtained underline the importance of using high-density rain-gauge networks to obtain information at high spatial and temporal resolution, for better understanding of local rainfall variation, to calibrate remotely sensed rainfall products.

1. Introduction

Accurate Quantitative Precipitation Estimation (QPE) is necessary at various spatial and temporal scales [1, 2]. Heavy rainfall events are expected to increase during the twenty-first century [3]. Better monitoring and prediction of such events and their consequences are of primary importance for hydrology (the hydrological rainfall-runoff relationship during flash floods [4–8]), particularly in mountainous regions [9, 10], for sustainable agriculture [11], and for urban planning [12–16]. National meteorological networks are generally not dense enough to fully document local scale rainfall estimates.

New-generation high-resolution weather radar systems offer opportunities to detect heavy rainfall events with applications for many domains, such as nowcasting, climatology, hydrology, and agriculture [17]. During the last decade, various countries have deployed a number of major technological evolutions (e.g., Doppler and dual-polarization), in addition to the densification of their radar networks (e.g., ARAMIS in France or NEXRAD in the USA). All radar-based rainfall estimates share the same basic physical principles (see pioneering work by Marshall et al. in 1947 [18]), thus requiring correction and calibration, which remains a challenging issue [19, 20]. Rainfall rate (R) is estimated

using the conventional $Z-R$ relationship. The coefficients of the $Z-R$ relationship [18, 21–24] are related to the drop-size distribution (DSD).

Despite the use of the dual-polarization technique, signal attenuation during heavy rainfall may induce underestimation, especially for X- and C-band radar, the radars most frequently used in France [25, 26]. To prevent excessive underestimation, it is necessary to integrate rain gauge measurements for attenuation correction and empirical adjustment [17, 27–30].

The potential value of new-generation high-resolution weather radar systems for QPE has been evaluated and used in recent studies [2, 31–34]. Despite encouraging results for rainfall estimation and its application at mesoscale (10–500 km [35]), the quality of radar rainfall estimates may vary greatly, in relation to (1) the coefficient applied for attenuation correction, that is, calibration of the changing $Z-R$ relationship; (2) the location and size of heavy rainfall events; (3) the density of the rain gauge network used to compute the single-bias adjustment factor and to generate products merging radar rainfall with interpolated rain gauge data. With regard to attenuation correction, a new polarimetric processing chain provides improved rainfall estimates (e.g., [32]).

Rainfall event characteristics and network density must both be taken into account in rainfall estimates [36]. The location and size of rainfall events at mesoscale, together with bias adjustment factors and merged product construction, are usually based on data from mesoscale national rain gauge networks. Radar-based QPE has generally been evaluated using networks of similar density (e.g., [34, 37]), but few robust estimates exist at local scale (0.1 m–50 km [35]). Rain gauges are generally not deployed in sufficient density on hilly terrain or in remote locations. The HydraVitis rain gauge network, recently installed in Burgundy, northeastern France (45 rain gauges over 28 km² [38]), was designed to capture the spatiotemporal variability of rainfall, particularly the contrasted patterns that may arise at local scale over a complex terrain during heavy rainfall episodes. The density of the HydraVitis network thus provides the opportunity to assess the capability of radar products to document a heavy rainfall event at local scale [39]. In this study, HydraVitis is therefore taken as reference for the capture of rainfall at local scale.

The main aim is to assess the quality of QPE in PANTHERE and ANTILOPE radar-based products, during a heavy rainfall event. First, total rainfall for the 24-hour event was assessed at both mesoscale and local scale. The second analysis focuses on hourly, local scale rainfall patterns.

In the following sections, the heavy rainfall event occurring on November 3 to 4, 2014, is presented, and the two reference rain gauge network datasets (Météo France and HydraVitis) are described. The main characteristics of the radar products are explained, as is the method for comparing point and gridded products. Finally, the ability of radar products to capture the spatiotemporal variability of the rainfall event is evaluated.

2. The Study Event and the Reference Rain Gauge Networks Specifications

This case study is a 24-hour rainfall event, from 9.00 pm on November 3 to 8.00 pm on November 4, 2014. An unstable rainy disturbance was moving slowly southeastward across France, generating strong rainfall accumulations along axis oriented SSW/NNE [40]. Rainfall data for this event were collected at both mesoscale (150 km radius) and local scale (28 km²). The interest of this particular event is that the rainy front presented both stratiform and convective particularities [40]. This exceptional event generated the equivalent of a month of rainfall in 24 hours, with accumulations ranging from 70 to 110 mm [41]. Many floods resulted from this event and a state of natural disaster was recognized for 40 towns in the Saône-et-Loire administrative area (“département” in French).

The event of November 3 to 4, 2014, is an interesting case study for high-resolution radar product evaluation because of (1) its nature (both stratiform and convective), making adjustment of the $Z-R$ relationship challenging; (2) its strong accumulations, which may attenuate the beam; (3) its local spatial variability, which cannot be captured by the low-density national rain gauge network; and (4) its consequences for hydrometeorological, urban, and agricultural questions.

To analyze this event, two rain gauge networks are used. The first is a subset of the national Météo France network, an operational network composed of SPIEA direct reading and automatic tipping-bucket rain gauges. We extracted data collected by 122 Météo France stations, located up to 150 km away from the centroid of the HydraVitis network, to form the subset used in this study, the Météo France rain gauge network (MFRN; Figure 1(a)). The average distance from an MFRN gauge to its nearest neighbor is 14.4 km. One of these rain gauges is located within the study area covered by the high-resolution HydraVitis network.

The second network, HydraVitis, is composed of 45 tipping-bucket rain gauges (RAINEW 111, RainWise® Inc.), covering an area of 28 km² (Figure 1(b)). Based on Humphrey et al. [42], rain gauge average measurement error ranged from 0.6% to 4.2%, from the lowest (2 mm) to the highest (200 mm) rainfall intensity [38].

The gauge implementation was based on Météo France recommendations, deployed at a minimum distance of four times the height of the nearest obstacle. Each gauge was linked to a Hobo Pendant UA-002-64 event temperature logger (Onset® Corp.). This device records rainfall data every second, with a 0.258 mm resolution. In order to evaluate measurement uncertainty, four gauges were deployed in pairs less than three meters apart. Network implementation and control are detailed in Pauthier et al. [38]. The average distance to the nearest neighboring gauge is 512 m. Figure 2 indicates the main exposure and slope of the study area and the distribution of rain gauge exposure and slope, showing that the HydraVitis rain gauges cover the main terrain features of the study area. Hourly rainfall amounts were calculated for each rain gauge, as density of the HydraVitis network corresponds to the density recommended in Villarini et al. in 2008 [39].

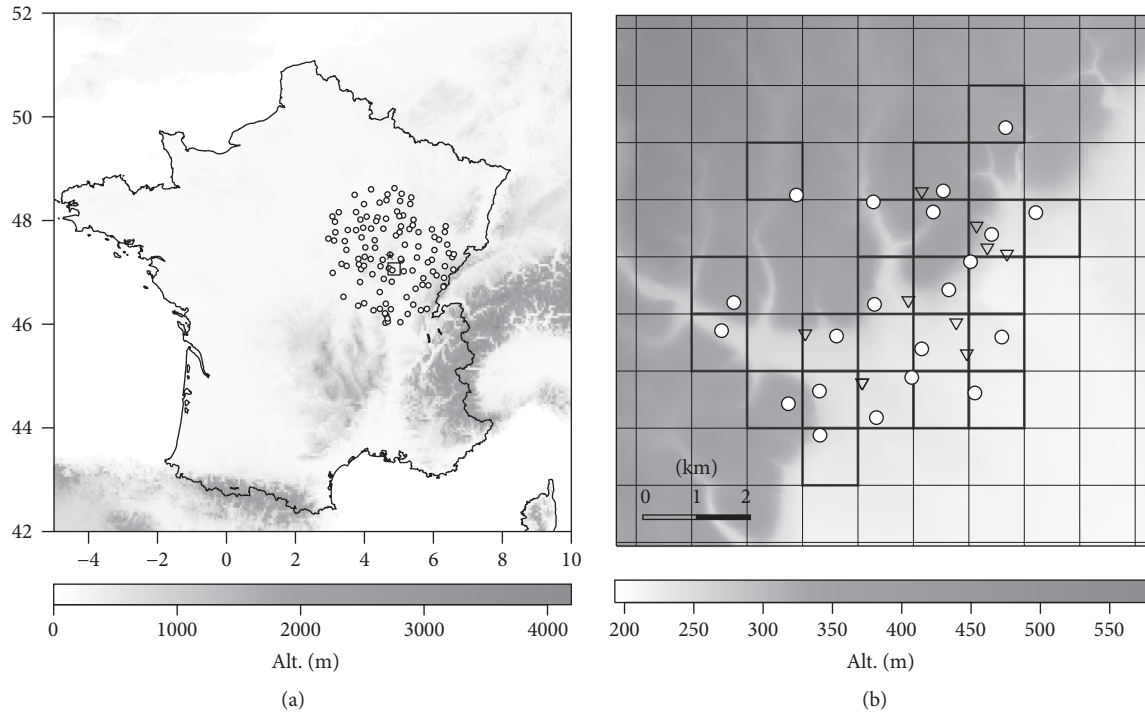


FIGURE 1: The mesoscale and local scale rain gauge network. (a) The star indicates the radar position. Small circles indicate the location of MFRN rain gauges located less than 150 km from the radar. The square indicates the position of the HydraVitis network. (b) White circles indicate the location of the rain gauges providing the HydraVitis data used in this study. The bold gridlines show the boundaries of the 1 km² radar pixels in which a rain gauge was available for comparison.

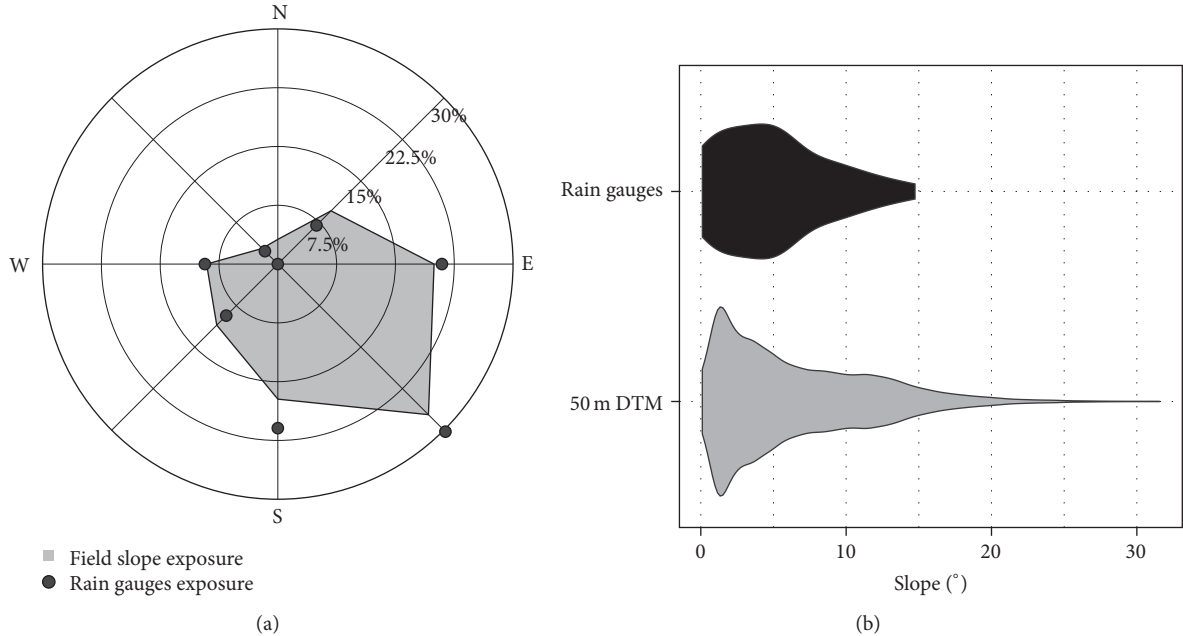


FIGURE 2: (a) Field slope exposure (grey surface) and rain gauge exposure (dark grey points). (b) Slope distribution over the study area. The black zone represents the distribution of HydraVitis rain gauges in relation to topography. The grey zone represents slope distribution for 50 m DTM.

3. Radar-Based Products: PANTHERE and ANTILOPE

Two main products derived from weather radar systems are available in France for the monitoring and estimation of rainfall events. The PANTHERE product includes several postprocessing steps aimed at correcting for ground clutter, partial beam blocking, Vertical Profile of Reflectivity (VPR) effects, and synchronisation of radar measurements (see [37] for a full description of the radar processing procedure). In this study, PANTHERE was applied to data collected by the closest radar system, located 31 km north of the HydraVitis network (Figure 1(a), Blaisy-Haut, 47.355278°N 4.775833°E). This radar is equipped with a dual-polarized C-band antenna. Over the study area, the radar signal benefits from low beam blocking at 0.5° (the maximum beam blockage is systematically under 5%).

The PANTHERE product has a 1km² resolution and is computed to provide 5-minute time step rainfall fields. In this study, PANTHERE data were aggregated with an hourly time step.

In order to overcome any difficulty in inferring realistic rainfall amounts, particularly in convective situations, a composite product merging radar-based and rain gauge rainfall is also available. It adjusts PANTHERE estimates by means of *post hoc* integration of kriged data from the Météo France rain gauge network. This corrected product, recently developed by Météo France, is called ANTILOPE [43, 44]. The ANTILOPE data are available at the same time step and spatial resolution as PANTHERE and were also aggregated at an hourly time step in this study.

4. Method for Comparing Networks and Gridded Products

The PANTHERE and ANTILOPE radar products (pixel grids) were compared with the MFRN and HydraVitis rain gauge networks (points) at two different scales. For mesoscale comparison, the 122 MFRN 24-hour cumulated rainfall measurement points were individually compared to the relevant PANTHERE QPE grid-pixel (Figure 1(a)). As ANTILOPE is partly composed of spatialized MFRN data, this comparison was only conducted on the PANTHERE data to avoid interdataset dependency.

Local scale comparison was based on HydraVitis data. Only one rain gauge measurement point was used for a given grid-pixel; the nearest rain gauge to the pixel center was systematically selected. Data from 21 rain gauges were therefore compared with 21 grid-pixels from each radar product, at an hourly time step (Figure 1(b)).

5. Results

5.1. Whole Event Rainfall Analysis. Figure 3(a) shows the radar-based 24-hour cumulated PANTHERE QPE (from Nov. 3 at 21:00 to Nov. 4 at 20:00, covering the whole event). The radar-based QPE exhibits a SSW/NNE elongated pattern where precipitation reached up to 85.2 mm in 24 hours,

according to PANTHERE data. Rain gauges at mesoscale are collected up to 129.6 mm, which is significantly higher than the maximum value registered by PANTHERE product. Radar-derived rainfall is underestimated (Figure 3(b)), especially in zones where cumulated rainfall was close to the maximum value (Figure 3(a)). Previous works [45] indicate that as distance increases, radar-based QPE increasingly underestimates high values. In this case, distance from the radar did not strongly affect PANTHERE QPE (i.e., notable underestimates are found at both 30 km and 150 km from the radar). These underestimates may be attributed to greater attenuation of the radar signal with more intense precipitation. Indeed, Figure 3(a) shows that the strongest precipitation coincides with the greatest underestimation. Red dots in Figure 3(b) are the rain gauges located where the radar beam encountered the greatest cumulated quantities of rainfall between radar and rain gauge. For these rain gauges, QPE values are often largely underestimated (up to 51.5 mm). Such attenuation effects have frequently been reported in the literature [17, 27, 46] and have previously been noted as a limitation of the PANTHERE algorithm.

At local scale, PANTHERE systematically underestimates rainfall (Figures 3(c) and 3(d)). Underestimations are homogeneous around the mean bias value (31.2 mm). The Nash criterion (-20.7) confirms this mismatch. The spatial structure of the rainfall is adequately captured by this radar product (Figure 3(d)). The rain gauges receiving the highest amounts of rainfall are located in the grid-pixels with maximum PANTHERE QPE (Pearson correlation coefficient = 0.73).

ANTILOPE, a product merging spatial interpolation of Météo France rain gauge data with radar-based rainfall data, shows better QPE. It only slightly underestimates rainfall (mean bias = -3.2), as captured by HydraVitis rain gauges (Figures 3(e) and 3(f)). Furthermore, ANTILOPE depicts the rainfall field rather successfully at local scale, as supported by the Pearson correlation (0.72) and Nash criterion (0.49) scores.

5.2. Hourly Time Step Local Analysis. Radar (PANTHERE) and composite (ANTILOPE) products were compared to values for those rain gauges located closest to each grid point (from 101 to 647 m), within the area covered by the HydraVitis network. Figure 4 describes the hourly evolution of the QPEs (PANTHERE and ANTILOPE) against rain gauge *in situ* measurements.

Over the 24-hour period, PANTHERE values are underestimated from 0:00 to 6 am, when rainfall intensities were highest. The spatial variability is adequately reproduced for only a few hours (1:00, 2:00, and 7:00 am).

The ability of the composite product, ANTILOPE, to reduce the PANTHERE biases is confirmed at the hourly time scale. The ANTILOPE QPE values are almost systematically closer to rain gauge values than to PANTHERE estimates. For hours when rain gauges show a spatial structure, the ANTILOPE QPE retrieves this structure at least as well as PANTHERE.

Figure 5(a) presents hourly rainfall records averages for radar-derived products and rain gauges. Rainfall intensities

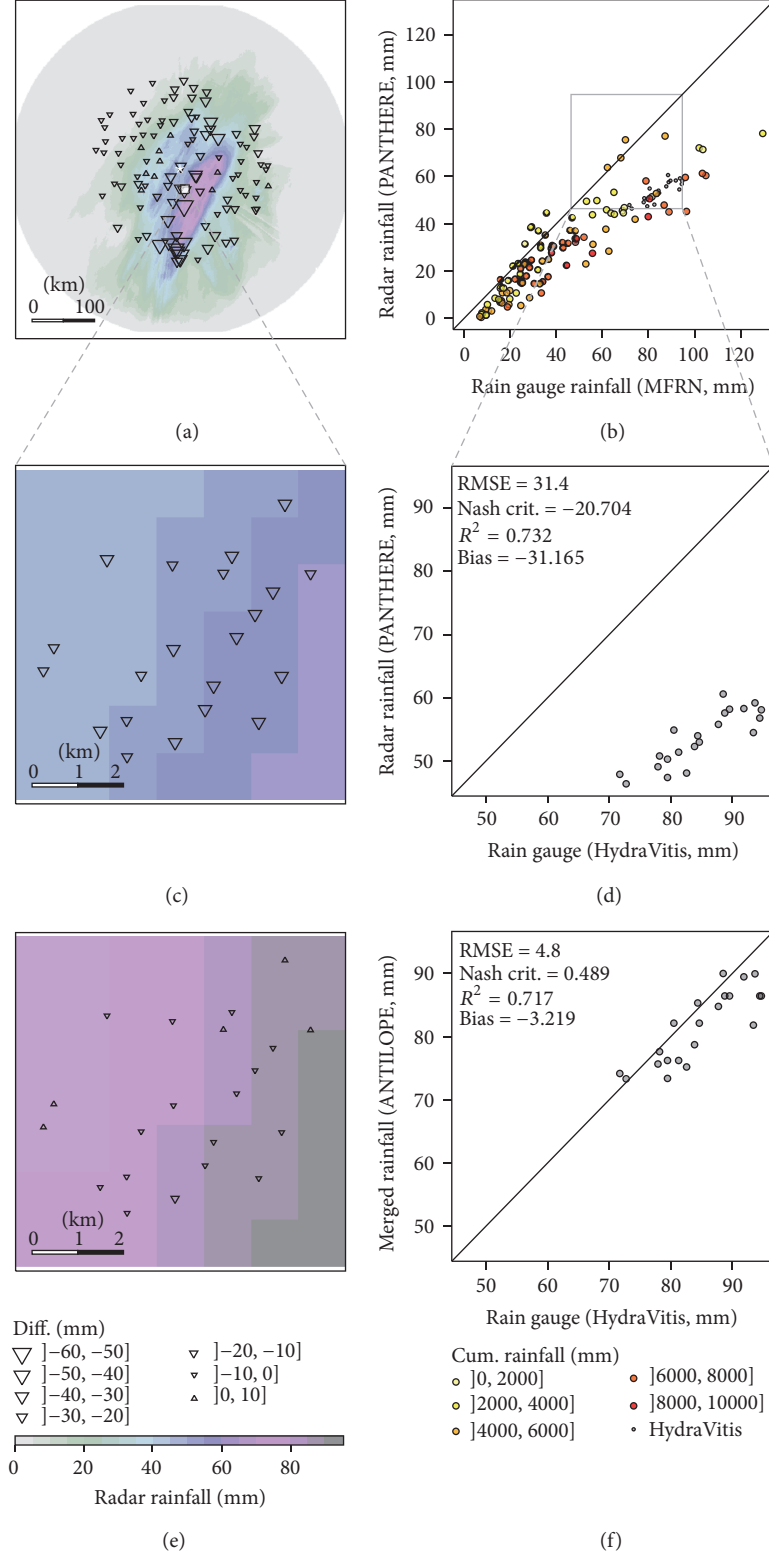


FIGURE 3: Comparison of 24-hour cumulated rainfall values from radar (PANTHERE) and rain gauges, from Nov. 3 at 21:00 to Nov. 4 at 20:00. (a) Radar rainfall map. The white star indicates the radar position and the white square indicates the HydraVitis network position. Triangle size (MFRN rain gauges) is proportional to the difference between values for radar and rain gauges; inverted triangles represent underestimated values; the regular triangles represent accurate or slightly overestimated values. (b) Scatterplot comparing PANTHERE to rain gauge rainfall data. Points are colored according to the rainfall summed for all pixels between the radar and each rain gauge (source of potential attenuation effect). (c) Zoom of (a) over the HydraVitis local scale rain gauge network. Triangle size (HydraVitis rain gauges) is proportional to the difference between values for radar and rain gauges. (d) Scatterplot comparing PANTHERE to rain gauge rainfall data. ((e) and (f)) The same as (c) and (d), respectively, but using the merged radar-based/MFRN rain gauge ANTILOPE data, instead of PANTHERE radar data.

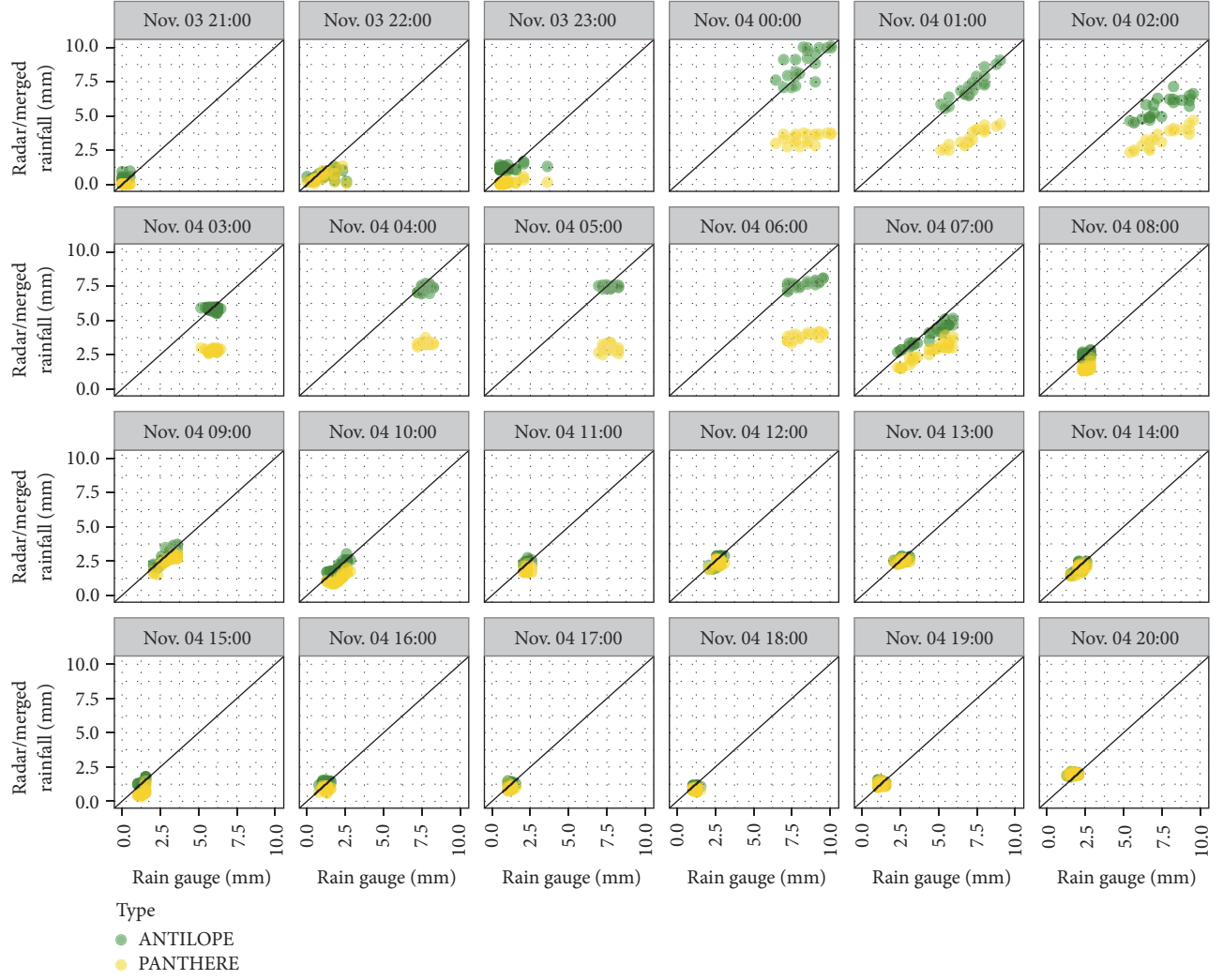


FIGURE 4: Hourly comparison between grid-pixels for PANTHERE and ANTILOPE radar products and HydraVitis rain gauges.

(mm/h) increase sharply at 0:00 on Nov. 4 to 8.3 mm/h (rain gauge average). From 0:00 to 2:00, rainfall spatial variability is at its maximum (rain gauge standard deviation, vertical blue bars in Figure 5(a), from 1.03 to 1.3 mm/h). From 3:00 to 5:00, hourly rainfall remains high (5.9 to 7.7 mm/h) but is rather homogeneous in space (standard deviations from 0.31 to 0.38 mm/h). At 6:00, rainfall intensity rises to 8.3 mm/h (rain gauges average) with a strong spatial variability and decreases from 4 to 2 mm/h approximately, until 13:00 (i.e., 1 pm), with little spatial variation at local scale (standard deviations ranging from 0.18 to 0.51 mm/h during this period). Rainfall finally falls to about 1.5 mm/h after 15:00. Intensities are homogenous in space throughout the study area (standard deviation from 0.18 to 0.22 mm/h).

PANTHERE QPE is almost systematically underestimated during the whole period (except rainfall from 19:00 and 20:00 on Nov. 4; Figure 5(b)). From midnight to 6:00 on November 4, PANTHERE underestimated hourly rainfall rates (3–5 mm), while rain gauge values were almost twice as high (5–9 mm). This underestimation can be linked to

fluctuations in the Z-R relationship, calibration biases, or signal attenuation due to stronger rainfall between the radar site and the study zone [37].

The ANTILOPE QPE provided limited bias (Figure 5(b); mean bias = -0.13 mm/h). The largest underestimation is at 2:00 on Nov. 4 (bias = -1.88 mm/h). Both radar-based QPEs provide spatially consistent hourly precipitation fields (though largely underestimated for PANTHERE) compared to rain gauge data, in many cases. PANTHERE is significantly correlated (Figure 5(c)) with rain gauge data during the whole event but not from 3:00 to 5:00, at 11:00, and from 16:00 to 20:00 on November 4. The ANTILOPE hourly rainfall correlations are also not significant during the first 3 hours of the event. ANTILOPE provides very accurate hourly rainfall fields at local scale, at 1:00, 7:00, 9:00, and 10:00 am on November 4 (Nash criteria equal to 0.843, 0.706, 0.721, and 0.778, resp., Figure 5(d)).

Because PANTHERE underestimates precipitation, a good match to rain gauges is never observed (Nash criterion is always below 0, which is not considered as satisfactory,

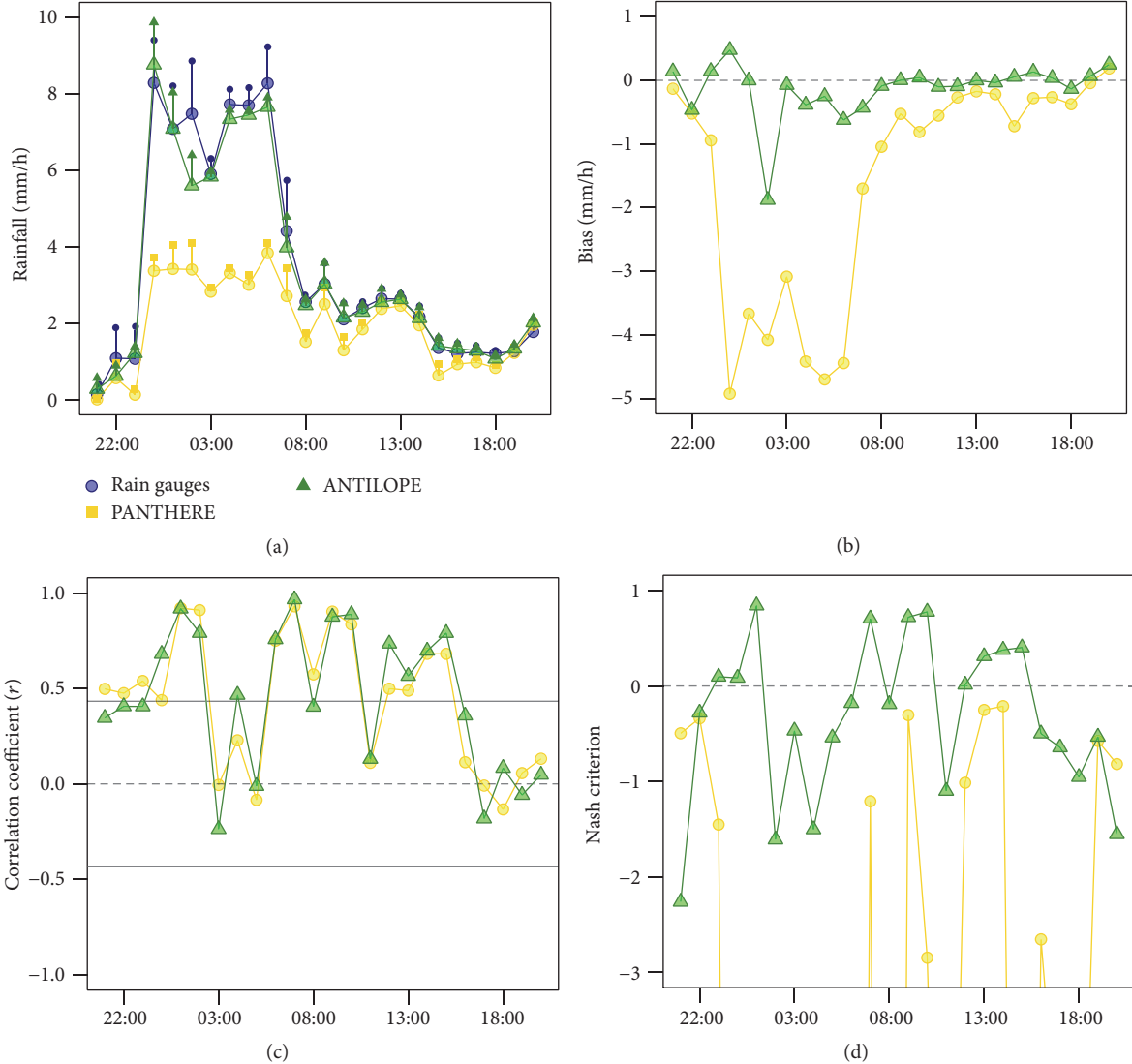


FIGURE 5: Hourly statistics for radar-derived products and HydraVitis rain gauges ($N = 21$ pixels/rain gauges). (a) Hourly rainfall averaged for 21 pixels (rain gauges) at local scale. Vertical bars indicate the standard deviation (i.e., spatial variability). (b) The mean difference between radar-derived products and rain gauges. (c) Pearson correlation coefficients. The solid grey horizontal lines indicate the value corresponding to statistically significant r (Student dist., p value = 5%). (d) Nash criterion. Light green triangles and yellow circles, respectively, represent ANTILOPE and PANTHERE products.

following [47]), despite good correlation with rain gauges (e.g., at 7:00 Nov. 4; Figure 5).

6. Discussion and Conclusion

This study analyzed the performance of two operational radar-derived products in Northern France, during a long, heavy rainfall event that resulted in flooding and heavy damage. The analysis of this event corroborates previous evaluations of radar rainfall and provides novel results regarding the capacity of radar products to capture the spatial variability of rainfall at mesoscale and more particularly at local scale. This analysis confirms the relevance of these products for hydrological modelling, real-time flood assessment,

and water management for agriculture at the farm level, for example. Our main findings at hourly scale supported by 24 patterns are summed up and discussed hereafter.

(a) Despite considerable improvement in radar technology and algorithms, radar QPE fails to estimate rainfall fields accurately at mesoscale for such events. Although, in our study, the PANTHERE cumulated QPE spatial pattern is similar to that of rain gauges, the strong underestimation makes this product unreliable for meteorological, hydrological, or agricultural applications. The long sought-after goal of using radar rainfall data to replace costly rain gauge networks for rainfall measurement has not yet been attained. Even so, considerable improvements have been made

- through the decades [48]; since its first applications [18], the use of mesoscale rain gauge networks to readjust radar rainfall is still required to provide satisfactory QPE [2, 49]. Our results clearly corroborate these previous observations.
- (b) It is possible to reduce underestimation by merging interpolated mesoscale rain gauge data with radar QPE, as in the ANTILOPE product [43, 44]. Such merging provides useful products to estimate hourly QPE fields at local scale, even in situations where considerable attenuation is expected. Hourly precipitation data from the HydraVitis network are well correlated with both radar and merged products. High-resolution rainfall fields are crucial for hydrological applications, especially flood event prediction. Composite products, such as ANTILOPE, provide a viable alternative to high-density rain gauge networks, which are practically and financially difficult to deploy and exploit. Careful consideration of the quality and representativeness of the rain gauge network should be considered in conjunction with refinements to mathematical techniques when developing rain gauge radar merging products [36].
- (c) Improving radar rainfall products requires high density and quality ground data for validation [48, 50]. The HydraVitis network (currently composed of 45 rain gauges from 2 m to 6 km apart) aims to provide reliable information about local spatiotemporal variation in rainfall and thus help to improve remotely sensed rainfall products. The two-year dataset recorded by the HydraVitis network (2014–2016) offers the opportunity to statistically assess and quantify these preliminary results in the near future.
- ## Competing Interests
- The authors declare that they have no competing interests.
- ## References
- [1] S. V. Vasiloff, D.-J. Seo, K. W. Howard et al., “Improving QPE and very short term QPF: an initiative for a community-wide integrated approach,” *Bulletin of the American Meteorological Society*, vol. 88, no. 12, pp. 1899–1911, 2007.
 - [2] E. Goudenhoofdt and L. Delobbe, “Evaluation of radar-gauge merging methods for quantitative precipitation estimates,” *Hydrology and Earth System Sciences*, vol. 13, no. 2, pp. 195–203, 2009.
 - [3] T. F. Stocker, D. Qin, G. K. Plattner et al., *IPCC, 2013: Climate Change 2013: The Physical Science Basis. Contribution of Working Group I to the Fifth Assessment Report of the Intergovernmental Panel on Climate Change*, Cambridge University Press, Cambridge, UK, 2013.
 - [4] A. Berne, G. Delrieu, J.-D. Creutin, and C. Obled, “Temporal and spatial resolution of rainfall measurements required for urban hydrology,” *Journal of Hydrology*, vol. 299, no. 3–4, pp. 166–179, 2004.
 - [5] E. Gaume, M. Livet, M. Desbordes, and J.-P. Villeneuve, “Hydrological analysis of the river Aude, France, flash flood on 12 and 13 November 1999,” *Journal of Hydrology*, vol. 286, no. 1–4, pp. 135–154, 2004.
 - [6] X. He, T. O. Sonnenborg, J. C. Refsgaard, F. Vejen, and K. H. Jensen, “Evaluation of the value of radar QPE data and rain gauge data for hydrological modeling,” *Water Resources Research*, vol. 49, no. 9, pp. 5989–6005, 2013.
 - [7] Z. Li, D. Yang, Y. Hong, Y. Qi, and Q. Cao, “Evaluation of radar-based precipitation estimates for flash flood forecasting in the Three Gorges Region,” *Proceedings of the International Association of Hydrological Sciences*, vol. 368, pp. 89–95, 2015.
 - [8] A. Rafieeinab, A. Norouzi, S. Kim et al., “Toward high-resolution flash flood prediction in large urban areas—analysis of sensitivity to spatiotemporal resolution of rainfall input and hydrologic modeling,” *Journal of Hydrology*, vol. 531, pp. 370–388, 2015.
 - [9] M. Borga, E. N. Anagnostou, and E. Frank, “On the use of real-time radar rainfall estimates for flood prediction in mountainous basins,” *Journal of Geophysical Research Atmospheres*, vol. 105, no. D2, pp. 2269–2280, 2000.
 - [10] S. Westrelin, P. Mériaux, S. Dalle, B. Fradon, and G. Jamet, “Déploiement d’un réseau de radars pour anticiper les risques hydrométéorologiques,” *La Météorologie*, vol. 8, no. 83, 11 pages, 2013.
 - [11] M. R. Duncan, B. Austin, F. Fabry, and G. L. Austin, “The effect of gauge sampling density on the accuracy of streamflow prediction for rural catchments,” *Journal of Hydrology*, vol. 142, no. 1–4, pp. 445–476, 1993.
 - [12] F. Fabry, A. Bellon, M. R. Duncan, and G. L. Austin, “High resolution rainfall measurements by radar for very small basins: the sampling problem reexamined,” *Journal of Hydrology*, vol. 161, no. 1–4, pp. 415–428, 1994.
 - [13] T. Einfalt, K. Arnbjerg-Nielsen, C. Golz et al., “Towards a roadmap for use of radar rainfall data in urban drainage,” *Journal of Hydrology*, vol. 299, no. 3–4, pp. 186–202, 2004.
 - [14] F. Russo, F. Napolitano, and E. Gorgucci, “Rainfall monitoring systems over an urban area: the city of Rome,” *Hydrological Processes*, vol. 19, no. 5, pp. 1007–1019, 2005.
 - [15] F. Renard, *Le risque pluvial en milieu urbain: de la caractérisation de l’aléa à l’évaluation de la vulnérabilité: le cas du Grand Lyon [Ph.D. dissertation]*, Université Jean Moulin Lyon 3, Lyon, France, 2010.
 - [16] L.-P. Wang, S. Ochoa-Rodríguez, J. Van Assel et al., “Enhancement of radar rainfall estimates for urban hydrology through optical flow temporal interpolation and Bayesian gauge-based adjustment,” *Journal of Hydrology*, vol. 531, pp. 408–426, 2015.
 - [17] P. Tabary, C. Augros, J.-L. Champeaux et al., “Le réseau et les produits radars de Météo-France,” *La Météorologie Rubrique* 83, 2013.
 - [18] J. S. Marshall, R. C. Langille, and W. Mc. K. Palmer, “Measurement of rainfall by radar,” *Journal of Meteorology*, vol. 4, no. 6, pp. 186–192, 1947.
 - [19] D. Atlas, “Radar calibration: some simple approaches,” *Bulletin of the American Meteorological Society*, vol. 83, no. 9, pp. 1313–1316, 2002.
 - [20] P. Tabary, “Efforts to improve the monitoring of the French radar network,” in *Proceedings of the 1st Conference on Radar Meteorology*, pp. 482–485, 2003.
 - [21] D. M. A. Jones, “Rainfall drop size-distribution and radar reflectivity,” Illinois State Water Survey 6, University of Illinois, Urbana, Ill, USA, 1956.

- [22] A. Sims, "Case studies of areal variations in raindrop size distributions," in *Proceedings of the 11th Radar Weather Conference*, pp. 162–165, American Meteorological Society, Boulder, Colo, USA, 1964.
- [23] H. Sauvageot and J.-P. Lacaux, "The shape of averaged drop size distributions," *Journal of the Atmospheric Sciences*, vol. 52, no. 8, pp. 1070–1083, 1995.
- [24] A. Libertino, P. Allamano, P. Claps, R. Cremonini, and F. Laio, "Radar estimation of intense rainfall rates through adaptive calibration of the Z-R relation," *Atmosphere*, vol. 6, no. 10, pp. 1559–1577, 2015.
- [25] J.-Y. Gu, A. Ryzhkov, P. Zhang et al., "Polarimetric attenuation correction in heavy rain at C band," *Journal of Applied Meteorology and Climatology*, vol. 50, no. 1, pp. 39–58, 2011.
- [26] P. Tabary, A.-A. Boumahmoud, H. Andrieu et al., "Evaluation of two 'integrated' polarimetric Quantitative Precipitation Estimation (QPE) algorithms at C-band," *Journal of Hydrology*, vol. 405, no. 3-4, pp. 248–260, 2011.
- [27] J. J. Gourley, P. Tabary, and J. Parent du Chatelet, "Empirical estimation of attenuation from differential propagation phase measurements at C band," *Journal of Applied Meteorology and Climatology*, vol. 46, no. 3, pp. 306–317, 2007.
- [28] E. N. Anagnostou, M. N. Anagnostou, W. F. Krajewski, A. Kruger, and B. J. Miriovsky, "High-resolution rainfall estimation from X-band polarimetric radar measurements," *Journal of Hydrometeorology*, vol. 5, no. 1, pp. 110–128, 2004.
- [29] M. N. Anagnostou, J. Kalogiros, E. N. Anagnostou, M. Tarolli, A. Papadopoulos, and M. Borga, "Performance evaluation of high-resolution rainfall estimation by X-band dual-polarization radar for flash flood applications in mountainous basins," *Journal of Hydrology*, vol. 394, no. 1-2, pp. 4–16, 2010.
- [30] A. Gires, I. Tchiguirinskaia, D. Schertzer, A. Schellart, A. Berne, and S. Lovejoy, "Influence of small scale rainfall variability on standard comparison tools between radar and rain gauge data," *Atmospheric Research*, vol. 138, pp. 125–138, 2014.
- [31] L. Bouilloud, G. Delrieu, B. Boudevillain, and P.-E. Kirstetter, "Radar rainfall estimation in the context of post-event analysis of flash-flood events," *Journal of Hydrology*, vol. 394, no. 1-2, pp. 17–27, 2010.
- [32] J. F. I. Ventura and P. Tabary, "The new French operational polarimetric radar rainfall rate product," *Journal of Applied Meteorology and Climatology*, vol. 52, no. 8, pp. 1817–1835, 2013.
- [33] C. Birman, F. Karbou, and J.-F. Mahfouf, "Daily rainfall detection and estimation over land using microwave surface emissivities," *Journal of Applied Meteorology and Climatology*, vol. 54, no. 4, pp. 880–895, 2015.
- [34] L. K. Cunha, J. A. Smith, W. F. Krajewski, M. L. Baeck, and B.-C. Seo, "NEXRAD NWS polarimetric precipitation product evaluation for IFloodS," *Journal of Hydrometeorology*, vol. 16, no. 4, pp. 1676–1699, 2015.
- [35] T. R. Oke, *Boundary Layer Climates*, Methuen, London, UK, 1978.
- [36] S. A. Jewell and N. Gaussiat, "An assessment of kriging-based rain-gauge-radar merging techniques," *Quarterly Journal of the Royal Meteorological Society*, vol. 141, no. 691, pp. 2300–2313, 2015.
- [37] P. Tabary, J. Desplats, K. Do Khac, F. Eideliman, C. Gueguen, and J.-C. Heinrich, "The new French operational radar rainfall product. Part II: validation," *Weather and Forecasting*, vol. 22, no. 3, pp. 409–427, 2007.
- [38] B. Pauthier, B. Bois, T. Castel, and Y. Richard, "Note technique d'implantation d'un réseau de pluviomètres en terrain viticole sur la côte de Beaune (France)," *Climatologie*, vol. 11, pp. 34–46, 2014.
- [39] G. Villarini, P. V. Mandapaka, W. F. Krajewski, and R. J. Moore, "Rainfall and sampling uncertainties: a rain gauge perspective," *Journal of Geophysical Research: Atmospheres*, vol. 113, no. D11, 2008.
- [40] Météo France, 2014: bulletin climatique quotidien, https://donneespubliques.meteofrance.fr/donnees_libres/bulletins/BQA/20141103.pdf.
- [41] Météo France, Données climatiques de la station de Dijon, 2016, <http://www.meteofrance.com/climat/france/dijon/21473001/normales>.
- [42] M. Humphrey, J. Istok, J. Lee, J. Hevesi, and A. Flint, "A new method for automated dynamic calibration of tipping-bucket rain gauges," *Journal of the American Meteorological Society*, vol. 14, no. 6, pp. 1513–1519, 1997.
- [43] J. L. Champeaux, P. O. Dupuy, I. Laurantin, P. Soulan, P. Tabary, and J. M. Soubeiroux, "Les mesures de précipitations et l'estimation des lames d'eau à Météo-France: état de l'art et perspectives," *La Houille Blanche*, vol. 5, pp. 28–34, 2009.
- [44] J. L. Champeaux, O. Laurantin, B. Mercier, F. Mounier, P. Lassegues, and P. Tabary, "Quantitative precipitation estimations using rain gauges and radar networks: inventory and prospects at Meteo-France," 2011.
- [45] F. Fabry, G. L. Austin, and D. Tees, "The accuracy of rainfall estimates by radar as a function of range," *Quarterly Journal of the Royal Meteorological Society*, vol. 118, no. 505, pp. 435–453, 1992.
- [46] G. Delrieu, H. Andrieu, and J. D. Creutin, "Quantification of path-integrated attenuation for X- and C-band weather radar systems operating in mediterranean heavy rainfall," *Journal of Applied Meteorology*, vol. 39, no. 6, pp. 840–850, 2000.
- [47] D. N. Moriasi, J. G. Arnold, M. W. Van Liew, R. L. Bingner, R. D. Harmel, and T. L. Veith, "Model evaluation guidelines for systematic quantification of accuracy in watershed simulations," *Transactions of the ASABE*, vol. 50, no. 3, pp. 885–900, 2007.
- [48] W. F. Krajewski, G. Villarini, and J. A. Smith, "Radar-rainfall uncertainties: where are we after thirty years of effort," *Bulletin of the American Meteorological Society*, vol. 91, no. 1, pp. 87–94, 2010.
- [49] S. Sinclair and G. Pegram, "Combining radar and rain gauge rainfall estimates using conditional merging," *Atmospheric Science Letters*, vol. 6, no. 1, pp. 19–22, 2005.
- [50] M. Steiner, J. A. Smith, S. J. Burges, C. V. Alonso, and R. W. Darden, "Effect of bias adjustment and rain gauge data quality control on radar rainfall estimation," *Water Resources Research*, vol. 35, no. 8, pp. 2487–2503, 1999.

Research Article

Evaluation and Correction of Quantitative Precipitation Forecast by Storm-Scale NWP Model in Jiangsu, China

Gaili Wang,^{1,2} Dan Wang,³ Ji Yang,² and Liping Liu¹

¹State Key Laboratory of Severe Weather, Chinese Academy of Meteorological Science, 46 Zhongguancun South Street, Haidian District, Beijing 100081, China

²Jiangsu Institute of Meteorological Science, 16 Kunlun Road, Nanjing, Jiangsu 210009, China

³National Meteorological Center, China Meteorological Administration, 46 Zhongguancun South Street, Haidian District, Beijing 100081, China

Correspondence should be addressed to Gaili Wang; wgl3111@camsoma.cn

Received 25 March 2016; Accepted 11 July 2016

Academic Editor: Enrico Ferrero

Copyright © 2016 Gaili Wang et al. This is an open access article distributed under the Creative Commons Attribution License, which permits unrestricted use, distribution, and reproduction in any medium, provided the original work is properly cited.

With the development of high-performance computer systems and data assimilation techniques, storm-scale numerical weather prediction (NWP) models are gradually used for short-term deterministic forecasts. The primary objective of this study is to evaluate and correct precipitation forecasts of a storm-scale NWP model called the advanced regional prediction system (ARPS). The evaluation and correction consider five heavy precipitation events that occurred in the summer of 2015 in Jiangsu, China. The performances of the original and corrected ARPS precipitation forecasts are evaluated as a function of lead time using standard measurements and a spatial verification method called Structure-Amplitude-Location (SAL). In general, the ARPS could not produce optimal forecasts for very short lead times, and the forecast accuracy improves with increasing lead time. The ARPS overestimates precipitation for all lead times, which is confirmed by large bias in many forecasts in the first and second quadrant of the diagram of SAL, especially at the 1 h lead time. The amplitude correction is performed by matching percentile values of the ARPS precipitation forecasts and observations for each lead time. Amplitude correction significantly improved the ARPS precipitation forecasts in terms of the considered performance indices of standard measures and A-component and S-component of SAL.

1. Introduction

Heavy rain is one of the most severe weather events in China, causing floods and other geological and hydrological disasters. High-resolution quantitative precipitation forecasts (QPFs) play an important role in flash flood warning and emergency response.

NWP models with atmospheric dynamic constraints have been used to operate for middle and long term weather forecast. However, the accuracy of NWP model forecasts during the first few hours is always influenced by the “spin-up” problem [1]. Therefore, precipitation forecasts of NWP models are less accurate than predictions of extrapolation-based techniques at short-term lead times [2]. Recently, with the development of high-performance computers and the use of rapid-update-cycle (RUC) approach, the “spin-up” problem of NWP models has been significantly reduced.

The forecast accuracy at the first several hours has been improved significantly by assimilating various types of observation data [3–9]. NWP models with high spatial and temporal resolution have been applied for nowcasting of precipitation gradually. The high-resolution rapid refresh [10] developed by the National Oceanic and Atmospheric Administration, Weather Research and Forecasting model (WRF) with RUC technique used in the Beijing Meteorological Bureau, Chinese Meteorological Administration, and the advanced regional prediction system (ARPS) developed by the Center for Analysis and Prediction of Storms (CAPS) have been operationally applied for nowcasting precipitation.

The Jiangsu Observatory introduced the ARPS model from CAPS to provide high quality and resolution weather forecast services during the second Youth Olympics Games held in Nanjing, China, in 2014. The purpose of this paper is to evaluate and correct the ARPS precipitation nowcasting in

Jiangsu, China. The evaluation and correction are performed for hourly precipitation forecasts at lead times from 1 to 6 h. The eight convective heavy rain events that occurred during the summer of 2014 and 2015 in Jiangsu are selected in this study. Three heavy precipitation events occurring during the summer of 2014 were used for deriving the ARPS model correction parameters. Five heavy precipitation events occurring during the summers of 2014 and 2015 were used for verification data. The two verification events occurring in April 2014 were convective precipitation and lasted for about one day. The three verification events in 2015 lasted for several days and were accompanied by floods that cause significant economic losses and even casualties. The forecast of such events is beneficial for preventing disasters and reducing damage.

The paper is organized as follows. Section 2 describes data used in this study. The ARPS model and correction scheme are introduced in Sections 3 and 4, respectively. The evaluation methods are described in Section 5, and the results of the evaluation the ARPS original and corrected precipitation forecasts based on the five verification heavy rain events are presented in Section 6. The conclusions and discussions are drawn in Section 7.

2. Data and Case Study

In this study, quantitative precipitation estimations (QPEs) based radar is used to evaluate the original and corrected ARPS precipitation forecasts and derive the calibration parameters of the ARPS model. Figure 1 gives the study domain, in which six single polarization S-band radar positions are marked with triangles. Radar data were measured in standard precipitation mode of 9 elevation scans with 6 min by the Chinese Meteorological Administration (CMA) radar network. Radar data are expressed in spherical coordinates (elevation, azimuth, and gate), with radial resolution of 1 km and azimuth resolution of 1°. The single radar data underwent quality control to reduce ground clutter, electronic interference, and anomalous propagations by a fuzzy logic algorithm [11]. The single radar data were merged using an exponential weighting average scheme to yield the mosaic reflectivity value in the overlapping coverage areas [12]. Rainfall rates are calculated using the local radar reflectivity-rainfall rate (Z - R) relationship of $Z = 386R^{1.43}$ at an elevation of 3 km above sea level with a spatial resolution of 0.01°. The rain rates are integrated over time to calculate hourly precipitation [13]. Due to asymmetric distribution of precipitation, the raindrop spectrum changes with time, space, and different types of precipitation. The fixed Z - R relationship results in the radar-based QPEs underestimation for light rain and basic satisfaction for heavy rain. Because heavy rain often occurs in summer in Jiangsu, in this study, the radar-based hourly QPEs were used as observations for the verification and correction of the ARPS forecasts.

Because Jiangsu is located in a transitional climate zone between subtropics and warm temperate zone, continuous heavy precipitation events often occur in June and July every year called Meiyu. The flood disaster in Jianghuai River

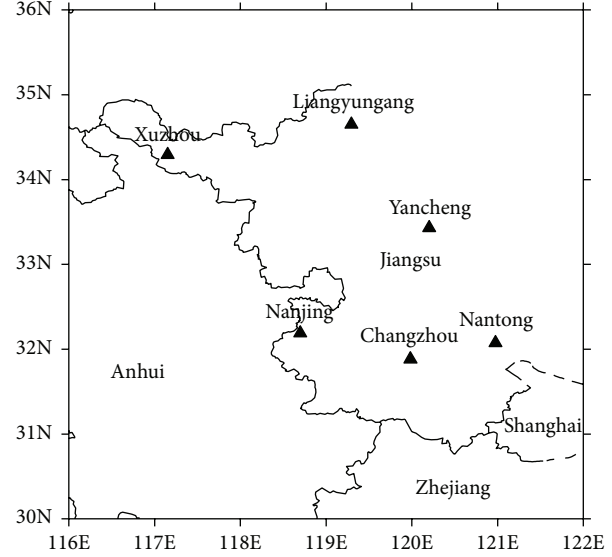


FIGURE 1: The study domain and locations (as triangles) of Doppler radars.

caused by Meiyu is one of important meteorological disasters. That is why the forecast of such events is beneficial. Therefore, eight convective heavy rain events in the summer of 2014 and 2015 in Jiangsu are selected in this study. Figure 2 shows one representative image of each event. Three heavy precipitation events occurred during the summer of 2014 as calibration data were used for deriving the ARPS model correction parameters. The other five heavy precipitation events were used to evaluate the original and corrected ARPS precipitation forecasts. Among the five heavy rain events, the disaster from 23rd of June 2015 heavy rain event was the most serious, affecting 93.5 million people, with one death, and economic losses of 2.1 billion RMB.

3. Advanced Regional Prediction System

The Advanced Regional Prediction System (ARPS) is developed at the Center for Analysis and Prediction of Storms at the University of Oklahoma and suitable to explicitly predict storm-scale convective systems as well as other scales weather systems. The ARPS is a nonhydrostatic compressible model and includes its own data ingest, quality control, and objective analysis packages, a three-dimensional variational (3D-Var) system, the forward prediction component, and a self-contained postprocessing, diagnostic and verification package [14–16]. The ARPS could predict 3D velocity vector (u , v , and w), pressure (p), turbulence kinetic energy (TKE), potential temperature (θ), water vapor mixing ratio (q_v), and the mixing ratios of cloud water, rainwater, ice, snow, and hail (q_c , q_r , q_i , q_s , and q_h , resp.). In the ARPS, subgrid-scale turbulent mixing is handled by three subgrid-scale closure schemes: first-order Smagorinsky/Lilly scheme, the 1.5-order TKE-based scheme, and the Germano dynamic closure scheme [17–20]. The combination of the 3D, 1.5-order TKE-based turbulence scheme and an ensemble turbulence

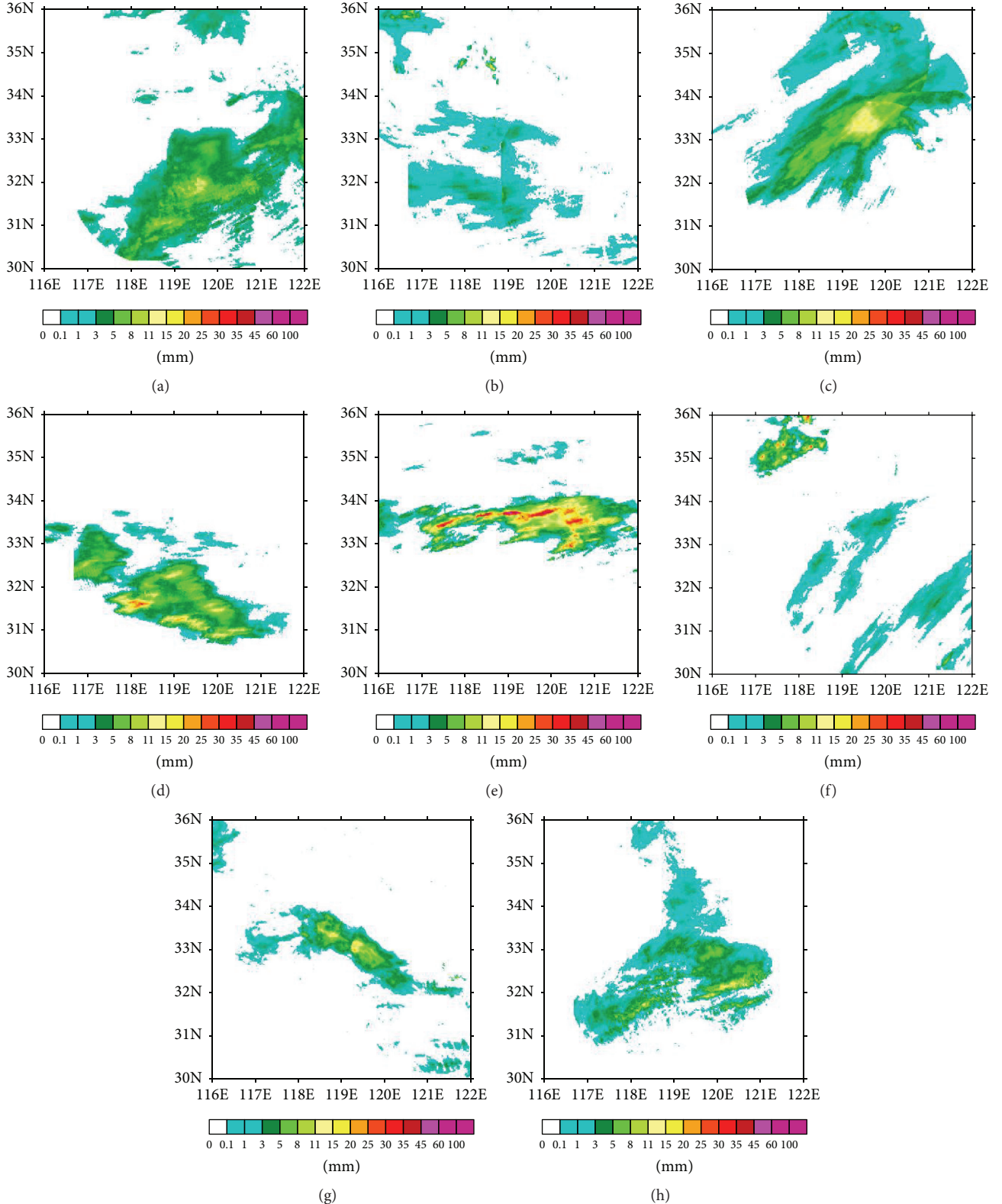


FIGURE 2: Precipitation images of 1 h QPE of six heavy rain events used in this study. Image at 0400 BJT on 1st of June 2014 for event 1 (a), image at 2300 BJT on 16th of June 2014 for event 2 (b), image at 0100 BJT on 13th of August 2014 for event 3 (c), image at 0900 BJT on 16th of June 2015 for event 4 (d), image at 1500 BJT on 24th of June 2015 for event 5 (e), image at 1200 BJT on 6th of July 2015 for event 6 (f), image at 0900 BJT on 11th of April 2014 for event 7 (g), and image at 2100 BJT on 17th of April 2014 for event 8 (h).

closure scheme of Sun and Chang [21] is used to treat convective boundary layer turbulence.

For the precipitation processes, the Kessler two-category liquid water scheme and the modified three-category ice schemes are used in the ARPS [22]. A fourth-order monotonic flux-corrected transport scheme [23] is applied to potential temperature, water variables, and TKE. Details on these physics and computational options can be found in Xue et al., [14–16].

To obtain the initial conditions, six S-band radar observations in Jiangsu, including Doppler velocity and reflectivity factor, are assimilated with a 3D variational cloud analysis system in the ARPS [24–27]. The ARPS has been operating in Jiangsu Observatory and initialized every 3 hours since 2014. The ARPS produces forecasts up to 24 h ahead, with high spatial resolution of $3\text{ km} \times 3\text{ km}$ and temporal interval of 1 h. Considering the importance and difficulty of precipitation nowcasting, the ARPS original and corrected forecast precipitation for the next 6 hours was evaluated and compared in this paper.

4. Correction of ARPS Forecasts

Hoffman and Grassotti [28] decomposed forecast error into displacement error, amplitude error, and residual error; moreover, displacement error and amplitude error must be large scale. The displacement error and amplitude error could be reduced by analyzing and correcting the differences between the forecast fields and observations [25, 29]. For the ARPS, considering the amplitude error is more remarkable than displacement error, an amplitude-correcting scheme was applied to improve forecast accuracy of the ARPS in this study.

Precipitation is unarguably the vital input data for various hydrologic models. Obtaining accurate and reliable precipitation data is thus very important for local, regional, and global hydrologic prediction and water resources management. In this study, the ARPS overestimates precipitation in terms of amplitude based on standard measures and a spatial verification, which causes the difference between distribution function of the ARPS forecasts and observations. The amplitude correction is performed by matching percentile values of the ARPS precipitation forecasts y_k^{NWP} and observations O_k [30, 31]. All nonzero ARPS precipitation forecasts and observations from calibration data set were sorted separately in ascending order. The percentile values of ARPS forecasts Y_i and observations O_i , $i = 1, \dots, 101$, for percentiles 0.01, 1, 2, …, 99 and 99.9 of y_k^{NWP} and O_k were calculated and saved in tables. The corrected precipitation forecast y_k^{Cor} was obtained using the following:

$$\begin{aligned} y_k^{\text{Cor}} &= y_k^{\text{NWP}} \quad \text{if } y_k^{\text{NWP}} < Y_1 \\ y_k^{\text{Cor}} &= y_k^{\text{NWP}} + O_{101} - Y_{101} \quad \text{else if } y_k^{\text{NWP}} > Y_{101} \\ y_k^{\text{Cor}} &= O_i + \frac{O_{i+1} - O_i}{Y_{i+1} - Y_i} (y_k^{\text{NWP}} - Y_i) \quad (1) \\ &\quad \text{else if } Y_i < y_k^{\text{NWP}} < Y_{i+1}. \end{aligned}$$

Taking into account that amplitude error is a function with lead time, the correction parameters are derived for each lead time. The corrected precipitation forecasts were evaluated and compared with the original ARPS forecasts over the five heavy rain events in the summers of 2014 and 2015.

5. Verification Methods of Forecasts

Because convective precipitation fields change quickly with time and space, it is difficult to evaluate the convective precipitation forecasts using uniform verification method [32]. We applied standard methods and a spatial verification method in this study. Among the standard methods, we used Bias (B_s), agreement index (d), mean absolute error (MAE), and root mean square error (RMSE) to quantitatively evaluate precipitation forecasts based on grids. The bias is an important measure for hydrologic applications. The agreement index, instead of correlation coefficient, was used to measure the agreement between forecasts and observations because the correlation coefficient has the disadvantage of not being sensitive to linear differences of observation and prediction [31]. MAE and RMSE can quantitatively evaluate forecast error. B_s , d , MAE, and RMSE are computed from the following formulas:

$$\begin{aligned} B_s &= \frac{\sum_{i=1}^N F_i}{\sum_{i=1}^N O_i} \\ d &= 1 - \frac{\sum_{i=1}^N (O_i - F_i)^2}{\sum_{i=1}^N (|O_i - \bar{O}| + |F_i - \bar{O}|)^2} \\ \text{MAE} &= \frac{1}{N} \sum_{i=1}^N |O_i - F_i| \\ \text{RMSE} &= \sqrt{\frac{\sum_{i=1}^N (O_i - F_i)^2}{N}}, \end{aligned} \quad (2)$$

where F_i and O_i are the predicted and observed rainfall at the i th grid point, the number of observations and forecasts is N , and the bar indicates the mean value. A perfect forecast means predicted rainfall field is the same as observation field and would result in $B_s = 1$, $d = 1$, $\text{MAE} = 0$, and $\text{RMSE} = 0$. Although being easily performed, the standard methods have the problem known as the “double penalty” for those precipitation fields with complex structures [31, 33].

To avoid the “double penalty,” spatial verification methods, which can identify the sources of forecasts error, have been applied to evaluate high resolution NWP forecasts of precipitation in the last decades. We used the Structure-Amplitude-Location (SAL) score as the supplement for the standard measures in this study. The SAL is an object-based measure method, which considers three components of the structure (S), amplitude (A), and location (L) of precipitation field [33]. The amplitude component A measures the mean precipitation difference over the considered domain between forecasts and observations. The location component L combines information about the distance between the centers of

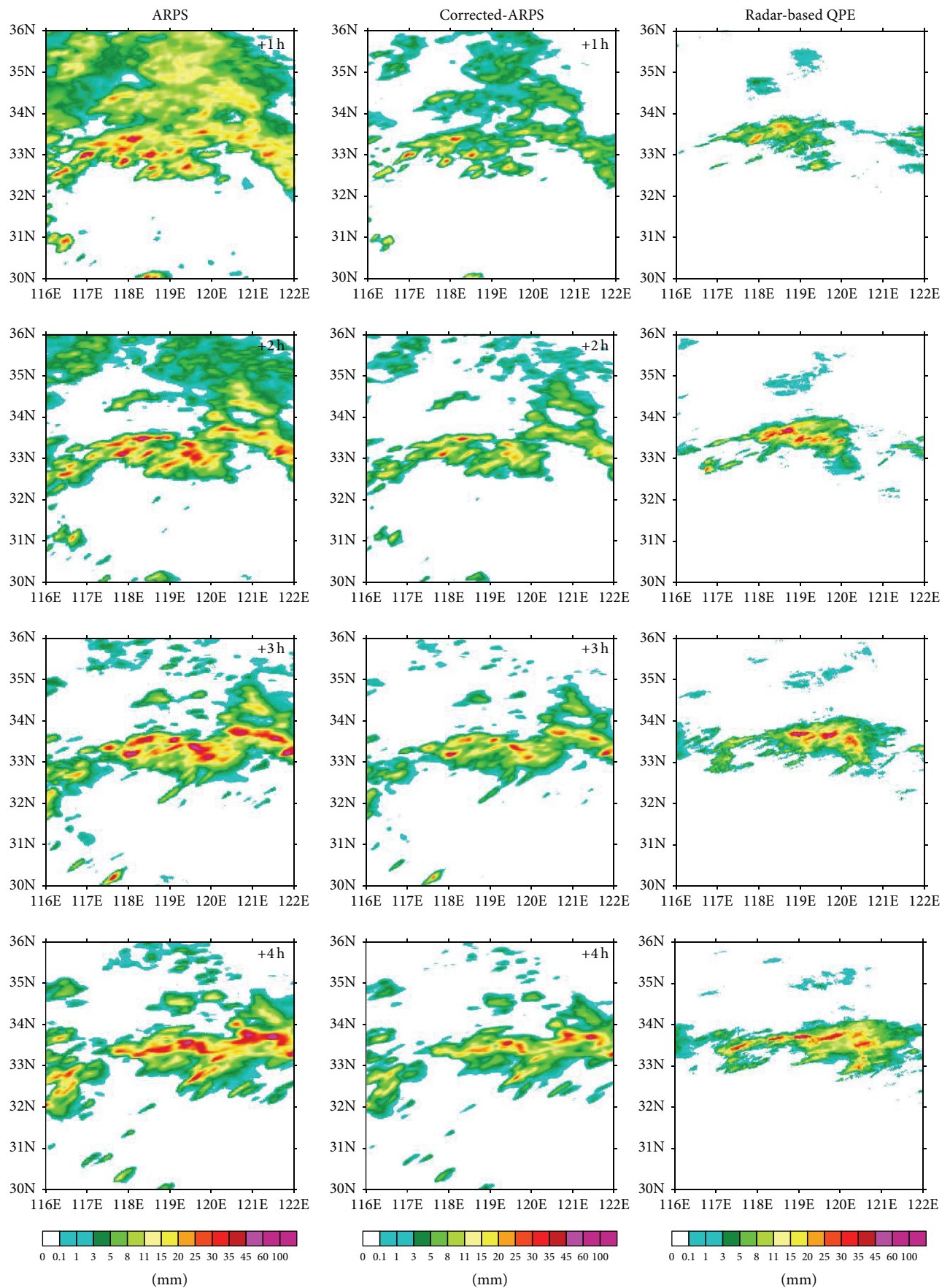


FIGURE 3: Continued.

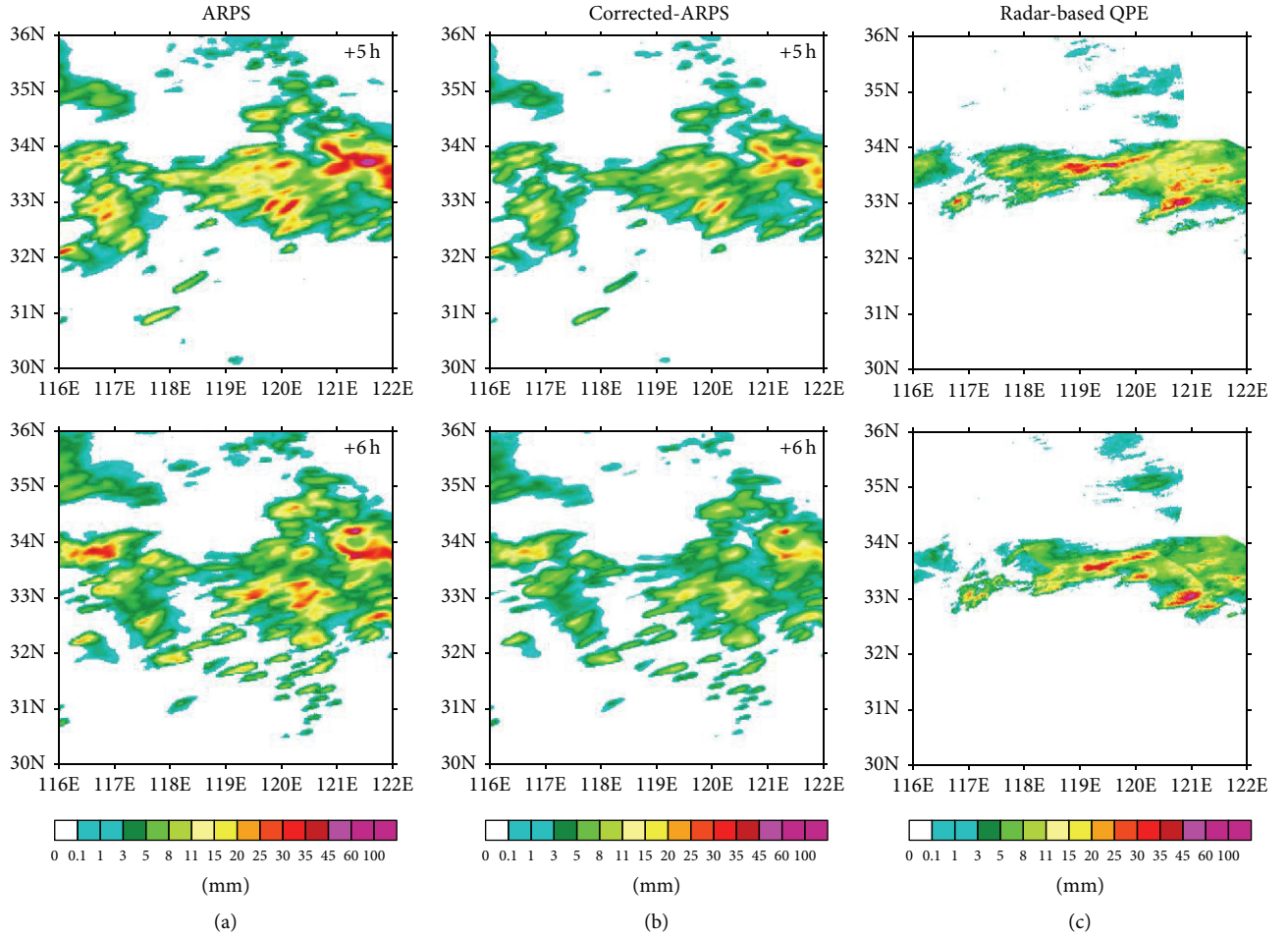


FIGURE 3: Comparison of forecasted precipitation by the original (a) and corrected (b) ARPS initialized at 1500 BJT on 24 June 2015 from 1 h to 6 h lead times with corresponding radar observations (c).

mass of the predicted and observed precipitation of the total field and about the mean displacement of the precipitation objects from the center of mass of the total precipitations field. The structure component S compares the volume of predicted and observed precipitation fields. Positive (negative) value of S indicates widespread (sharp) predicted precipitation fields compared to the observed ones. A perfect forecast would result in $S = 0$, $A = 0$, and $L = 0$.

6. Results and Discussion

The ARPS model has been operated in Jiangsu Observatory since 2014. In this study, three precipitation events during the summer of 2014 were used to develop the ARPS model correction parameters, and five precipitation events during the summers of 2014 and 2015 were used to evaluate the original and corrected precipitation forecasts. The evaluation was performed up to 6 h lead times with a spatial resolution of $3\text{ km} \times 3\text{ km}$ and 1 h intervals.

Figure 3 shows an example of the ARPS original and corrected hourly precipitation forecasts at lead times from 1 to 6 h with 1 h intervals at a base time of 1500 BJT (Beijing

Time) on June 24, 2015, and corresponding radar-based QPEs. In general, the original ARPS precipitation forecasts (Figure 3(a)) overestimate precipitation rate and precipitation extension, while with perfect position of rain band. The overestimation is the most significant at the lead time of 1 h and reduces with increasing lead time. The amplitude correction scheme successfully reduced the amplitude error of the original ARPS forecasts and produced the corrected precipitation forecasts (i.e., Figure 3(b)) similar to observations.

The performance of the original ARPS precipitation forecast and effectiveness of the amplitude correction scheme were quantitatively evaluated with agreement index, bias, MAE, and RMSE. Figure 4 shows the comparison of the performances between the original and corrected ARPS precipitation forecasts up to the lead time of 6 h with 1 h interval initialized at 1500 BJT on 24 June, 2015. The original ARPS forecast has lower agreement index and higher bias, MAE and RMSE at the lead time of 1 h, which indicates the ARPS may not produce optimal forecasts for very short lead time. The forecast accuracy increases with lead time. The amplitude correction scheme substantially improves the

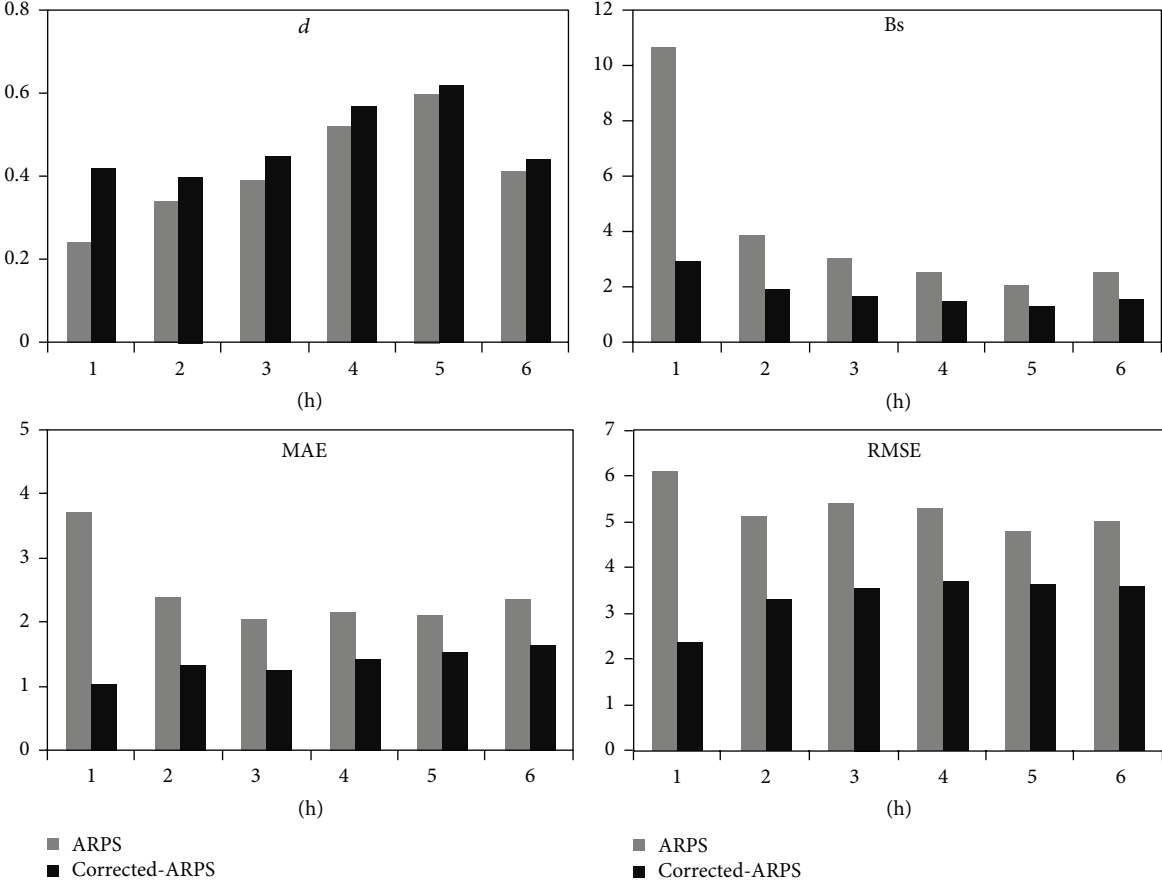


FIGURE 4: Quantitatively compare corrected ARPS precipitation forecasts with the original ARPS precipitation forecasts initialized at 1500 BJT on 24 June 2015.

ARPS precipitation forecasts for all the lead times in terms of the considered performance indices of the standard methods. Particularly, the improvement is significant at the lead time of 1 h.

Table 1 shows quantitative results of the original and corrected ARPS forecasts for lead times of 1–6 h and a comparison of their outputs by standard measures for each event. In general, the correction scheme improves the forecast performances based on standard measurements for all lead times and each event, especially at 1 h lead time.

To obtain meaningful verification and comparison of the results, average performance indices over five verification heavy precipitation events in the summers of 2014 and 2015 are given in Figure 5. As far as the original ARPS forecasts are concerned, the forecast performances except for agreement index improve with increasing lead time. The agreement index changes little over the forecast period. This is the fact that NWP models may not produce optimal predictions at the first short-term due to sensitive to the initial field, spatial resolution, and assimilation data. And the forecast skill improves as they dynamically resolve large-scale flow [10, 34–36].

The amplitude correction scheme shows significant improvement in the original ARPS forecasts in terms of the considered performance indices. Especially at the 1 h ahead,

the agreement index is improved from 0.24 to 0.46, the bias for the original ARPS forecast is 12.55, and that is reduced to 2.89 by the amplitude correction scheme. RMSE for the original and corrected ARPS forecasts are 3.67 and 1.35, respectively. The performance of the corrected ARPS forecast changes little over the lead times. It seems that the amplitude correction scheme covered the shortage of NWP models not producing optimal forecast for very short lead times.

Evaluation of the original and corrected ARPS forecasts by SAL based on the three considered heavy rain events is shown in Figure 6. Most the original ARPS forecasts are characterized by positive A-component values for all the considered lead times, indicating an overestimation of the original ARPS precipitation forecast. Especially for the lead time of 1h, a cluster of dots are found in the top hand corner of Figure 6(a), which indicates that the ARPS produced very widespread precipitation objects and significantly overestimated precipitation rate. With the increasing lead time, some forecasts can be seen in the second quadrant of the diagram, which implies that the ARPS forecasted overestimated precipitation, with very small and/or too peak objects. Most of the original middle ARPS forecasts are indicated by the red and purple dots at the 1 h lead time, meaning a high-quality forecast in terms of the location of predicted precipitation field. The location of predicted

TABLE 1: Mean forecast performances based on standard measurements of the original and the corrected ARPS for lead times from 1 h to 6 h for five heavy rain events.

	<i>d</i>				
	Event 1	Event 2	Event 3	Event 4	Event 5
	ARPS/Corrected-ARPS	ARPS/Corrected-ARPS	ARPS/Corrected-ARPS	ARPS/Corrected-ARPS	ARPS/Corrected-ARPS
1 h	0.28/0.44	0.29/0.43	0.28/0.51	0.27/0.53	0.10/0.37
2 h	0.28/0.36	0.28/0.37	0.30/0.40	0.36/0.47	0.17/0.27
3 h	0.27/0.35	0.27/0.34	0.28/0.35	0.37/0.43	0.19/0.25
4 h	0.26/0.34	0.24/0.32	0.26/0.29	0.34/0.38	0.18/0.23
5 h	0.29/0.37	0.25/0.29	0.19/0.23	0.32/0.36	0.17/0.21
6 h	0.29/0.36	0.22/0.26	0.19/0.23	0.28/0.31	0.20/0.23
	<i>B_s</i>				
	Event 1	Event 2	Event 3	Event 4	Event 5
	ARPS/Corrected-ARPS	ARPS/Corrected-ARPS	ARPS/Corrected-ARPS	ARPS/Corrected-ARPS	ARPS/Corrected-ARPS
1 h	12.15/2.89	10.26/2.89	12.63/2.79	14.91/2.74	12.81/3.15
2 h	6.76/3.23	5.88/2.88	6.75/2.77	6.14/2.61	6.71/3.11
3 h	6.67/3.48	4.39/2.32	4.93/2.33	3.83/1.97	4.50/2.32
4 h	6.19/3.43	4.05/2.42	4.94/2.51	3.36/1.92	3.66/2.06
5 h	5.24/3.26	3.76/2.37	5.14/2.78	3.12/2.02	2.80/1.78
6 h	4.47/2.77	3.40/2.07	4.22/2.26	2.90/1.88	2.08/1.31
	MAE (mm)				
	Event 1	Event 2	Event 3	Event 4	Event 5
	ARPS/Corrected-ARPS	ARPS/Corrected-ARPS	ARPS/Corrected-ARPS	ARPS/Corrected-ARPS	ARPS/Corrected-ARPS
1 h	2.26/0.62	2.52/0.76	2.07/0.57	1.41/0.27	1.22/0.31
2 h	1.27/0.70	1.53/0.84	0.96/0.57	0.64/0.30	0.65/0.32
3 h	1.21/0.71	1.42/0.84	0.84/0.58	0.48/0.28	0.45/0.26
4 h	1.20/0.73	1.32/0.91	1.09/0.63	0.45/0.29	0.39/0.24
5 h	1.08/0.73	1.39/0.97	0.88/0.67	0.43/0.30	0.37/0.25
6 h	0.99/0.67	1.36/0.94	0.84/0.63	0.42/0.31	0.34/0.23
	RMSE (mm)				
	Event 1	Event 2	Event 3	Event 4	Event 5
	ARPS/Corrected-ARPS	ARPS/Corrected-ARPS	ARPS/Corrected-ARPS	ARPS/Corrected-ARPS	ARPS/Corrected-ARPS
1 h	4.29/1.53	4.83/2.00	3.95/1.48	2.76/0.70	2.97/1.05
2 h	3.12/1.78	3.84/2.22	2.66/1.61	1.47/0.76	1.99/1.10
3 h	3.14/1.80	3.80/2.25	2.57/1.69	1.24/0.76	1.55/0.92
4 h	3.06/1.85	3.56/2.44	3.01/1.76	1.18/0.79	1.39/0.90
5 h	2.79/1.85	3.69/2.53	2.57/1.86	1.10/0.79	1.28/0.93
6 h	2.54/1.63	3.63/2.40	2.44/1.69	1.12/0.84	1.15/0.82

precipitation field is slightly getting poor with the increasing lead time. As shown in Table 1, both the mean values of S-component and A-component move towards centerline with lead time, whereas the mean value of L-component slightly departs from centerline with lead time.

For the corrected ARPS forecast, at the 1 h lead time, most forecasts are found in the first and second quadrant of the diagram. In the first quadrant, both A-component and S-component of SAL are overestimated. In the second quadrant, forecasts overestimate A-component, whereas underestimate S-component. Compared to the original ARPS forecast, the overestimation of precipitation account is significantly improved. As the increasing lead time, the high density of dots move towards the centerline of the diagram, indicating the overestimation is gradually improving.

In general, as shown in Table 2, the mean A-components and S-components of the corrected ARPS forecast move towards the centers of the diagram, and the mean L-components are almost unchanged (compared to the original ARPS). The amplitude correction scheme improves the original ARPS precipitation forecast on both the amplitude and structure of precipitation.

7. Summary and Conclusions

This paper quantitatively evaluated the original ARPS precipitation forecasts and addressed and corrected the forecast error in Jiangsu. The forecast performances were evaluated and compared as a function of lead times of 1 h to 6 h using standard measures and a spatial verification method.

TABLE 2: Mean values of S-component, A-component, and L-component of the original and corrected ARPS over three heavy rain events.

Lead times	S (ARPS)	S (Corrected-ARPS)	A (ARPS)	A (Corrected-ARPS)	L (ARPS)	L (Corrected-ARPS)
1 h	1.36	0.08	1.58	0.73	0.22	0.20
2 h	0.70	0.16	1.26	0.71	0.24	0.25
3 h	0.59	0.24	1.05	0.53	0.28	0.28
4 h	0.64	0.25	0.97	0.50	0.30	0.30
5 h	0.47	0.23	0.81	0.43	0.30	0.31
6 h	0.24	0.14	0.66	0.26	0.33	0.34

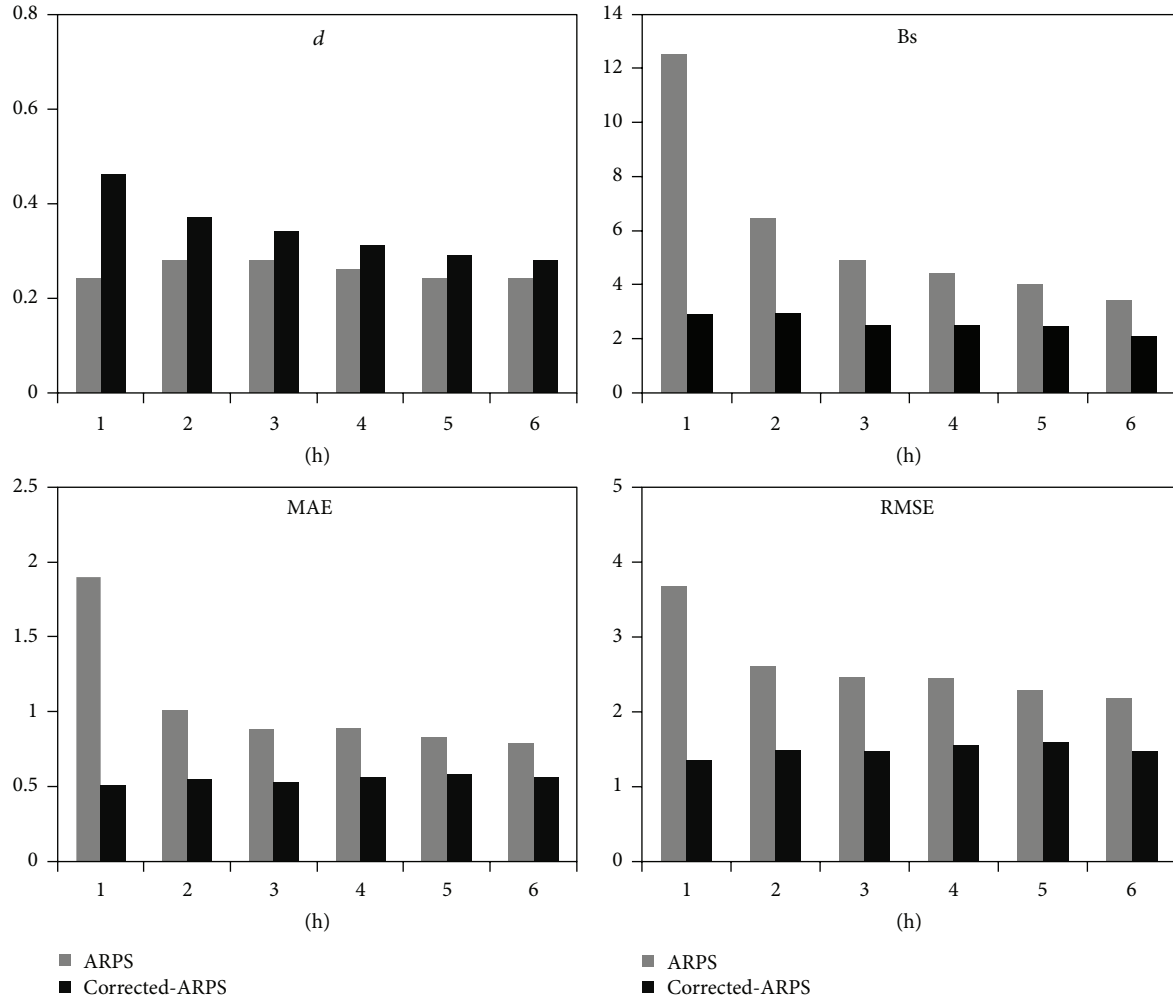


FIGURE 5: Average forecast performance indices over the considered three heavy precipitation events for lead times from 1 h to 6 h.

Even with atmospheric dynamic constraints and data assimilation techniques, the ARPS may not produce optimal forecasts for very short lead times due to its sensitivity to the initial field. In general, the ARPS model yields overestimated and widespread precipitation at a lead time of 1 h, which was confirmed by the significantly large bias and that most forecasts were concentrated in the top hand corner of Figure 6(a). The forecasting skill gradually improves with lead time; however the ARPS model overestimates precipitation at all of the considered lead times.

The amplitude correction scheme based on distribution function matching methods successfully improved the original ARPS precipitation forecasts, which can be confirmed by the considered performances indices of standard measures and both mean A-component and S-component of SAL. Especially at the lead time of 1 h, the amplitude correction scheme significantly reduces the forecast errors. It seems that the amplitude correction scheme effectively overcomes the problem of the ARPS sensitive to the initial field, resulting in the forecast skill of the corrected ARPS changing little with increasing lead time.

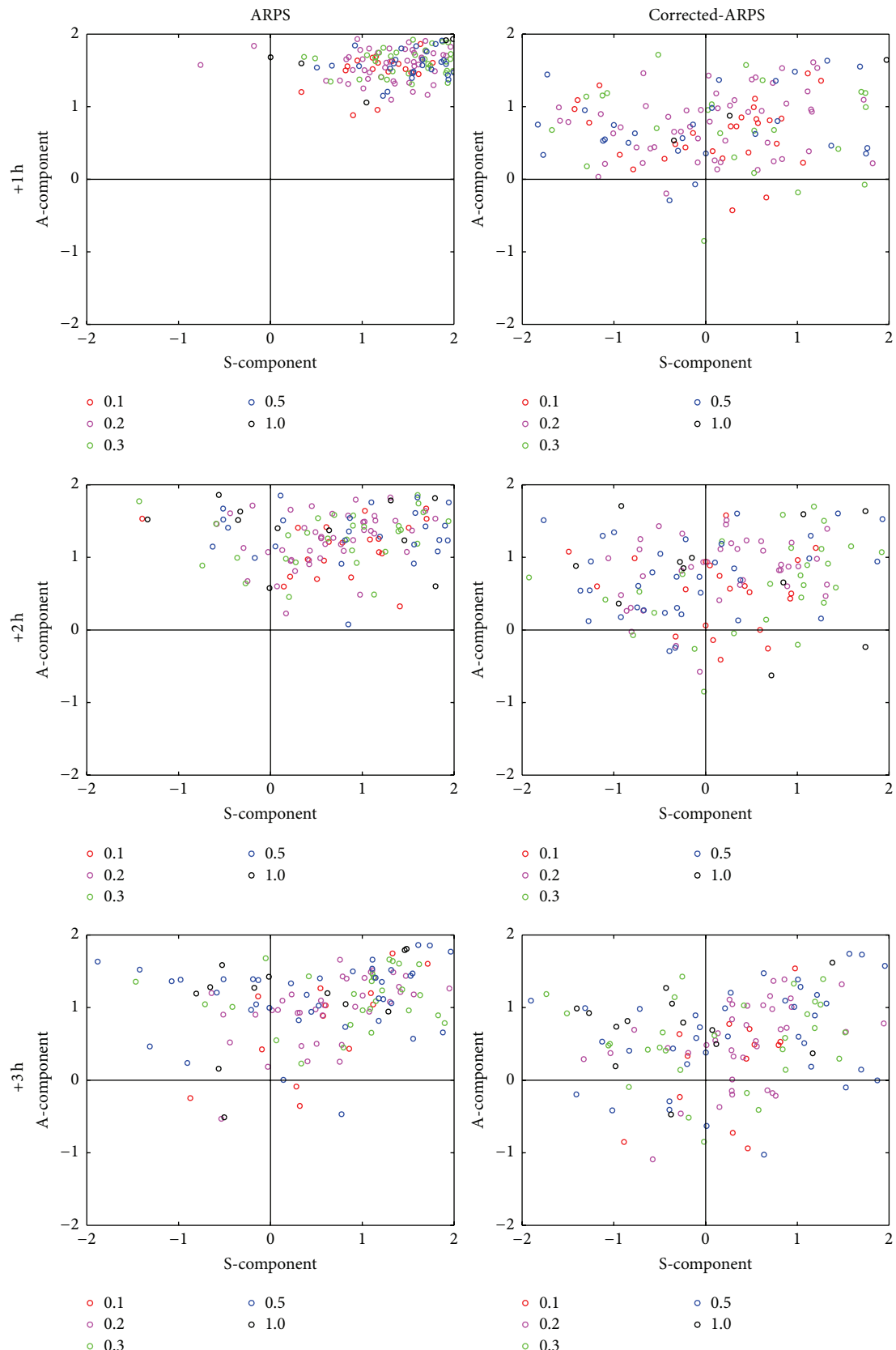


FIGURE 6: Continued.

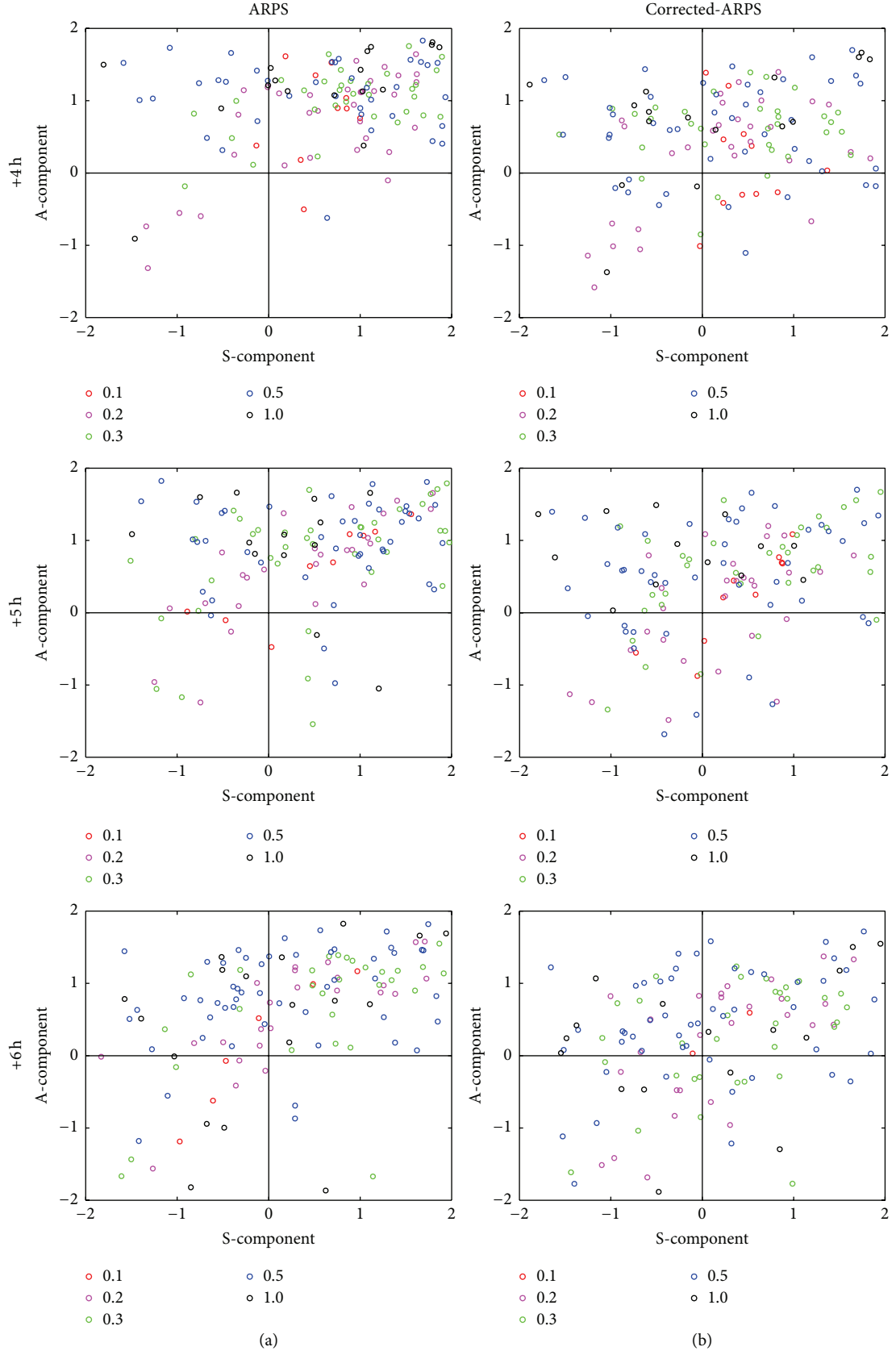


FIGURE 6: SAL diagrams for the hourly precipitation forecasts of the original (a) and the corrected (b) ARPS for lead times from 1 h to 6 h. Every circle indicates three components of SAL for a forecast. The L component is shown by the color of the circles.

The applicability and portability of the correction methods depend on the NWP forecasts and local precipitation types. The correction methods should be recalibrated if the methods are used for other area.

Competing Interests

The authors declare that they have no competing interests.

Acknowledgments

This study was supported by Beijige fund from Jiangsu Institute of Meteorological Science (Grant no. BJJG201303) and Major Science and Technology Program for Water Pollution Control and Treatment (2013ZX07304-001-1). The authors would also acknowledge Jiangsu Observatory for providing the datasets used in the study.

References

- [1] R. Daley, *Atmospheric Data Analysis*, Cambridge University Press, Cambridge, UK, 1991.
- [2] Z. Sokol and P. Pešice, “Comparing nowcastings of three severe convective events by statistical and NWP models,” *Atmospheric Research*, vol. 93, no. 1-3, pp. 397–407, 2009.
- [3] B. Macpherson, “Operational experience with assimilation of rainfall data in the Met Office mesoscale model,” *Meteorology and Atmospheric Physics*, vol. 76, no. 1-2, pp. 3–8, 2001.
- [4] S. S. Weygandt, A. Shapiro, and K. K. Droege, “Retrieval of model initial fields from single-Doppler observations of a supercell thunderstorm. Part I: single-doppler velocity retrieval,” *Monthly Weather Review*, vol. 130, no. 3, pp. 433–453, 2002.
- [5] S. G. Benjamin, D. Dévényi, S. S. Weygandt et al., “An hourly assimilation-forecast cycle: the RUC,” *Monthly Weather Review*, vol. 132, no. 2, pp. 495–518, 2004.
- [6] A. Caya, J. Sun, and C. Snyder, “A comparison between the 4D VAR and the ensemble Kalman filter techniques for radar data assimilation,” *Monthly Weather Review*, vol. 133, no. 11, pp. 3081–3094, 2005.
- [7] M. Tong and M. Xue, “Ensemble Kalman filter assimilation of Doppler radar data with a compressible nonhydrostatic model: OSS experiments,” *Monthly Weather Review*, vol. 133, no. 7, pp. 1789–1807, 2005.
- [8] Z. Sokol, “Utilization of radar reflectivity for a very short range precipitation forecast,” *Czech Meteorology Bull*, vol. 60, pp. 136–146, 2007.
- [9] Z. Sokol and P. Pesice, “Nowcasting of precipitation—advective statistical forecast model (SAM) for the Czech Republic,” *Atmospheric Research*, vol. 103, pp. 70–79, 2012.
- [10] A. Zahraei, K.-L. Hsu, S. Sorooshian et al., “Quantitative precipitation nowcasting: a lagrangian pixel-based approach,” *Atmospheric Research*, vol. 118, pp. 418–434, 2012.
- [11] W. Zhuang, L. P. Liu, Y. Q. Yu, and H. Y. Wang, “Improvement of the fuzzy logical technique for identifying ground clutter and its verification,” *Acta Meteorologica Sinica*, vol. 70, no. 3, pp. 576–584, 2012 (Chinese).
- [12] Y. J. Xiao and L. P. Liu, “Study of methods for interpolating data from weather radar network to 3-D grid and mosaics,” *Acta Meteorologica Sinica*, vol. 64, no. 5, pp. 647–656, 2006 (Chinese).
- [13] C. L. Cheng, M. X. Chen, J. J. Wang, F. Gao, and H. X. Yang, “Short-term quantitative precipitation forecast experiments based on blending of nowcasting with numerical weather prediction,” *Acta Meteorologica Sinica*, vol. 71, no. 3, pp. 397–415, 2013 (Chinese).
- [14] M. Xue, K. K. Droege, and V. Wong, “The Advanced Regional Prediction System (ARPS)-a multi-scale nonhydrostatic atmospheric simulation and prediction model. Part I: model dynamics and verification,” *Meteorology and Atmospheric Physics*, vol. 75, no. 3-4, pp. 161–193, 2000.
- [15] M. Xue, K. K. Droege, V. Wong et al., “The Advanced Regional Prediction System (ARPS)—a multi-scale nonhydrostatic atmospheric simulation and prediction tool. Part II: Model physics and applications,” *Meteorology and Atmospheric Physics*, vol. 76, no. 3-4, pp. 143–165, 2001.
- [16] M. Xue, D. Wang, J. Gao, K. Brewster, and K. K. Droege, “The Advanced Regional Prediction System (ARPS), storm-scale numerical weather prediction and data assimilation,” *Meteorology and Atmospheric Physics*, vol. 82, no. 1-4, pp. 139–170, 2003.
- [17] J. Smagorinsky, “General circulation experiments with the primitive equations. Part I. The basic experiment,” *Monthly Weather Review*, vol. 91, no. 3, pp. 99–164, 1963.
- [18] D. K. Lilly, “On the numerical simulation of buoyant convection,” *Tellus*, vol. 14, no. 2, pp. 148–172, 1962.
- [19] J. W. Deardorff, “Stratocumulus-capped mixed layers derived from a three-dimensional model,” *Boundary-Layer Meteorology*, vol. 18, no. 4, pp. 495–527, 1980.
- [20] V. C. Wong and D. K. Lilly, “A comparison of two dynamic subgrid closure methods for turbulent thermal convection,” *Physics of Fluids*, vol. 6, no. 2, pp. 1016–1023, 1994.
- [21] W.-Y. Sun and C.-Z. Chang, “Diffusion model for a convective layer—part I: a numerical simulation of convective boundary layer,” *Journal of Climate & Applied Meteorology*, vol. 25, no. 10, pp. 1445–1453, 1986.
- [22] Y.-L. Lin, R. D. Farley, and H. D. Orville, “Bulk parameterization of the snow field in a cloud model,” *Journal of Climate and Applied Meteorology*, vol. 22, no. 6, pp. 1065–1092, 1983.
- [23] S. T. Zalesak, “Fully multidimensional flux-corrected transport algorithms for fluids,” *Journal of Computational Physics*, vol. 31, no. 3, pp. 335–362, 1979.
- [24] J. Gao, M. Xue, K. Brewster, and K. K. Droege, “A three-dimensional variational data analysis method with recursive filter for Doppler radars,” *Journal of Atmospheric and Oceanic Technology*, vol. 21, no. 3, pp. 457–469, 2004.
- [25] K. A. Brewster, “Phase-correcting data assimilation and application to storm-scale numerical weather prediction. Part I: method description and simulation testing,” *Monthly Weather Review*, vol. 131, no. 3, pp. 480–492, 2003.
- [26] M. Hu, M. Xue, and K. Brewster, “3DVAR and cloud analysis with WSR-88D level-II data for the prediction of the Fort Worth, Texas, tornadic thunderstorms. Part I: cloud analysis and its impact,” *Monthly Weather Review*, vol. 134, no. 2, pp. 675–698, 2006.
- [27] M. Hu, M. Xue, J. Gao, and K. Brewster, “3DVAR and cloud analysis with WSR-88D level-II data for the prediction of the Fort Worth, Texas, tornadic thunderstorms. Part II: impact of radial velocity analysis via 3DVAR,” *Monthly Weather Review*, vol. 134, no. 2, pp. 699–721, 2006.
- [28] R. N. Hoffman and C. Grassotti, “A technique for assimilating SSM/I observations of marine atmospheric storms: tests with

- ECMWF analyses," *Journal of Applied Meteorology*, vol. 35, no. 8, pp. 1177–1188, 1996.
- [29] R. N. Hoffman, Z. Liu, J. F. Louis, and C. Grassotti, "Distortion representation of forecast errors," *Monthly Weather Review*, vol. 123, no. 9, pp. 2758–2770, 1995.
- [30] Z. Sokol, "Utilization of regression models for rainfall estimates using radar-derived rainfall data and rain gauge data," *Journal of Hydrology*, vol. 278, no. 1–4, pp. 144–152, 2003.
- [31] Z. Sokol, D. Kitzmiller, P. Pesice, and J. Mejsnar, "Comparison of precipitation nowcasting by extrapolation and statistical-advection methods," *Atmospheric Research*, vol. 123, pp. 17–30, 2013.
- [32] D. R. Legates and G. J. McCabe Jr., "Evaluating the use of 'goodness-of-fit' measures in hydrologic and hydroclimatic model validation," *Water Resources Research*, vol. 35, no. 1, pp. 233–241, 1999.
- [33] H. Wernli, M. Paulat, M. Hagen, and C. Frei, "SAL—a novel quality measure for the verification of quantitative precipitation forecasts," *Monthly Weather Review*, vol. 136, no. 11, pp. 4470–4487, 2008.
- [34] C. Lin, S. Vasić, A. Kilambi, B. Turner, and I. Zawadzki, "Precipitation forecast skill of numerical weather prediction models and radar nowcasts," *Geophysical Research Letters*, vol. 32, no. 14, Article ID L14801, 2005.
- [35] B. W. Golding, "Nimrod: a system for generating automated very short range forecasts," *Meteorological Applications*, vol. 5, no. 1, pp. 1–16, 1998.
- [36] A. R. Ganguly and R. L. Bras, "Distributed quantitative precipitation forecasting using information from radar and numerical weather prediction models," *Journal of Hydrometeorology*, vol. 4, no. 6, pp. 1168–1180, 2003.